Understanding the Thermal Conductance of Thin Film Structures for Improved Sensitivity and Refrigeration of Superconducting Microwave Polarimeters

by

A. H. Harke-Hosemann

B.S., University of Illinois at Urbana-Champaign, 2016

M.S., University of Colorado Boulder, 2020

A thesis submitted to the

Faculty of the Graduate School of the

University of Colorado in partial fulfillment

of the requirements for the degree of

Doctor of Philosophy

Department of Astrophysical and Planetary Sciences

2024

Committee Members:

Prof. Nils Halverson, Chair

Dr. Joel Ullom

Dr. Johannes Hubmayr

Prof. Lauren Blum

Dr. Brian Flemming

Harke-Hosemann, A. H. (Ph.D., Astrophysical and Planetary Sciences)

Understanding the Thermal Conductance of Thin Film Structures for Improved Sensitivity and Refrigeration of Superconducting Microwave Polarimeters

Thesis directed by Dr. Joel Ullom

The recent advent of low temperature detectors has enabled incredibly precise measurements of the sub-millimeter sky that have revolutionized our understanding of the origin, structure, and formation history of our Universe. One such detector technology is the transition edge sensor (TES) bolometer, a photon-noise-limited detector that takes advantage of the sharp change in resistance with temperature of a superconducting thin film biased into its phase transition. The sensitivity of TES bolometers increases with lower bath temperatures and lower thermal conductance to the bath temperature.

My PhD work has aimed to push TES sensitivity limits further on two fronts. First, I have studied and measured the thermal conductance of the membrane and microstrip wiring thin films that constitute the TES legs. I have found that in our case of very thin membranes, the thermal conductance of the often-neglected microstrip significantly dominates that of the membrane. Second, I have contributed to the development of integrating normal metal-insulator-superconductor junction refrigerators onto TES bolometers to cool the local TES bath temperature from 300 mK to below 150 mK. These devices have demonstrated TES cooling from 300 mK to 187 mK.

Dedication

To my parents, who deserve the world, and to my best friend & best dog Toby, who was my world and my rock through so many transitions.

Acknowledgements

I had the privilege of completing my scientific training at NIST with world-class experimentalists who are the absolute best at what they do and are exceedingly generous with their time. I could approach anyone asking,"Hey, are you busy?" and they would respond (somewhat dishonestly), "No, how can I help?" We would then head to my lab and stay there until we'd worked through the issue. This person was likely a world expert in the system we were debugging.

None of the work detailed in this thesis would have been possible without my advisor Joel Ullom's guidance and incredible intuition. No one else besides Shannon Duff, the best microfabrication hand in the West, could execute the complex NIS-TES fabrication. I will forever be impressed by Peter Lowell's patience and memory as he fielded questions on an experiment he had not touched in years. I was lucky to have a second mentor in Hannes Hubmayr, who took this role very seriously by providing many coffees. He also watered my office plants that one time. I am grateful to Nate Ortiz, who I relied on for his talents as an engineer and a machinist, and John Gard, who possesses a wealth of electronics expertise and always reminded me to use flux. I thank Nils Halverson for serving as a third mentor and sanity check, even though I don't think he was officially obligated to do so. I appreciate Tom Silva for helping this astrophysicist navigate the world of phonon physics.

My tenure as a graduate student has been made infinitely better by my union and the dear friends I have made while organizing. I commend the Department of APS for being a haven of compassion and quirkiness in academia. Finally, I owe so much to Carl Sagan, Kurt Vonnegut, & Ursula K. Le Guin, who remind me that despite how small our little world is in this vast universe, we are still so very significant.

Contents

Chapter

1 Introduction **1**

1.1 Gravitational Wave Cosmology 4

1.1.1 Primordial Soup 5

1.1.2 Gravitational Wave Background 6

1.1.3 Cosmic Microwave Background Polarization 8

1.2 Low Temperature Detectors for Precision Cosmology 10

1.3 A Brief History of NIS Refrigerators 13

2 Local SMBH Mass Function from the $M_\bullet$ - M_{bulge} Scaling Relation **17**

2.1 Background 20

2.1.1 Gravitational Wave Background 20

2.1.2 The Local Supermassive Black Hole Mass Function 21

2.1.3 Black Hole & Host Galaxy Scaling Relations 22

2.2 Methods 24

2.2.1 SDSS-DR7 Galaxy Sample 24

2.2.2 Bulge Fraction & False disc Corrections 26

2.2.3 Malmquist Bias Correction 28

2.3 SMBH Mass Function & Error Estimation 30

2.4 Schechter Function Fits 32

2.5 Literature Review . . . 34
2.6 Summary & Future Work . . . 36

3 Phonon Transport in Thin Films at sub-Kelvin Temperatures 39

3.1 Ballistic Phonon Transport . . . 41
3.1.1 3D Plane Waves . . . 42
3.1.2 Elastic Eigenmodes in Thin Films . . . 43
3.1.3 Ballistic Thermal Conductance . . . 50
3.1.4 2D-3D Transition of the Phonon Gas . . . 53
3.1.5 1D Ballistic Transport . . . 55
3.2 Diffusive Phonon Transport . . . 55
3.2.1 Diffusive Thermal Conductance . . . 56
3.2.2 Mean Free Path . . . 58
3.3 Total Thermal Conductance . . . 63
3.4 Film Thickness Dependence . . . 63
3.5 Future Work . . . 66

4 Thermal Conductance of Individual TES Leg Layers 67

4.1 Bolometers Under Test . . . 69
4.2 Thermal Conductance Modeling . . . 71
4.3 G of Individual Layers . . . 72
4.4 Discussion . . . 74
4.4.1 Literature Comparison . . . 74
4.4.2 Legacy Data G Predictions . . . 78
4.4.3 SO MF Saturation Power . . . 81
4.4.4 Noise Implications . . . 83
4.5 Summary & Conclusions . . . 85
4.6 Future Work . . . 86

5 Physics of NIS Refrigeration **87**

5.1 Motivation . . . 88

5.2 Junction Tunneling . . . 89

5.2.1 Occupied States in a Normal Metal . . . 89

5.2.2 Occupied States in a Superconductor . . . 89

5.2.3 Tunneling Across a Barrier . . . 91

5.2.4 Current in a Normal Metal / Insulator / Normal Metal Junction . . . 91

5.2.5 Current in a Normal Metal / Insulator / Superconductor Junction . . . 93

5.3 Cooling Electrons . . . 96

5.4 Cooling Phonons . . . 98

5.4.1 NIS Thermal Model . . . 98

5.4.2 Results . . . 107

6 NIS-cooled TES Bolometers **111**

6.1 NIS Refrigerator Junctions . . . 112

6.2 Transition Edge Sensors . . . 113

6.3 Experimental Apparatus . . . 116

6.3.1 Cryogenic Test Bed . . . 116

6.3.2 NIS Characterization . . . 122

6.3.3 TES Characterization . . . 126

6.3.4 NIS-TES Refrigeration Measurements . . . 131

6.4 Results & Discussion . . . 133

6.4.1 NIS-TES v1 & v2 . . . 133

6.4.2 NIS-TES v2b & v3 . . . 140

6.5 Future Work . . . 142

7 Future Work **144**

7.1 TES Leg Thermal Conductance Modeling . . . 144

7.2 NIS-TES Integrated Detectors 144

7.2.1 Impacts Beyond (Sub-)mm Astronomy 146

Bibliography **147**

Appendix

A Appendix **167**

A.1 Thermal Conductance Equations 167

A.1.1 G_{TES} of Bolometers 1-8 168

A.1.2 G_{leg} of Legs A-G 168

A.2 Non-Standard Width Scaling 169

A.3 Alternative Thin Film G Models 169

A.3.1 Four Layer Model 169

A.3.2 Constrained α Model 170

Tables

Table

2.1 Power law parameters for scaling relations between SMBH mass and various host galaxy properties. 24

2.2 Single and Double Schechter Function Fit Parameters with 1-σ errors. 32

3.1 G dependence on thin film geometry and associated α values in different phonon transport regimes. 65

4.1 Layer thicknesses in nm for each bolometer leg studied. S is the mechanical substrate consisting of a SiO_x-SiN_x bi-layer, W1&2 are Nb wiring layers, and I1&2 are SiN_x insulating layers. W1-W2 and I1-I2 stacks are treated as a single layer. 69

4.2 Leg geometries and G_{TES} values of the TES bolometers in this study. Legs A-G refer to film stack geometries in Table 4.1. 70

4.3 Fit parameters and the resulting G_{micro} for the constrained and unconstrained models. Reduced chi-squared (χ^2_ν) values are included for comparison. G_x values are the normalized thermal conductances G_0 for a single 400-nm-thick × 5-µm-wide × 220-µm-long layer of type x, and the thermal conductance of a film with thickness d is $G_0(d/d_0)^{1+\alpha}$. 74

5.1 Σ and n_{ep} measurements for AlMn. 98

5.2 Table of parameters used in example power balance model. These parameters are representative of measurements from NIS-TES v2 devices. 107

6.1 TES parameters from the power law fit in Figure 6.13 at 80% R_N. All parameters with a temperature dependency, i.e., G(T) and $P_{sat}(T)$ are evaluated at 168 mK. . . 130

6.2 The NIS-TES v1 and v2 devices with the best cooling performance. TES power law parameters are evaluated at 70% R_N and 156 mK. Cooling experiment measurements and projected cooling from 300 mK with eight live junctions are given at the bottom. 136

Figures

Figure

1.1 CMB temperature, E-mode polarization, and B-mode polarization power spectra with measurements from various observatories summarized in Choi et al. 2020 [28]. The primordial B-mode signal calculated for $r = 0.1$ is also shown. 9

1.2 The phase transition of a superconducting film with $T_c \sim 96$ mK. Figure originally from [47]. 11

2.1 A conceptual strain spectrum h_C for frequency bands covered by multiple detection strategies from [24] (adapted from a figure by NANOGrav). The figure emphasizes the complementary nature and frequency sensitivities of the multiple strategies, including the search for primordial gravitational waves (PGWs) in the cosmic microwave background (CMB) in the lowest frequency band followed by PGWs and SMBH binary radiation observed at higher frequencies with PTAs. The inset highlights the predicted GWB and limits in the PTA band current at the time of publishing, adapted from Shannon et al. 2015 [97] with updates from Arzoumanian et al. 2015a [11] and Lentati et al. 2015 [62]. 19

2.2 (a) Redshift, (b) stellar mass, and (c) r-band apparent magnitude cuts on the M+13 catalog when constructing the galaxy sample. Greyed areas represent galaxies in M+13 that were removed from our sample. 26

2.3 Bulge fraction of the sample as a function of redshift and stellar mass. 27

2.4 Mass function from bulge mass scaling relation. (a) shows the majority of the distribution and (b) highlights black holes with $M_\bullet > 10^6 M_\odot$, i.e., the black holes expected to contribute significantly to the GWB. 31

2.5 Single and Double Schechter Function fits to supermassive black hole mass function of sample from bulge mass scaling relation. 33

2.6 Comparison of SMBH mass functions calculated using various host galaxy scaling relations in the literature. The MF calculated in this work is given by black points for all galaxies in (a) and blue points for elliptical galaxies in (b). Marconi et al. 2004 [70] calculate a MF from luminosity scaling relations for all galaxies (a) and early type galaxies (b). Shankar et al. 2009 [96] summarize a range of mass functions calculated $M_\bullet$-L_{bulge}, $M_\bullet$-σ, and $M_\bullet$-$M_\star$ scaling relations. 35

2.7 Summary of pulsar data collection for the 15-year NANOgrav data set from [7]. Top: Sky locations of the 67 pulsars observed. Observatories include the Very Large Array (VLT), Arecibo Observatory (Arecibo), and Green Bank Telescope (GBT). Bottom: Angular separations probed in the data. 37

3.1 The dominant phonon wavelength λ_D at sub-Kelvin temperatures in amorphous SiN_x. 40

3.2 (a) Schematic of a thin film with thickness d, width w, and length L. (b) Reflections of horizontal (H), symmetric (S) and antisymmetric (A) polarized plane waves at the boundaries of a semi-infinite plane, located at $\pm d/2$. H modes depicted on the left are polarized parallel to the film boundaries. Reflections at the boundary couple the S and A Lamb modes. Depicted on the right is an incident A mode that reflects into both A and S polarizations. 44

3.3 Behavior of antisymmetric (A) and symmetric (S) Lamb modes. The dotted lines represent the equilibrium position $\mathbf{r}$. The displacement from the equilibrium $\mathbf{u}(\mathbf{r},t)$ is also shown. 46

3.4 Normalized dispersion curves of a thin film separated by polarization into the antisymmetric Lamb (A), symmetric Lamb (S), and horizontal (H) modes. The inset highlights the low temperature behavior of the acoustic modes. 49

3.5 Numerical calculations of G for a 5-µm-wide thin film of a-SiNx at 170 mK. The minimum conductance occurs at d_c=139 nm. Red dashed lines are power law fits to calculations for the thinnest and thickest d values, which approach the elastic theory predictions that the ballistic G $\propto 1/\sqrt{d}$ for $d << d_c$ and G $\propto d$ for $d >> d_c$. 54

3.6 The diffusive boundary scattering effect on the phonon path. The red arrows indicate the mean free path in the thermal gradient direction $\ell_x = \ell' \cos\phi$, where ℓ_i is the mean free path of intrinsic scattering mechanisms. The mean free path magnitude ℓ' is equal to ℓ_i for $\phi \leq \phi_i$ and is shortened by the boundary for larger ϕ. For $\phi > \phi_i$, the phonon scatters diffusively at the boundary and $\ell' = \ell_i \sin\phi$. 59

3.7 Example calculation of the mean free path ℓ including boundary effects normalized to the mean free path assuming no diffusive boundary scattering for various P_d. The inset is the corresponding calculation of ϕ_i. Contributions from angles limited by intrinsic scattering $|\phi| \leq \phi_i$ and angles at which phonons diffusively scatter off the film boundaries $|\phi| > \phi_i$ are also shown. We set ℓ_i= 20 µm and d = 1 µm. 61

3.8 Calculations of ℓ as a function of d/ℓ_i for diffuse scattering probabilities of 10%, 50%, and 100%. 62

3.9 Total G as a function of length through the ballistic-diffusive transition. 64

4.1 a) One TES bolometer under test. The AlMn TES is a thin film in the middle of the island suspended from the thermal bath via four 220 µm-long, 5 µm-wide legs. b) The cross-section of a TES leg on device (a) imaged with FIB-SEM. This leg consists of a full microstrip (W1-I1-W2-I2) on top of the substrate (S). 70

4.2 G_{TES} data (red) and model predictions (★) for Bolos 1-8 are shown as a function of the cross-sectional area of all four TES legs. Contributions from the S (⧫), W (ForestGreen), and I layers (Plum) are also shown. The residuals are normalized with respect to the prediction errors. 75

4.3 Mean free paths normalized by the square root of the width in various thin film SiN_x beams. S and I are measurements in this work. W+11 [113] mean free paths from two wafers in which they measure 21% (squares) and 29% (circles) diffusive reflection at the boundaries in 1-um-thick x 640-um-long Si3N4 beams at various widths. K+06[52] markers correspond to those in the original figures. 77

4.4 Thermal conductance measurements and model predictions for various CMB telescope TES bolometers fabricated at NIST Boulder. Bolometer 1 measurement and model prediction are also shown. The residuals are normalized with respect to the prediction error. 79

4.5 Model predictions (black stars) compared to predictions from scaling $P_{sat} = 4.1$ pW linearly with film dimensions (red circles). Residuals as a % of the measured value are also shown. 82

4.6 SO MF bolometer P_{sat} predictions a) treating I1 & I2 as separate layers over the entire leg compared to b) treating I1-I2 as a single layer for leg widths beyond W1. . 83

4.7 Model predictions of thermal fluctuation NEP $\pm 1\sigma$ for Bolometer 1 with and without microstrip wiring layers for a range of leg widths. Film dimensions are otherwise identical to Leg A in Table 4.1, with a ∼400-nm-thick substrate bi-layer. W1 layers are as wide as the leg until reaching a maximum width of 5 µm. All W2 layers are 2 µm skinnier than W1. 84

5.1 Occupation diagram of (a) an unbiased and (b) a voltage biased NIN junction. The dotted line indicates the Fermi energy ϵ_F. The junction is at a nonzero temperature, and thus the state occupation is "smeared." In (b), the energy level in the normal metal is raised by eV_{bias}. When biased, the electrons on the left can tunnel over to the available states on the right. 92

5.2 Occupation diagram of (a) an unbiased and (b) a voltage biased NIS junction. The dotted blue line indicates the Fermi energy ϵ_F. Δ is the gap energy of the superconducting metal layer. The density of states in the region $\epsilon_F \pm \Delta$ is 0. The junction is at a nonzero temperature, and thus the state occupation is "smeared" in the normal metal. In (b), the energy level in the normal metal is raised by eV_{bias}. The highest energy, i.e., hottest, electrons will tunnel across the insulating layer into the available states above $\epsilon_F + \Delta$ in the superconducting layer. 95

5.3 Normalized IV Characteristic of an NIS junction at various fractions of T_C in (a) linear and (b) log scale. At 0 K (in blue), there is no current at voltages below Δ. Above 0 K, thermal smearing allows the hottest electrons to tunnel through the junction. At voltages above Δ, the junction behaves as a resistor with constant dV/dI. At temperatures above T_c, the superconductor is normal and the junction behaves as a resistor at all voltage biases. 95

5.4 Power deposited in the normal metal electron system from the tunneling current driven by V_b at various ratios of T/T_c. Negative power indicates electron refrigeration. 97

5.5 Infinitesimal element of our 1D thermal model described by Equation 5.20. 100

5.6 Profile view of a NIS cooler integrated onto one TES leg, not to scale. A top view of one such leg is highlighted in the inset. Region 1 extends from the wafer to the edge of the NIS junction. Region 2 represents the dead length in which the substrate extends past the junction. Positive dead length is shown in (a), and negative dead length is shown in (b). No dead length is ideal for cooling performance. For better electron-phonon coupling, the normal metal extends onto the membrane in Regions 3 & 4, and in Region 4, another normal metal is added for thermalization. Region 5 is the leg between the cold finger and the TES. Region 6 is the TES bolometer. . . . 102

5.7 Electron-electron (ee), electron-phonon (ep), and phonon-phonon (pp) thermal conductances for a 20-µm-wide × 100-µm-long cold finger consisting of a 30-nm-thick film of AlMn on a 420 nm thick film of SiN_x. Between 70 mK and 500 mK, $G_{ee} > G_{ep} > G_{pp}$. 106

5.8 The various power loads on the electrons and phonons described in Equation 5.26. . 106

5.9 Sample result from the power balance model. The temperature at no voltage bias is the bath temperature. The electron temperature refers to the electron temperature in the normal metal of the junction. 108

5.10 Electron and phonon temperatures along the cold finger of a single leg cooled with two junctions illustrated in Figure 5.6 with a 5 µm dead length (DL) (a) excluding the power load from the microstrip P_{MS} and (b) including P_{MS}. T_e and $T_{p,N}$ are the electron and phonon temperatures in the AlMn base electrode of the NIS junction. $T_{p,MN}$ is the phonon temperature of the microstrip running parallel to the cold finger along the TES leg. The 80-µm-long Ti-Au thermalization layer (TL) begins 20 µm after the NIS junction and 15 µm after the DL. $T_{p,N}$ at the end of the thermalization layer is 19 mK higher when the microstrip is included. 110

5.11 T_e, $T_{p,N}$ and $T_{p,MS}$ at the end of the thermalization layer for various dead lengths. . 110

6.1 Scanning electron scanning microscope images of two NIS junctions in series. (a) Tunneling current flows from the left-side superconductor through the normal metal base electrode into the superconductor on the right. Overlayer quasiparticle traps (OLTs) sit atop the S layers. The 30-nm-thick base electrode is barely visible. (b) Another SEM cross-section of a similar structure, but zoomed into the center structure. The junction sits on top of a SiO_x-SiN_x bi-layer membrane, all on a Si wafer. . 114

6.2 A photo of an integrated NIS-TES device. The white dashed line highlights the deep etch outline, which defines where the membrane is released from the Si substrate. Two NIS junctions are visible at the end of each TES bolometer leg. 115

6.3 (a) The TES bias circuit, and (b) the Thévenin equivalent of the TES bias circuit, adapted from Irwin & Hilton 2005 [47]. 115

6.4 (a) Photograph of the wet cryostat, including the electronics tower and the liquid cryogen tanks. (b) Photograph of the ADR unit and cold stages. 117

6.5 Photographs of the dry cryostat. (a) The cryostat configuration while taking measurements with a room-temperature magnetic field surrounding the sealed vacuum jacket. (b) The cold stages of the cryostat. All components are thermalized to the 4K plate except for the sample box, which is thermalized to the FAA at 50 mK, and the loom wires, which are heat sunk to the GGG at 1 K on their way to the sample box. (c) The cryostat with the vacuum and radiation shields removed. The cold stage in (b) exists below the 4 K plate. 118

6.6 (a) Side view and (b) top view of the ADR unit in the wet dewar. The salt pills are at the center of the unit and are surrounded by the magnet solenoid, which is seated inside μ-metal magnetic shielding. 119

6.7 Photographs of the ADR unit in the dry cryostat, progressively removing components towards the ADR salt pills. a) The ADR package inside the thermalization shell made of gold-plated copper. b) The μ-metal magnetic shielding around the ADR magnet inside the thermalization. c) The solenoid that houses the superconducting magnet. d) The FAA and GGG salt pills inside the superconducting magnet. 119

6.8 Photograph of the 50 mK sample box. Four-wire filtering and protection diodes are located on the right of the box. Chips are mounted on the left. Stage 1 SQUIDs (SQ1) and TES voltage bias shunt resistors R_{sh} are used for TES readout. Samples are mounted on Cu stages for thermal sinking. The sample box RuOx thermometer is located near the samples between two SQ1s. NIS four-wire measurement lines are connected to the μ-D connectors on the right. TES readout lines and connections to the RuOx thermometer are connected to the μ-D on the left. 121

6.9 The four-wire measurement circuit of the voltage V and current I across two NIS junctions in series, each with resistance R_{jnc}. 122

6.10 a) Theoretical isothermal IV characteristics and IV measurements of 8 NIS junctions in series from different bath temperatures. Both the data and the theoretical IVs transition out of the subgap and onto the normal branch at ∼1.5 mV. For a single junction, we measure a Q value of 3113 and $\Delta = 187.2$ eV, which is consistent with $8 \times \Delta/e$ ∼1.5 mV. b) NIS junction electron temperature at each data point in (a) interpolated from the isothermal theory curves. 125

6.11 Measurement of TES saturation power at T_b=156 mK. 126

6.12 Circuit diagram of the SQUID-based TES readout circuit. At 100 mK, the current through the TES is inductively coupled to the stage 1 (S1) SQUID. SQ1 is also inductively coupled to the SQ1 feedback line, which injects a null current monitored and controlled by a feedback box at room temperature. At 4K, the SQUID array (SQA) amplifies the signal from SQ1 before sending it to the feedback box. The raw TES signal is the nulling bias in the SQ1 feedback line. 127

6.13 Characterization of the TES on the best-performing NIS-TES v2 device. IV characteristics were taken at a range of bath temperatures between 156 mK and 240 mK. The inset shows P_{sat} measurements from these IV characteristics evaluated at 70% R_N. These P_{sat} measurements are fit to Equation 6.4, and the resulting best fit parameters are given in Table 6.1. 129

6.14 (a) Cooling experiment for the best-performing NIS-TES v1 device that cooled the TES from 300 mK to 187 mK at the optimal NIS bias of 2.8 mV. The solid colored lines are TES temperature calibration IVs taken with the NIS off. The dashed curves are IVs taken while iterating through NIS V_{bias} at a 300 mK bath temperature. The optimal NIS bias is highlighted as a black solid line (b) Interpolated TES temperature at each NIS voltage bias using the calibration curves in (a). 132

6.15 TES noise measurements at 165 mK. The orange curve is with NIS bias off, and the blue curve is with NIS bias on. 134

6.16 AMF scans of (a) the vendor SiN_x substrate and (b) the NIST-grown substrate. Note that (a) and (b) have different color bars. 135

6.17 Dead length (DL) comparison between an NIS-TES (a) v1 and (b) v2 device. The v2 device DL is $\sim$ 5µm. The NIS refrigerator junctions are to the left of the TES leg, and the cold finger (CF) is the normal metal base electrode that extends onto the TES on the right. The top photo is an NIS-TES device, with the region imaged in (a) and (b) highlighted. 137

6.18 Model predictions for TES temperature vs TES thermal conductivity with P_{TES} set to 0.5 pW. In (a), κ_0 is the measured NIS-TES v1 thermal conductivity of 272 pW/(K μm) at 156 mK. The beige area covers the 80% to 325% thermal conductivity range measured in the v2 devices. The gray dotted line is the maximum cooling measured with a v2 device. In (b), we instead scale κ_0 to 797 pW/(K μm), the value necessary to predict the v1 data point. We also scale the v2 κ range accordingly. 139

6.19 SEM image of a cold finger. The normal metal base electrode extends onto the SiN_x TES leg with a TiAu thermalization layer. 141

A.1 Constrained model predictions of a) the devices under test and b) the CMB legacy bolometer data. 170

Chapter 1

Introduction

Jobu Tupaki: Every new discovery is just a reminder –

Evelyn Wang: We're all small & stupid.

Everything Everywhere All At Once [1]

The recent advent of low temperature detectors has enabled incredibly precise measurements of the (sub-)millimeter sky, ushering in the age of precision cosmology. These measurements continue to revolutionize our understanding of our Universe's origin, structure, and formation history and the galaxies within. Spectral surveys in the (sub-)mm enable mapping the star formation history from cosmic noon to reionization, epochs inaccessible to Spitzer and Herschel [23, 32]. Precise measurements of the temperature and polarization of the cosmic microwave background (CMB), which peaks at $\sim$1 mm, have told us that the Universe is both flat and isotropic and has placed tight constraints on the curvature, baryon density, and dark matter density of the Universe [9]. The thermodynamic properties of galaxies and galaxy clusters can be measured through the spectral distortion of the CMB known as the Sunyaev Zel'dovich effect, and the gravitational lensing of the CMB allows us to map the matter between us and the surface of last scattering [44]. CMB polarimetry can distinguish between inflationary, cyclic, and bouncing models of the Universe by measuring the primordial gravitational wave B-mode signal in the polarization of the CMB [2, 51]. Measurement of this signal would provide insight into the early origins of our Universe.

The most widely accepted cosmological paradigm is inflation, the theory that the very early

Universe underwent an epoch of exponential expansion. After this epoch, the Universe continued to expand, though at a much slower rate. Eventually the Universe cooled enough for photons to decouple from baryons, filling the Universe with the background radiation now known as the cosmic microwave background. While inflation explains many cosmological observations confirmed with precise measurements of the CMB, cosmologists have yet to prove inflationary theory with direct evidence. Many experiments online today are searching for inflation's unambiguous signature in the CMB polarization: divergence-free "B-modes" imprinted onto the CMB by inflationary gravitational waves. Detecting this signal would provide the first strong experimental evidence of inflationary theory.

Millimeter and submillimeter wavelength astronomy is a contemporary window through which to probe the CMB and the high redshift Universe. Cryogenic superconducting detectors are the technology of choice for these wavelengths due to their high sensitivity and suitability for scaling into imaging arrays. The transition-edge sensor (TES) is a superconducting film electrically biased into the sharp superconducting-to-normal phase transition. Microwave polarimeters based on TESs are used in numerous contemporary instruments to measure the polarization of the CMB.

In a TES, lower operation temperatures decrease both Johnson and phonon noise. Additionally, lowering the bath temperature allows for a larger thermal conductance, and thus more mechanically robust geometries, without increasing phonon noise. Many experiments access temperatures below 300 mK, the bath temperature provided by pumped ^{3}He, by adding an adiabatic demagnetization refrigerator (ADR) or a dilution refrigerator (DR) to their cooling chain. ADRs exchange heat and magnetic energy in a paramagnetic salt pill to control the temperature of the test bed, with a typical base temperature below 100 mK in astronomical applications. DRs cool by mixing pure ^{3}He with a ^{3}He-^{4}He mixture. Adding either an ADR or a DR to the cooling chain introduces mass, power consumption, complexity, and magnetic shielding in the case of an ADR. Observations in the sub-mm must also mitigate water absorption and emission in the atmosphere, a disadvantage experiments attempt to circumvent with high-altitude ground-based sites, balloons, or satellites. The complexities involved with adding a DR or ADR become significant issues on

a mountaintop, in Antarctica, on a balloon, or in space where the power and mass budgets are limited.

The work herein will push the sensitivity limits even further, enabling tests of inflation by searching for the B-mode signal in the CMB. In this work, I discuss research and development (R&D) of solid state on-chip refrigeration of TESs using Normal metal-Insulator-Superconductor (NIS) junction refrigerators, developing a simpler and more economical means of reaching 100 mK bath temperatures than currently exists. This work is done with the Quantum Sensors Division at the National Institute for Standards and Technology (NIST). We have integrated NIS refrigerators onto TESs to provide localized cooling to the detector, and the goal of this work is to cool TES bolometers from a bath temperature of 300 mK to 100 mK or below.

The first NIS-TES integrated prototypes demonstrated NIS refrigeration of TES bolometers from a bath temperature of 300 mK to 187 mK with seven functional NIS junctions of the eight on the device. These prototypes suffered from a low junction yield of $\sim 50\%$, which we remedied in the second iteration by moving to a smoother substrate. With this change, we recovered $\sim$100% NIS junction yield but measured a significant reduction in cooling performance. We investigate potential explanations for the discrepancy between the two prototypes and suspect that extra thermal loading from the substrate hinders cooling performance. We aim to recover and surpass the cooling performance of the first prototypes by suppressing the thermal conductance between the substrate and the TES membrane in future iterations.

Towards this end, we have studied the thermal conductance of TES bolometers suspended on thin-film membranes, including the often neglected contributions from the microstrip wiring layers. Thermal conductance is a crucial TES design parameter because it sets the thermal fluctuation noise and detector saturation power. Thermal transport in thin films is more complex than the familiar diffusive transport in bulk materials and, depending on the transport regime, can scale with thin film geometry in non-intuitive ways. If thermal transport is poorly understood, detector R&D can be an unnecessarily prolonged process involving multiple iterations of detector geometry.

We find that in our case of very thin membranes ($\sim$ 400 nm), the TES microstrip not only

contributes significantly but dominates the thermal conductance of the membrane by nearly a factor of 4, equivalent to $> 100\%$ increase in thermal fluctuation noise equivalent power. Therefore, for TESs with saturation powers of picoWatts, the microstrip layers must be included in noise predictions during detector design.

We have predicted the thermal conductance of various other CMB TES bolometers fabricated in the NIST clean room over the past decade using these measurements. Despite having significantly thicker membranes and wider legs than the bolometers under test, we find excellent agreement between our predictions and the measured thermal conductances for bolometers with leg lengths < 1 mm. This model also accurately predicts the saturation power of Simons Observatory mid-frequency prototype bolometers and explains the measured non-linear scaling with leg dimensions.

1.1 Gravitational Wave Cosmology

Inflationary theory has been widely adopted as the standard cosmology with the addition of dark energy and cold dark matter. This is primarily because inflation solves many issues that plagued early Big Bang models, such as the horizon and flatness problems. Increasingly precise measurements of the CMB power spectra have placed progressively tighter constraints on cosmological parameters, continuing to rule out alternative cosmological theories and validate predictions from inflationary theory.

Cosmological inflation explains the observed homogeneity of the Universe reflected in the high degree of CMB isotropy to nearly one part in 10^5. It does this by placing regions now separated to superhorizon scales initially into causal contact. Additionally, the exponential expansion during inflation flattens any initial curvature in the geometry of the Universe. This prediction agrees with Planck's CMB angular power spectrum measurements that restrict the Universe to a flat geometry within 1% [86].

Yet in all its elegance and insight, inflationary theory has yet to be proven with direct evidence. Observational cosmologists are searching for such evidence in the relic radiation of the Big Bang. To understand these signals echoing from the inflationary epoch, we must first understand

the initial conditions of the infant Universe.

1.1.1 Primordial Soup

In the beginning, our Universe was condensed into an extraordinarily hot, fully ionized primordial soup of photons and baryons. The constant scattering between photons and electrons in this plasma state produced an opaque and incredibly isotropic universe. The only deviations from this equilibrium were density perturbations caused by quantum fluctuations of the inflation field.

The accelerated expansion marking inflation stretched the Universe by a factor of 10^{25} in 10^{-33} seconds. This amplified the quantum fluctuations to superhorizon scales, breaking causal contact within the photon-baryon fluid and freezing these overdensities in place. These quantum-scale fluctuations seeded gravitational instabilities that, over the intervening $\sim$13 billion years, would grow into filaments of galaxy clusters arranged in a cosmic web.

As the Universe expanded, it eventually cooled enough for the electrons and protons to combine into neutral hydrogen, releasing the relic radiation from the Big Bang. This phase transition is referred to as the epoch of recombination, which occurred when the Universe was 380,000 years old. The location of the CMB photon-baryon decoupling is known as the surface of last scattering.

The CMB photons released during this sudden (cosmologically-speaking) transition provide a snapshot of the primordial plasma during recombination, capturing both the overwhelming homogeneity and the extremely minute quantum-level fluctuations that seeded the large scale structure of the Universe. The opacity of the Universe before recombination prevents us from observing our Universe beyond the surface of last scattering, where the initial conditions of the CMB were set.

In addition to the scalar density perturbations, the unrelenting expansion of spacetime during inflation amplified tensor perturbations to produce an isotropic background of inflationary gravitational waves. These gravitational waves would have left an imprint on the polarization of the CMB and could fall into the nHz gravitational wave band of pulsar timing arrays. The magnitude of these signals will be very small and are still unknown. However, these uncertainties fail to deter observational cosmologists as detection of these primordial gravitational waves – either directly with

a gravitational wave observatory or through the inflationary signature in the CMB polarization – would provide unambiguous evidence for inflationary theory.

1.1.2 Gravitational Wave Background

Cosmology considers the properties and history of the Universe in its entirety. This breadth of scale contains the most extreme phenomena allowed by nature, from galactic collisions to the accelerating expansion of spacetime to phase transitions of the Universe itself. Similar to how the extremely energetic process of nuclear fusion in a stellar core results in the emission of electromagnetic radiation, cosmological events involving supermassive objects and distortions of the spacetime metric emit gravitational wave radiation in the form of ripples in spacetime. Humans have been observing electromagnetic radiation for centuries, progressively expanding our observation capabilities into larger portions of the electromagnetic spectrum. All the while, gravitational radiation has passed through the Earth undetected.

Although Einstein predicted the existence of gravitational waves in 1916 [34], it wasn't until recent decades that we have been able to listen for this cosmic messenger. In 2002, observational cosmologists began measuring the CMB polarization to search for evidence of inflationary gravitational waves [56]. That same year, the Laser Interferometer Gravitational-Wave Observatory (LIGO) began using laser interferometry to detect length changes caused by gravitational waves passing through two 4-km-long beams. In 2005, the North American Nanohertz Observatory for Gravitational Waves (NANOGrav) began monitoring a collection of pulsars in an observing strategy referred to as a pulsar timing array to search for a stochastic gravitational wave background in the nHz band [31].

Advanced LIGO would first detect gravitational waves in 2015 [3], almost a century after Einstein's prediction. In 2022, NANOGrav detected the stochastic gravitational wave background, and CMB observations have placed increasingly stringent limits on the amplitude of the primordial gravitational wave signal. Through these experiments and future gravitational wave observatories, we can test our models of cosmology at more extreme energy scales than are accessible with light.

The dominant source of gravitational wave background detected by NANOGrav is expected to be inspiraling supermassive black hole (SMBH) binaries. SMBH binaries are created when the black holes at the center of two merging galaxies become gravitationally bound. Correlations between SMBH mass and host galaxy properties suggest that the two co-evolve, and therefore galaxy formation history should influence the SMBH binary gravitational wave background signal.

One challenging aspect of modeling galaxy evolution is explaining the variety of observed galaxy morphologies. Hubble categorized regular galaxies as ranging from featureless elliptical galaxies with randomly oriented stellar orbits to grand design spiral galaxies, whose stars are so elegantly arranged into arms of a spiraling disk that they seem to suggest divine intervention [45].

Contemporary models favor a "bottom-up" evolution history in which galaxies begin as structured spirals and evolve into ellipticals through multiple galaxy mergers [101]. Hierarchical structure formation is consistent with Λ cold dark matter (ΛCDM) cosmology, where the first galaxies were formed around gravitational instabilities seeded by quantum fluctuations in the primordial plasma. These first galaxies merged into larger galaxies through mutual gravitational attraction, further amplifying these gravitational instabilities and leading to more galaxy mergers. This is consistent with measurements of galaxy mass distributions shifting to higher mass with lower redshift.

The opposite has been observed for black hole formation history, in which lower mass black hole populations increase at lower redshifts. Though seemingly contradictory, a hierarchical galactic evolution paradigm does not necessarily conflict with an anti-hierarchical black hole growth, which could be a symptom of the physics of black hole accretion and the dynamics of dark matter halos [106]. The implications of this are that the majority of SMBHs that contribute to the GWB will exist at the centers of the older, more massive elliptical galaxies and that black hole formation is driven by the galaxy mergers that pair black holes into binary systems [43].

The SMBH mass function determines the strength of the GWB signal and is inextricably tied to the cosmological context and galaxy formation history through SMBH-host galaxy co-evolution. The cosmological implications of this now-detected signal are an active area of research. The influence and effect of cosmology on the interpretation of the GWB signal will co-evolve as our

understanding of the local SMBH mass function and the GWB signal-to-noise ratio grow.

1.1.3 Cosmic Microwave Background Polarization

Measurements of the CMB power spectra are responsible for much of what we understand about the particular cosmology of our Universe. From the temperature anisotropy power spectrum, we now know that the Universe is flat and that it consists of 27% dark matter and 5% baryonic matter. The polarization spectra provide complementary constraints on the cosmological parameters from the temperature power spectrum. The CMB polarization can also isolate signals from the reionization and inflationary epochs.

Both the scalar and tensor perturbations in the inflaton field polarize the CMB photons through Thomson scattering, the elastic scattering of photons and charged particles. Polarization patterns can be separated into curl-free E-modes and divergence-free and B-modes. Scalar density perturbations only produce E-modes, while the gravitational wave signature, or tensor perturbations, would produce a mixture of E- and B-modes. Any CMB photon-baryon interactions between the surface of last scattering and observation today would produce the same E-mode polarization as the scalar perturbations from inflation. Gravitational lensing can convert E-modes to B-modes on sub-degree scales, but no cosmological processes are expected to produce B-modes on angular scales larger than a degree.

In recent decades, observational cosmologists have been thoroughly mapping the polarization of this relic radiation from the high deserts of the South Pole and the Chilean Andes [14, 65, 4]. The Degree Angular Scale Interferometer first detected E-modes in 2002 [56]. Lensing B-modes were observed in 2013 [42], yet B-mode signals at large angular scales remain elusive.

Measurements of the CMB temperature, E-mode polarization, and B-mode polarization power spectra from [28] are shown in Figure 1.1. The multipole moment ℓ[1] increases with decreasing angular scale θ. The power spectrum amplitude represents the square of the temperature anisotropy magnitude $(\Delta T)^2$. Notably, the polarization signals are orders of magnitude smaller

[1] Beyond this introduction, ℓ refers to the phonon mean free path.

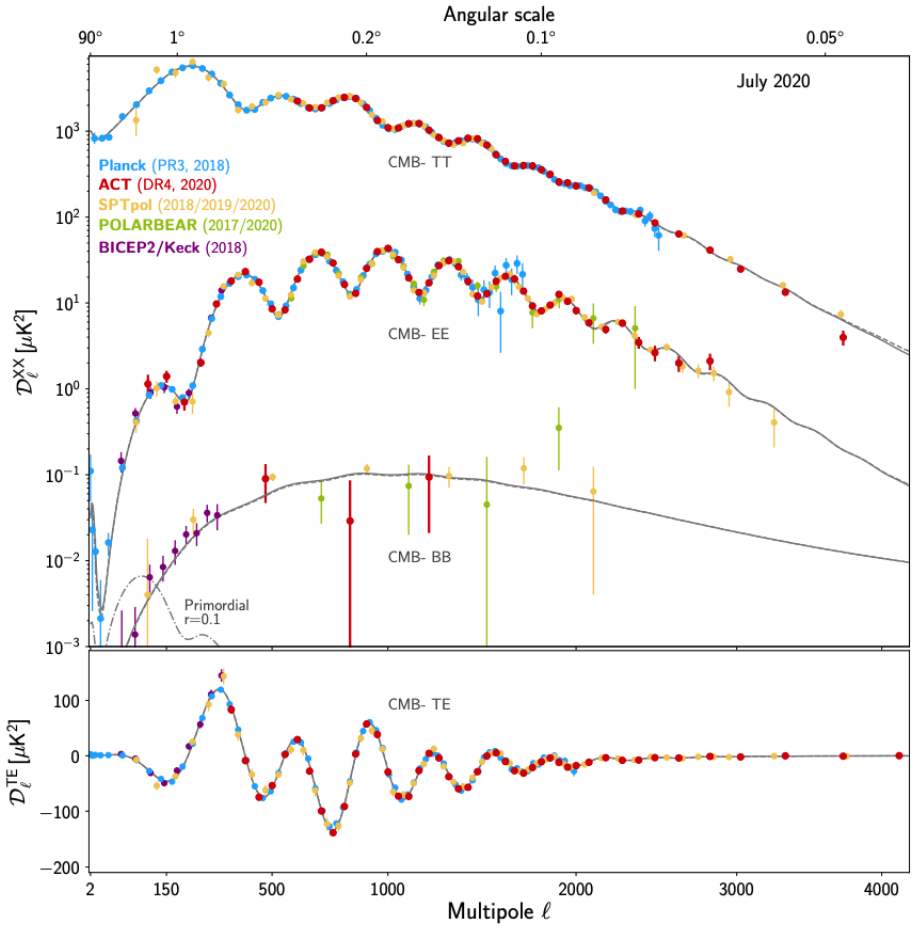

Figure 1.1: CMB temperature, E-mode polarization, and B-mode polarization power spectra with measurements from various observatories summarized in Choi et al. 2020 [28]. The primordial B-mode signal calculated for $r = 0.1$ is also shown.

than the temperature power spectrum.

B-modes at $\ell > 100$ inform our understanding of the matter distribution in the Universe and structure formation from gravitational lensing. Below $\ell \sim 10$, the B-mode spectrum is solely comprised of the inflationary gravitational wave signal. This signal peaks at $\ell \sim 100$ due to photon-electron scattering during recombination and again at $\ell < 20$ due to scattering at reionization [2]. No other processes are expected to produce B-modes on larger scales, and such a discovery would be the first observation directly from the inflationary epoch.

Detection of this small signal is predicated on pushing sensitivity limits below the gravitational wave B-mode signal. Moreover, the strength of this signal depends on the unknown tensor-to-scalar ratio r, which has recently been constrained to $r < 0.036$ with 95% confidence [5].

Observing the inflationary gravitational waves in the relic radiation from the Big Bang will require unprecedented sensitivity. Large arrays of extremely sensitive low temperature detectors, such as Transition Edge Sensors, have enabled us to measure the properties of our Universe to incredible precision. The work presented in this thesis aims to push the sensitivity limits of future CMB polarimeters further by understanding the thermal conductance of Transition Edge Sensors and cooling these sensors with NIS junction refrigerators.

1.2 Low Temperature Detectors for Precision Cosmology

The scientific returns enjoyed in sub-mm astrophysics arose from packing many low-noise, high-sensitivity superconducting sensors into steadily larger focal planes. The energy gap corresponding to the breaking of Cooper pairs is $\sim 100\times$ smaller than semiconductor band gaps, allowing superconducting sensors to access longer wavelengths beyond the realm of CCDs and into the sub-mm. The predominant superconducting sensors in sub-mm astronomy are Transition Edge Sensors (TESs) and Kinetic Inductance Detectors (KIDs).

TESs are a state-of-the-art photon-noise-limited detector technology that takes advantage of the sharp change in resistance with temperature of a superconducting thin film biased into its phase transition [47, 73]. The transition of a Mo/Cu bi-layer TES is shown in Figure 1.2. While

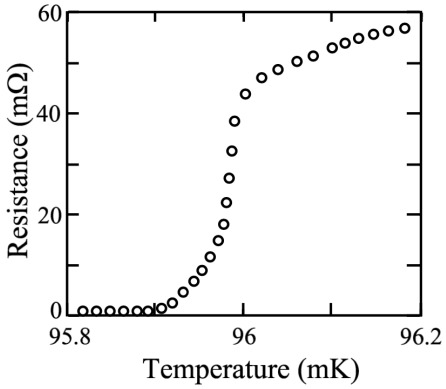

Figure 1.2: The phase transition of a superconducting film with $T_c \sim 96$ mK. Figure originally from [47].

in operation, the TES is biased in the center of this transition, which in this device occurs at its transition temperature T_c of 96 mK. This steep change in resistance with temperature makes TESs well-suited for sensitive thermometry.

In sub-mm astronomy, these sensors are used as bolometers to measure on-sky microwave power. In the X-ray, TESs are used as calorimeters to measure energy pulses. During operation, the TES is cooled below T_c and voltage-biased into the phase transition. A voltage bias scheme significantly increases the stability of these detectors in the extremely narrow phase transition due to negative electrothermal feedback (NETF). Higher signal power deposited onto the TES increases resistance of the sensor, which decreases the electrical power $P_e=V^2/R$. This bias scheme, coupled with SQUID current amplifiers, has enabled multiplexing these detectors into large arrays.

KIDs are superconducting micro-resonators that are simple to fabricate and are easily multiplexed into dense networks of up to hundreds of detectors per single coaxial transmission line. Photons absorbed by the resonator break Cooper pairs in the superconducting film, increasing the kinetic inductance due to the quasiparticle population enhancement. This is measured as a shift in both the resonant frequency and quality factor of the resonator [127, 29].

Superconducting detector performance increases with decreasing bath temperatures (T_b). Much of the thermal noise and sensor geometry constraints at 300 mK, the bath temperature provided by pumped ^{3}He, are mitigated at T$\leq$100 mK, providing significant science returns and improved detector fabrication yields. In TESs, Johnson-Nyquist noise equivalent power (NEP_J) scales with bath temperature as $T_b^{1/2}$ and thermal fluctuation NEP (NEP_{TF}) scales linearly with T_b [47], resulting in a 1.7$\times$ and 3$\times$ noise reduction respectively when the bath temperature is lowered from 300 mK to 100 mK. TES bolometers operated at 100 mK also require less thermal isolation, allowing for significantly stronger membrane leg geometries. Quasiparticle generation-recombination noise, the fundamental noise source in KIDs, decreases exponentially with temperature [30].

The Decadal Survey on Astronomy and Astrophysics 2020 highlights the recent shift to achieving a comparable scientific return in higher frequency bands, from FIR to optical through X-ray and gamma-ray, by adopting ultra-sensitive low temperature detectors. X-ray observatories

like Athena have been moving from semiconductor detectors towards low temperature detectors [15]. Mission concepts for the FIR and X-ray probes plan to use cryogenic sensors on their focal plane, as were The Lynx X-ray Observatory and the Origins Space Telescope, two of four previously proposed flagship mission concepts [37, 60].

As future observatories opt for the ultra-high sensitivity of low temperature detectors, refrigeration technologies to cool these detectors to ∼100 mK will become increasingly desirable. NIS junction refrigerators could aid this transition by integrating the refrigerator on-chip with the superconducting detector, allowing projects to adopt superconducting sensor technology without the weight, cost, and power requirements of ADRs and DRs.

1.3 A Brief History of NIS Refrigerators

NIS junctions were first made in 1960 by Ivar Giaever to measure the superconducting energy gap Δ of lead, producing the best measurement at the time [39]. He was awarded the Nobel Prize in 1973 for his subsequent work measuring Δ of many metals using NIS and SIS junctions. The first concept of the selective tunneling mechanism behind NIS refrigeration came from Parmenter in 1961, who posited that the critical temperature of a superconductor should be increased if thermally excited electrons were removed from the system and suggested this could be accomplished using an SIS junction [85]. Tunnel junction enhancements of Δ_{Al} were later measured by Gray and Willemsen in 1977 [41], Chi and Clarke in 1979 [27], and Blamire et al. in 1991 [20].

In 1994, Nahum et al. at the National Institute of Standards and Technology (NIST) theorized that the gap enhancement seen in these junctions was due to the electron system being cooled [79]. They modeled the tunneling of electrons/quasiparticles and holes through the junctions and used this model to derive the IV characteristics of a NIS junction as well as the energy transfer between the normal metal and superconductor. From their findings, they noted that at certain bias voltages, this energy transfer cools the electron system in the normal metal. The authors determined that the electron temperature in the normal metal would reach equilibrium when the NIS cooling power balanced the heat load from electron-phonon coupling to the hotter lattice electrons. They

demonstrated this theory by fabricating NIS junction refrigerators that cooled electrons from 100 mK to 85 mK.

Following the work of Nahum et al., Leivo et al. demonstrated a significant temperature reduction in a NIS junction of 300 mK to ∼100 mK by reducing the tunneling resistance and the heat leak through the bias contact [61]. Phonons were first cooled via a SINIS refrigerator in 1997 by suspending a thermometer NIS junction on a SiN_x membrane and extending the normal metal layer onto the membrane for better electron-phonon coupling [69]. The first cooling of a detector was performed by Tarasov et al. in 2003, where they cooled the electrons in a NIS junction as a hot-electron bolometer from 250 mK to 90 mK using another NIS junction as a refrigerator [103]. This improved their detector response from 1.6 mV/K to 2.1 mV/K. Notably, cooling the electron system in the detector required that the junction and the detector be electrically connected.

The first phonon refrigeration of a cryogenic detector by a NIS junction was demonstrated in 2008 by Miller et al. at NIST [76]. Using an X-ray TES as a Johnson noise thermometer, they suspended this TES on a SiN_x membrane with four legs and four pairs of NIS junctions placed on top of the bulk Si at the membrane-substrate boundary. This device cooled the detector from 300 mK to 190 mK. Vercruyssen et al. demonstrated NIS cooling of a superconducting resonator suspended on a membrane in 2011 [111].

The first demonstration of significant temperature reductions with considerable cooling powers was in 2012 by O'Neil et al. at NIST [84]. The quasiparticle trapping in their devices was significantly improved by adding large overlayer quasiparticle traps on top of the superconducting electrodes in addition to the lateral traps that were conventional at the time. Lateral traps were restricted to the film thickness and tunnel resistance of the normal metal base electrode since they were fabricated from the same layer. The overlayer traps, however, were fabricated after the deposition of the superconducting electrode, and thus could incorporate more transparent oxidation layers and significantly increased volume over the base electrode, which are better suited for quasiparticle trapping. They also provided a more direct path for quasiparticles leaving the normal metal by being closer to the junction. These improvements significantly reduced the fraction of

power that backscattered from the superconductor into the normal metal defined as β, and enabled the authors to demonstrate electron cooling from 300 mK to 82 mK, a significant improvement over comparably-sized junctions at the time and the greatest electron cooling from 300 mK measured to date.

The same group demonstrated the first general-purpose NIS junction refrigerators, cooling a copper payload stage from 290 mK to 256 mK [66] and measured the largest phonon cooling to date from 300 mK to 154 mK [67]. They subsequently improved these macroscopic refrigerators, cooling the cold stage from 291 mK to 228 mK [123]. Numerical modeling enabled these accomplishments by allowing for precise optimization of the integrated NIS-membrane device design. In 2015, Nguyen et al. demonstrated phonon cooling of a SiN_x membrane from 305 mK to 200 mK [81], and in 2016, the same group demonstrated electron cooling from 300 mK to 100 mK using a 2-stage cascade NIS refrigerator [82].

In 2016, the group at NIST integrated these optimized NIS refrigerators onto prototype TES bolometers designed for (sub-)mm wavelength observations on a balloon-borne experiment. The TESs were suspended on a SiN_x membrane via four 600-µm-long $\times$ 5-µm-wide legs with two NIS refrigerators located next to these legs at the wafer-membrane boundary. Using the TES as a thermometer, the prototype devices demonstrated promising refrigeration capabilities, cooling the TES bolometer from 300 to 187 mK. With NIS refrigerator applications in mind, Zhang et al. studied the effect of phononic filters on the thermal conductance from the Si wafer to TES bolometers on a membrane. This heat load significantly impacts NIS cooling performance [121].

This rich history of NIS refrigerator R&D, much of it done here at NIST, provided the foundation of my PhD work described in the following chapters. Chapter 2 discusses the characterization of the local SMBH mass function for predicting and understanding the nHz gravitational wave background. In Chapter 3, I discuss phononic thermal transport in thin films at low temperatures spanning the relevant phonon transport regimes in the context of TES bolometers. With this foundation, I share thermal transport measurements in ultra-low G TES bolometers, including the previously unaccounted-for microstrip wiring layers in Chapter 4. In Chapter 5, I discuss using

NIS junctions as phonon refrigerators, and in Chapter 6, I characterize the cooling performance of NIS refrigerators integrated onto TES bolometers. In Chapter 7, I discuss the next steps toward scaling NIS-cooled TES bolometers to pixels and, eventually, arrays.

Chapter 2

Local SMBH Mass Function from the $M_\bullet$ - M_{bulge} Scaling Relation

The density of charged particles in the primordial plasma kept the photons of the early Universe in an incredibly uniform equilibrium state, giving the CMB its signature isotropic nature. It wasn't until the epoch of recombination, when the Universe had sufficiently cooled for electrons and protons to snap together into neutral H atoms, that the first photons were free to propagate through space. The opacity of the early universe prohibits us from probing earlier than the surface of last scattering.

Unlike electromagnetic radiation, gravitational waves (GWs) were unimpeded by the plasma state of the infant Universe. In fact, it is during the inflationary epoch that the exponential expansion of the universe would produce primordial gravitational waves. Observational cosmologists seek to observe these primordial GWs indirectly by detecting their imprint in the CMB polarization. However, direct detection of these GWs with a GW observatory would probe directly into the inflationary epoch, allowing us to observe the Universe from an earlier cosmic time than previously possible.

Beyond inflation, many other astrophysical phenomena can produce gravitational radiation, and gravitational wave observatories have begun to observe this new cosmic messenger. In 2015, the Laser Interferometer Gravitational-Wave Observatory (LIGO) made the first direct observation of gravitational waves as a 10 ms chirp resulting from a stellar mass black hole merger [3]. In 2022, the North American Nanohertz Observatory for Gravitational Wave (NANOgrav) detected a stochastic gravitational wave background (GWB) by monitoring the arrival time signals from a collection of

pulsars over 15 years, an observation strategy referred to as a pulsar timing array (PTA) [7].

Existing and proposed gravitational wave observatories cover the majority of frequency space between $10^{-10} - 10^{2}$ Hz, shown in Figure 2.1. Sources predicted to produce gravitational radiation in these bands range from cosmic inflation to neutron star mergers. The search for primordial gravitational wave signature in the B-mode polarization of the CMB complements these strategies and extends GW observation capabilities to the lowest frequencies allowed by nature [2].

In this work, we are particularly interested in the stochastic gravitational wave background accessible with pulsar timing arrays. PTAs take advantage of the exceptional rotational stability of pulsars that allow them to be used as standard clocks. As gravitational waves propagate, they create ripples in the spacetime around the pulsar, causing a variation in the otherwise incredibly stable pulsar rotation. These gravitational waves are detected by correlating this variation in a collection of pulsars. PTAs are sensitive to the nHz-μHz gravitational wave band, seated between the frequency ranges accessible by the CMB power spectrum and proposed laser interferometers shown in Figure 2.1.

Supermassive black hole (SMBH) binaries are likely a significant source of this GW background radiation. To predict and understand this signal, we must understand the local SMBH mass function. Towards this end, we measure this mass function using a scaling relation between SMBH mass and the bulge mass of its host galaxy.

In Section 2.1, I discuss the gravitational wave background signal and outline the various scaling relations between SMBH masses and their host galaxy properties. Section 2.2 outlines how we build our galaxy sample from the Sloan Digital Sky Survey Data Release 7. Our measurement of the SMBH mass function is presented in Section 2.3. We attempt to characterize this mass function using the single and double Schechter Functions in Section 2.4. In Section 2.5, I compare our measurements to other SMBH mass functions in the literature. I then summarize this work and present future steps in Section 2.6.

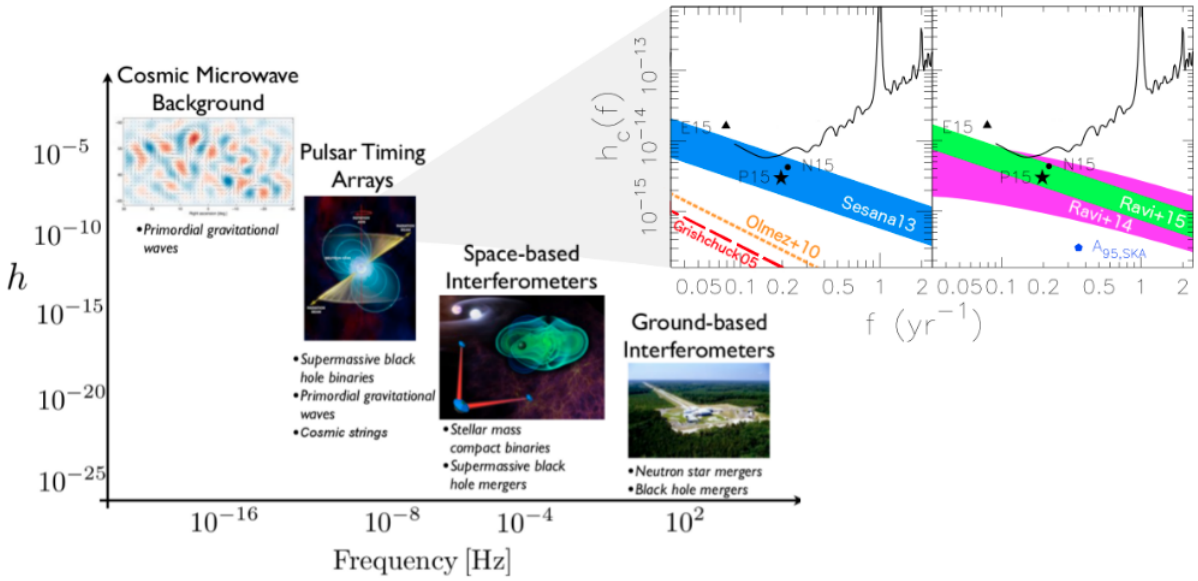

Figure 2.1: A conceptual strain spectrum h_C for frequency bands covered by multiple detection strategies from [24] (adapted from a figure by NANOGrav). The figure emphasizes the complementary nature and frequency sensitivities of the multiple strategies, including the search for primordial gravitational waves (PGWs) in the cosmic microwave background (CMB) in the lowest frequency band followed by PGWs and SMBH binary radiation observed at higher frequencies with PTAs. The inset highlights the predicted GWB and limits in the PTA band current at the time of publishing, adapted from Shannon et al. 2015 [97] with updates from Arzoumanian et al. 2015a [11] and Lentati et al. 2015 [62].

2.1 Background

2.1.1 Gravitational Wave Background

Unlike the individual transient GW signals detected by ground-based interferometers like LIGO, the stochastic gravitational wave background (GWB) in the PTA band is the quadrature sum of many signals from the GW source population. To discern a cosmological story from this signal, we must understand the sources of the nHz gravitational radiation. This is an active area of research in the gravitational wave community.

Many candidate GWB sources are cosmological in nature. The relic gravitational radiation from tensor and scalar perturbations that were stretched to superhorizon scales during inflation may be accessible via pulsar timing arrays. Artifacts from any first-order phase transitions that occurred while the universe was in its plasma state could also produce GWB signals, including bubble-plasma interactions and topological defects, such as cosmic strings.

The dominant GWB source, however, is expected to be inspiraling supermassive black hole ($M_\bullet \sim 10^8 - 10^{10} M_\odot$) binaries. All galaxies are expected to host a massive black hole in their nuclei [70], and correlations between the central black hole mass and properties of their host galaxy suggest the two coevolve. SMBH binaries are created when two galaxies merge and their central black holes become gravitationally bound. Once bound, the black holes co-orbit each other, continuing to inspiral long after the merger is complete [16].

SMBH binaries are thought to radiate gravitational waves of shifting frequency as they inspiral, resulting in a broadband gravitation background signal in the nHz band [8, 6]. During the inspiral, a binary system loses energy by emitting this gravitational radiation. For a SMBH binary to merge within a Hubble time, however, it is often necessary for the system to exchange orbital energy through interactions with the local galactic environment [16]. The shape of the emitted gravitational spectrum is sensitive to those environmental conditions and depends on the sub-parsec evolution of the binary, another regime inaccessible to electromagnetic radiation. The amplitude of the stochastic background signal depends on the mass and abundance of these SMBH

binaries [8].

The spectrum of the gravitational wave background is

$$\Omega_{GW}(f) = \frac{2\pi^2}{3H_0^2} f^2 h_c(f)^2$$

where H_0 is the Hubble constant and f is frequency. This gravitational signal is characterized by the dimensionless characteristic strain spectrum h_c:

$$h_c^2(f) = \iiint \frac{d^4N}{dz\ dM\ dq\ d(ln(f))} h_S^2\ dz\ dM\ dq \tag{2.1}$$

where d^4N is the number N of SMBH binaries in the redshift range dz, mass range dM, and black hole binary mass ratio range dq emitted in the frequency range $d(ln(f))$. The rotation- and sky-averaged strain of an individual source is h_s [100].

The frequency dependence in Equation 2.1 can be separated from the dimensionless term A_{yr}:

$$h_c(f) = A_{yr} \left(\frac{f}{1\ yr^{-1}} \right)^{\alpha} \tag{2.2}$$

where α[1] is the power spectral index that depends on the signal source [24]. The GW spectrum from the SMBH binaries contribution has an associated $\alpha = -2/3$. The shape of the cosmic string contribution is $\alpha \in [-5/3, -7/8]$, and $\alpha \in [-2, -1/2]$ is expected from primordial gravitational waves from the inflationary epoch. GWs from primordial black holes and QCD phase transitions do not have a power-law spectral dependence (see [24] and references therein).

2.1.2 The Local Supermassive Black Hole Mass Function

Due to the resolution required, direct measurements of black hole masses via dust and stellar dynamics have been made for <100 black holes in the very closest and brightest local galaxies. For galaxies fainter or further away, the black hole mass can instead be estimated via established relations between supermassive black hole mass and host galaxy spheroidal properties that come from these dynamical measurements. With these scaling relations, astronomers can use density

[1] Outside of this chapter, α characterizes how the thermal conductance of a thin film scales with thickness.

distributions describing the massive galaxies that should host SMBHs as a proxy for SMBH binary distributions. Empirical relations between the black hole mass $M_\bullet$ and the host galaxy observables have been measured using the galactic stellar mass ($M_\bullet$-$M_\star$), bulge mass ($M_\bullet$-M_b), bulge luminosity ($M_\bullet$-L_b), velocity dispersion ($M_\bullet$-σ), and Sérsic index [55].

The density of SMBH binaries can be predicted from the density of host galaxy mergers:

$$\frac{d^3N}{dz\ dM\ dq} = \frac{dN}{dM}\frac{d^2N}{dz\ dq} \tag{2.3}$$

$$= \Phi(z, M)R(z, M, q) \tag{2.4}$$

where the merger density is broken down into the SMBH mass function (SMBH MF) $\Phi(z, M) = dN/dM$ and the galaxy merger rate $R(z, M, q) = d^2N/(dz\ dq)$. The merger rate can be further broken down into the merger timescale $\tau(z, M)$ and the galaxy pair fraction $f_{pair}(z)$:

$$R(z, M, q) = \frac{df_{\rm pair}}{dq}\frac{1}{\tau}\frac{dt}{dz} \tag{2.5}$$

It is convenient to convert the number of binaries per Earth-observed frequency bin $d(\ln f)$ to the number of binaries per co-moving volume shell V_c via

$$\frac{dN}{d(ln(f))} = \frac{dV_c}{dz}\frac{dz}{dt}\frac{dt}{d(\ln f)} \tag{2.6}$$

Using Equations 2.1 - 2.6, the strain amplitude A_{yr} becomes [100]:

$$A^2_{\rm yr} = \iiint \Phi\frac{1}{\tau}\frac{df_{\rm pair}}{dq}\frac{dV_c}{dz}\left(\frac{dt}{d(\ln f)}h_s^2\right)\Bigg|_{f_{\rm yr}} dz\ dM\ dq \tag{2.7}$$

The following work focuses on characterizing the SMBH mass function Φ, which can be inferred from various scaling relations between SMBH mass and properties of its host galaxy.

2.1.3 Black Hole & Host Galaxy Scaling Relations

Using dynamical measurements of local SMBH masses, correlations between SMBH mass $M_\bullet$ and properties of their host galaxies have been measured. These scaling relations often take the

form of a power-law:

$$\log M_\bullet = \beta + \gamma \log X \tag{2.8}$$

where X is the normalized host galaxy property. Examples of such properties include the stellar velocity dispersion $X = \sigma/(200\ km/s)$, the V-band bulge luminosity $X = L_V/(10^{11} M_\odot)$, and the bulge mass $X = M_b/(10^{11} M_\odot)$ [74, 55].

McConnell & Ma 2013 [74] give the following relation for the galactic stellar velocity dispersion σ:

$$\log\left(\frac{M_\bullet}{10^9 M_\odot}\right) = (8.32 \pm 0.05) + (5.64 \pm 0.31) \log\left(\frac{\sigma}{200\ km/s}\right) \tag{2.9}$$

with a scatter ε_s of 0.38 dex. We infer σ from the observable stellar mass, effective radius r_e and Sérsic index n_b from measurements of SDSS galaxies in Bezanson et al. 2011 [19]:

$$\sigma = \sqrt{\frac{G M_\star}{K_\star r_e}} \tag{2.10}$$

The circularized effective radius is $r_e = \sqrt{ab}$, where a and b are the respective semi-major and semi-minor axes of the galaxy. The virial constant $K_\star$ depends on the Sérsic index n_b:

$$K_\star = 0.557 \left(\frac{73.3}{10.465 + (n_b - 0.94)^2} + 0.954\right) \tag{2.11}$$

The local $M_\bullet$–σ_* relationship has been successfully reproduced in smoothed particle hydrodynamics simulations of feedback-drive black hole growth.

McConnell & Ma 2013 also give the scaling relation for the host galaxy's V-band luminosity:

$$\log\left(\frac{M_\bullet}{10^9 M_\odot}\right) = (9.23 \pm 0.10) + (1.11 \pm 0.13) \log_{10}\left(\frac{L_V}{10^{11} L_\odot}\right) \tag{2.12}$$

for $L > 10^{10.8} M_\odot$.

Kormandy & Ho 2013 [55] give the following relation for galactic bulge mass M_b in their Equation 10 with an intrinsic scatter of 0.29 dex:

$$\log\left(\frac{M_\bullet}{10^9 M_\odot}\right) = (0.49^{+0.06}_{-0.05}) + (1.16 \pm 0.08) \log\left(\frac{M_b}{10^{11} M_\odot}\right) \tag{2.13}$$

In this work, we focus on the SMBH mass function estimation from the $M_\bullet - M_b$ scaling relation in Equation 2.13 and compare these results to the literature. Though outside the scope of

X	$\boldsymbol{\beta}$	$\boldsymbol{\gamma}$	$\boldsymbol{\varepsilon_s}$ **[dex]**
$\sigma/(200\ km/s)$	8.32±0.05	5.64±0.31	0.38
$L_V/(10^{11}M_\odot)$	9.27±0.13	1.12±0.82	0.47
$M_b/(10^{11}M_\odot)$	$0.49^{+0.06}_{-0.05}$	1.16±0.08	0.29

Table 2.1: Power law parameters for scaling relations between SMBH mass and various host galaxy properties.

this work, SMBH mass function estimates from σ and L_V are also of great interest and would be the immediate next steps.

2.2 Methods

To measure the local SMBH mass function, we construct a sample of galaxies from the Sloan Digital Sky Survey Data Release 7 (SDSS-DR7), selecting for spectroscopic and mass completeness. We use disc, bulge, and total stellar masses, redshift z, and galaxy type from the decomposition in Mendel et al. 2013 ([75], hereafter M+13). We use the galaxy Sérsic index n_b, ellipticity e, and semi-major axis half-light radius R_{SMA} values in Simard et al. 2011 ([98], hereafter S+11). We convert R_{SMA} to R_e, circular half-light radius, using the relation $R_e = R_{SMA}(1-e)$.

When constructing the MF from the bulge mass scaling relation, we correct for Malmquist bias using the $1/\mathrm{V}_{max}$ completeness correction [98, 104] and we use a Monte Carlo bootstrap method to account for the errors in the bulge mass and scaling relation parameters as well as the inherent scatter in the scaling relation. We adopt the standard cosmological model with $H_0 = 100$h km/s/Mpc, h = 0.7, $\Omega_M = 0.3$, and $\Omega_\Lambda = 0.7$.

2.2.1 SDSS-DR7 Galaxy Sample

Our galaxy sample is built as prescribed in Thanjavur et al. 2016 [104] and consists of 550,427 galaxies from the Sloan Digital Sky Survey Data Release 7 (SDSS-DR7). This sample consists of low redshift (z∼0.1) galaxies in the public release of [75] catalogs, which extend [75] g- and r-band photometry into SDSS u, i, and z bands to decompose the galaxies into bulge + disc and Sérsic profiles.

In the catalog presented in S+11, galaxies in SDSS-DR7 were decomposed into bulges and discs using the GIM2D software package [99]. This catalog contains only galaxies flagged by SDSS as extended objects that are unsaturated and have been properly deblended. In addition to the two-component decomposition, the authors also fit a single-component (pure Sérsic) profile to these galaxies and include both the resulting Sérsic index n_b and the probability that the galaxy is pure single-component galaxy P_{PS} in their catalog. They apply k-corrections and correct for galactic extinction when calculating photometric values of galaxy properties. The cataloged data and measurements performed by GIM2D were screened using multiple quality assessment metrics outlined in [99]. The resulting catalog contains photometric measurements of 1,123,718 SDSS-DR7 galaxies.

M+13 restricts the S+11 catalog by selecting objects that are spectroscopically classified as galaxies (SDSS $specClass$=2) and for which the morphology fit was flagged as successful in all filters by the GIM2D fitting software (GIM2D $prcflag$=0). They only select objects whose photometry is flagged as uncontaminated by nearby neighbors ($contam\_flag$=0 and $-0.2 \leq delta\_fiber \leq 0.2$) and are consistent with the SDSS fiber aperture magnitudes. The uncertainties in their measurements of M_{B+D}, M_B and M_D are $\sim$0.13, 0.14 and 0.15 dex, respectively. The M+13 catalog consists of 657,996 galaxies selected from the S+11 catalog with updated $ugriz$ photometry.

Beginning with the M+13 catalog, we restrict our sample to galaxies with redshifts $0.02 \leq z \leq 0.2$ as per the SDSS spectroscopic completeness criterion, which removes 45,168 galaxies. We also remove 5,518 galaxies with stellar masses $\log 10(M_*/M_\odot) \leq 8.9$ since the surface brightness of lower mass galaxies may drop below detection limits, compromising sample completeness. We adhere to the SDSS main galaxy sample selection criterion by limiting the relative Petrosian r-band magnitude to $m_{P,r} \leq 17.77$ mag, removing an additional 48,315 galaxies. Measurements of $\mathrm{M}_{\star,r}$ or M_b are flagged for 8,568 of the remaining galaxies, and are therefore excluded from the sample as well. These cuts are shown in Figure 2.2. Our final sample consists of 550,427 galaxies after removing 107,569 galaxies, or 16.3%, from the M+13 catalog.

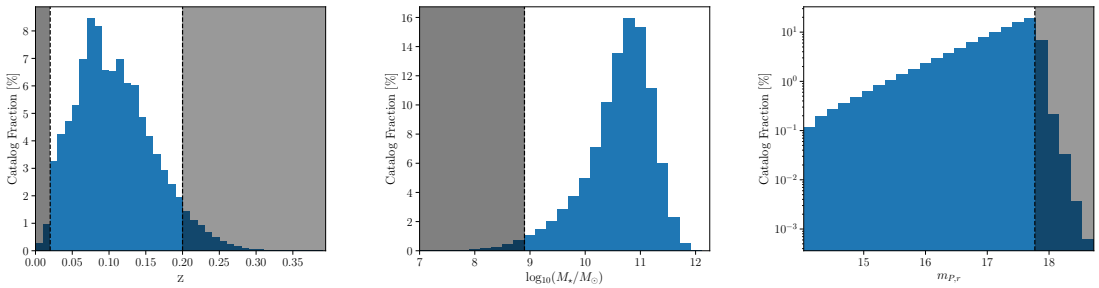

Figure 2.2: (a) Redshift, (b) stellar mass, and (c) r-band apparent magnitude cuts on the M+13 catalog when constructing the galaxy sample. Greyed areas represent galaxies in M+13 that were removed from our sample.

2.2.2 Bulge Fraction & False disc Corrections

For the majority of galaxies in this sample, we take galactic stellar mass $M_\star$ to be the sum of M_b and M_d from MT14 decomposition. However, for 9.2% of the sample (N=50,509), this sum M_{B+D} is inconsistent with the total mass from MT14's single component fit M_{BD}, meaning that the difference between M_{B+D} and M_{BD} is larger than their combined standard errors. Bluck et al. 2014 [21] suggest that a potential explanation for this discrepancy is that large errors in the color gradient lead to measurements of unphysically red bulges in predominantly bulgeless systems.

We correct for these unphysical measurements as prescribed in Bluck et al. 2014 [21] and executed in Thanjavur et al. 2014 [104]. For this subset of galaxies, we instead set $M_\star$ to the value from the single component fit M_{BD} and calculate M_b using the photometric bulge fraction, or the fraction of the galaxy's mass that resides in the bulge, in the r-band GIM2D catalog $(B/T)_r$. The bulge and disc component masses are determined via $M_b = M_{BD} \times (B/T)_r$ and $M_d = M_{BD} \times (1 - (B/T)_r)$, respectively.

Additionally, for 20.9% of galaxies in our sample (N=114,991), GIM2D incorrectly identifies disc components in pure spheroidal galaxies due to the fixed bulge Sérsic index $n_b = 4$ profile. Following the procedure advised in Bluck et al. 2014 [21], as well as personal correspondence with Prof. Asa Bluck, we identify galaxies with false discs as those with a calculated bulge fraction $(B/T) > 0.7$, bulge Sérsic index $n_b > 4$, and the probability that the galaxy is purely Sérsic

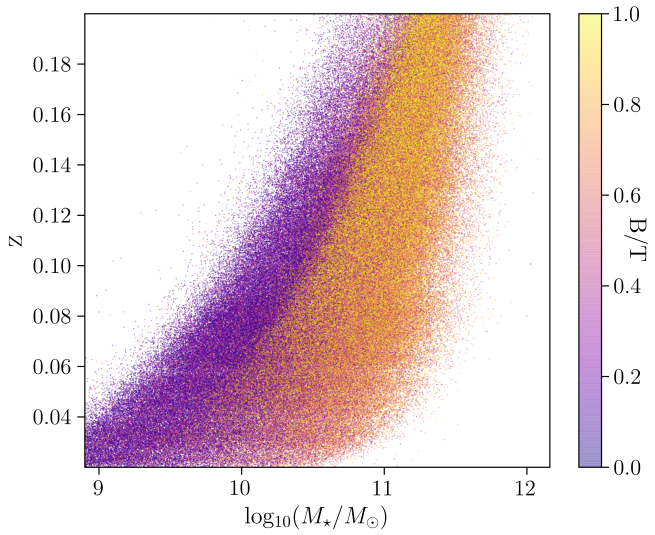

Figure 2.3: Bulge fraction of the sample as a function of redshift and stellar mass.

$P_{pS} > 0.32$. For these galaxies, we set $(B/T) = 1$ and $M_b = M_\star$. The corrected bulge fractions as a function of redshift and stellar mass of this sample are shown in Figure 2.3.

2.2.3 Malmquist Bias Correction

Despite the careful curation discussed in Section 2.2.1, our sample is still vulnerable to Malmquist bias, i.e., the relative undercounting of intrinsically faint sources in real galaxy surveys that occurs because the apparent magnitude of fainter sources will fall below survey magnitude limits at earlier redshifts than brighter sources. To correct for this bias, we weight the measurement of individual galaxies by $1/\mathrm{V}_{max,g}$, where $\mathrm{V}_{max,g}$ is the maximum volume at which the galaxy is detectable [93]. This strategy weights the fainter objects more heavily, correcting for the undercounting.

We use $\mathrm{V}_{max,g}$ for galaxy g calculated in [98]:

$$V_{\mathrm{max},g} = \frac{1}{4\pi} \int d\Omega f(\theta,\phi) \int_{z_{\mathrm{min}}(\theta,\phi)}^{z_{\mathrm{max}}(\theta,\phi)} \frac{d_A^2(z)}{H(z)(1+z)} c dz \tag{2.14}$$

where $H(z)$ is the Hubble parameter, $d_A(z)$ is the angular distance to the galaxy, and $f(\Theta,\phi)$ is the sampling fraction as a function of sky position. The angular part of Equation 2.14 in this case is simply the fraction of the sky covered by the survey. Using the SDSS-DR7 survey areal coverage of $\Omega_{SDSS} = 8032$ deg^2 and the all-sky surface area $\Omega_{sky} = 41{,}253$ deg^2, the left side of the equation becomes $8032/41253 = 0.1947$ and we find that $\mathrm{V}_{max,g}$ depends solely on redshift.

The bounds z_{min} and z_{max} are the respective minimum and maximum redshifts at which the source can be detected given SDSS spectroscopic completeness constraint $14 \leq m_{P,r} \leq 17.77$ and effective surface brightness completeness $\mu_r \leq 23$ mag/arcsec^2. Calculations of z_{min} and z_{max} are outlined in [98], which I will summarize here. Bounds from the relative magnitude are the redshifts corresponding to the luminosity distance d_L at which the relative magnitude m_r falls outside the

survey limits $m_{r,min}$ and $m_{r,max}$, in our case 14 and 17.77 respectively.

$$d_L(z_{min,m}) = d_L(z)10^{-0.2(m_r - m_{r,min})} \tag{2.15}$$

$$d_L(z_{max,m}) = d_L(z)10^{-0.2(m_r - m_{r,max})} \tag{2.16}$$

The maximum redshift for which a galaxy with r-band surface brightness μ_r can be detected is:

$$z_{max,\mu} = (1+z)10^{(\mu_{max} - mu_r)/10} - 1 \tag{2.17}$$

The effective Petrosian surface brightness is given in [49]:

$$\mu = m_{P,r} + 2.5\log(2\pi R_P^2) - 10\log(1+z) - e_r - k_r \tag{2.18}$$

where $m_{P,r}$ is the Petrosian relative magnitude, R_P is the Petrosian radius, e_r is the line-of-sight extinction and k_r is the r-band k-correction.

We use k_r corrections from the GIM2D catalog and line-of-sight galactic extinction e_r from the SDSS database. k_r corrections are not explicitly given in S+11, but can be solved for using their Equation 3b:

$$k_r = m_r - e_r - DM(z) - M_r \tag{2.19}$$

where m_r and M_r are the respective apparent and absolute magnitudes measured in S+11 and $DM(z)$ is the distance modulus at redshift z.

The minimum bound is set by either $z_{min,m}$ or the lowest redshift of the sample, whichever is larger. The maximum bound is the lowest redshift between $z_{max,m}$ and $z_{max,\mu}$:

$$z_{min} = max(z_{min,m}, 0.02) \tag{2.20}$$

$$z_{max} = max(z_{max,m}, z_{max,\mu}) \tag{2.21}$$

If galaxies are uniformly distributed over the sample volume, the median volume ratio $< V_g/V_{max} >$ will be 0.5, where V_g is the SDSS spectroscopic survey volume measured at the redshift of the galaxy [104]. We calculate that for our sample, $<V_g/V_{max}> = 0.398$, suggesting that our sample may be biased towards intrinsically dimmer, lighter galaxies. More work is needed to investigate this potential bias.

2.3 SMBH Mass Function & Error Estimation

The SMBH mass function is equivalent to the black hole number density per mass bin:

$$\Phi_j d(\log M) = \sum_i^{N_{bin}} \frac{1}{V_{max,i}} \tag{2.22}$$

In addition to the M_b measurement error, the scaling relation itself contributes to the uncertainty of $M_\bullet$ due to the error on the scaling parameters β and γ and the intrinsic scatter ε_s of the relation. We account for these uncertainties using a 10^3-iteration Monte Carlo simulation in which M_b, β and γ are resampled to produce 10^3 estimates of $M_\bullet$ for each galaxy.

During each iteration i of the simulation, we first sample the scaling factors β_i and γ_i from a normal distribution defined by the values and 1-σ errors in Table 2.1. We then sample $M_{b,i}$ of each galaxy from a uniform distribution within the 16th and 84th percentile log stellar mass measurement from [75]. The simulated β_i, γ_i, and $M_{b,i}$ values produce initial estimates of $M_{\bullet,i,0}$ using Equation 2.8. Finally, we introduce the uncertainty from the intrinsic scatter by sampling the actual $M_{\bullet,i}$ estimates from a normal distribution centered at $M_{\bullet,i,0}$ with a standard deviation of ε_s.

For each iteration i we bin $M_{\bullet,i}$ of the sample weighted by $1/\mathrm{V}_{max}$, in steps of $\sim$0.1 dex. The final SMBH mass function Φ is the mean density in each bin over those 10^3 iterations, and the 1-σ error is the standard deviation. A comparison between the resulting mass function and the direct scaling of M_b using Equation 2.13 is shown in Figure 2.4.

Including the measurement errors and scatter both smooths the distribution between 10^5 and $10^7 M_\odot$ and spreads the volume density to higher and lower masses. The uncertainty on measurements of M_b grows $\sim$1-5 orders of magnitude for stellar masses $< 3{\times}10^{12} M_\odot$, leading to very large error bars on the low mass end of the SMBH mass function. From this mass function, SMBHs ($M_\bullet \geq 10^8 M_\odot$) constitute 17.3% of the total sample volume density, compared to 17.6% using the direct scaling relation. Both provide a median SMBH volume density of $\sim$ 0.026 $\mathrm{Mpc}^{-3}\mathrm{dex}^{-1}$. Since the error on the low mass end is so large and because we expect black holes with mass $\geq 10^6 M_\odot$ to significantly contribute to the GWB, the remaining analysis only considers the mass

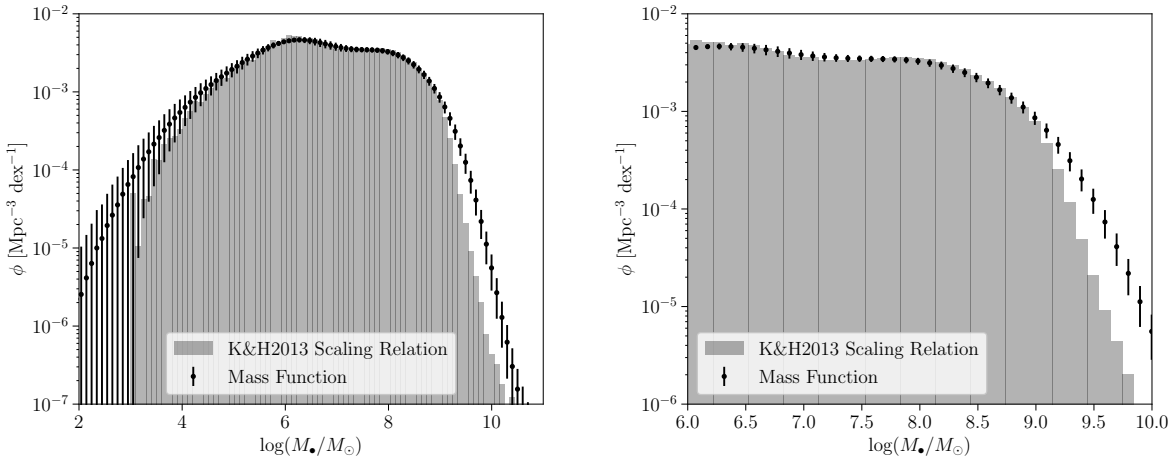

(a) Mass function of the entire sample.

(b) Mass function for $M_\bullet \geq 10^6 M_\odot$.

Figure 2.4: Mass function from bulge mass scaling relation. (a) shows the majority of the distribution and (b) highlights black holes with $M_\bullet > 10^6 M_\odot$, i.e., the black holes expected to contribute significantly to the GWB.

Parameter	Double SF	Single SF
$\log_{10}(M^*)$	8.91 ± 0.03	8.99 ± 0.03
$\log_{10}(\Phi_1^*)$	-2.88 ± 0.03	-2.93 ± 0.03
$\log_{10}(\Phi_2^*)$	-5.56 ± 0.53	
α_1	-1.06 ± 0.02	-1.09 ± 0.02
α_2	3.41 ± 0.66	

Table 2.2: Single and Double Schechter Function Fit Parameters with 1-σ errors.

function for $M\bullet \geq 10^6 M_\odot$, highlighted in Figure 2.4b.

2.4 Schechter Function Fits

In 1976, Schechter formulated an expression to parameterize the luminosity function of galaxies [92] that has since been used to characterize the stellar mass and luminosity functions for a range of redshift and galaxy sub-populations [114]. This Schechter Function takes the following form in $\log M$ space:

$$\begin{aligned}\Phi\ d\log(M) = \ln(10)\Phi^* \exp(-10^{\log M - \log M^*}) \\ \times (10^{\log M - \log M^*})^{\alpha+1}\ d\log M\end{aligned} \tag{2.23}$$

where M^* is the mass at which the mass function transitions from a power law at lower masses to an exponential at higher masses and Φ^* is the number density at M^*. In some cases, the mass function is better described by the Double Schechter Function, which is the sum of two single Schechter Functions that share the same M^*:

$$\begin{aligned}\Phi\ d\log(M) = \ln(10) \exp(-10^{\log M - \log M^*}) \\ \times \left[\Phi_1^*(10^{\log M - \log M^*})^{\alpha_1+1} + \Phi_2^*(10^{\log M - \log M^*})^{\alpha_2+1}\right]\ d\log M\end{aligned} \tag{2.24}$$

We fit both a single and double Schechter Function (SF) to the measured SMBH MF using a least squares minimization routine. For the double Schechter function fit, α_1 was constrained to [-4, 0] and α_2 was constrained to [0, 4] to avoid fitting between two equivalent solutions.

The resulting SF fits and standardized residuals are shown in Figure 2.5, and the fit parameters are in Table 2.2. The low mass end of this galaxy sample has an upturn characteristic to red, quiescent galaxies that we expect to be best described by a double SF. The double SF fit, however,

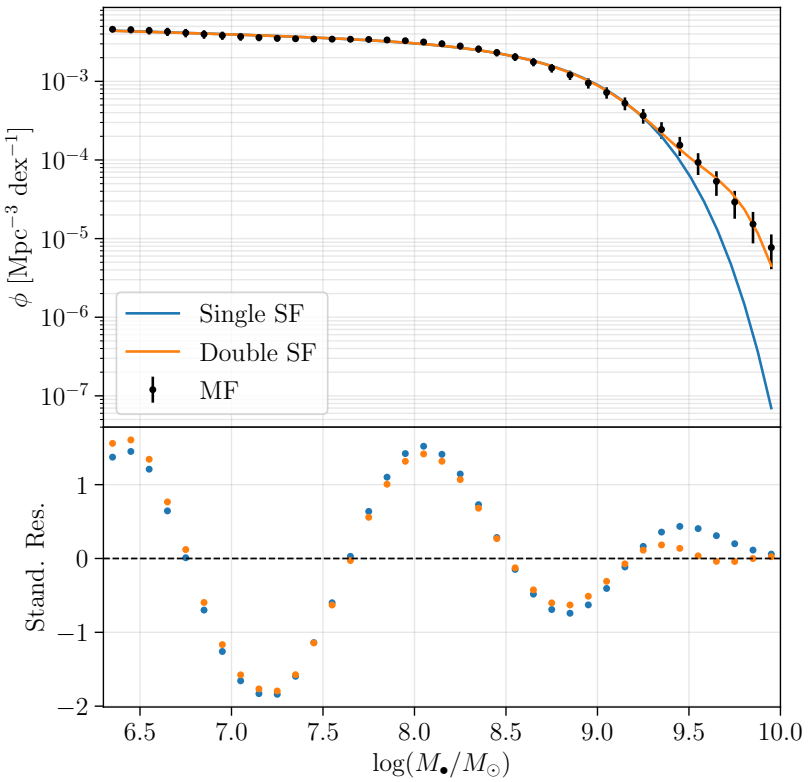

Figure 2.5: Single and Double Schechter Function fits to supermassive black hole mass function of sample from bulge mass scaling relation.

does not capture this nonlinearity and instead injects nonlinearity into the high mass end, hence the sinusoidal pattern in the standardized residuals. It seems that the Schechter Function does not capture the measured SMBH mass distribution as well as it describes galactic stellar mass functions. This is potentially due to the smoothing of the peaks in the distribution and the spreading of the high mass tail introduced by including uncertainties and intrinsic scatter in the mass function calculation.

2.5 Literature Review

We compare this measurement of the SMBH MF with other measurements in the literature in Figure 2.6. Our measurement is given as the black points in (a) for all galaxies and blue points in (b) for elliptical galaxies with 1-σ errors as calculated in Section 2.3. Marconi et al. 2004 ([70], hereafter Marconi+2004) estimate the local SMBH MF from four measurements of the luminosity function measured with different surveys and photometric bands, namely [18], [71], [54] and [80]. The resulting MF for all galaxies is shown in Figure 2.6a and only the elliptical galaxies in (b).

Shankar et al. 2009 ([96], hereafter Shankar+2009) compile a range of SMBH MF estimates using various measurements of the $M_\bullet - L_\star$, $M_\bullet - \sigma$, and $M_\bullet - M_b$ scaling relations. The shaded regions in Figure 2.6a capture the range of these measurements. The pink region summarizes MF estimates at z=0.02 and the purple region at z=0.26, capturing the redshift range of our sample. These mass functions deviate for $M_\bullet < 10^8$, indicating the formation of lower mass black holes between z = 0.26 and 0.02. This is consistent with the observation from Marconi et. al 2004 [70] that black hole growth is anti-hierarchical with lower mass black hole growth at later redshifts.

Our mass function for the entire sample agrees with Marconi+2004 at lower masses but deviates from both mass functions to higher densities for all $M_\bullet > 10^8 M_\odot$. The relationship between Shankar+2009 and this MF may be equivalent to the relationship between the direct scaling and the mass function including the scatter in that our mass function smooths out the peaks around $M_\bullet \sim 10^{5-6} M_\odot$ and spreads those galaxies out into the high mass tail. Given the mass functions in Marconi and Shankar result from directly scaling host galaxy properties, it could

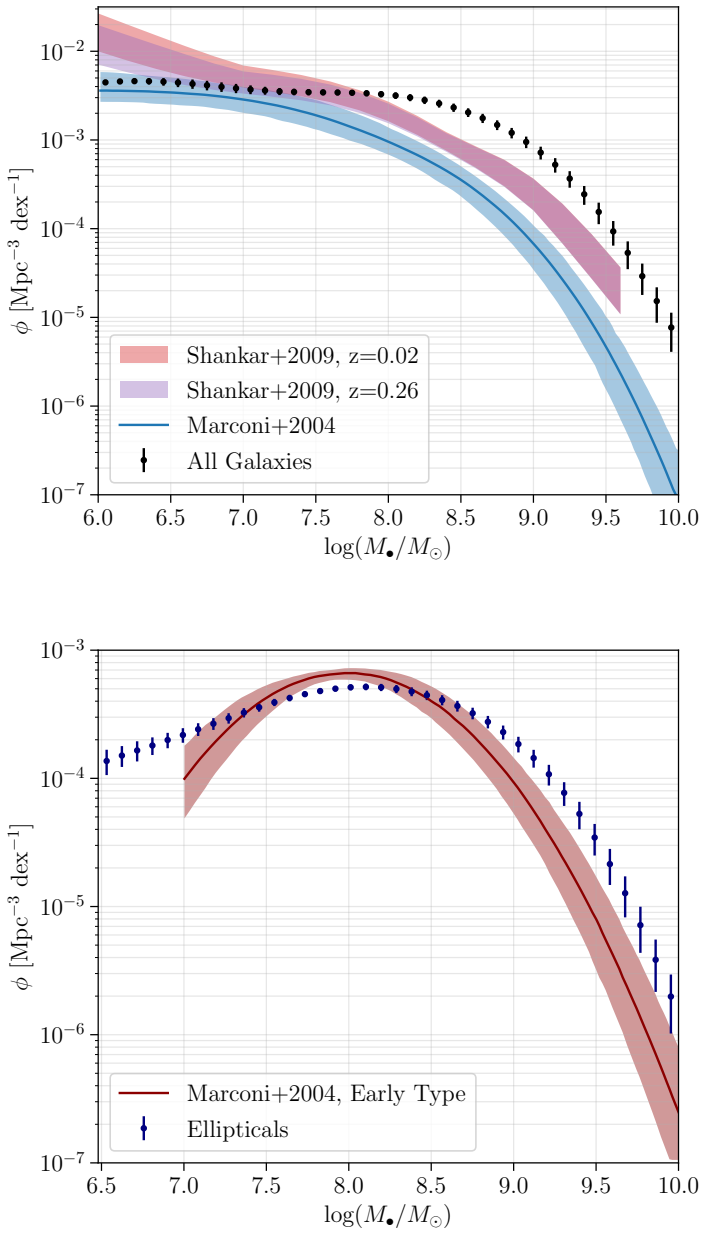

Figure 2.6: Comparison of SMBH mass functions calculated using various host galaxy scaling relations in the literature. The MF calculated in this work is given by black points for all galaxies in (a) and blue points for elliptical galaxies in (b). Marconi et al. 2004 [70] calculate a MF from luminosity scaling relations for all galaxies (a) and early type galaxies (b). Shankar et al. 2009 [96] summarize a range of mass functions calculated $M_\bullet$-L_{bulge}, $M_\bullet$-σ, and $M_\bullet$-$M_\star$ scaling relations.

be that the discrepancies between our measured mass function and those in the literature stem from the relative effect the inherent scatter has on the shape of the distribution, similar to the comparison between the MF and the distribution from the direct scaling in Figure 2.4. This results in a suppression of the peaks around $M_\bullet \sim 10^{5-6} M_\odot$ and a larger density of galaxies in the high mass tail $M_\bullet > 10^8 M_\odot$.

This trend is consistent when we compare our mass function of elliptical galaxies to the Marconi+2004 mass function of early-type galaxies for $M_\bullet > 10^{8.5} M_\odot$. When considering only the elliptical galaxies and comparing it to the mass function of early type galaxies in Marconi+2004, we again see a relative suppression of the peak around $M_\bullet > 10^8 M_\odot$ and spreading of the distribution into the high and low mass tails. In both Marconi+2004 and Shankar+2009, the authors use a direct scaling, so it's expected that our mass function will have shorter peaks and longer tails at the mass extremities.

2.6 Summary & Future Work

Using our sample of >550,000 local galaxies from SDSS-DR7, we have measured the SMBH mass function from the host galaxy bulge mass scaling relation given in Kormendy & Ho 2013 [55]. We include the intrinsic scatter of the scaling relation, the error in the scaling relation parameter fit, and the error in the M_b measurement in our estimation using a Monte Carlo bootstrap method. We address Malmquist bias with the $1/\mathrm{V}_{max}$ strategy. Our galaxy sample may be biased towards less massive galaxies given $<\mathrm{V}_g/\mathrm{V}_{max}> \sim 0.4$, where an unbiased sample will produce $<\mathrm{V}_g/\mathrm{V}_{max}> = 0.5$.

The resulting SMBH mass function both smooths and spreads the $M_\bullet$ distribution compared to a direct scaling of the bulge mass. This is also true of the comparison between our mass function and other SMBH mass functions in the literature are calculated from direct scalings of the host galaxy velocity dispersion, the bulge luminosity, and the bulge mass. Our mass function is not well described by either a single or double Schechter function. This could be the result of the aforementioned effect of the inherent scatter on the shape of the distribution.

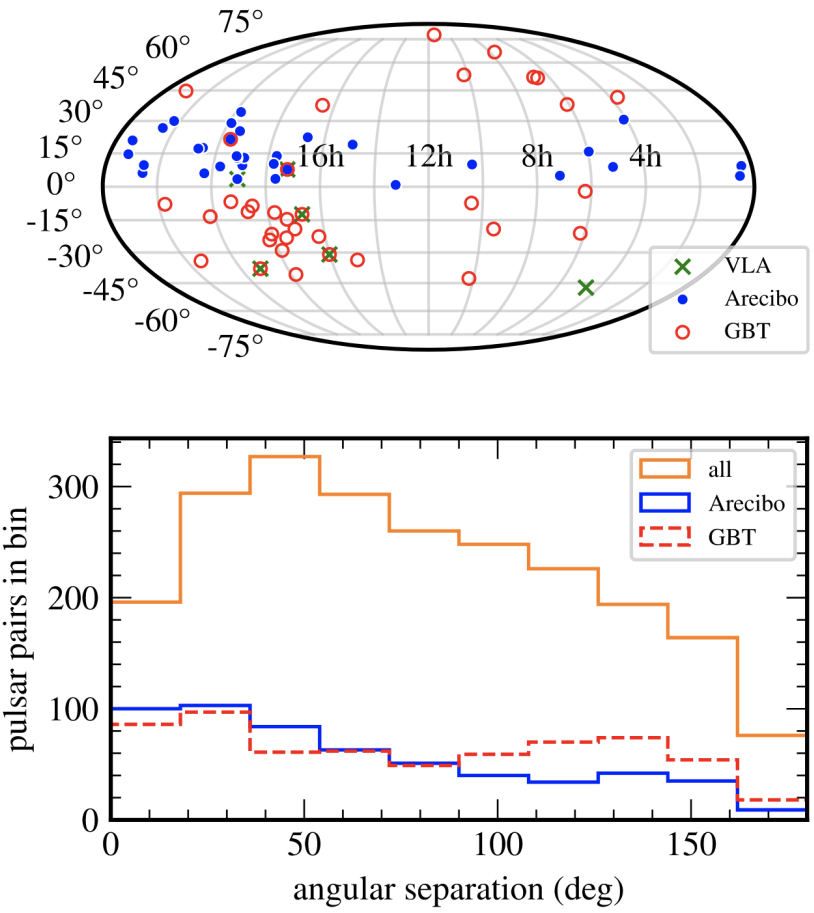

Figure 2.7: Summary of pulsar data collection for the 15-year NANOgrav data set from [7]. Top: Sky locations of the 67 pulsars observed. Observatories include the Very Large Array (VLT), Arecibo Observatory (Arecibo), and Green Bank Telescope (GBT). Bottom: Angular separations probed in the data.

In the time since the conclusion of this work, NANOGrav has detected strong evidence of a stochastic GW background signal in their 15 years of PTA data in 2023 [7]. This detection was made by monitoring 67 pulsars across various observatories shown in Figure 2.7. They determine that the source of this stochastic background is indeed likely to be SMBH binaries resulting from galaxy mergers, though other exotic cosmological sources such as primordial gravitational waves or decay of cosmic strings cannot be ruled out. In fact, their Bayesian analysis often favors the cosmological sources over the astrophysical SMBH binaries, but the authors caution that these results are highly dependent on the assumed priors, and argue that the case for a SMBH binary signal is hindered by a current lack of understanding of this signal and the noise.

A more precise characterization of the SMBH binary signal is necessary to interpret the physics behind this recently detected novel signal. Given this, the field would greatly benefit from examining the SMBH mass function using various other $M_\bullet$ scaling relations and comparing them to the now-measured GW background signal.

Chapter 3

Phonon Transport in Thin Films at sub-Kelvin Temperatures

The thermal conductance (G) of a TES bolometer is a key design parameter that sets the sensitivity, dynamic range, and temporal response of the detector. To control the thermal conductance of these sensors, they are often suspended on a membrane via long, thin legs. Imprecise control over the thermal conductance can lead to multiple iterations of leg dimensions until a target saturation power is achieved, leading to longer project timelines and larger R&D budgets.

Thermal isolation requirements are becoming even more stringent as current and proposed missions will extend TES observations from the sub-mm to higher frequency bands such as the FIR, equivalent to a 10^{-3} drop in signal power. Saturation powers of picoWatts have been achieved by relying on diffusive transport in long, narrow TES legs, but scaling leg geometries to reach signal powers of femtoWatts may be incompatible with reasonable mechanical yield. Additionally, diffusive scattering processes come with an intrinsic scatter that cannot be engineered away, where variances in G as large as 20% have been recorded [118]. An alternative thermal isolation strategy in active development is phonon filters, also referred to as phononic crystals, which are structures designed to create band stops in the phonon spectrum of the TES leg [121, 90, 120, 117, 116]. Designing these filters requires advanced modeling techniques and a deep understanding of phonon transport in thin films. Reaching the sensitivities required to open a window into the FIR universe and beyond will require a robust understanding and precise control of TES bolometer thermal conductance.

To understand the thermal conductance of TES bolometers suspended on a membrane, we

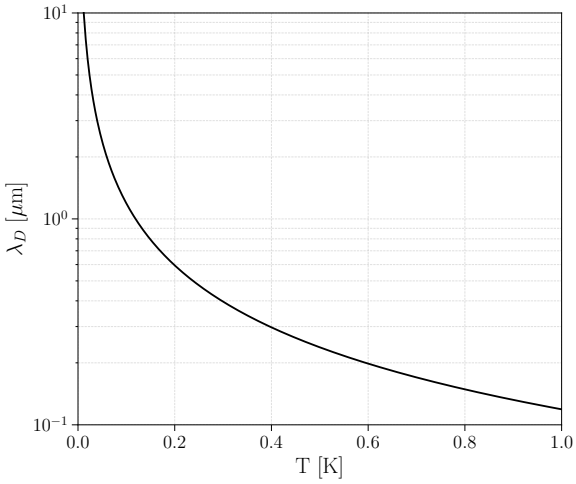

Figure 3.1: The dominant phonon wavelength λ_D at sub-Kelvin temperatures in amorphous SiN_x.

must first understand thermal transport in the thin film layers that constitute the TES legs. In dielectric thin films below 1 K and superconducting thin films at $T << T_c$, heat is transported via phonons. The thermal conductance of the phonon gas in a thin film is often given by scaling the thermal conductivity κ to the geometry of the film:

$$G = \frac{A}{L}\kappa \tag{3.1}$$

where A is the cross-sectional area and L is the length of the thermal link. In thin films, A is the product of the width w and the thickness d. The thermal conductivity is described by kinetic gas theory as

$$\kappa = C_v v_s \ell/3 \tag{3.2}$$

where C_v is the specific heat of the phonon gas, v_s is the mode-averaged speed of sound, and ℓ is the phonon mean free path.

In bulk (3D) materials, ℓ is set by intrinsic scattering mechanisms, and thermal conductivity is intrinsic to the material. The resulting conductance scales linearly with the film thickness d, width w, and inversely with length L. As thin film dimensions approach the dominant phonon wavelength $\lambda_D = \hbar v_s/(2.82 k_B T)$, however, phonons will interact with the boundaries of the film.

We calculate λ_D for amorphous SiN_x (a-SiN) in Figure 3.1 using the average sound speed $v_s = 6986$ m/s [113]. In a-SiN, λ_D is 400 nm at 300 mK and longer than 1 µm below 100 mK.

These phonon-boundary interactions suppress the conductance with respect to the bulk case and change the geometry dependence of G. In sufficiently thin films at low temperatures, the geometry of the film will restrict phonons to the lowest-order modes, reducing the dimensionality of the phonon gas and suppressing the thermal conductance. If the surfaces of the film are rough, the film boundary itself can become a site for diffusive scattering, which further suppresses the conductance and introduces a mean free path that depends on geometry.

The phonon physics in thin films is described by Rayleigh-Lamb treatments of the phonon dispersion relations in which mode mixing occurs at the free surfaces of the film [57, 48, 59]. This approach is informed by elastic theory and acoustics. This chapter summarizes and builds upon the work of Zhang [121] and Kühn [59], using the theory of thin film phonon transport to predict and understand the thermal conductance of TES bolometers.

In Section 3.1, I describe phonon transport in the ballistic transport regime $L << \ell$, using elastic theory to predict thin film thermal properties in the absence of diffusive scattering. In Section 3.2, I discuss phonon transport in the diffusive scattering limit $L >> \ell$, including the implications of scattering at the film boundaries. In Section 3.3, I model the total thermal conductance of a thin film as a parallel sum of the conductances in the ballistic and diffusive limits. Finally, in Section 3.4, I parameterize how thermal conductance scales with the film thickness in these different transport regimes.

3.1 Ballistic Phonon Transport

In the regime of ballistic phonon transport, phonon scattering events are negligible and the thin film acts as a phonon waveguide. We can calculate the thermal conductance from classical elastic wave theory from the geometry and elastic properties of the material. In elastic theory, solids are treated as continuous, which is valid when considering length scales much larger than inter-atomic distances. The equilibrium position of a volume element $\delta V = \delta x \delta y \delta z$ is given by $\mathbf{r}$,

and the displacement field $\mathbf{u}(\mathbf{r}, t)$ describes motion about the equilibrium in the solid.

3.1.1 3D Plane Waves

3.1.1.1 Equation of Motion

Elastic theory describes phonon transport within a material in the absence of diffusive scattering. The equation of motion in elastic media is

$$\partial_t^2 = \partial_j p_{ji} \tag{3.3}$$

$$= \rho^{-1} \partial_j c_{ijkl} (\partial_k u_l + \partial_l u_k)/2 \tag{3.4}$$

$$= \rho^{-1} c_{ijkl} \partial_j \partial_k u_l \tag{3.5}$$

where p_{ji} is the stress tensor T_{ijkl} divided by the mass density ρ and c_{ijkl} is the elasticity tensor [59]. Assuming isotropic media and taking advantage of the symmetries in [[c]], the fourth-rank tensor is reduced to a 6×6 matrix:

$$[c] = \begin{pmatrix} c_{11} & c_{12} & c_{12} & 0 & 0 & 0 \\ c_{12} & c_{11} & c_{12} & 0 & 0 & 0 \\ c_{12} & c_{12} & c_{11} & 0 & 0 & 0 \\ 0 & 0 & 0 & c_{44} & 0 & 0 \\ 0 & 0 & 0 & 0 & c_{44} & 0 \\ 0 & 0 & 0 & 0 & 0 & c_{44} \end{pmatrix} \tag{3.6}$$

where $c_{12} = c_{11} - 2c_{44}$. Therefore, the only independent parameters in [[c]] are c_{11} and c_{44} [110]. These parameters are related to the elastic properties of the material, specifically the Young's Modulus E and Poisson's ratio ν:

$$c_{11} = \frac{(1-\nu)E}{(1+\nu)(1-2\nu)} \tag{3.7}$$

$$c_{44} = \frac{E}{2(1+\nu)} \tag{3.8}$$

Young's modulus is the ratio of the stress σ and the induced strain ϵ, i.e., $E = \sigma/\epsilon$. Poisson's ratio measures the amount of lateral elongation upon compression and takes values between 0 and 0.5 [12, 59].

These matrix components also define the longitudinal and transverse sound speeds:

$$v_l = \sqrt{c_{44}/\rho_m} \tag{3.9}$$

$$= \sqrt{\frac{(1-\nu)E}{(1+\nu)(1-2\nu)}\frac{1}{\rho_m}} \tag{3.10}$$

$$v_t = \sqrt{c_{11}/\rho_m} \tag{3.11}$$

$$= \sqrt{\frac{E}{2(1+\nu)}\frac{1}{\rho_m}} \tag{3.12}$$

where ρ_m is mass density. The mode-averaged sound speed v_s is

$$v_s = \left(\frac{1}{2}\left[\frac{1}{v_l^2} + \frac{2}{v_t^2}\right]\right)^{-1/2} \tag{3.13}$$

In the bulk limit with no boundary interactions, Equation 3.5 has three independent plane wave solutions with linear dispersion relations

$$\omega_{l/t} = v_{l,t}k \tag{3.14}$$

for two transversely-polarized waves and one longitudinally-polarized wave.

3.1.2 Elastic Eigenmodes in Thin Films

As with all systems of finite size, the dispersion relation in a thin film is split into branches. The 3D plane wave solutions consist of longitudinal waves, which are polarized parallel to the wave vector $\mathbf{k}$, and transverse waves, which are polarized perpendicular to $\mathbf{k}$. Transverse waves can be further decomposed into two polarizations perpendicular to each other. In the case of a thin film depicted in Figure 3.2a, it is convenient to define one transverse polarization to be perpendicular to the plane of incidence, referred to as shear vertical polarization, and the other parallel to the plane of incidence, or shear horizontal polarization.

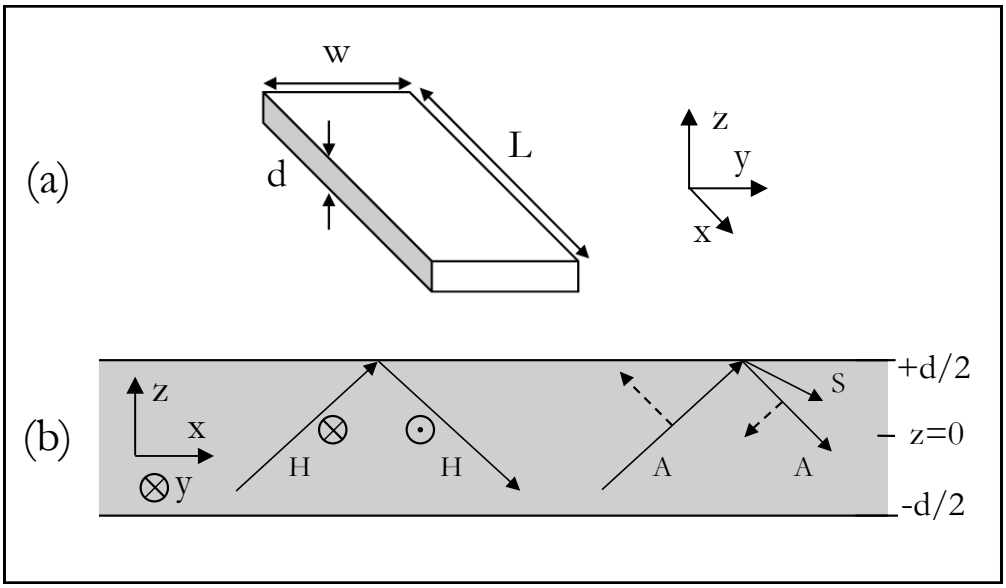

Figure 3.2: (a) Schematic of a thin film with thickness d, width w, and length L. (b) Reflections of horizontal (H), symmetric (S) and antisymmetric (A) polarized plane waves at the boundaries of a semi-infinite plane, located at $\pm d/2$. H modes depicted on the left are polarized parallel to the film boundaries. Reflections at the boundary couple the S and A Lamb modes. Depicted on the right is an incident A mode that reflects into both A and S polarizations.

The wave vector $\mathbf{k}$ of a plane wave incident on a free surface can be decomposed into the component pointing along the surface $\mathbf{k}_{\parallel}$ and perpendicular to the surface $\mathbf{k}_{\sigma}$:

$$\hat{\mathbf{u}}e^{i(\mathbf{k}\cdot\mathbf{r}-\omega t)} = \hat{\mathbf{u}}e^{i((\mathbf{k}_{\parallel}+\mathbf{k}_{\sigma})\cdot\mathbf{r}-\omega t)} \tag{3.15}$$

where $\hat{\mathbf{u}}$ is the polarization of the wave. We denote $\mathbf{k}_{\sigma}$ as $\mathbf{k_l}$ for longitudinal waves and $\mathbf{k_t}$ for transverse (shear) waves.

In thin films, the thickness dimension d is much smaller than the width w and length L. To derive the phonon dispersion modes in a thin film, we consider the semi-infinite plane constrained in the $\hat{z}$-direction at $z = \pm d/2$, shown in Figure 3.2b. We choose the plane of incidence to be the $x-z$ plane, and the boundaries of the film are located at $z = \pm d/2$. While these three polarizations propagate independently in bulk samples, in thin film mode mixing is possible via reflections at the free boundaries.

We define the polarization vector of the shear horizontal waves (H) as parallel to the plane of incidence. Components of the polarization vector for the shear vertical and longitudinal waves are perpendicular to the plane of incidence and are coupled through interactions with the boundary. These coupled waves are referred to as Lamb modes, and the behavior of these modes is illustrated in Figure 3.3. Longitudinal waves represent compression of the beam, which are symmetric across the x-axis and referred to as symmetric Lamb modes (S). The shear vertical waves bend the beam antisymmetrically across the x-axis and are referred to as antisymmetric Lamb modes (A).

3.1.2.1 Shear Horizontal Modes

We have defined shear horizontal modes such that they are independent of the S and A modes, and therefore still behave as if propagating through bulk material. We apply the free surface boundary condition, meaning there is no parallel shear stress acting on the surface, to the film surfaces at $z = \pm d/2$:

$$(\hat{n}_i p_{ij})(\mathbf{r} \in \delta V) = 0 \tag{3.16}$$

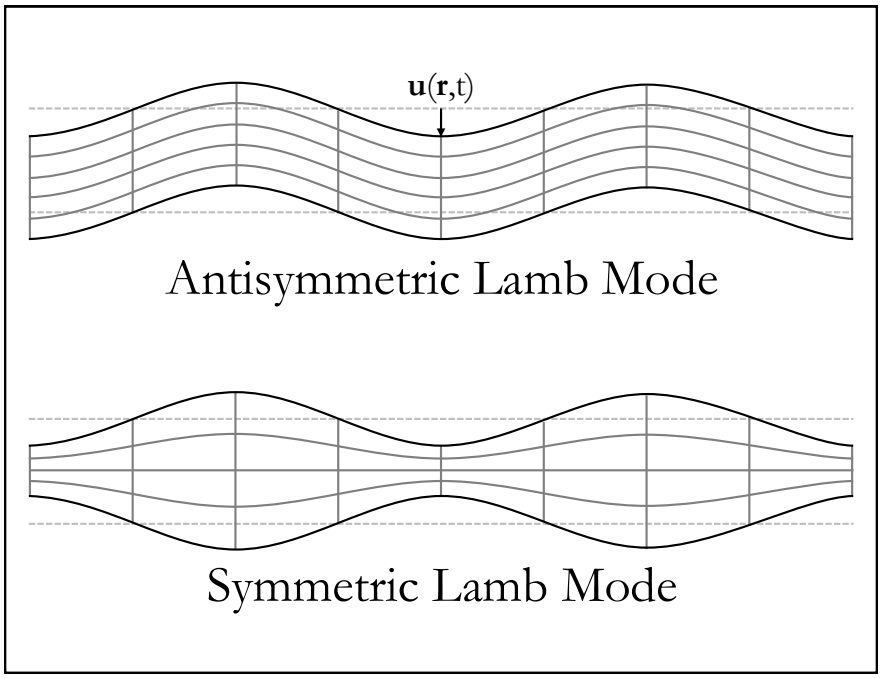

Figure 3.3: Behavior of antisymmetric (A) and symmetric (S) Lamb modes. The dotted lines represent the equilibrium position **r**. The displacement from the equilibrium **u**(**r**,t) is also shown.

$\hat{n}_i$ is the normal of a surface element δV of a solid of volume V and p_{ij} is the stress tensor normalized by the mass density T_{ij}/ρ_m. This produces the following dispersion relation for the H modes:

$$\omega_{H,m}(k_\parallel) = v_t\sqrt{k_\parallel^2 + (m\pi/d)^2} \tag{3.17}$$

where v_t is the transverse sound speed, $k_\parallel$ is the wave vector parallel to the direction of propagation, defined as $\hat{x}$ in Figure 3.2, and $m \in [0, \infty)$ is the mode number. The acoustic modes are the lowest energy modes defined by the property $\omega(k_\parallel = 0) = 0$, which occurs for $m = 0$.

The displacement field is given by

$$\mathbf{u}_H = N_H \cos\left[k_H(z - d/2)\right](\hat{\mathbf{k}_\parallel} \times \hat{\mathbf{z}})e^{i(\mathbf{k}_\parallel \cdot \mathbf{r} - \omega t)} \tag{3.18}$$

where the normalization constant N_H is

$$N_H = \begin{cases} \sqrt{1/V} & \text{for } m = 0 \\ \sqrt{2/V} & \text{for } m > 0 \end{cases} \tag{3.19}$$

3.1.2.2 Lamb Modes

The coupling of the symmetric and antisymmetric Lamb modes through reflections at the boundary complicates the dispersion relations of these modes with respect to the bulk case. To derive these dispersion relations, we begin with the displacements of the incident (I) and reflected (R) Lamb waves:

$$\begin{aligned} u_x^I &= I_S k_\parallel e^{i(k_\parallel x + k_S z - \omega t)} - I_A k_A e^{i(k_\parallel x + k_A z - \omega t)} \\ u_z^I &= I_S k_S e^{i(k_\parallel x + k_S z - \omega t)} + I_A k_\parallel e^{i(k_\parallel x + k_A z - \omega t)} \\ u_z^R &= R_S k_\parallel e^{i(k_\parallel x - k_S z - \omega t)} - R_A k_\parallel e^{i(k_\parallel x + k_A z - \omega t)} \\ u_z^R &= -R_S k_S e^{i(k_\parallel x - k_S z - \omega t)} - R_A k_\parallel e^{i(k_\parallel x + k_A z - \omega t)} \end{aligned} \tag{3.20}$$

Applying the free surface boundary condition 3.16 at $z = \pm d/2$ gives the following transcendental relation for the A modes:

$$\frac{4k_A k_S k_\parallel^2}{(k_A^2 - k_S^2)^2} = -\frac{\tan(k_S d/2)}{\tan(k_A d/2)} \tag{3.21}$$

and

$$\frac{4k_A k_S k_\parallel^2}{(k_A^2 - k_S^2)^2} = -\frac{\tan(k_A d/2)}{\tan(k_S d/2)} \tag{3.22}$$

for the S modes. Combining this with Snell's Law:

$$v_t^2(k_t^2 + k_\parallel^2) = v_l^2(k_l^2 + k_\parallel^2) = \omega^2 \tag{3.23}$$

we can solve for k_S and k_A as a function of $k_\parallel$ and calculate the dispersion relations $\omega(k_\parallel)$, which are shown in Figure 3.4.

The dispersion relations of the A and S modes are not as tidy as the analytical solution for the H modes. However, we can solve for the cutoff frequencies of these modes $\omega_c = \omega(k_\parallel = 0)$ by setting $k_\parallel = 0$ in Equations 3.22 and 3.21. For the A modes, the cutoff frequencies are

$$\omega_{c,A} = \begin{cases} 2n\pi v_t/d \\ (2n+1)\pi v_l/d \end{cases} \tag{3.24}$$

for integer $n \in [0, \infty)$. Similarly, for the S modes, the cutoff frequencies are given by

$$\omega_{c,S} = \begin{cases} (2n+1)\pi v_t/d \\ 2\pi v_l/d \end{cases} \tag{3.25}$$

The integer n denotes unique modes but is technically not equivalent to the mode number m since ω_c does not increase monotonically with n.

As can be seen by Equations 3.17, 3.24, and 3.25, ω_c of optical modes, or modes for which $m, n \neq 0$, increase with decreasing film thickness d. This means that optical modes in thinner films are less likely to be occupied at low temperatures, as per Bose-Einstein statistics.

3.1.2.3 Low Temperature Limit

At sub-Kelvin temperatures, the power spectral density in our thin films is dominated by the acoustic modes since very few phonons populate states with energy $\geq \hbar\omega_c$ of the optical modes. We can expand the acoustic modes (m=0, $\omega(k_\parallel = 0) = 0$) described by Equations 3.17, 3.22 and

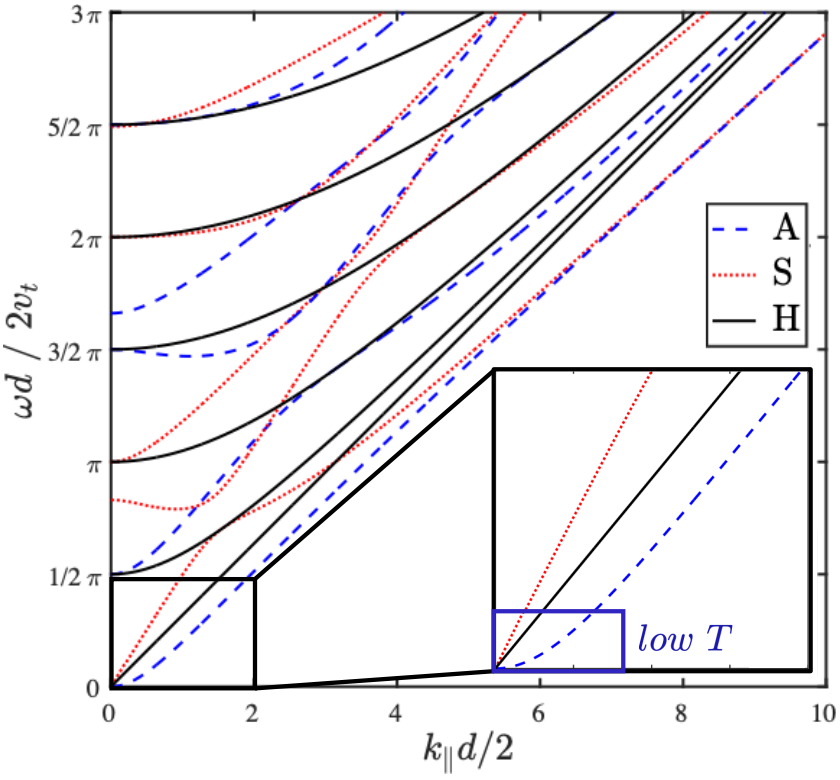

Figure 3.4: Normalized dispersion curves of a thin film separated by polarization into the antisymmetric Lamb (A), symmetric Lamb (S), and horizontal (H) modes. The inset highlights the low temperature behavior of the acoustic modes.

3.21 about $k_\parallel$ to obtain the low energy behavior of these modes, highlighted in the inset of Figure 3.4.

Setting $m = 0$ in Equation 3.17, we find that for the acoustic H mode, $\omega_{H,0}$ is linearly proportional to $k_\parallel$ for all $k_\parallel$:

$$\omega_{H,0}(k_\parallel) = v_t k_\parallel \tag{3.26}$$

Expanding Equation 3.22 in $k_\parallel$ to first order, we find ω of the acoustic symmetric Lamb mode is also linearly proportional to $k_\parallel$ at low temperatures:

$$\begin{aligned} \omega_{S,0} &= 2\frac{v_t}{v_l}\sqrt{v_l^2 - v_t^2}k_\parallel \\ &\equiv v_{SL}k_\parallel \end{aligned} \tag{3.27}$$

We expand Equation 3.21 to the second order to obtain a non-trivial result. We find ω depends linearly on d for the acoustic antisymmetric Lamb mode:

$$\begin{aligned} \omega_{A,0} &= d\sqrt{\frac{v_l^2 - v_t^2}{3v_l^2}}k_\parallel^2 \\ &\equiv \frac{\hbar}{2m^*}k_\parallel^2 \end{aligned} \tag{3.28}$$

Kühn 2007 [59] likens this behavior to that of a massive particle with a mass that is inversely proportional to d.

3.1.3 Ballistic Thermal Conductance

With the dispersion relations of the H, S, and A modes, we can now calculate the thermal conductance of a thin film in the ballistic limit, i.e., the conductance in the absence of diffusive scattering. We begin with the general heat flux of the phonon field, which has units of power per area

$$\vec{\dot{Q}} = \frac{1}{V}\sum_\mu \hbar\omega_\mu \vec{v}_\mu n_\mu \tag{3.29}$$

where $\hbar$ is the reduced Planck's constant, $\vec{v}_\mu = \partial\omega_\mu/\partial k_\parallel$ is the phonon group velocity, and the sum $\mu = (k_\parallel, m, p)$ is over the wave number parallel to the x-axis $k_\parallel$, mode number m, and polarization

$p = (H, A, S)$. The Bose-Einstein distribution describes the phonon distribution function n_μ:

$$n_\mu = \frac{1}{\exp\left(\hbar\omega_\mu / k_B T\right) - 1} \tag{3.30}$$

where k_B is the Boltzmann constant. We are only concerned with the heat flux propagating through the $\hat{y} - \hat{z}$ plane in the $\hat{x}$ direction. Therefore, the radiating surface $\vec{s}$ is the cross-section of the film with area $A = d \times w$. This radiated power is

$$P_{ball} = \int_{\vec{s}} d\vec{s} \cdot \dot{\vec{Q}} = \frac{1}{V} \sum_\mu \iint dy\ dz\ \hbar\omega_\mu n_\mu (\vec{v}_\mu \cdot \hat{n}_s) \tag{3.31}$$

where $\hat{n}_s$ is the surface normal $\hat{y} \times \hat{z} = \hat{x}$. The quantity $(\vec{v}_\mu \cdot \hat{n}_s) = |\vec{v}_\mu| \cos\phi$ is the group velocity perpendicular to the radiating surface. We are only interested in the power flow out of $\vec{s}$ and therefore restrict ϕ to $[-\pi/2, \pi/2]$. The sum over $k_\parallel$ can be converted to an integral over $k_\parallel$ space using

$$\sum_{k_\parallel} = \frac{wL}{(2\pi)^2} \iint d^2 k_\parallel \tag{3.32}$$

$$= \frac{wL}{(2\pi)^2} \iint k_\parallel dk_\parallel d\phi \tag{3.33}$$

Restricting ϕ to $[-\pi/2, \pi/2]$ and remembering $\vec{v}_\mu = \partial\omega_\mu / \partial k_\parallel$, Equation 3.31 becomes

$$P_{ball} = \frac{1}{V} \int_0^w \int_0^d dy\ dz\ \frac{wL}{(2\pi)^2} \sum_{m,p} \iint \left|\frac{\partial\omega_\mu}{\partial k_\parallel}\right| \frac{\hbar\omega_\mu k_\parallel}{\exp\left(\hbar\omega_\mu / k_B T\right) - 1} dk_\parallel \cos\phi d\phi \tag{3.34}$$

$$= \frac{dwL}{V} \frac{w}{(2\pi)^2} \sum_{m,p} \int_0^\infty \left|\frac{\partial\omega_\mu}{\partial k_\parallel}\right| \frac{\hbar\omega_\mu k_\parallel}{\exp\left(\hbar\omega_\mu / k_B T\right) - 1} dk_\parallel \int_{-\pi/2}^{\pi/2} \cos\phi d\phi \tag{3.35}$$

$$= \frac{w}{2\pi^2} \sum_{m,p} \int_0^\infty \left|\frac{\partial\omega_\mu}{\partial k_\parallel}\right| \frac{\hbar\omega_\mu k_\parallel}{\exp\left(\hbar\omega_\mu / k_B T\right) - 1} dk_\parallel \tag{3.36}$$

From this, we calculate the ballistic thermal conductance:

$$G_{ball} = \frac{\partial P_{ball}}{\partial T} = \frac{w}{2\pi^2} \sum_{m,p} \int_0^\infty k_B \left(\frac{\hbar\omega_\mu}{k_B T}\right)^2 \frac{\exp\left(\hbar\omega_\mu / k_B T\right)}{\left(\exp\left(\hbar\omega_\mu / k_B T\right) - 1\right)^2} \left|\frac{\partial\omega_\mu}{\partial k_\parallel}\right| k_\parallel dk_\parallel \tag{3.37}$$

$$= \frac{w}{2\pi^2} \sum_{m,p} \int_0^\infty k_B \left(\frac{\hbar\omega_\mu}{k_B T}\right)^2 \frac{k_\parallel \exp\left(\hbar\omega_\mu / k_B T\right)}{\left(\exp\left(\hbar\omega_\mu / k_B T\right) - 1\right)^2} d\omega_\mu \tag{3.38}$$

$$= \frac{w}{2\pi^2} \sum_{m,p} \int_0^\infty k_B \xi^2 \frac{k_\parallel \exp\left(\xi\right)}{\left(\exp\left(\xi\right) - 1\right)^2} \frac{k_B T}{\hbar} d\xi \tag{3.39}$$

$$= \frac{w}{2\pi^2} \frac{k_B^2 T}{\hbar} \sum_{m,p} \int_0^\infty \frac{k_\parallel \xi^2 \exp\left(\xi\right)}{\left(\exp\left(\xi - 1\right)^2\right.} d\xi \tag{3.40}$$

where $\xi = \hbar\omega_\mu / k_B T$. This expression can only be calculated numerically in the general case, but we can use dispersion relations in the bulk and low temperature limits to solve for the thermal conductance in the 3D and 2D cases.

In the bulk limit, the S and A modes do not interact with the boundary and all modes are decoupled. Dispersion relations for all polarizations take the form of $\omega_{p,m} = v_p\sqrt{k_\parallel^2 + (m\pi/d)^2}$, where v_p is v_l for the S modes and v_t for the A and H modes. The 3D radiated power is

$$P_{3D} = \frac{dw\hbar}{8\pi^2}\left(\frac{k_B T}{\hbar}\right)^4 \left(\frac{2}{v_t^2} + \frac{1}{v_l^2}\right)\Gamma(4)\zeta(4) \tag{3.41}$$

where $\Gamma(4)$ and $\zeta(4)$ are the Gamma and Reimann zeta functions respectively. The 3D thermal conductance is

$$G_{3D} = \frac{dw\hbar}{2\pi^2}T^3\left(\frac{k_B}{\hbar}\right)^4 \left(\frac{2}{v_t^2} + \frac{1}{v_l^2}\right)\Gamma(4)\zeta(4) \tag{3.42}$$

In the 3D ballistic limit, G is linearly proportional to d and T^3, which is consistent with the low temperature limit of the Debye model.

In the 2D limit, only the acoustic modes are occupied. Using the low temperature expansions of the acoustic mode dispersion relations in Equations 3.26-3.28, we can solve for the 2D power:

$$P_{2D} = \frac{w\hbar}{2\pi^2}\left[\left(\frac{1}{v_t} + \frac{1}{v_{SL}}\right)\Gamma(3)\zeta(3)\left(\frac{k_B T}{\hbar}\right)^3 + \sqrt{\frac{2m^*}{\hbar}}\Gamma\left(\frac{5}{2}\right)\zeta\left(\frac{5}{2}\right)\left(\frac{k_B T}{\hbar}\right)^{5/2}\right] \tag{3.43}$$

where v_{SL} is defined in 3.28. The last term comes from the treatment of acoustic antisymmetric mode as a particle with mass m^* defined in Equation 3.28:

$$m^* \equiv \frac{\hbar}{2d}\sqrt{\frac{3v_l^2}{v_l^2 - v_t^2}} \tag{3.44}$$

The 2D thermal conductance is

$$G_{2D} = \frac{w\hbar}{2\pi^2}\left[3\left(\frac{1}{v_t} + \frac{1}{v_{SL}}\right)\Gamma(3)\zeta(3)\left(\frac{k_B}{\hbar}\right)^3 T^2 + \frac{5}{2}\sqrt{\frac{2m^*}{\hbar}}\Gamma\left(\frac{5}{2}\right)\zeta\left(\frac{5}{2}\right)\left(\frac{k_B}{\hbar}\right)^{5/2} T^{3/2}\right] \tag{3.45}$$

At very low temperatures, deep into the 2D regime, the antisymmetric mode term in which $G \sim T^{3/2}$ dominates, giving the surprising result $G_{2D} \propto 1/\sqrt{d}$. In the quasi-2D limit at intermediate temperatures, the left term dominates, and G_{q2D} is independent of film thickness. Therefore, in the ballistic transport regime, the dimensionality of the phonon gas dictates how G scales with the film thickness.

3.1.4 2D-3D Transition of the Phonon Gas

As shown in Equations 3.24 and 3.25, the cutoff frequencies of the optical modes increase with decreasing thickness. As a consequence, the dimensionality of the phonon gas in thinner films is suppressed at lower temperatures. Put another way, the dimensionality of the phonon gas depends on the relative sizes of the thin film geometry and the dominant phonon wavelength $\lambda_D = \hbar v_s/(2.82 k_B T)$ [124].

In thin films, 2D-3D dimensionality is set by the ratio between d and λ_D. If $\lambda_D << d$, a significant number of optical modes are accessible and the number of occupied modes increases with film thickness. In this case, the phonon gas is fully 3-dimensional. However, if $\lambda_D >> d$, only the acoustic modes are accessible and the number of occupied modes is agnostic to thickness, condensing the phonon gas into a 2-dimensional state. The transition between these states occurs when $d \sim \lambda_D$. At constant temperature T, the 2D-3D crossover thickness [58, 68] is

$$d_c = \frac{\hbar v_t}{2 k_B T} \tag{3.46}$$

This transition can be seen in Figure 3.5, where we have made numerical calculations of G vs d for a 5-µm-wide film of amorphous silicon nitride (a-SiN_x) at 170 mK. We use the sound speeds for stoichiometric Si_3N_4 of $v_t = 6280$ m/s for transversely polarized waves, $v_l = 1115$ m/s for longitudinally-polarized waves, and $v_s = 6986$ m/s is average sound speed [22]. At this temperature, the transition occurs at d_c ∼140 nm, coinciding with a minimum conductance of 6.7 pW/K. The red dashed lines show power law fits of both the thinnest and thickest films.

For the thinnest films in which $d <<$ 140 nm, G is approaching the 2D limit in which $G \propto 1/\sqrt{d}$. The $G \propto d^{-1/4}$ result suggests that the antisymmetric Lamb mode contributes significantly but does not yet dominate the thermal conductance. Calculations of the thickest films approach the 3D limit $d >>$ 140 nm, recovering G∼ d behavior. This figure also illustrates the surprising result that in the absence of diffusive scattering, a 10-nm-thick film of a-SiNx is nearly as conductive as a 600-nm-thick film. It is clear from these results that the naive assumption $G \propto d$ insufficiently describes the phonon physics in thin films at low temperatures, and that the effects of suppressed

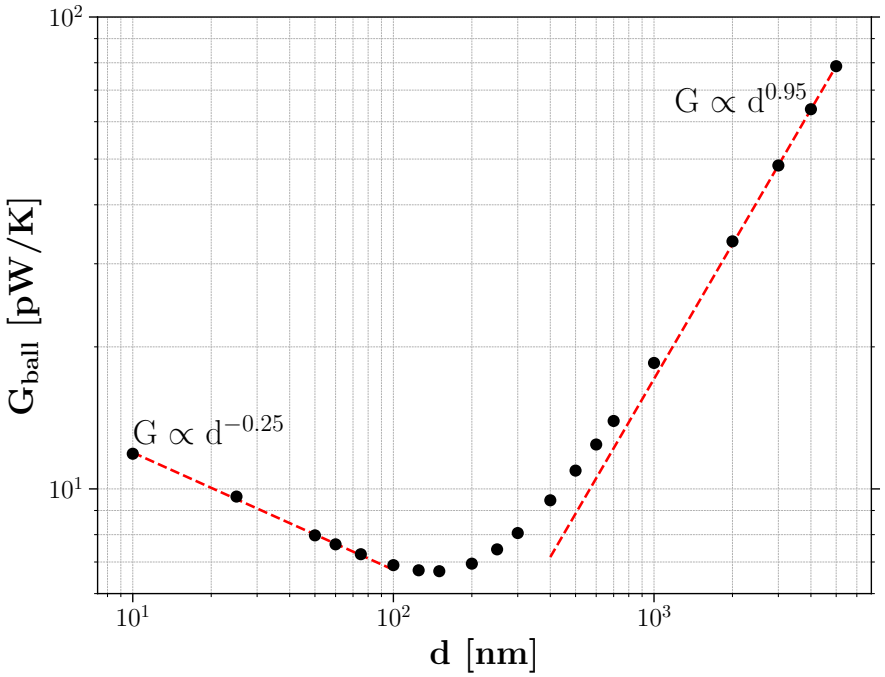

Figure 3.5: Numerical calculations of G for a 5-µm-wide thin film of a-SiNx at 170 mK. The minimum conductance occurs at d_c=139 nm. Red dashed lines are power law fits to calculations for the thinnest and thickest d values, which approach the elastic theory predictions that the ballistic G $\propto 1/\sqrt{d}$ for $d << d_c$ and G $\propto d$ for $d >> d_c$.

dimensionality must be included when modeling their thermal conductance.

3.1.5 1D Ballistic Transport

In films where the width also approaches λ_D, the phonon gas loses dimensionality in the $\hat{y}$ direction, and ballistic phonon transport is 1-dimensional. The power transmitted down a 1D thermal link is

$$P_{1D} = \sum_{m,p} \int_0^\infty \frac{dk}{2\pi} \hbar\omega_\mu \left| \frac{\partial \omega_\mu}{\partial k_\parallel} \right| n_\mu \tag{3.47}$$

From this, we can calculate the 1D thermal conductance:

$$G_{1D} = \frac{\partial P_{ball}}{\partial T} = \frac{1}{2\pi} \sum_{m,p} \int_0^\infty k_B \left(\frac{\hbar\omega_\mu}{k_B T} \right)^2 \frac{\exp\left(\hbar\omega_\mu / k_B T\right)}{\left(\exp\left(\hbar\omega_\mu / k_B T\right) - 1\right)^2} \left| \frac{\partial \omega_\mu}{\partial k_\parallel} \right| \, dk_\parallel \tag{3.48}$$

$$= \frac{1}{2\pi} \sum_{m,p} \int_0^\infty k_B \left(\frac{\hbar\omega_\mu}{k_B T} \right)^2 \frac{\exp\left(\hbar\omega_\mu / k_B T\right)}{\left(\exp\left(\hbar\omega_\mu / k_B T\right) - 1\right)^2} d\omega_\mu \tag{3.49}$$

$$= \frac{k_B^2 T}{h} \sum_{m,p} \int_0^\infty \frac{\xi^2 \exp\left(\xi\right)}{\left(\exp\left(\xi\right) - 1\right)^2} d\xi \tag{3.50}$$

$$= \left(\frac{\pi^2 k_B^2 T}{3h} \right) N_m \equiv g_0 N_m \tag{3.51}$$

where $g_0 = (0.946 \ pW/K^2) \times T$ is the quantum thermal conductance and N_m is the number of modes. In the 1D limit, phonons occupy the only four lowest modes, of which there is one longitudinal, one torsional, and two shear degrees of freedom. Therefore, in 1D ballistic phonon transport, the thermal conductance is quantized and no longer depends on sample geometry or particle statistics [94].

3.2 Diffusive Phonon Transport

In the previous section, we explored the limit where the phonon mean free path is much longer than the length of the film $\ell >> L$ and the phonons propagate radiatively across the film. In the opposite limit $\ell << L$, phonons will scatter many times while traveling across the film, leading to diffusive phonon transport. Any diffusive scattering processes suppress G with respect to the ballistic case and introduce a $G \propto 1/L$ dependency.

In dielectric thin films at sub-Kelvin temperatures and superconducting thin films at $T << T_c$, although phonon-quasiparticle scattering is negligible due to low quasiparticle densities, inhomogeneities that are intrinsic to the material, such as density inhomogeneities and two-level systems, can be sites for diffusive phonon scattering. The mean free path associated with these intrinsic scattering processes ℓ_i is independent of geometry. If the surface roughness of a film is comparable to phonon wavelengths, the boundary itself becomes a site for diffusive scattering, introducing a mean free path that depends on film geometry. To accurately describe general phonon transport in thin films, we must include the effects of intrinsic and boundary scattering on the thermal conductance.

3.2.1 Diffusive Thermal Conductance

In diffusive transport, the heat flux density is set by the thermal conductivity κ:

$$\dot{\vec{Q}} = -\kappa \vec{\nabla} T \tag{3.52}$$

From this, we see that heat flow is a non-equilibrium process and that $\dot{\vec{Q}}$ is non-zero only in the presence of a temperature gradient $\vec{\nabla} T$. For the phonon number n_μ to be defined, we must assume the variations in T are sufficiently small such that any position along the gradient is in a local thermodynamic equilibrium. Therefore, n_μ becomes a function of position and can be approximated as $n_\mu = n_{\mu,0} + \delta n_\mu$, where δn_μ is a small change with the global $n_{\mu,0}$. Only deviations from the equilibrium distribution can produce the thermal gradient necessary for conduction, therefore only δn_μ can contribute to the heat flux. Given this, Equation 3.29 becomes

$$\dot{\vec{Q}} = \frac{1}{V} \sum_\mu \hbar \omega_\mu \vec{v}_\mu \delta n_\mu \tag{3.53}$$

Changes in the phonon distribution result from diffusive scattering phonon decay and temperature changes along the thermal gradient. The phonon distribution at time t and position $\vec{r}$ is the distribution at $t - dt$ and position $\vec{r} - \vec{v}_\mu dt$ minus the phonon decay during dt:

$$n_\mu(x,t) = n_\mu(\vec{r} - \vec{v}_\mu dt, t - dt) - \left(\frac{\delta n_\mu}{\tau_\mu} \right) dt \tag{3.54}$$

where we've introduced the decay relaxation time τ_μ. Using a first-order Taylor expansion of $n_{\mu,0} = n_\mu(\vec{r} - \vec{v}_\mu dt, t - dt)$,

$$\frac{\delta n_\mu}{\tau_\mu} dt = -\frac{\partial n_{\mu,0}}{\partial t} dt - \vec{v}_\mu \cdot \vec{\nabla} n_{\mu,0} dt \tag{3.55}$$

We are only interested in steady state solutions, so the partial time derivative is 0. Since the positional dependence of n_μ is inherited from the dependence on T, we solve for δn_μ in terms of the thermal gradient:

$$\delta n_\mu = -\tau_\mu \vec{v}_\mu \cdot \frac{\partial n_{\mu,0}}{\partial T} \vec{\nabla} T \tag{3.56}$$

This gives the following heat flux for diffusive phonon transport:

$$\vec{\dot{Q}} = -\frac{1}{V} \sum_\mu \hbar \omega_\mu \frac{\partial n_{\mu,0}}{\partial T} \tau_\mu \vec{v}_\mu \cdot (\vec{v}_\mu \cdot \vec{\nabla} T) \tag{3.57}$$

with units of power per area.

It is common to characterize diffusive phonon transport by the distance between scattering events, which for a phonon of mode μ and velocity $\vec{v}$ is

$$\vec{\ell}_\mu = \tau_\mu \vec{v}_\mu \tag{3.58}$$

Inserting $\vec{\ell}_\mu$ into Equation 3.57 gives

$$\dot{Q} = -\frac{1}{V} \sum_\mu \hbar \omega_\mu \frac{\partial n_{\mu,0}}{\partial T} \vec{\ell}_\mu \cdot (\vec{v}_\mu \cdot \vec{\nabla} T) \tag{3.59}$$

From Equation 3.52, the thermal conductivity of the film is

$$\kappa = \frac{1}{V} \sum_\mu \hbar \omega_\mu \frac{\partial n_{\mu,0}}{\partial T} \vec{\ell}_\mu \cdot (\vec{v}_\mu \cdot \hat{n}_s) \tag{3.60}$$

It is conventional to reduce $\vec{\ell}_\mu$ to the mode- and angle-averaged mean free path ℓ, which is a statistical quantity defined by describing the probability that a phonon will travel a distance dx as $\sim \exp(-dx/\ell)$ [50]. Using Equation 3.33 and recalling that we have defined the thermal gradient

to be non-zero only in $\hat{x}$, the thermal conductivity becomes

$$\kappa = \frac{wL}{V(2\pi)^2}\int_0^\infty \sum_{m,p} \hbar\omega_\mu k_B \left(\frac{\hbar\omega_\mu}{k_BT}\right)^2 \frac{\exp\left(\hbar\omega_\mu/k_BT\right)}{\left(\exp\left(\hbar\omega_\mu/k_BT\right)-1\right)^2} k_\parallel dk_\parallel \int_{-\pi/2}^{\pi/2} |v_\mu|\cos(\phi)\ell\cos(\phi)d\phi \tag{3.61}$$

$$= \frac{\ell}{(2\pi)^2 d}\int_0^\infty \sum_{m,p} \hbar\omega_\mu |v_\mu| k_B \left(\frac{\hbar\omega_\mu}{k_BT}\right)^2 \frac{\exp\left(\hbar\omega_\mu/k_BT\right)}{\left(\exp\left(\hbar\omega_\mu/k_BT\right)-1\right)^2} k_\parallel dk_\parallel \int_{-\pi/2}^{\pi/2} \cos^2(\phi)d\phi \tag{3.62}$$

$$= \frac{\ell}{8\pi d}\int_0^\infty \sum_{m,p} \hbar\omega_\mu |v_\mu| k_B \left(\frac{\hbar\omega_\mu}{k_BT}\right)^2 \frac{\exp\left(\hbar\omega_\mu/k_BT\right)}{\left(\exp\left(\hbar\omega_\mu/k_BT\right)-1\right)^2} k_\parallel dk_\parallel \tag{3.63}$$

where $v_{\mu,x} = |v_\mu|\cos(\phi)$ and $\ell_x = \ell\cos(\phi)$. As with the ballistic thermal conductance derivation, ϕ is the angle between $\vec{v_\mu}$ and the surface normal $\hat{n}_s$. The diffusive thermal conductance is

$$G_{diff} = (A/L)\times\kappa \tag{3.64}$$

$$= \frac{\ell}{4L}\frac{w}{2\pi}\int_0^\infty \sum_{\mu} |v_\mu| k_B \left(\frac{\hbar\omega_\mu}{k_BT}\right)^2 \frac{\exp\left(\hbar\omega_\mu/k_BT\right)}{\left(\exp\left(\hbar\omega_\mu/k_BT\right)-1\right)^2} k_\parallel dk_\parallel \tag{3.65}$$

$$= G_{ball}\times\frac{\pi\ell}{4L} \tag{3.66}$$

The ratio L/ℓ is the average number of diffusive phonon scattering events along the length of the film. Therefore, we can see that diffusive thermal conductance is approximately the ballistic conductance suppressed by the number of diffusive scattering events along the film. In the bulk diffusive limit, $G_{diff} \propto A/L$ and κ is intrinsic to the material. However, any amount of ballistic transport, diffusive boundary scattering, or reduced dimensionality will alter how G scales with thin film geometry and will introduce a geometry dependence into κ.

3.2.2 Mean Free Path

As shown in the previous section, the phonon mean free path ℓ sets the diffusive thermal conductance. The limiting diffusive scattering processes in the film determine the overall mean free path. If phonon transport is limited by boundary scattering, ℓ will depend on film geometry. As defined in Equation 3.73, ℓ is the length between scattering events projected onto the direction of the thermal gradient averaged over all modes and integrated over $\phi \in [-\pi/2, \pi/2]$:

$$\ell = \frac{1}{\pi}\int_{-\pi/2}^{\pi/2} \ell_x d\phi \tag{3.67}$$

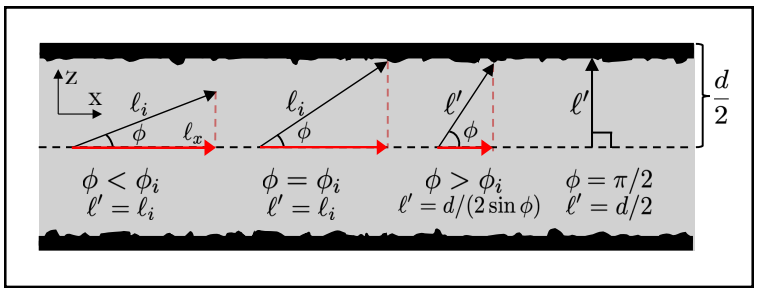

Figure 3.6: The diffusive boundary scattering effect on the phonon path. The red arrows indicate the mean free path in the thermal gradient direction $\ell_x = \ell' \cos\phi$, where ℓ_i is the mean free path of intrinsic scattering mechanisms. The mean free path magnitude ℓ' is equal to ℓ_i for $\phi \leq \phi_i$ and is shortened by the boundary for larger ϕ. For $\phi > \phi_i$, the phonon scatters diffusively at the boundary and $\ell' = \ell_i \sin\phi$.

where ℓ_x is the projection of $|\ell_\mu|$ onto the x-axis summed over all modes μ.

If phonon transport is limited by intrinsic scattering mechanisms, $\ell_x = \ell_i \cos\phi$ for all ϕ and ℓ is simply

$$\ell_0 = \frac{1}{\pi}\int_{-\pi/2}^{\pi/2} \ell_i \cos\phi d\phi = \frac{2}{\pi}\ell_i \tag{3.68}$$

However, if phonons also diffusively scatter at the film surfaces, ℓ_x becomes more complicated. For angles $|\phi| \leq \phi_i = \sin^{-1}(d/2\ell_i)$, illustrated on the left in Figure 3.6, the phonon will scatter from intrinsic processes before encountering the surface and ℓ_x is still $\ell_i \cos\phi$. Note that we have assumed that boundary scattering occurs exclusively at the top and bottom surfaces of the film. If phonons instead scatter at the edges of the film, d should be replaced by w.

For $|\phi| > \phi_i$, illustrated as the third scenario in Figure 3.6, ℓ_x is shortened by the boundary to $\ell_x = d/(2\sin\phi) \times \cos\phi$. On the very right of the figure, $\ell_x = (d/2)\cos(\pi/2) = 0$. Accounting for these boundary interactions, ℓ_x is

$$\ell_x = \begin{cases} \ell_i \cos\phi & \text{for } \phi < \phi_i \\ (d/2) \times \cot\phi & \text{for } \phi \geq \phi_i \end{cases} \tag{3.69}$$

So far, we have assumed 100% of phonon interactions with the surface result in diffusive scattering. However, it is often the case that phonon-boundary interactions are a mixture of both diffusive and specular scattering. In diffusive scattering, the phonon is absorbed by the boundary

and reemitted isotropically. In specular scattering, the phonon reflects off the surface, and phonon propagation is unimpeded by the boundary interaction.

The expectation value of ℓ for diffusive scattering probability P_d on both the top and bottom surfaces is given by the infinite sum

$$< \ell > = P_d\ell_0 + P_d(1-P_d)2\ell_0 + P_d(1-P_d)^2 3\ell_0 + ... \tag{3.70}$$

$$= \ell_0 \sum_{m=0}^{\infty} mP_d(1-P_d)^{m-1} \tag{3.71}$$

$$= \ell_0/P_d \tag{3.72}$$

where ℓ_0 is the mean free path for 100% diffusive scattering probability.

Therefore, if diffusive scattering P_d is less than unity, the thickness is effectively extended to $d_{eff} = d/P_d$. For example, if 50% of boundary scattering events are diffusive, phonon propagation is interrupted by only 50% of boundary interactions. This effect is equivalent to 100% diffusive scattering in a film with twice the thickness. Including the effect of specular scattering, ℓ becomes

$$\ell = \frac{1}{\pi}\int_{-\phi_i}^{\phi_i} \ell_i \cos\phi d\phi + \frac{d}{2P_d}\left(\frac{1}{\pi}\int_{-\pi/2}^{-\phi_i} \cot\phi d\phi + \frac{1}{\pi}\int_{\phi_i}^{\pi/2} \cot\phi d\phi\right) \tag{3.73}$$

using the adjusted $\phi_i = \sin^{-1}[d/(2\ell_i \times P_d)]$.

An example calculation of ϕ_i and ℓ/ℓ_0 for a range of diffuse scattering probability is shown in Figure 3.7. For this calculation, we set $\ell_i = 20$ µm and $d = 1$ µm. For $P_d \leq d/(2\ell_i)$, we set $\phi_i = \pi/2$ since $\sin^{-1}(x > 1)$ is nonphysical. This produces the plateau in ℓ/ℓ_0 for $P_d \leq 2.5\%$. For this geometry, we find that a 10% probability of diffusive boundary scattering suppresses ℓ by $> 40\%$. If 100% of phonon-boundary interactions result in diffusive scattering, ℓ is suppressed by nearly 90%. For $P_d \leq d/\ell_i = 2.5\%$, $\phi_i = \pi/2$ and diffusive boundary scattering has no effect on ℓ.

Figure 3.8 shows calculations of ℓ as a function of d/ℓ_i for the diffuse scattering probabilities of 10%, 50%, and 100%. For the phonon mean free path not to be suppressed by boundary scattering, the internal scattering mean free path ℓ_i must be $\leq d/2$. Internal scattering dominates at $d/\ell_i = 0.2$ for $P_d = 10\%$ and $d/\ell_i = 1$ for $P_d = 50\%$.

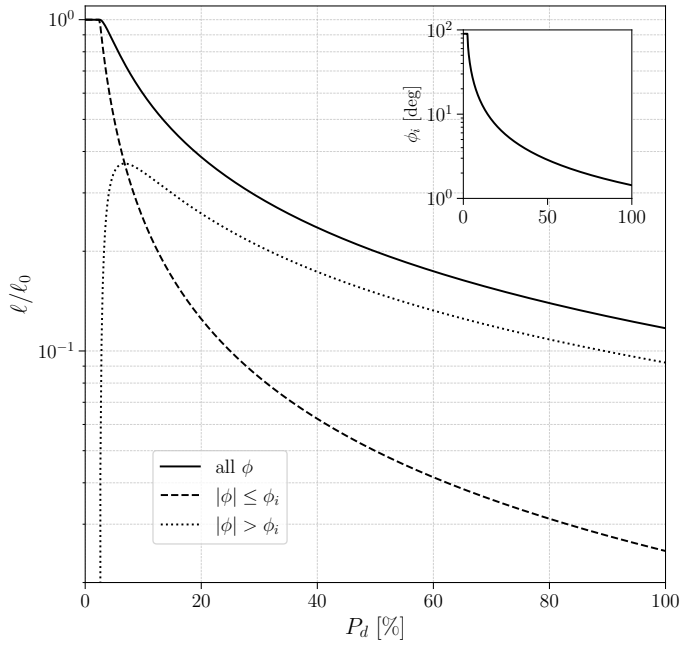

Figure 3.7: Example calculation of the mean free path ℓ including boundary effects normalized to the mean free path assuming no diffusive boundary scattering for various P_d. The inset is the corresponding calculation of ϕ_i. Contributions from angles limited by intrinsic scattering $|\phi| \leq \phi_i$ and angles at which phonons diffusively scatter off the film boundaries $|\phi| > \phi_i$ are also shown. We set ℓ_i= 20 µm and d = 1 µm.

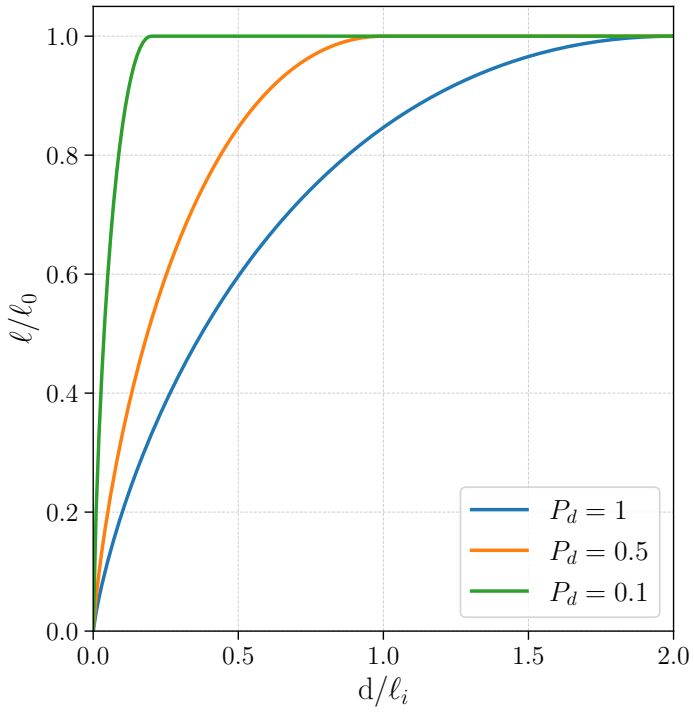

Figure 3.8: Calculations of ℓ as a function of d/ℓ_i for diffuse scattering probabilities of 10%, 50%, and 100%.

3.3 Total Thermal Conductance

In cryogenic detectors, it is not uncommon for phonon transport to be a mixture of ballistic and diffusive transport with a variety of scattering mechanisms. Therefore, for a thermal conductance model to be generally applicable, it must accommodate all phonon transport regimes. We model the total thermal conductance as the parallel sum of G_{ball} and G_{diff}. Similarly, the mean free path ℓ is the parallel sum of all ℓ for all significant scattering mechanisms.

Using Equations 3.40 and 3.66, we calculate the total thermal conductance as

$$G_{tot} = \left(\frac{1}{G_{ball}} + \frac{1}{G_{diff}}\right)^{-1} \tag{3.74}$$

$$= G_{ball}\left(1 + \frac{4L}{\pi\ell}\right)^{-1} \tag{3.75}$$

The total thermal conductance through the ballistic-diffusive transition is shown in Figure 3.9. In the limit that the mean free path is much shorter than the length of the film $L/\ell >> 1$, the second term dominates and we recover $G_{tot} = G_{ball} \times (\pi\ell/4L) = G_{diff}$. In the ballistic limit where $\ell/L >> 1$, L/ℓ is negligible and $G_{tot} = G_{ball}$. Transport is fully diffusive with $G \propto 1/L$ at $L = 10\ell$, and diffusive scattering begins to suppress the thermal conductance at L$\sim$ 10% ℓ.

Withington et al. 2017 [118] measured the thermal conductance of a-SiN_x films through the ballistic-diffusive transition and report the same length scaling behavior. They refer to the quantity $L_a = \pi\ell/4$ as the thermal elastic-wave attenuation length. They measure $L_a = 20$ µm in a-SiN_x films < 2 µm wide and < 200 nm thick with a length ranging from ~ 1 µm to 500 µm, corresponding to a mean free path of 27 µm. They favor two-level systems as the limiting diffusive scattering process in their films.

3.4 Film Thickness Dependence

As shown in the previous sections, the phonon gas dimensionality and scattering mechanisms (or lack thereof) determine how G scales with film geometry. We characterize boundary effects

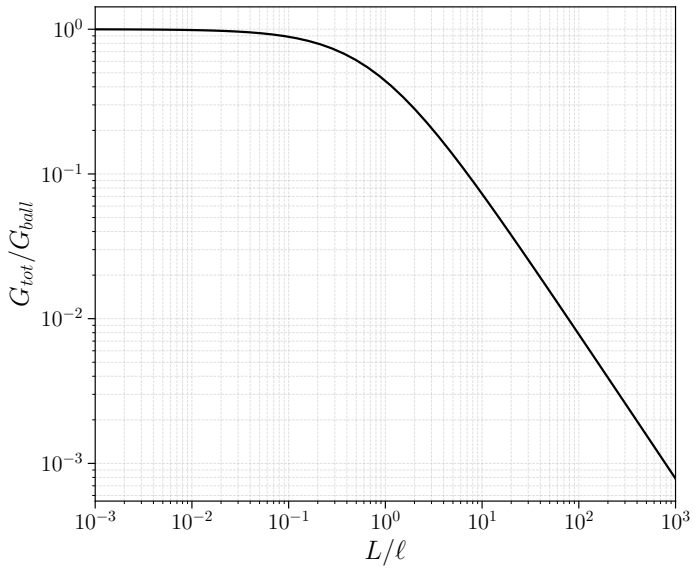

Figure 3.9: Total G as a function of length through the ballistic-diffusive transition.

involving the top and bottom surfaces of the film as

$$G \propto d^{1+\alpha} \tag{3.76}$$

where α captures deviations from the linear bulk case. The dimensionality dependencies and associated α values are given in Table 3.1.

		Boundary Scattering	**Intrinsic Scattering**	**Ballistic**
3D	$G \propto$	d^2w/L	dw/L	dw
	$\alpha =$	1	0	0
Quasi-2D	$G \propto$	dw/L	w/L	w
	$\alpha =$	0	-1	-1
2D	$G \propto$	$\sqrt{d}w/L$	$w/(L\sqrt{d})$	$w/\sqrt{d}$
	$\alpha =$	-1/2	-3/2	-3/2
1D	$G \propto$	d/L	1/L	g_0
	$\alpha =$	0	-1	-1

Table 3.1: G dependence on thin film geometry and associated α values in different phonon transport regimes.

In the ballistic regime, the phonon mean free path $\ell >>$ the length of the film L and α is set by the dimensionality of the phonon gas. In the bulk (3D) case, G is proportional to the cross-sectional area of the film $A = wd$ and $\alpha = 0$. As the film thickness shrinks to $d \sim \lambda_D$, the phonon gas condenses to a quasi-2D state where G is independent of d and $\alpha = -1$. In the fully 2D limit $d << \lambda_D$, the behavior of the acoustic antisymmetric mode dominates, resulting in $G \propto 1/\sqrt{d}$ and $\alpha = -3/2$. If the width of the film is also shrunk to $w << \lambda_D$, G is reduced to the thermal conductance quantum $g_0 = \pi^2 k_B^2 T/3h$ for each mode and is independent of film dimensions [94], with an associated α value of -1.

Diffusive scattering will suppress G with respect to the ballistic case and introduce a $G \propto 1/L$ dependency. If scattering is dominated by intrinsic scattering mechanisms, the associated mean free path ℓ_i is independent of film dimensions, and a $1/L$ dependence is introduced with respect to

the ballistic case. If, however, diffusive scattering is dominated by phonon-boundary interactions with the top and the bottom surfaces of the film, ℓ is set by the boundary scattering mean free path ℓ_B, which is proportional to d. In diffusive boundary scattering limit, α is $\alpha_{ball} + 1$, where α_{ball} is the value in the ballistic limit and is dictated by phonon dimensionality. For example, if the film is 3-dimensional and intrinsic scattering dominates, $G \propto dw/L$ and $\alpha = 0$. If instead the boundary scattering dominates, $G \propto d^2w/L$ and $\alpha = 1$.

The interpretation of a measured value of α is ambiguous without prior knowledge of the system, such as the film surface roughness. For example, an α value of 0 could result from a thin film in the 3D limit dominated by intrinsic diffusive scattering, 3D ballistic transport, or quasi-2D transport dominated by surface scattering. Measurements of the length scaling, if possible, will differentiate the diffusive and ballistic regimes. The dominant diffusive scattering mechanisms can change with stoichiometry, substrate roughness, and other fabrication variables that can produce large variances in G in nominally identical films. Film interfaces add to the complexity of predicting G in stacks of thin films.

3.5 Future Work

We have numerically calculated the dispersion curves in individual thin films, and this calculation can be repeated for any isotropic material on a TES leg if the elastic properties are known. TES legs, however, are composite multi-layer stacks. If reflection at each layer interface is perfect, the films can be treated as separate phonon channels and the total thermal conductance of the leg is the parallel sum of these channels.

However, there is likely some phonon transmission between layers. To more accurately model TES thermal conductance, the dispersion curves for the composite leg as a whole should be calculated. Such calculations have been accomplished using a spectral collocation method [88] and could be applied to our simple TES leg structures.

Chapter 4

Thermal Conductance of Individual TES Leg Layers

The dynamic range, sensitivity, and temporal response of a TES bolometer are determined by its thermal isolation from the thermal bath of the surrounding substrate. This isolation is usually achieved by suspending the TES on a micromachined island via long, thin legs of silicon nitride or silicon. The TES bias signal and, in microwave polarimetry, the signals of interest are brought onto the micromachined island with additional superconducting and dielectric layers.

The Noise-Equivalent Power (NEP) from thermal fluctuations between the TES and the thermal bath is the limiting noise source in a TES and is set by the thermal conductance: $\mathrm{NEP_{TF}} = \sqrt{4_{\mathrm{B}} T_c^2 G(T_{\mathrm{c}})}$, where the numerical factor $\gamma \leq 1$ accounts for the effect of the thermal gradient across the leg on G(T) [72]. The thermal conductance must be large enough to accommodate the anticipated signal power yet not so large that there is an unnecessary noise penalty.

G must be made extremely small for observations with low signal and background power, such as measurements conducted from a balloon or satellite. For example, TES bolometers for the CMB balloon experiment SPIDER-2 were designed for saturation powers ($\mathrm{P_{sat}}$) of 3 pW and G of 34 pW/K at a bath temperature of 300 mK [46]. Future FIR satellite NEP and bath temperature requirements will require $\mathrm{P_{sat}} < 1.5$ fW and G $<$ 50 fW/K to achieve low resolution FIR spectroscopy [35].

During design, the thermal conductance of the TES island is often assumed to be set entirely by the mechanical leg structure, neglecting the contribution from the microstrip. Once more, a typical TES R&D process involves prototyping multiple iterations of TES leg dimensions until

achieving the design conductance within some tolerance. To shorten R&D timelines and precisely optimize bolometer sensitivity, more rigorous engineering of TES thermal conductance that includes the contribution of the microstrip layers is required.

The previous chapter covered several regimes of phonon transport in thin films at low temperatures. We parameterized the dependence of thermal conductance G on layer thickness d as $G \propto d^{1+\alpha}$, where α captures any deviations from the bulk non-linear case. With this foundation, we can better understand the thermal conductance of a TES (G_{TES}), whose legs are comprised of multi-layer thin film structures.

We measure the total thermal conductance of TES bolometers with various leg geometries and deduce the thermal conductance of the individual metal and insulator layers. We do this by fitting these measurements to a model that adopts the α parametrization. We determine the dependence of thermal conductance on layer thickness and find that in our case of $\sim$ 400-nm-thick substrate layers, the microstrip not only dominates G_{TES} but is $\sim 4\times$ larger than G of the substrate. This is mainly due to the highly conductive SiN_x insulating layers. We find evidence for diffusive phonon-boundary scattering and measure a corresponding $\alpha > 0$ in the insulating layers.

This model accurately predicts G_{TES} for dozens of other CMB bolometers with significantly thicker and wider legs than our bolometers under test within 65% of the measured value. This model also accurately predicts P_{sat} measurements of Simons Observatory (SO) prototype mid-frequency (MF) detectors. With this model can explain the observed non-linear dependence on leg width in the SO MF prototypes. These results suggest our model can be more generally applied to low-G microwave polarimeters beyond our bolometers under test.

In Section 4.1, I discuss the TES bolometers under test and measurements of their total thermal conductances. The model used to describe this data is defined in Section 4.2, and the resulting thermal conductance and thickness-scaling measurements from fitting this model are shared in Section 4.3. In Section 4.4, I compare our measurements to literature values and assess the prediction power of this model for bolometers with significantly thicker and wider legs than the bolometers under test. I also use this model to illustrate the implications of neglecting the microstrip when

Leg	Film Stack	S	W1	I1	W2	I2
A	S-W1-I1-W2-I2	386±17	167±7	305±27	358±3	298±26
B	S-W1-I1-W2	386±17	167±7	305±27	317±8	-
C	S-I1-W2-I2	312±13	-	305±27	358±3	298±26
D	S-W1-I1-I2	386±17	167±7	604±14	-	-
E	S-W1-W2	280±12	418±17	-	-	-
F	S-I1-I2	312±13	-	604±14	-	-
G	S	235±10	-	-	-	-

Table 4.1: Layer thicknesses in nm for each bolometer leg studied. S is the mechanical substrate consisting of a SiO_x-SiN_x bi-layer, W1&2 are Nb wiring layers, and I1&2 are SiN_x insulating layers. W1-W2 and I1-I2 stacks are treated as a single layer.

forecasting detector thermal fluctuation noise. I then summarize this work in Section 4.5 and share future steps in Section 4.6.

4.1 Bolometers Under Test

We present a study of the thermal conductance of the wiring, insulation, and mechanical leg layers in AlMn TES bolometers designed for polarimetry of the CMB. The TES bolometers under test have a superconducting transition temperature T_c of 171±0.7 and are suspended by four legs that are 5 µm wide and 220 µm long. The substrate layer (S) is a SiO_x-SiN_x bi-layer that provides mechanical support from the wafer to the island. The microstrip sits on top of this substrate layer and consists of two niobium wiring layers (W1 & W2) and two silicon nitride insulating layers (I1 & I2) that separate and protect the wiring layers. Figure 4.1a shows one TES device under test. Figure 4.1b is the cross-section of a TES leg with the full substrate-microstrip film stack (S-W1-I1-W2-I2) that was cut with a Focused Ion Beam and imaged with a Scanning Electron Microscope (FIB-SEM).

Film stacks that constitute the bolometer legs measured in this study and the corresponding layer thicknesses, measured from FIB-SEM-imaged cross-sections, are outlined in Table 4.1. These legs include the nominal microstrip (S-W1-I1-W2-I2) and variations in which one or more microstrip layers are removed. Layer thickness can vary with film stack geometry as successive patterning and etch steps remove material. For example, the substrate layer in Leg Geometry C is thinned during

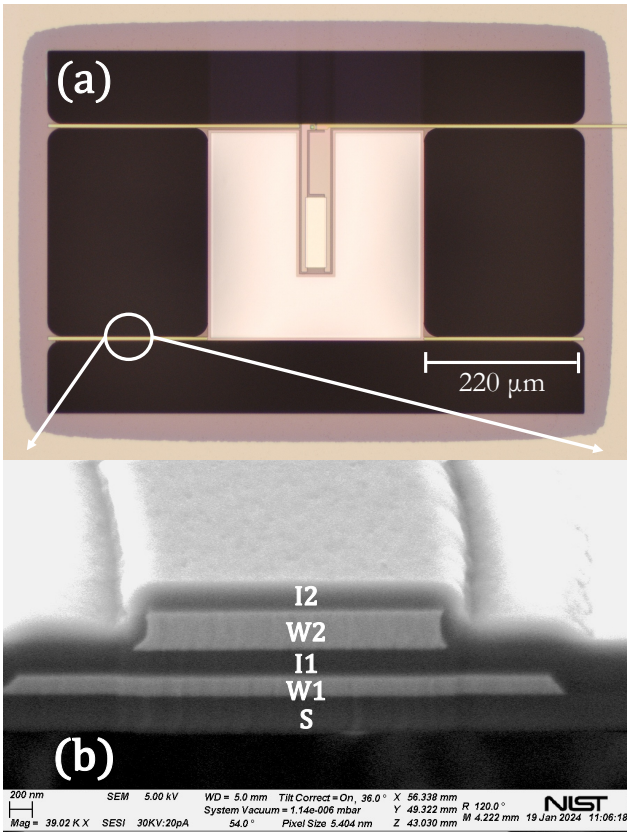

Figure 4.1: a) One TES bolometer under test. The AlMn TES is a thin film in the middle of the island suspended from the thermal bath via four 220 µm-long, 5 µm-wide legs. b) The cross-section of a TES leg on device (a) imaged with FIB-SEM. This leg consists of a full microstrip (W1-I1-W2-I2) on top of the substrate (S).

Bolometer	**Leg Geometry**	**G_{TES} [pW/K]**
1	4×A	13.96±0.08
2	1×A & 3×G	4.72 ±0.04
3	2×A & 2×G	7.90±0.04
4	3×A & 1×G	10.11±0.05
5	1×B & 3×F	17.23±0.10
6	1×B & 3×E	5.66±0.02
7	2×A & 1×C & 1×D	15.95±0.09
8	1×B & 3×G	3.51±0.02

Table 4.2: Leg geometries and G_{TES} values of the TES bolometers in this study. Legs A-G refer to film stack geometries in Table 4.1.

exposure to the W1 and I1 layer etch steps.

We deduce the thermal conductance contributions from individual substrate and microstrip layers by measuring the total thermal conductance G_{TES} of TES bolometers with eight unique leg geometries and modeling this data with the α parametrization, which allows for a range and mixture of phonon transport regimes. G_{TES} measurement methodology is described later in this thesis in Section 6.3.3.2. G_{TES} measurements for each bolometer under test are given in Table 4.2.

4.2 Thermal Conductance Modeling

In layers of insulating materials and superconducting metals below T_c, heat is transported via phonons. In the bulk case, the phonon mean free path ℓ is set by internal scattering mechanisms and G$\propto$ (dw/L) scales linearly with the film thickness d, width w, and inversely with length L. As discussed in Chapter 3, phonon interactions with the film boundaries can suppress the dimensionality of the phonon gas or introduce a diffusive scattering mean free path that is set by the film geometry. These boundary interactions will alter how G scales with film dimensions. These scalings and corresponding α values are given in Table 3.1.

In this work, all the leg layers share the same 220-µm length and 5-µm width, except the 3-µm-wide W2 layers. Therefore, our measurements are only sensitive to scaling with thickness. In the case of W2, we assume linear scaling with width. More work is needed to accommodate the possibility of phonon interactions with the edges of the film.

The total TES thermal conductance G_{TES} is the sum of the contributions from each film that constitute the four TES legs:

$$G_{\mathrm{TES}} = \sum_{layer\ x} G_x \left(\frac{d_x}{d_0}\right)^{1+\alpha_x} \tag{4.1}$$

summing over all S, W, and I layers, where the normalized thickness $d_0 = 400$ nm. The physical significance of α values is summarized in Table 3.1. The conductance of the microstrip is $G_{micro} = G_{W1} + G_{I1} + G_{W2} + G_{I2}$. This thermal model results in eight versions of Equation 4.1 describing the bolometer geometries in Table 4.2 using six free parameters: G_x and α_x for layers x = S, W,

and I. These equations are given in the Appendix A.1.

Our data indicates that the thermal conductance of I1-I2 and W1-W2 film stacks on Legs D-F may be larger than the sum of the individual layers. For example, Bolometer 5 and 7 are more conductive than Bolometer 1 due to the presence of I1-I2 stacks despite having less material overall. This suggests these stacks behave as a single thick layer and support some $\alpha_x > 0$. We allow the heat carriers to pass between layers of the same material without scattering by setting $d_x = d_1 + d_2$.

We estimate the normalized thermal conductance G_x and power law strength α_x for the S, W, and I layers using a parametric bootstrap chi-squared (χ^2) minimization routine. Since α_x is unknown, there is no simple analytical method to propagate the measurement uncertainty in d into the uncertainty of the model parameters $\vec{p} = [G_S,\ G_W,\ G_I,\ \alpha_S,\ \alpha_W,\ \alpha_I]$. Therefore, a single minimization over a goodness-of-fit metric will neglect the significant σ_d contribution to the model uncertainty. We instead fit this model 10^4 times during a Monte Carlo simulation in which we vary both $\mathrm{G_{TES}}$ and d about their measured values, resulting in 10^4 estimates of $\vec{p}$. We take these estimates' median and standard deviation as the final model parameters and errors, respectively.

More explicitly, during each iteration of the simulation, we pull a simulated data set G^*_{TES} from a normal distribution characterized by the measurements in Table 4.2, i.e., $\mathcal{N}(\mathrm{G_{TES}},\ \sigma^2_{\mathrm{G_{TES}}})$. We resample layer thicknesses d^* via the same procedure using the measurements in Table 4.1. We then fit Equations A.1a-h to G^*_{TES} by minimizing over the value $\chi^2 = \sum_i [(G^*_{\mathrm{TES},i} - G_{\mathrm{pred},i}(d^*_i))/\sigma_{\mathrm{G_{TES}}}]^2$, where $\mathrm{G_{pred},}_i$ is the model-predicted thermal conductance for bolometer geometry i with layer thicknesses d^*_i.

4.3 G of Individual Layers

The final values for G_x and α_x are given in Table 4.3. Model-predicted thermal conductances and uncertainties, e.g., $\mathrm{G_{TES}}$ predictions and $\sigma_{\mathrm{G_{pred}}}$ in Figure 4.2, are the median and standard deviation of the predictions calculated using the 10^4 simulated $\vec{p}$ estimates. We consider two versions of this model: one in which α is constrained to [-1,1] (constrained model), and another in which

$\alpha \in (-\infty, \infty)$ (unconstrained model). There is no obvious physical motivation for α larger than 1, but the unconstrained model does produce $\alpha_I > 1$.

In both models, the substrate layer is notably less conductive than the W and I layers. Phonon transport in S could be further suppressed due to an acoustic mismatch at the SiO_2-SiN_x boundary or the exposed silicon oxide surface on the bottom of the leg which serves as the etch stop during the membrane release. A larger volume of more conductive material produces a microstrip that not only contributes to but dominates the thermal conductance of the bolometer. In the case of Bolometer 1, where a microstrip runs along all four legs, a conventional design for TES bolometers, the microstrip is $> 3\times$ more thermally conductive than the mechanical substrate supporting it.

We compare these two models by calculating the reduced chi-squared χ^2_v using $\sigma_{\mathrm{G_{pred}}}$, which captures the uncertainty contributions from both $\sigma_{\mathrm{G_{TES}}}$ and σ_d: $\chi^2_v = \sum_i [(G_{\mathrm{TES},i} - G_{\mathrm{pred},i}(d))/\sigma_{\mathrm{pred},\,i}]^2$. For eight unique TES geometries and six best fit parameters, the estimated number of degrees of freedom $\nu = 1$ for both models. The unconstrained model χ^2_v value is 1.52, which is closer to the ideal value of 1 than the χ^2_v value of 2.98 of the constrained model.

In the constrained fit, α_I and α_W consistently settle at 1, the maximum value allowed. However, this model misses the global minimum in the parameter space, biasing G_{S} and G_{I} to higher values to compensate for the weaker d scaling. This higher G_{S} leads to significantly overestimating $\mathrm{G_{TES}}$ predictions for bolometers of other geometries discussed below. The rest of this work uses the unconstrained model. Still, we acknowledge the constrained results may indicate α_{W} and α_{I} are equal to 1, meaning boundary scattering may dominate transport in these layers. Additional discussion of the constrained model and an alternative four-layer model is given in the Appendix A.3.

In the unconstrained model results, power law strengths α_I and $\alpha_W > 0$ confirm the presence of significant diffusive boundary scattering in these layers. An α_W value > 0 but < 1 could result from some ballistic transport, reduced dimensionality, or other scattering processes independent of d in addition to diffusive boundary scattering. An $\alpha_S \sim 0$ suggests that phonon transport in the substrate is primarily ballistic or dominated by another scattering process with a shorter ℓ.

Parameter	$\alpha \in$**[-1,1]**	$\alpha \in$**(-∞,∞)**
$\mathbf{G_S}$ **[pW/K]**	0.86±0.14	0.75±0.08
$\mathbf{G_W}$ **[pW/K]**	0.90±0.12	1.0±0.09
$\mathbf{G_I}$ **[pW/K]**	1.81±0.16	1.79±0.16
$\alpha_\mathbf{S}$	0.25±0.47	-0.09±0.22
$\alpha_\mathbf{W}$	1.00±0.14	0.55±0.11
$\alpha_\mathbf{I}$	1.00±0.04	1.26±0.22
$\mathbf{G_{micro}}$ **[pW/K]**	2.66±0.25	2.66±0.28
χ^2_ν	2.95	1.52

Table 4.3: Fit parameters and the resulting G_{micro} for the constrained and unconstrained models. Reduced chi-squared (χ^2_ν) values are included for comparison. G_x values are the normalized thermal conductances G_0 for a single 400-nm-thick × 5-µm-wide × 220-µm-long layer of type x, and the thermal conductance of a film with thickness d is $G_0(d/d_0)^{1+\alpha}$.

The latter case is consistent with the comparatively low conductance due to additional scattering at the bi-layer interface. Other potential scattering sources that are independent of d include density inhomogeneities and two-level systems, which have been reported in SiN_x films at sub-Kelvin temperatures [125, 118].

G_{TES} measurements and model predictions are compared in Figure 4.2, as well as the predicted contributions from the S, W, and I layers. The residuals normalized with respect to prediction errors are also shown. Insulting layers dominate the thermal conductance of most bolometers due to the comparable amount of material, higher thermal conductance, and stronger thickness scaling than the substrate bi-layer. This effect is compounded due to $\alpha_I > 0$ in the I-layer stacks on Bolometers 5 and 7.

4.4 Discussion

4.4.1 Literature Comparison

Measurements of thin films at low temperatures are difficult to compare given the range of dimensionality, surface roughness, and stoichiometry. No quantity normalized to film geometry is intrinsic in all possible transport regimes. For example, if phonon transport is ballistic, G is independent of length and κ increases with L, whereas if diffusive boundary scattering dominates,

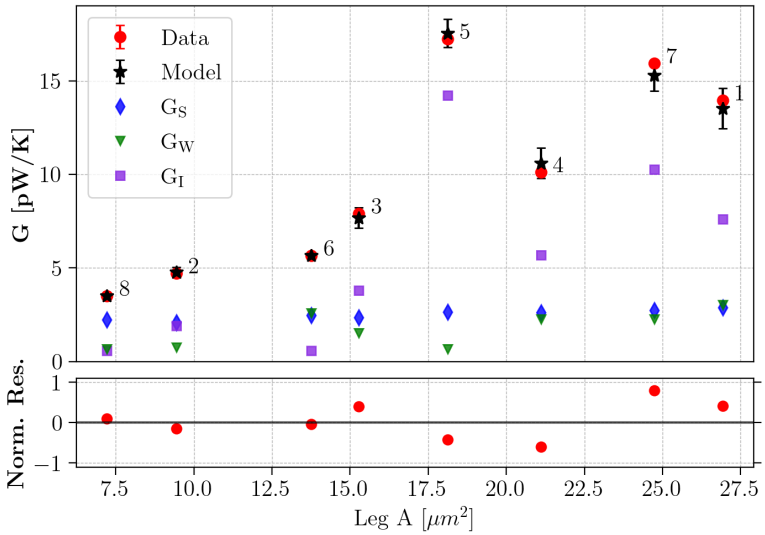

Figure 4.2: G_{TES} data (●) and model predictions (★) for Bolos 1-8 are shown as a function of the cross-sectional area of all four TES legs. Contributions from the S (♦), W (▼), and I layers (■) are also shown. The residuals are normalized with respect to the prediction errors.

κ is independent of L but scales linearly with d. We compare our measurements of κ and ℓ at 170 mK to other measurements in the literature, though these values do not give exact comparisons.

We estimate the phonon mean free path from the measured thermal conductivity $\ell = 3\kappa/\mathrm{C}_v\mathrm{v}_s$ using $v_{s,\ Nb} = 3480$ m/s [91] and $v_{s,\ SiN} = 6986$ m/s [113]. The Debye model gives the phonon specific heat in the low temperature limit: $\mathrm{C}_{v,\ \mathrm{Debye}} = 12\pi^4 k_B n_a/5 \times (T/\Theta)^3$, where k_B is the Stefan Boltzmann constant, n_a is the atomic density, T is the temperature, and Θ is the Debye temperature of 275 K for Nb [63] and 985 K for amorphous silicon nitride (a-SiN_x) [125]. Although $\mathrm{C}_v > \mathrm{C}_{v,\ \mathrm{Debye}}$ has been measured in a-SiN_x [113], the excess specific heat from non-phononic excitations and should not be included in the estimation of ℓ [125].

We measure the thermal conductivity κ of the 400-nm-thick $\times$ 5-µm-wide $\times$ 220-µm-long superconducting Nb wire at 170 mK to be 105±10 pW/K/µm with a mean free path $\ell_{\mathrm{W}} = 2.1 \pm 0.2$ µm. Feshchenko et al. 2017 [36] (F+17) report κ of 200-nm-thick $\times$ 1-µm-wide $\times$ 5- and 10-µm-long Nb wires to be 10.5 and 18.7 pW/K/µm respectively. Their measurements of a 20-µm-long Nb wire are noisy below 250 mK and are not considered here. Measurements of κ in this work and F+17 are suppressed with respect to the bulk thermal conductivity ∼100 nW/K/µm [10] by 2-3 orders of magnitude, emphasizing the importance of boundary effects in thin films.

The short leg lengths $\leq$ 10 µm and κ that increase with length suggests the Nb wires in F+17 are ballistic. The intrinsic quantity in 3D ballistic transport is G/A, which is 2.4 and 1.7 pW/K/µm^2 in the 5- and 10-µm-long wires, respectively. The smaller G/A = 0.5 pW/K/µm^2 in our Nb wire supports the $\alpha_W > 0$ result that conductance in our wire is suppressed by diffusive scattering.

The thermal conductance of our 400-nm-thick×5-µm-wide×220-µm-long S layer is 81.6±8.5 pW/K/µm with a mean free path ℓ_S of 144 ± 15 µm. For an I layer of the same dimensions, κ_I is 197.6 ± 17.2 pW/K/µm with an ℓ_I of 349 ± 31 µm. When boundary scattering at the sides of the film is considered, ℓ_I is consistent with measurements of $\mathrm{SiN_x}$ films that are boundary scattering limited, and ℓ_S is consistent with literature values in which phonon propagation is likely suppressed with respect to the boundary scattering case.

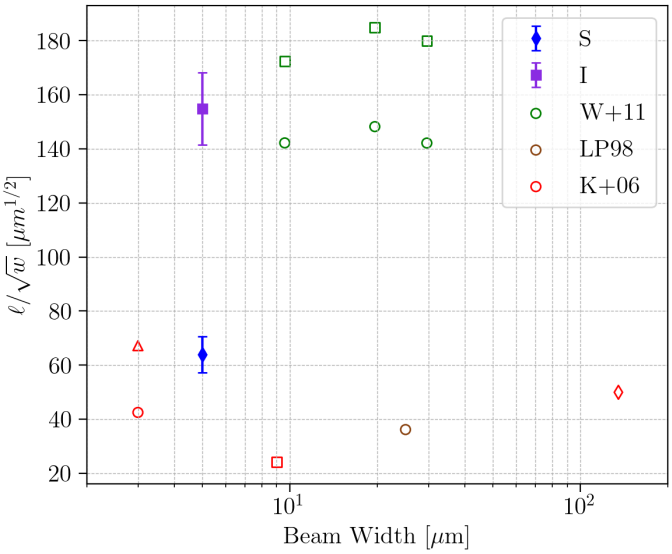

Figure 4.3: Mean free paths normalized by the square root of the width in various thin film SiN_x beams. S and I are measurements in this work. W+11 [113] mean free paths from two wafers in which they measure 21% (squares) and 29% (circles) diffusive reflection at the boundaries in 1-um-thick x 640-um-long Si3N4 beams at various widths. K+06[52] markers correspond to those in the original figures.

In Figure 4.3, we compare ℓ normalized by $\sqrt{w}$ of the S- and I- layers with other measurements of SiN_x beams of varying geometries. All films are thicker than d_c and will exhibit quasi-2D to 3D behavior. Most literature ℓ_{SiN} values are calculated from published values of κ at 170 mK with the procedure above, with the exception of W+11. W+11 measure κ at 450 mK and $C_{v,SiN}(T) = 0.082T + 0.502T^3 J/K/m^3$, then calculate ℓ using $C_{v,SiN}$. We scale their thermal conductivity to 170 mK via $\kappa_{170} = C_{v,SiN}(170\text{ mK})v_s\ell/3$ using their published ℓ, then calculate $\ell_{W+11}(170\ mK) = 3\kappa_{170}/v_s C_{v,\ Debye}$.

W+11 shows that in thin films with high aspect ratios dominated by boundary scattering, there is a $\kappa \propto \sqrt{w}$ dependence. Normalizing by this width dependence separates the samples into two groups: films that are likely dominated by boundary scattering and films that are further suppressed another scattering mechanism with a thickness-independent ℓ. Our measured ℓ_I falls into the former group, and ℓ_S falls into the latter. This is consistent with $\alpha_I \geq 0$ and $\alpha_S \sim 0$, indicating transport in the I layer is dominated by diffusive boundary scattering and that transport is suppressed with $\ell < \ell_{BS}$ in the S layer, likely due to an acoustic impedance at the SiO_x-SiN_x interface.

4.4.2 Legacy Data G Predictions

Over the last decade, NIST has fabricated TES bolometers with different geometries and TES saturation powers for a variety of CMB experiments [33, 46]. This historical data provides an opportunity to test our model of thermal transport in bolometer legs further. In Figure 4.4, we plot G_{TES} evaluated at 170 mK for 81 of these TES bolometers as a function of leg length. This family of bolometers includes leg lengths of 50 - 1250 µm, leg widths of 10 - 41.5 µm, and T_c values of 141 to 193 mK. The substrate bi-layers of these devices consist of a 2-µm-thick layer of SiN_x on top of a 450-nm-thick SiO_x. These thicker films were chosen for ground-based observations with higher optical power. Microstrip (W1-I1-W2-I2) layer thicknesses are similar to that of Leg A, though variation within fabrication tolerances is expected. W1 and W2 widths are respectively 8 and 5 µm. S and I layers are as wide as the leg.

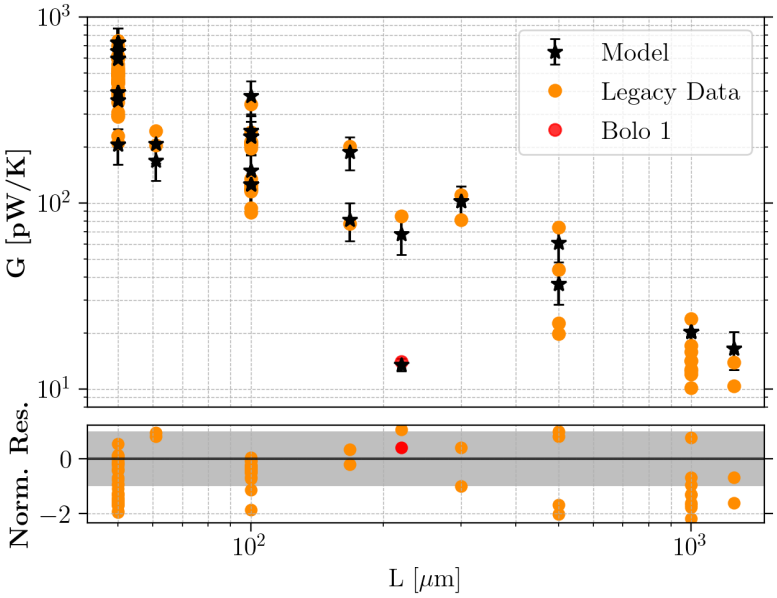

Figure 4.4: Thermal conductance measurements and model predictions for various CMB telescope TES bolometers fabricated at NIST Boulder. Bolometer 1 measurement and model prediction are also shown. The residuals are normalized with respect to the prediction error.

It can be seen that at a constant length, there is a considerable spread of 15-25% in the historical data that will challenge any simple model of heat transport in the legs. Thermal conductance variations of $\geq$15% in long, narrow legs in nominally identical devices from the same wafer have been recorded elsewhere [118], which has been attributed to phonon localization in disordered SiN_x. Processing residues that affect phonon scattering at surfaces and wafer-to-wafer material variation may also contribute to this spread. We also find that there can be variation in G_{TES} between nominally identical TESs located at different positions on a 150 mm wafer or on wafers fabricated at different times.

Additionally, this data is culminated across many institutions with some variance in measurement procedure. Although $G(T_c)$ of these bolometers were measured using the standard method described in Section 6.3.3.2, in some cases, the exponent n was fixed to 3 while in others n was allowed to float. To remove the temperature dependence of G_{TES}, we scale these historical $G(T_c)$ measurements to G(170 mK). An inaccurate value for n will bias this temperature scaling and may introduce spread in G_{TES} for bolometers of the same length but different T_c.

Model predictions of this historical data, as well as the residuals normalized to the error of those predictions, are also shown in Figure 4.4. This data spans the ballistic-diffuse transition, presenting as a shift in length scaling, which can be seen in this data near L = 150 µm. We account for the shifting length dependence by adopting the acoustic length scaling described in Withington et al. [118]. This treatment falls out of adding the ballistic and diffusive thermal conductances in parallel: $G_{TES} = G_{ball}(1 + L/L_a)^{-1}$, where the acoustic length scale L_a is proportional to the phonon mean free path.

We measure L_a of the composite leg by fitting this historical data via χ^2 minimization and find L_a = 152.3 µm with a reduced $\chi^2_\nu = 1.0$, which is the length scale associated with the knee in the historical data in Figure 4.4. Withington et al. [118] measure L_a = 20 µm for a quasi-1D amorphous SiN_x beam, which they suggest indicates their beams are dominated by Two-Level system scattering. We suspect predominantly boundary scattering in our quasi-2D composite legs, which will be associated with a longer thickness-dependent mean free path.

With this length scaling, model predictions agree well for bolometers with legs shorter than 1 mm despite the significantly thicker and wider legs than the bolometers under test used to build this model. The model overestimates the conductance of the longest legs deep into the diffusive regime. The conductance may be further suppressed by boundary scattering at the film edges, which our measurements are not sensitive to and, therefore, our model does not account for.

4.4.3 SO MF Saturation Power

During R&D of Simons Observatory Mid-Frequency (SO MF) TES bolometers, multiple iterations of leg geometries uncovered a non-linear dependence in P_{sat} on bolometer leg dimensions. This resulted in larger P_{sat} values than designed, leading to excess thermal fluctuation noise in their detectors. We applied this thermal conductance model to predict P_{sat} of the SO MF prototype geometries since it accommodates non-linear geometry effects. A comparison between model predictions and the nominal linear geometry scaling is shown in Figure 4.5, where the linear predictions scale the $P_{sat} = 4.1$ pW measurement according to $P_{sat} \propto (dw/L)$. We found that our model, including the acoustic scaling of the legacy data, better predicts the measured saturation powers than the nominal linear scaling.

These bolometers are included in the legacy data and share the same layer thicknesses and W-layer widths. Bolometer legs are either 100 or 167.8 µm long and are between 10 and 20 µm wide. These lengths straddle the ballistic-diffusive transition seen in the legacy data, resulting in a weaker length dependence than the fully diffusive case where $P_{sat} \propto 1/L$.

All SO MF bolometer legs extend beyond the 8-µm-width of the W1 layer. Consequently, further widening of the leg only extends the S-I1-I2 layer stacks. These regions are more conductive than regions in which W2 separates I1 and I2 due to $\alpha_I > 0$. This is the same effect that makes Bolometers 5 and 7 more conductive than Bolometer 1. Therefore, P_{sat} will increase more rapidly in wider geometries than a linear scaling would suggest.

By neglecting the non-linear scaling in length and width, the linearly-scaled predictions systematically underestimate P_{sat} by up to 40% of the measured values. In comparison, our model

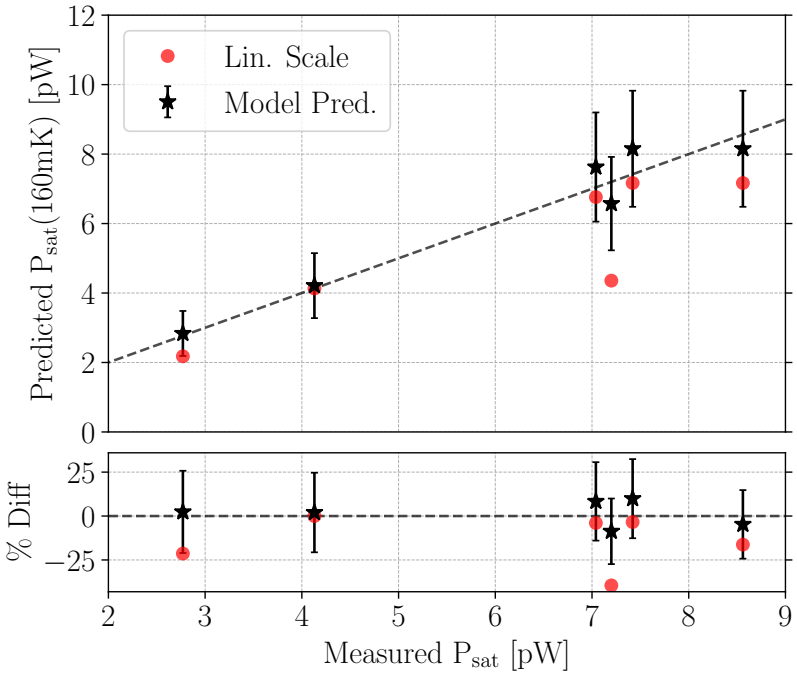

Figure 4.5: Model predictions (black stars) compared to predictions from scaling P_{sat} = 4.1 pW linearly with film dimensions (red circles). Residuals as a % of the measured value are also shown.

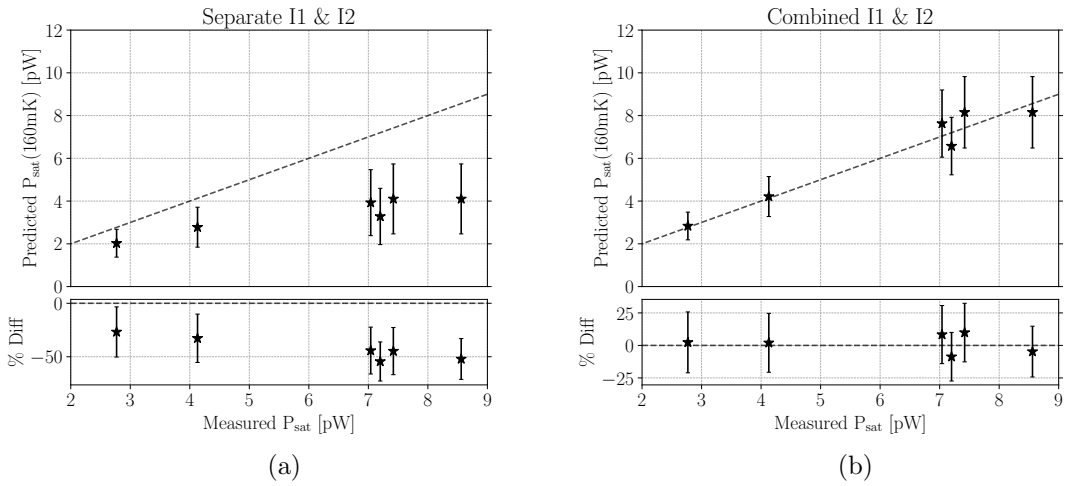

Figure 4.6: SO MF bolometer P_{sat} predictions a) treating I1 & I2 as separate layers over the entire leg compared to b) treating I1-I2 as a single layer for leg widths beyond W1.

predictions are all within 10% of the measured value and do not favor over- or underestimation. It is worth noting the scaled predictions rely on a measured value, and are greatly influenced by the choice of which measurement is extrapolated to other geometries. In contrast, predictions from our thermal conductance model are independent of these specific data points.

To emphasize the effect of the I-layer stacks when extending leg widths, Figure 4.6 compares model predictions treating I1 and I2 as separate layers over the entire leg and predictions treating I1 and I2 as a single layer for leg widths outside W1. When the I1-I2 stack effect is neglected, the model underestimates the 4 of the six measurements by 50% the measured value. While the linear scaling does sometimes produce accurate P_{sat} predictions, the extra-linear scaling effects captured in our model must be accounted for in a reliable TES design tool.

4.4.4 Noise Implications

Using this model, we predict the separate contributions of the substrate and microstrip layers to the NEP_{TF} normalized by the numerical factor $\sqrt{\gamma}$. Figure 4.7 shows NEP_{TF} predictions of Bolometer 1 at a range of leg widths for three geometries: (1) four legs of bare substrate, (2) four legs with 167 nm of Nb deposited on top of the membrane (a minimal wiring scheme), and (3)

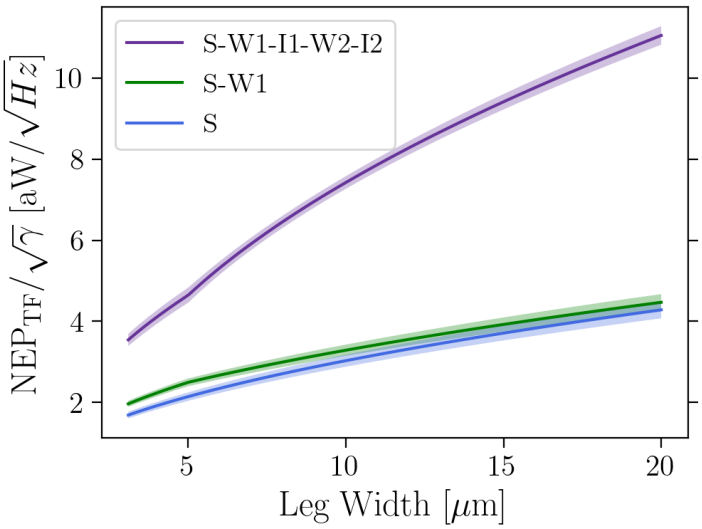

Figure 4.7: Model predictions of thermal fluctuation NEP $\pm 1\sigma$ for Bolometer 1 with and without microstrip wiring layers for a range of leg widths. Film dimensions are otherwise identical to Leg A in Table 4.1, with a ∼400-nm-thick substrate bi-layer. W1 layers are as wide as the leg until reaching a maximum width of 5 µm. All W2 layers are 2 µm skinnier than W1.

four legs with a full microstrip (W1-I1-W2-I2) deposited on each leg.

During leg TES design, W1 and W2 are often set to a fixed width, and increasing the leg width beyond W1 only grows S-I1-I2 film stacks. In our case, W2 is nominally 5 µm wide and W2 is 3 µm wide, where a 1 µm alignment buffer is trimmed from both sides of W2 as a precaution against shorts. For leg widths < 5 µm in Figure 4.7, W1 is as wide as the leg and W2 continues to be 2 µm skinnier than W1. $\mathrm{NEP_{TF}}$ predictions are omitted for the single niobium film of widths <1 µm and substrate widths <3 µm due to assumed fabrication constraints.

Our model predicts that a single layer of niobium wiring has little effect on $\mathrm{NEP_{TF}}$, and that beyond the maximum W1 width of 5 µm, the $\mathrm{NEP_{TF}}$ of the S-W1 stack approaches that of the substrate. However, the relatively large thermal conductance of the microstrip translates to a total $\mathrm{NEP_{TF}}$ prediction that is $> 2\times$ larger than the prediction for the bare substrate at all leg widths. This discrepancy is exaggerated when leg widths extend beyond W1 as S-I1-I2 film stacks, which are more conductive than the regions in which W2 separates I1 and I2 due to $\alpha_I > 0$. This results in an accelerated $\mathrm{NEP_{TF}}$ increase for leg widths > 5 µm when the full microstrip is included.

4.5 Summary & Conclusions

We have measured the thermal conductance of the individual membrane and microstrip layers on TESs designed for (sub-)millimeter observations on a balloon or satellite-borne experiment. We do this by measuring the total thermal conductance of bolometers with eight unique leg geometries and fitting this data to a model that allows for a range of phonon transport regimes. We find evidence for thermal transport limited by diffusive boundary scattering in the $\mathrm{SiN_x}$ insulating layers, resulting in G that scales non-linearly with film thickness. In our case of very thin membranes, the microstrip is nearly $4\times$ more conductive than the substrate that provides mechanical support for the TES island.

Model-predicted Gs for various other CMB TES bolometers with leg lengths $<$ 1mm are in excellent agreement with measurements despite significantly thicker membranes and wider legs than our bolometers under test. This model also reliably predicts the saturation power of CMB

prototype detectors, improving considerably on the nominal procedure of scaling measurements linearly with leg geometry. Using this model, we predict NEP_{TF} for Bolometer 1 with different film stack geometries. When we include the contribution from the microstrip, we predict a NEP_{TF} that is $> 2\times$ larger than the substrate alone. Therefore, for TESs with saturation powers of picoWatts, the microstrip layers must be included for accurate estimates of G and thermal fluctuation noise.

4.6 Future Work

Despite the broad predictability power of this model, the $\alpha_I > 1$ result does not have an obvious physical explanation. Though we neglect edge scattering effects in our model, our data is not totally independent of width scaling effects. SiN_x thin films dominated by diffusive edge scattering have been observed, therefore width effects should be investigated for a more complete description of the phonon transport in the bolometers measured here. The current α_I value may be compensating for unaccounted-for diffusive scattering at the edges of the film. However, parameterizing a non-linear width scaling would have two additional free parameters, requiring measurements of more bolometer geometries to fit the model.

Chapter 5

Physics of NIS Refrigeration

The current state-of-the-art refrigeration technologies for cooling below the pumped ^{3}He temperature of 300 mK are Adiabatic Demagnetization Refrigerators (ADR) and Dilution Refrigerators (DRs). ADRs and DRs are established technologies but can be a significant burden on the weight, electrical, or financial budget of an experiment, especially on a balloon- or satellite-borne mission.

There is a legacy of developing Normal metal - Insulator - Superconductor (NIS) junction refrigerators at NIST, for which the overarching goal is to aid or replace these heavy, complex, and expensive technologies with on-chip refrigeration. NIS refrigerators can be fabricated on the same wafer as the superconducting sensors they cool, adding no weight and negligible power demands to a cryogenic payload. Specifically, we aim to develop NIS refrigerators to cool cryogenic detectors from the pumped ^{3}He bath temperature of 300 mK to the more optimal operation temperatures of 100-130 mK.

In this chapter, I will motivate NIS R&D, explain the physics of NIS junctions and their application as a refrigeration technology, discuss the power balance model we use to design NIS-membrane structures to optimize cooling and share the implications of some of this modeling. This chapter draws much of the discussion from previous theses written on the NIS junction refrigerators at NIST, including [122], [67], [83] and [77]. In the following sections, I summarize the relevant derivations in Kittel [53] and Tinkham & Emery [105].

5.1 Motivation

As discussed in the Introduction (Ch. [1]), the sensitivity of superconducting detectors is greatly improved when cooled from the pumped ^{3}He temperature of 300 mK to 100-130 mK. Many experiments achieve temperatures <300 mK with the addition of an adiabatic demagnetization refrigerator (ADR) or a dilution refrigerator (DR) in their cooling chain. ADRs exchange heat and magnetic energy in a paramagnetic salt pill to control T_{bath}, with typical base temperatures <100 mK in astronomical applications. DRs cool by mixing pure ^{3}He with a ^{3}He-^{4}He mixture, achieving base temperatures of <20 mK.

The addition of an ADR or a DR to the cooling chain introduces mass, power consumption, complexity, and potentially magnetic shielding to a scientific payload. Observations in the (sub-)mm must also mitigate water absorption and emission in the atmosphere, a disadvantage some experiments circumvent with high-altitude ground-based sites, balloons, or satellites. The complexities involved with adding a DR or ADR become significant issues on a mountaintop, in Antarctica, on a balloon, or in space, where the power and mass budgets are limited.

NIS junctions are a simpler refrigeration technology that is fabricated directly onto the detector array, adding no weight and negligible power demands to the science payload. The operating principle behind an NIS junction as a refrigerator is illustrated in Figure 5.2. When the junction is optimally biased at $V_b \sim \Delta/e$, the hottest electrons in the normal metal tunnel across the insulator into the superconductor and away from the cooling target, lowering the electron temperature in the normal metal. The normal metal phonon temperature is cooled via electron-phonon coupling, allowing for the refrigeration of a nearby payload that is electrically isolated from the junction. When integrated with a TES bolometer, we extend the normal metal of the junction onto the leg of the TES island, or add a "cold finger," to maximize thermalization between the normal metal and the membrane.

5.2 Junction Tunneling

5.2.1 Occupied States in a Normal Metal

In a normal metal, the Pauli Exclusion Principle prevents electrons of the same spin from occupying the same energy state. At 0 K, electrons occupy all states up to the Fermi energy

$$\epsilon_F = \frac{\hbar^2}{2m}\left(\frac{3\pi^2 N}{V}\right)^{2/3}$$

where V is the volume of the metal, m is the electron mass, and N is the number of electrons. The single-particle density of states at 0 K is

$$D_N(\epsilon) = \frac{dN}{d\epsilon} = \frac{V}{2\pi^2}\left(\frac{2m}{\hbar^2}\right)^{3/2}\epsilon^{1/2}$$

For T > 0, the probability that an electron will occupy a state is given by the Fermi-Dirac distribution:

$$f(\epsilon, T) = \frac{1}{e^{(\epsilon-\epsilon_F)/k_B T}+1}$$

and the density of occupied states in a normal metal is $\mathrm{D}_N(\epsilon)f(\epsilon, T)$.

The Fermi function introduces the thermal smearing seen in the normal metal density of occupied states in Figure 5.2. An electron can tunnel from the normal metal across the insulating layer as long as there is an unoccupied state of the same energy in the superconductor.

5.2.2 Occupied States in a Superconductor

Bardeen-Cooper-Schrieffer (BCS) theory of superconductivity states that at sufficiently low temperatures, the normally repulsive electrons in a metal are bound into Cooper pairs via interactions with the lattice. The field of a free electron in a metal pulls on the lattice to create a mirror positive charge. This positive charge attracts another electron and binds the two together via their mutual interaction with the lattice.

The energy of this bound state is smaller than the Fermi energy and is easily overwhelmed by thermal excitations. Therefore, only at very low temperatures is this state accessible. Once it is available, the electron gas will condense into this lower energy bound state. When bound together, the paired electrons behave as a composite boson and are no longer subject to the Pauli Exclusion Principle. This bosonic behavior is responsible for the phenomenon of superconductivity.

The energy difference between this bound state and the Fermi energy is referred to as the superconducting gap energy Δ. At 0 K, only ground state excitations with energies $> \Delta$ can break Cooper pairs to produce quasiparticles in a superconductor. That is, the quasiparticle density of states in a superconductor is nonzero only for energy magnitudes above $\epsilon_F + \Delta$ and vanishes at energies within $\epsilon_F \pm \Delta$. The BCS density of quasiparticle states in the superconductor is:

$$D_{S,BCS}(\epsilon) = D_N(\epsilon) \left| Re(\frac{\epsilon}{\sqrt{\epsilon^2 - \Delta^2}}) \right| \tag{5.1}$$

While BCS theory predicts no states in the energy gap, tunneling in this region has been measured, suggesting the presence of sub-gap states. Possible physical explanations for these extra states include radiation-assisted tunneling of quasiparticles [13], magnetic impurities in the superconductor [126], or pinholes in the oxidized insulating layer acting as a resistor in parallel with the junction. A simple way of modeling the addition of these sub-gap states is to insert the Dynes parameter Γ into the BCS density of states:

$$D_S(\epsilon) = D_N(\epsilon) \left| \mathrm{Re} \left(\frac{\epsilon - i\Gamma}{\sqrt{(\epsilon - i\Gamma)^2 - \Delta^2}} \right) \right| \tag{5.2}$$

The Dynes parameter adds states into the forbidden region but does not change the total number of states. With this modified density of states, we can calculate the current-voltage (IV) characteristic of an NIS junction.

5.2.3 Tunneling Across a Barrier

To use NIS junctions as refrigerators, we take advantage of the physics of electron tunneling to remove the highest energy electrons. The current across a junction can be understood by first describing the probability that the electron will tunnel across an insulating barrier. For an electron in a potential U_1 with kinetic energy ϵ approaching a barrier with potential $U_2 > \epsilon$, the probability the electron will tunnel into region with potential U_3 can be determined with the time independent Schrödinger equation:

$$\epsilon\psi = \left(-\frac{\hbar}{2m}\nabla^2 + U\right)\psi \tag{5.3}$$

The solutions in regions 1, 2, and 3 are

$$\begin{aligned} \psi_1 &= A\exp\left(ik_1x\right) + B\exp\left(-ik_1x\right) & k_1 &= \tfrac{1}{\hbar}\left(2m\left(\epsilon - U_1\right)\right)^{1/2} \\ \psi_2 &= C\exp(k_2x) + D\exp(-k_2x) & k_2 &= \tfrac{1}{\hbar}\left(2m\left(U_2 - \epsilon\right)\right)^{1/2} \\ \psi_3 &= E\exp\left(ik_3x\right) & k_3 &= \tfrac{1}{\hbar}\left(2m\left(\epsilon - U_3\right)\right)^{1/2} \end{aligned} \tag{5.4}$$

Constants A-E can be determined by enforcing continuity in ψ and ψ' at $x = 0$ and $x = d$ for an insulating layer with thickness d. The tunneling probability is the ratio of the transmitted and incident intensity $\mathrm{T} = |E/A|^2 \sim \exp(-2k_2d)$. A typical insulating barrier in a junction has an energy of $\sim$1 eV. Provided U_3-U_1 is very small, meaning there are available states in Region 3 for the electron to tunnel to, we expect to observe tunneling (T=10^{-1}) in barriers $\sim$1 nm thick.

5.2.4 Current in a Normal Metal / Insulator / Normal Metal Junction

To understand the current-voltage (IV) characteristics of a junction, we begin with the simple example of a Normal Metal / Insulator / Normal Metal (NIN) junction. In thermal equilibrium, the electron distribution in both metals is described by the Fermi function as shown in Figure 5.1. When the normal metal (1) on the left is voltage biased, the energy of the electrons is elevated by eV_b. Provided there are unoccupied states of the same energy in normal metal (2), electrons will tunnel across the barrier, creating a current across the junction.

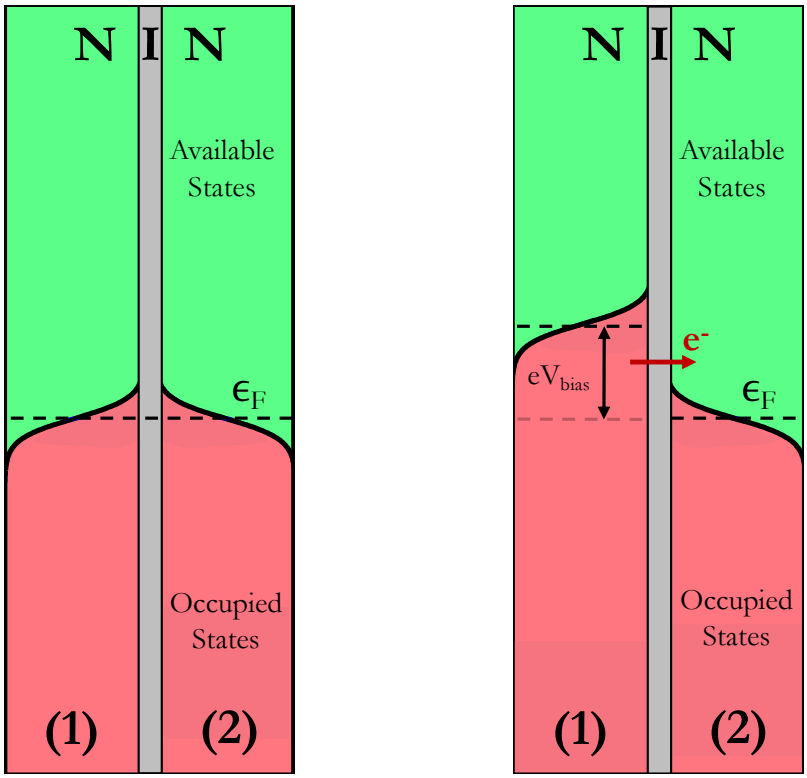

Figure 5.1: Occupation diagram of (a) an unbiased and (b) a voltage biased NIN junction. The dotted line indicates the Fermi energy ϵ_F. The junction is at a nonzero temperature, and thus the state occupation is "smeared." In (b), the energy level in the normal metal is raised by eV_{bias}. When biased, the electrons on the left can tunnel over to the available states on the right.

The tunneling from normal metal (1) to (2) is

$$\Gamma_{1\to2}(E) = P_{1\to2}(E)D_1(\epsilon)f_1(T,\epsilon - eV_b)D_2(\epsilon)[1 - f_2(T,\epsilon)] \tag{5.5}$$

where $P_{1\to2}$ is the tunneling probability, $D_1(\epsilon)f_1(T,\epsilon - eV_b)$ is the density of occupied states in layer 1 and $D_2(\epsilon)[1-f_1(T,\epsilon)]$ is the density of unoccupied states in layer 2. Similarly, the tunneling rate from normal metal (2) to (1) is

$$\Gamma_{2\to1}(E) = P_{2\to1}(E)D_1(\epsilon)[1 - f_1(T,\epsilon - eV_b)]D_2(\epsilon)f_2(T,\epsilon) \tag{5.6}$$

At temperatures much smaller than the Fermi temperature, ~10,000 K in normal metals, the density of states can be approximated as constant. For simplicity, we assume the probability of tunneling in both directions is the same and independent of energy. The current across the junction is the net tunneling rate for all ϵ multiplied by the electron charge e:

$$I_{NIN} = \int_{-\infty}^{\infty} e[\Gamma_{1\to2}(\epsilon) - \Gamma_{2\to1}(\epsilon)]\mathrm{d}\epsilon \tag{5.7}$$

$$= ePD_1(0)D_2(0)\int_{-\infty}^{\infty}[f_1(\epsilon - eV_b) - f_2(\epsilon)]\mathrm{d}\epsilon \tag{5.8}$$

$$\approx PD_1(0)D_2(0)e^2V_b \tag{5.9}$$

Therefore, an NIN junction behaves ohmically with the resistance

$$R_N = \frac{1}{PD_1(0)D_2(0)e^2} \tag{5.10}$$

5.2.5 Current in a Normal Metal / Insulator / Superconductor Junction

The current in an NIS junction can be derived by replacing $D_2(0)$ in the tunneling rates with the superconductor density of states given by Equation 5.2. The resulting current from the normal metal N to the superconductor S is

$$I_{NIS} = \int_{-\infty}^{\infty} e[\Gamma_{N\to S}(\epsilon) - \Gamma_{S\to N}(\epsilon)]\mathrm{d}\epsilon \tag{5.11}$$

$$= eP D_N(0)^2 \int_{-\infty}^{\infty} [f_N(\epsilon - eV_b, T) - f_S(\epsilon, T)]\,|\,\mathrm{Re}\left(\frac{\epsilon - i\Gamma}{\sqrt{(\epsilon - i\Gamma)^2 - \Delta^2}}\right)|\mathrm{d}\epsilon \tag{5.12}$$

The expression for I_{NIS} can be further simplified by changing the bounds to only positive energies and using the relations $D_S(-\epsilon) = D_S(\epsilon)$ and $f(-\epsilon, T) = 1 - f(\epsilon, T)$. With these simplifications, Equation 5.11 becomes

$$I_{NIS} = \frac{1}{eR_N}\int_0^{\infty} \left[f_N\left(\epsilon - eV_b, T\right) - f_N\left(\epsilon + eV_b, T\right)\right] \left|\mathrm{Re}\left(\frac{\epsilon - i\Gamma}{\sqrt{(\epsilon - i\Gamma)^2 - \Delta^2}}\right)\right| \mathrm{d}\epsilon \tag{5.13}$$

The mechanism behind the tunneling current in an NIS junction is illustrated in 5.2. The quasiparticle density of states is 0 in the superconductor for $|\epsilon| \leq \epsilon_F + \Delta$. When the junction is unbiased, the electron energy in the normal metal is the Fermi energy ϵ_F, with some thermal smearing at T > 0 K. In the absence of available tunneling states, there is no current in an unbiased junction. Placing a voltage bias V_b across the junction raises the energy of the normal metal electrons to $\mathrm{eV}_b + \epsilon_F$. At biases $V_b \gtrsim \Delta/e$, electrons will tunnel to the available states in the superconductor, creating a tunneling current.

Equation 5.13 shows that the current through the junction only depends on the electron temperature in the normal metal. The IV characteristics near Δ are highly sensitive to changes in temperature, as illustrated in Figure 5.3. At T = 0 K, no current flows through the junction at $V_b < \Delta/e$. With increasing temperature, however, both the quasiparticle population and the number of available states will increase, leading to higher sub-gap current. With an accurate measurement of current, voltage, Δ, and Γ, this temperature sensitivity allows us to use an NIS junction as a thermometer from its IV characteristic.

What must be characterized before using the junction as a thermometer is the quality factor Q, defined as the ratio of the sub-gap resistance R_Δ to the normal state resistance R_N at low temperature. R_Δ is measured by taking the maximum of dV/dI for an IV characteristic taken at

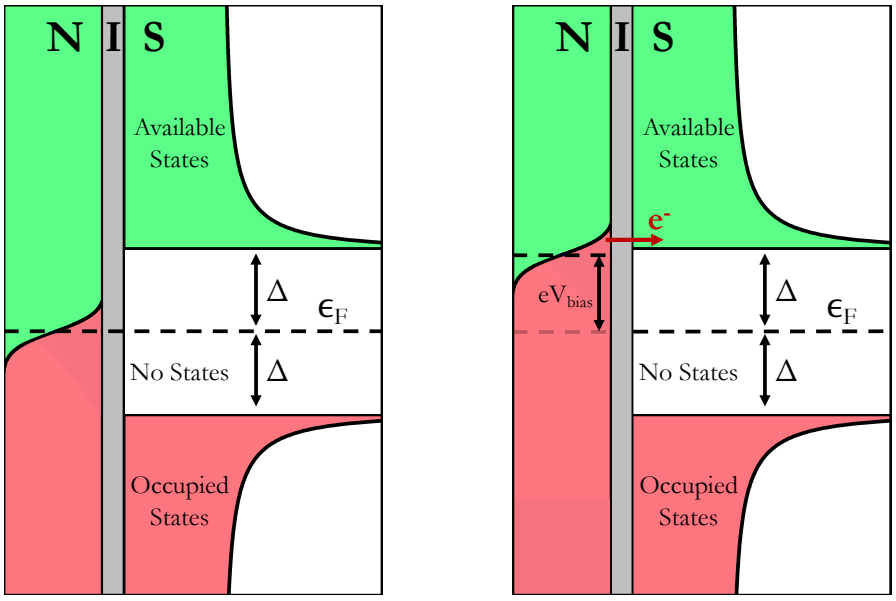

Figure 5.2: Occupation diagram of (a) an unbiased and (b) a voltage biased NIS junction. The dotted blue line indicates the Fermi energy ϵ_F. Δ is the gap energy of the superconducting metal layer. The density of states in the region $\epsilon_F \pm \Delta$ is 0. The junction is at a nonzero temperature, and thus the state occupation is "smeared" in the normal metal. In (b), the energy level in the normal metal is raised by eV_{bias}. The highest energy, i.e., hottest, electrons will tunnel across the insulating layer into the available states above $\epsilon_F + \Delta$ in the superconducting layer.

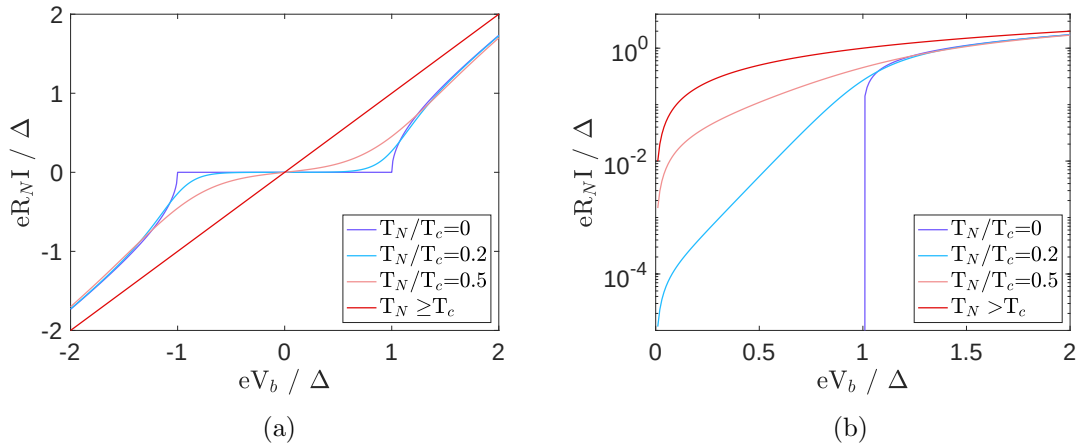

Figure 5.3: Normalized IV Characteristic of an NIS junction at various fractions of T_C in (a) linear and (b) log scale. At 0 K (in blue), there is no current at voltages below Δ. Above 0 K, thermal smearing allows the hottest electrons to tunnel through the junction. At voltages above Δ, the junction behaves as a resistor with constant dV/dI. At temperatures above T_c, the superconductor is normal and the junction behaves as a resistor at all voltage biases.

the base temperature of the cryostat, which is around 80 mK. A poor quality factor (<1000) allows for higher current in the subgap region, allowing both cool and hot electrons to tunnel across the insulator. This means loss of selective tunneling, making for a less sensitive thermometer and a less efficient refrigerator.

$$Q = \frac{R_\Delta}{R_N} \approx \frac{\Delta}{\Gamma} \tag{5.14}$$

where R_Δ is the resistance in the sub-gap region. Q should be measured at the lowest possible temperature to avoid excess subgap conductance.

5.3 Cooling Electrons

Electron refrigeration corresponds to negative power on the electron system. The power in the normal metal is the tunneling rate multiplied by the energy of each electron integrated over all energies:

$$P_N = \int_{-\infty}^{\infty} (eV_b - \epsilon) \left[\Gamma_{NS}(\epsilon) - \Gamma_{SN}(\epsilon)\right] \mathrm{d}\epsilon \tag{5.15}$$

$$= PD_N(0)^2 \int_{-\infty}^{\infty} (eV_b - \epsilon)[f_N(\epsilon - eV_b) - f_S(\epsilon)] \left|\mathrm{Re}\left(\frac{\epsilon - i\Gamma}{\sqrt{(\epsilon - i\Gamma)^2 - \Delta^2}}\right)\right| \mathrm{d}\epsilon \tag{5.16}$$

$$= \frac{1}{e^2 R_N} \int_{-\infty}^{\infty} (eV_b - \epsilon)[f_N(\epsilon - eV_b) - f_S(\epsilon)] \left|\mathrm{Re}\left(\frac{\epsilon - i\Gamma}{\sqrt{(\epsilon - i\Gamma)^2 - \Delta^2}}\right)\right| \mathrm{d}\epsilon \tag{5.17}$$

This power is plotted in Figure 5.4. For $V_b \lesssim \Delta/e$, negative power is indeed deposited on the normal metal, indicating refrigeration of the electron system. This is the basis behind NIS junction refrigeration. Unlike I_{NIS}, the P_N depends on the temperature of both the normal metal and the superconductor. The bath temperature affects the cooling power of an NIS refrigerator and is optimized at $T_{NIS} \sim 50\% T_c$. P_N is also inversely proportional to R_N, indicating more transparent junctions have higher cooling power.

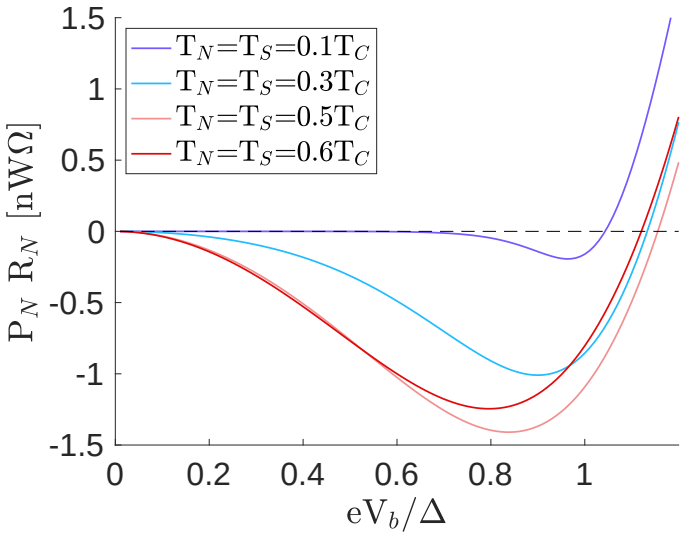

Figure 5.4: Power deposited in the normal metal electron system from the tunneling current driven by V_b at various ratios of T/T_c. Negative power indicates electron refrigeration.

T [mK]	Σ [nW/µm^3/K$^{n_{ep}}$]	n_{ep}
113	3.32	5.90
137	2.58	5.71
162	2.05	5.53
190	1.73	5.40
215	1.73	5.36
267	1.36	5.10
316	1.44	5.16
419	1.19	4.86
522	1.11	4.66
623	1.08	4.63

Table 5.1: Σ and n_{ep} measurements for AlMn.

5.4 Cooling Phonons

NIS refrigerators also cool payloads that are electrically isolated from the junction by coupling the cold electrons in the normal metal to the phonons of the cooling target. Phonons traveling through the normal metal shift the lattice structure, which in turn shifts the valence electron structure, providing a means for electron-phonon interactions. This coupling can be modeled as a scalar deformation potential, with notable theoretical developments by Reizer [89] and later Sergeev and Mitin [95]. From this theory, electron-phonon coupling in the normal metal is described by

$$P_{ep} = \Sigma V \left(T_e^{n_{ep}} - T_p^{n_{ep}} \right) \tag{5.18}$$

where Σ is the material-dependent electron-phonon coupling constant, V is the volume of the material, T_e is the electron temperature, T_p is the phonon temperature, and n_{ep} is a dimensionless number that ranges from 4 to 6. Measurements of Σ and n_{ep} for AlMn at various temperatures are presented in [109] and are summarized in Table 5.1.

5.4.1 NIS Thermal Model

To cool a sensor below the temperature of the Si wafer, it is necessary to thermally isolate the sensor from the hot phonons in the Si. As discussed in Chapter 3, precise control over the thermal

conductance (G) to the heat bath is also critical for optimizing sensor sensitivity, and for this reason, TESs are often suspended on a membrane via long, thin legs. In the dielectric and superconducting thin films that constitute these legs, the electron/quasiparticle thermal conductance is negligible. Therefore, this thermal isolation is achieved by controlling the phonon conduction between the wafer and the cooling target.

Below 1 K, electron-phonon interactions in a normal metal are so infrequent that the electron and phonon temperatures decouple. To cool the phonons in the sensor below the bath temperature, the conduction from the cold electrons and the membrane phonons must dominate the conduction between the membrane phonons and the hot phonons in the Si wafer despite this weakened electron-phonon coupling.

We can add thermal structures to the integrated NIS-membrane structure to either enhance the electron-phonon coupling or decrease the phonon-phonon coupling, such as the thermalization layer on the cold finger. On the other hand, non-optimal alignment of the membrane deep etch due to fabrication tolerances will hinder cooling performance. To model the effects of geometry and thermal structures on the electron and phonon temperatures and to design NIS-membrane structures with optimized cooler performance, we have built a thermal model to calculate the heat flow in NIS-cooled sensors.

We begin with the coupled 3D heat diffusion equations,

$$\frac{C_p \rho}{V}\frac{\partial T}{\partial t} - \vec{\nabla} \cdot [\kappa \vec{\nabla} T] = \dot{q} = P/V \tag{5.19}$$

where C_p is the heat capacity of the element, ρ is the mass density, κ is the thermal conductivity, V is the volume, and $\dot{q}$ is the heat source and sink terms acting on the element. We are interested in steady state solutions and set $\partial T/\partial t = 0$. We can further simplify this equation by assuming there are no temperature gradients in the thickness d or width w directions and by treating each thin film as a parallel conduction path. These assumptions reduce Equations 5.19 into the 1D equation

$$-\frac{\partial}{\partial x}\left[\kappa d \frac{\partial T}{\partial x}\right] = \frac{Pd}{V} = \frac{P}{A} \tag{5.20}$$

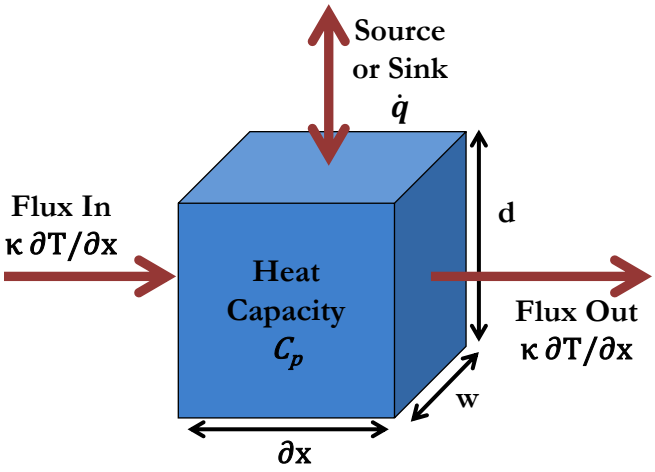

Figure 5.5: Infinitesimal element of our 1D thermal model described by Equation 5.20.

where $\kappa\ d\ \partial T/\partial x$ is the heat flux through the element times its thickness and P/A is the power per unit area $w\ dx$ from the heat sources and sinks $\dot{q}$ acting on an element shown in Figure 5.5 and ∂x runs along the length of the leg. Here we have scaled the terms in the equation by film thickness d. We assume materials are isotropic, meaning κ in a layer is constant along the leg. With this, Equation 5.20 becomes:

$$-\kappa d\frac{\partial^2 T}{\partial x^2} = \frac{P}{A} \tag{5.21}$$

The thermal conductivity of a given layer drives the heat flux term on the left side of this equation, and the heat source/sink term on the right captures the various power loads acting on the electrons or phonons in the layer. With Equation 5.21, we can now model the electron and phonon temperatures along an NIS-cooled membrane.

5.4.1.1 NIS-TES Membrane Structure

We integrate NIS refrigerators onto TES bolometers suspended on a membrane. One leg of an integrated NIS-TES device is illustrated in Figure 5.6. The bulk wafer is located on the left, and the membrane extends to the TES on the right. The regions of this structure are as follows:

Region 1 extends from the wafer to the edge of the NIS junction. The junction consists of a ∼1 nm AlO_x insulating layer sandwiched between a 300-nm-thick Al superconducting layer and the AlMn normal metal base electrode (BE). The SiOx layer on the left defines the junction area, where the junction itself is between the SiO_x and the end of the insulating layer on the right.

Region 2 represents the "dead length" region that can result from non-ideal deep etch alignment. One of the final fabrication steps is the deep etch that removes the silicon under the membrane, releasing the TES island from the wafer. This etch progresses laterally as it moves towards the membrane. Ideally, the end of the lateral etch lines up with the end of the junction, but due to fabrication constraints, the wafer can be under- or overetched.

Positive dead length, where the Si wafer extends past the edge of the junction, is represented in (a). In this case, the extended Si introduces a heat leak between the hot wafer phonons and the

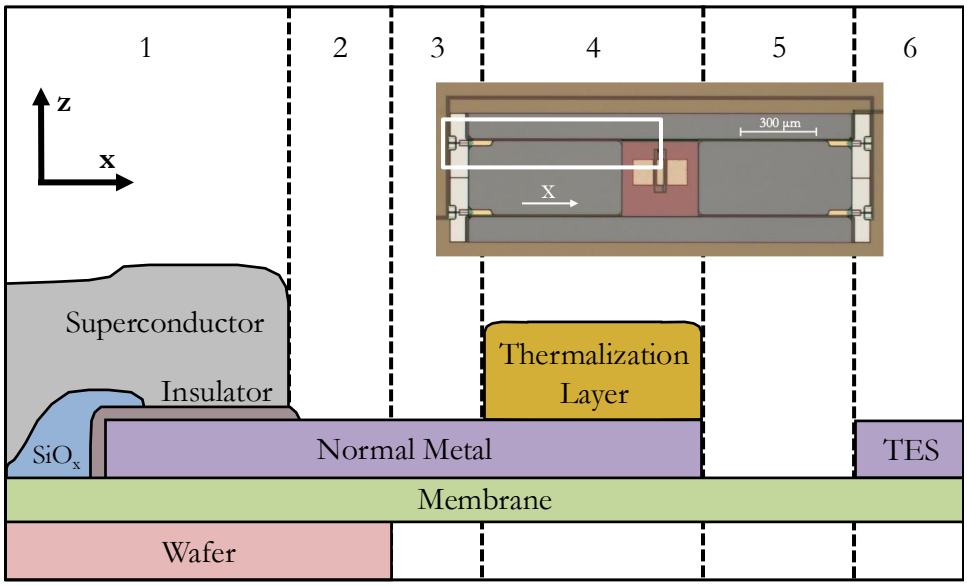

(a) Integrated structure with positive dead length.

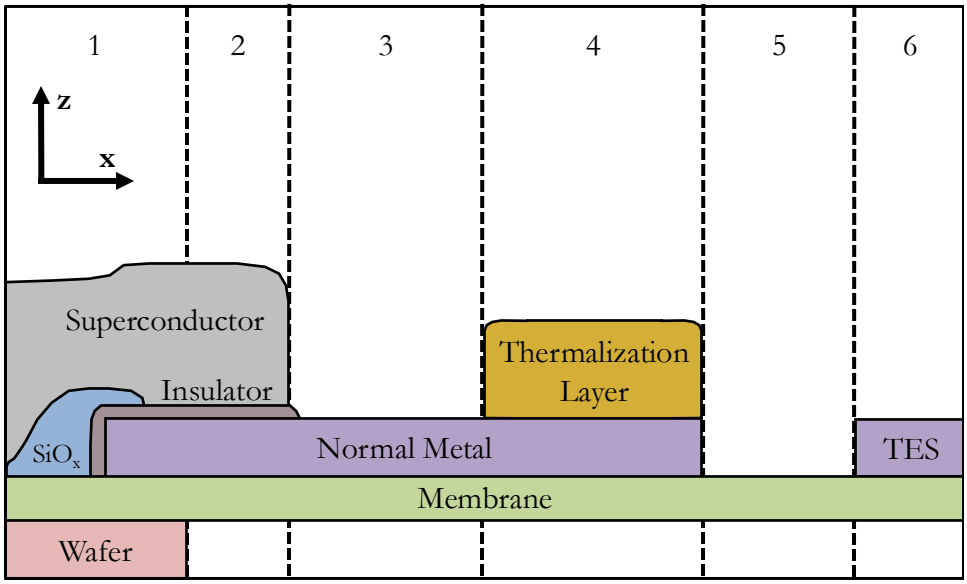

(b) Integrated structure with negative dead length.

Figure 5.6: Profile view of a NIS cooler integrated onto one TES leg, not to scale. A top view of one such leg is highlighted in the inset. Region 1 extends from the wafer to the edge of the NIS junction. Region 2 represents the dead length in which the substrate extends past the junction. Positive dead length is shown in (a), and negative dead length is shown in (b). No dead length is ideal for cooling performance. For better electron-phonon coupling, the normal metal extends onto the membrane in Regions 3 & 4, and in Region 4, another normal metal is added for thermalization. Region 5 is the leg between the cold finger and the TES. Region 6 is the TES bolometer.

membrane phonons. Negative dead length, where the Si undercuts the junction, is represented in (b). In this case, the junction extends out onto the membrane, and the junction bias introduces Joule heating onto the membrane. For ideal cooling, there is no dead length, i.e., no Region 2.

In **Regions 3 & 4**, the normal metal extends past the Si onto the membrane to increase the electron-phonon coupling in the BE. This is referred to as the cold finger. In Region 4, a Ti/Au bi-layer is added on top of the cold finger for thermalization. The Ti/Au is added further along the cold finger to thermalize the electron and phonon systems further from the hot substrate.

Region 5 is the TES leg between the cold finger and the TES and consists of the SiO_x-SiN_x membrane and the TES microstrip layers, which are not shown. Despite the depiction here, this region is the longest.

Region 6 is the AlMn TES bolometer, i.e., the cooling target. We treat the TES island structure pictured in the inset as a single power source on the right end of the leg.

In Region 1, the NIS junctions remove power from the electron system and deposit it onto the bulk Si substrate that acts as a thermal bath with temperature T_{bath}. We include this power removed as a heat sink term in $\dot{q}$. In Region 6, the TES power deposited at the center of the membrane is treated as a heat source and also included in $\dot{q}$. Therefore, we require that the heat flux through the boundaries in Regions 1 and 6 are 0.

5.4.1.2 Heat Flux Terms

In this section, I will restate some relevant discussion from Chapter 3 as a convenience to the reader.

The electron-phonon conductance is the temperature derivative of P_{ep} defined in Equation 5.18.

$$G_{ep} = \frac{\partial P_{ep}}{\partial T_e} = n_{ep}\Sigma V T_e^{n_{ep}-1} \tag{5.22}$$

The e-e and p-p conductance come from their respective thermal conductivities κ_{ee} and κ_{pp}, which are related via $G = \kappa \times dw/L$, where L is the length of the film and the cross-sectional area (different from the area defined earlier in this chapter) is $d \times w$.

The thermal conductivity of the phonon gas is given by kinetic gas theory:

$$\kappa_{pp} = C_v v_s \ell / 3 \tag{5.23}$$

where C_v is the phonon specific heat, v_s is the average sound velocity in the material, and ℓ is the phonon mean free path. The low temperature limit of the Debye model gives the specific heat:

$$C_{\text{V, Debye}} = \frac{12}{5}\pi^4 n k_B \left(\frac{T_p}{\Theta}\right)^3 \tag{5.24}$$

where k_B is the Stefan Boltzmann constant, n is the atomic density, T is the temperature, and Θ is the Debye temperature. Using the sound speed v_s For our AlMn base electrode, we use Al values for $v_s = 3700$ m/s, atomic density $n = 6 \times 10^{28}$ m^{-3}, and $\Theta = 428$ K. We estimate $\ell = 2$ µm from our measurements of ℓ_S in a 400-nm-thick SiO_x-SiN_x membrane (see Chapter 3).

In 2014, our group measured the thermal conductivity of similar SiN_x membranes used in NIS phonon coolers to be $\kappa_{SiN} = 1 \times 10^{-2} T^{2.2}$ W/(K m) [67]. This deviation from the T^3 scaling of the Debye model is a well-documented characteristic of amorphous materials and is likely due to the T^1 contributions to C_v from disorder and two-level systems in the material. This thermal conductivity evaluated at 170 mK is 203 pW/(K µm), which is consistent with our measurement of a 400-nm-thick film of SiN_x at 170 mK of 198 ± 18 pW/(K µm) in Chapter 4.

The electron thermal conductivity in the normal metal layers can be calculated from the electronic resistivity using the Wiedemann-Franz law:

$$\kappa_{ee} = \frac{L}{\rho_{el}} T_e \tag{5.25}$$

where L is the Lorenz number L = 2.44×10^{-8} WΩ/K^{-2}, ρ_{el} is the electrical resistivity and T_e is the electron temperature. We have measured $\rho_{AlMn} = 6.6 \times 10^{-8}$ Ωm in our devices.

In Figure 5.7, we calculate and compare the electron-electron (ee), electron-phonon (ep), and phonon-phonon (pp) thermal conductances for a 20-µm-wide x 100-µm-long region consisting of a 30-nm-thick film of AlMn on a 420 nm thick film of SiN_x. This geometry is similar to cold fingers on our integrated NIS-TES devices. Σ and n_{ep} depend on temperature and were interpolated from the

values measured in Table 5.1. It can be seen that between 70 and 500 mK, $G_{ee} > G_{ep} > G_{pp}$. This is significant because it shows that at these temperatures, the phonon cooling from the cold electrons in the BE dominates the heat loading from the Si substrate. Therefore, NIS-cooled electrons can cool the membrane phonons below the bath temperature.

5.4.1.3 Heat Source and Sink Terms

The power loads on the layers of the device are illustrated in Figure 5.8. In a steady state system, the various heat loads will be balanced with the cooling power of an NIS junction given by

$$-P_{NIS} = \Sigma V(T_e^{n_{ep}} - T_p^{n_{ep}}) + \beta I V_b + I^2 R_{pad} + I_2 V_b + P_{MS} + P_{load} \tag{5.26}$$

The first term on the right is the familiar electron-phonon coupling in the normal metal. The second term is the backscattering of hot quasiparticles, where β is the fraction of removed power P_{NIS} that returns to the normal metal. Extensive work has been done to minimize β in our NIS refrigerators, including the addition of quasiparticle traps overlayed on top of the superconducting electrode and laterally on either side of the BE. The overlayer traps (OLTs) are visible as the top layers in Figures 6.1 a and b. This work is detailed in [83] and [67]. With the addition of the quasiparticle traps, typical values of β are 1-2%.

Joule heating takes the form $\mathrm{P}_J = IR_{pad}^2$, where R_{pad} is the resistance of the normal metal layer between the two junctions. Junction current I_{NIS} from single-particle tunneling events is a first-order approximation of the total junction current. However, higher order tunneling events can add a secondary current. For example, even a perfect NIS junction will experience Andreev reflections in which electrons (holes) in the normal metal with $\epsilon < \Delta$ form Cooper pairs in the superconductor by reflecting holes (electrons) at the junction interface. The Andreev current and other second-order terms are lumped together into I_2, giving the additional power load $P_2 = VI_2$.

There is a thermal resistance between the phonon systems in the normal metal and the membrane due to differences in the material density, resulting from the same wave mechanics that describe light interacting at the interface of two optical media [102, 26]. This effect, referred to as

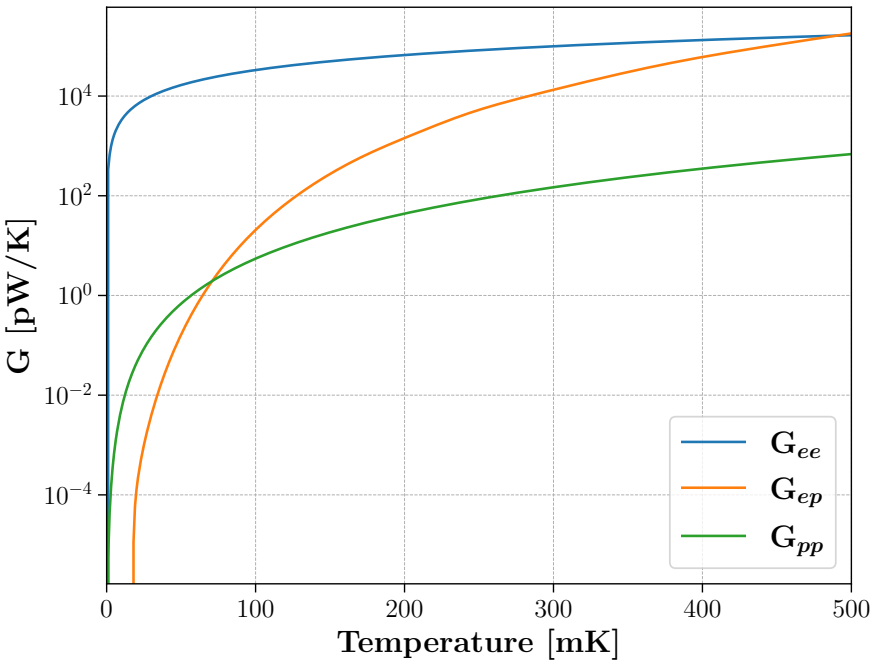

Figure 5.7: Electron-electron (ee), electron-phonon (ep), and phonon-phonon (pp) thermal conductances for a 20-µm-wide × 100-µm-long cold finger consisting of a 30-nm-thick film of AlMn on a 420 nm thick film of SiN_x. Between 70 mK and 500 mK, $G_{ee} > G_{ep} > G_{pp}$.

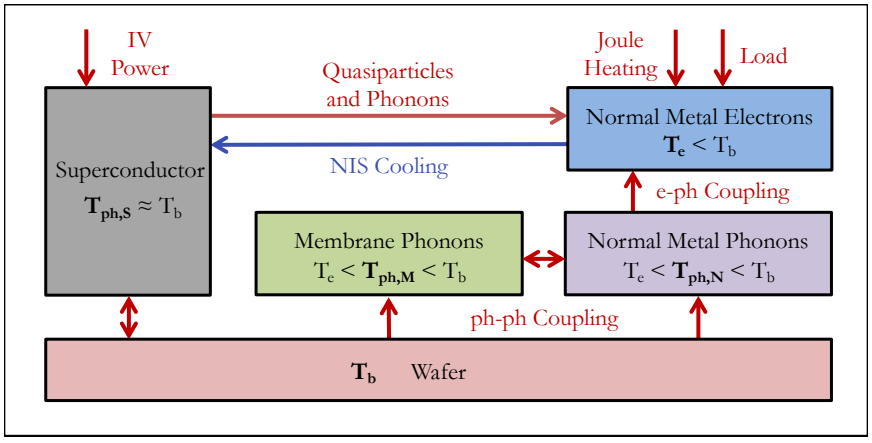

Figure 5.8: The various power loads on the electrons and phonons described in Equation 5.26.

Kapitza acoustic mismatch, has an associated heat flow

$$P_{AMM} = \xi(T_{ph,M}^4 - T_{ph,N}^4) \tag{5.27}$$

where $T_{ph,M}$ and $T_{ph,N}$ are the membrane and normal metal phonon temperatures, respectively, and ξ is a material dependent parameter. We use ξ=360 W/m^2/K^4 measured for Al on Si [102, 84].

P_{load} is the power load from the cooling target, which in our case is a TES bolometer, and any stray loading from the measurement environment. All terms in Equation 5.26 scale linearly with the number of devices, except for P_{load}, which is constant. To model NIS self-cooling for NIS-TES devices, we simply divide the power load from the TES ($\sim$ pW) by the number of NIS junctions per device.

Until recently, this concluded all the power loads included in the power balance model. From the measurements in Chapter 3, however, we have realized there is significant loading from the highly conductive microstrip used to bring the bias signal to the TES. The power load from the added conductance of the microstrip is

$$P_{MS} = \frac{G_{MS}}{3.2}(T_{ph,MS}^{3.2} - T_{ph,N}^{3.2}) \tag{5.28}$$

We have measured the thermal conductance of the microstrip G_{MS} to be 2.66 pW/K in our devices.

5.4.2 Results

Parameter	Value
Δ	187.2 μeV
Γ	60.14 neV
d_S	300 nm
d_N	30 nm
R_N	5.66 Ω
β	0.014
R_{pad}	0.328 Ω
V	9.7 μm^3

Table 5.2: Table of parameters used in example power balance model. These parameters are representative of measurements from NIS-TES v2 devices.

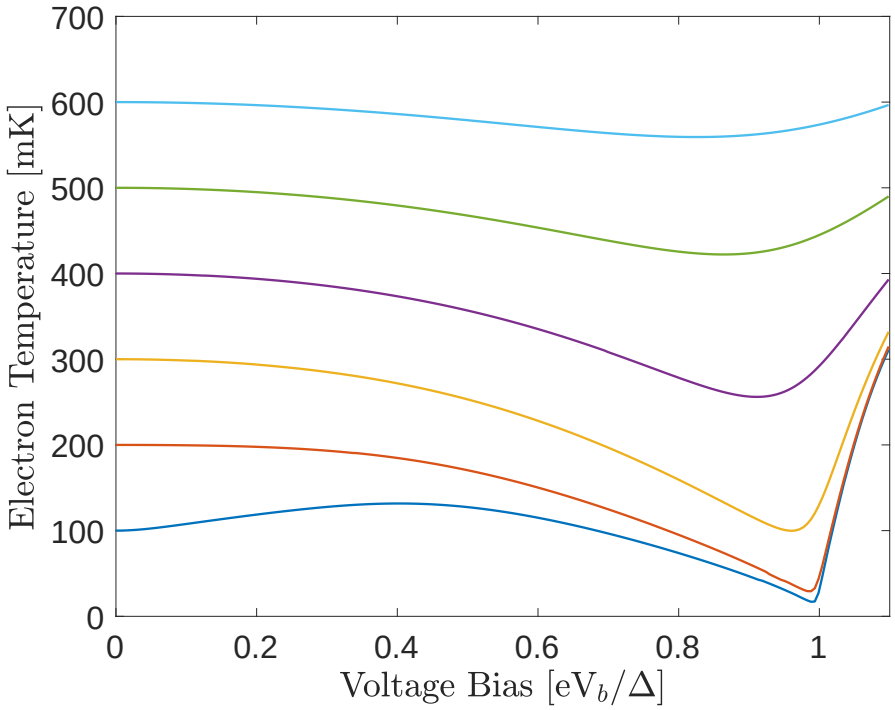

Figure 5.9: Sample result from the power balance model. The temperature at no voltage bias is the bath temperature. The electron temperature refers to the electron temperature in the normal metal of the junction.

Using this model, we calculate electron temperature in the normal metal T_e as a function of junction bias from various T_{bath} in Figure 5.9. We use the parameters in Table 5.2, which were chosen from junction measurements of our integrated NIS-TES devices. When the junction is unbiased, the electrons are in thermal equilibrium with the wafer. The optimal bias changes with T_{bath} but is always between 0.9 and 1.0 Δ. This model predicts that from 300 mK, the normal metal electrons are cooled to 113 mK.

Calculations of the electron temperature in the normal metal T_e, phonons in the normal metal $T_{p,N}$, and phonons in the microstrip $T_{p,MS}$ along an NIS-TES leg are shown in Figure 5.10. The junction is 32 µm long and, in this example case, is followed by 5 µm of dead length (DL), i.e., the Si wafer extends 5 µm past the edge of the junction. The 80-µm-long Ti-Au thermalization layer (TL) begins at x = 52 µm. The junctions and the thermalization layer are spaced 20 µm apart, and in this case, with a 5 µm dead length, is 15 µm away from the edge of the Si. P_{load} is set to 0 pW.

In Figure 5.10 are predictions of T_e, $T_{p,N}$, and $T_{p,MS}$ (a) neglecting P_{MS} and (b) including P_{MS} in the power balance. In (a), the model predicts that the normal metal phonons thermalize to 135 mK at the end of the TL. In (b), however, the normal metal phonons thermalize to 154 mK, 19 mK hotter than when the microstrip is neglected.

Figure 5.11 compares final thermalization temperatures for various dead lengths. If the deep etch alignment is perfect, meaning there is no dead length, the model predicts that the normal metal phonons thermalize to 134 mK, which is 20 mK colder than the 5 µm dead length case plotted above. In other words, adding 5 µm of dead length is akin to adding another microstrip on the other side of the cold finger, and both significantly impact cooling performance.

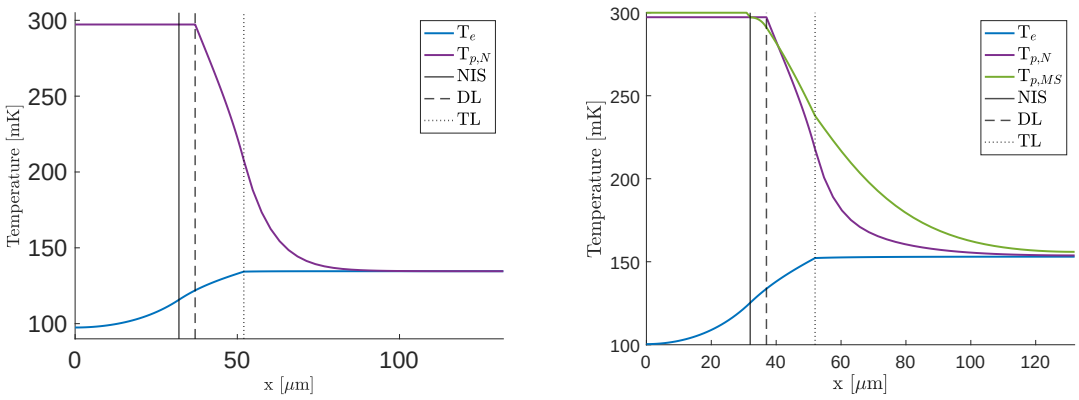

(a) Excluding P_{MS} (b) Including P_{MS}

Figure 5.10: Electron and phonon temperatures along the cold finger of a single leg cooled with two junctions illustrated in Figure 5.6 with a 5 µm dead length (DL) (a) excluding the power load from the microstrip P_{MS} and (b) including P_{MS}. T_e and $T_{p,N}$ are the electron and phonon temperatures in the AlMn base electrode of the NIS junction. $T_{p,MN}$ is the phonon temperature of the microstrip running parallel to the cold finger along the TES leg. The 80-µm-long Ti-Au thermalization layer (TL) begins 20 µm after the NIS junction and 15 µm after the DL. $T_{p,N}$ at the end of the thermalization layer is 19 mK higher when the microstrip is included.

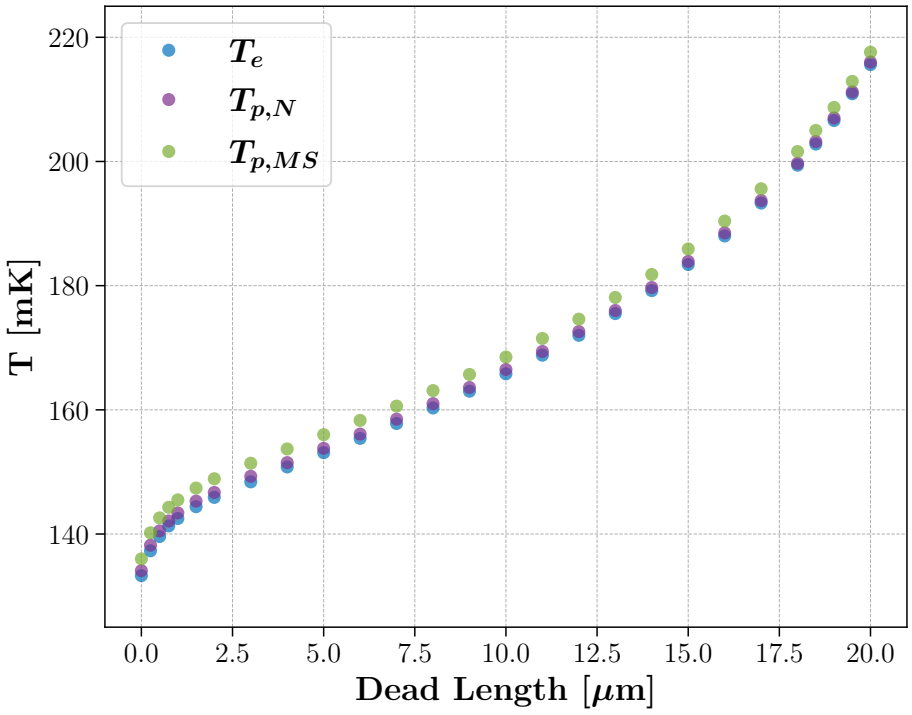

Figure 5.11: T_e, $T_{p,N}$ and $T_{p,MS}$ at the end of the thermalization layer for various dead lengths.

Chapter 6

NIS-cooled TES Bolometers

We are developing Normal metal - Insulator - Superconductor (NIS) junctions as a solid-state, on-chip refrigeration technology with the potential to cool cryogenic detectors from the pumped ^{3}He temperature of 300 mK to the more optimal operational temperatures of 100-130 mK. Compared to the current state of the art for cooling below 300 mK, this refrigerator technology is inexpensive, light, and compact, making it especially well suited for space applications.

As will be shown in this chapter, we have integrated NIS coolers onto transition edge sensor (TES) bolometers designed for observations of the sub-mm sky from a balloon-born experiment. These integrated devices consist of two NIS refrigerators that sit at the base of each of four TES island legs for a total of 8 junctions per bolometer. We have measured the NIS cooling of a TES from 300 mK to 187 mK on a device with six working NIS junctions and no measurable difference in detector noise. With eight operational NIS junctions, we predict TES cooling from 300 mK to 143 mK, which is equivalent to a $\sim$30% reduction in detector Johnson-Nyquist noise equivalent power and a $\sim$50% reduction in thermal fluctuation noise equivalent power. These prototypes suffered from a junction yield of $\sim$50% due to tall silicon (Si) islands in the substrate shorting through the few-nm-thick insulating layer.

After switching to a NIST-grown substrate with lower Si content, we have recovered junction yields of nearly 100%, but with diminished cooling performance. Potential causes of this impaired refrigeration include excess dead length and structural discontinuities, though the specific mechanisms are still under investigation. Once cooling performance is restored with maintained

near-unity junction yield, several design improvements involving decreasing the conductance to the heat bath and increasing NIS cooling power can be implemented to achieve TES refrigeration below 150 mK.

The NIS junction refrigerator component of these integrated NIS-TES devices is described in Section 6.1, and the TES bolometer component is described in Section 6.2. In Section 6.3, I describe the measurements we take to characterize integrated NIS-TES devices as well as the cryogenic test beds we use to make those measurements. Section 6.4 contains the results and cooling performance of the various NIS-TES prototypes, which span three versions. In Section 6.5, I share the next steps once cooing performance is recovered towards optimizing single-pixel performance before scaling to full-sized arrays of integrated NIS-TES detectors.

6.1 NIS Refrigerator Junctions

Normal metal - Insulator - Superconductor (NIS) junctions cool the electrons system in the normal metal by depositing the hottest electrons into the superconductor. To cool an arbitrary payload that is electrically isolated from the junction, the refrigeration of the normal metal electron system must translate to refrigeration of the phonon system in the payload. This is mitigated via electron-phonon coupling in the normal metal. When integrated onto a TES bolometer, we extend the normal metal of the junction onto the TES leg membrane to maximize thermalization between the normal metal and the membrane.

NIS cooling power increases linearly with the number of junctions. We place two junctions at the end of each TES leg to provide twice the cooling power without additional fabrication steps. The NIS refrigerators are AlMn/AlO_x/Al junctions with an area of 7 μm $\times$ 32 μm. We use aluminum because it can be oxidized to form a high quality barrier on the order of 1 nm, the size required for an insulating layer. The normal metal base electrode is a 30 nm-thick layer of AlMn, which is then oxidized to form a ~few nm insulating layer. A 300 nm-thick layer of Al is deposited on top of the insulator to form the superconducting counter electrode (CE). The 500-nm-thick AlMn overlayer trap (OLT) is deposited on top of the CE with a thin AlO_x layer sandwiched between the CE and

the OLT. Cross-sections of junction pairs in series imaged with a Scanning Electron Microscope are shown in Figure 6.1.

6.2 Transition Edge Sensors

The Transition Edge Sensor (TES) is a highly sensitive thermometer that takes advantage of the sharp change in resistance with temperature of a superconducting thin film biased into its phase transition. This incredible sensitivity in temperature makes TESs well suited for (sub-)mm astronomy applications, where signals are ∼picoWatts. TESs can be used as bolometers, which measure power, or calorimeters, which measure pulses of energy. This work focuses on TES bolometers, using the 280 GHz SPIDER TES design as a template for our detectors. SPIDER is a balloon-born CMB polarimeter aiming to find the inflationary signature in the CMB polarization. The 280 GHz TESs were added to the SPIDER focal plane after its first flight in 2015 to constrain the level of B-mode contamination from galactic dust emission [46]. The TES island is suspended via four legs with a cross-sectional area A∼7 µm^2 and a length of 600 µm. We added eight NIS junctions to this template, two per TES leg, shown in Figure 6.2.

The sensor itself is a superconducting AlMn-alloy thin film operated at a bath temperature below its critical temperature T_c and voltage biased into its phase transition [112, 115]. The power through a TES is the sum of the absorbed optical power P_o and the electrical power P_e. For enhanced stability and dynamic range in the extremely narrow phase transition, TESs are voltage biased to take advantage of negative electrothermal feedback (ETF).

The TES bias circuit is shown in Figure 6.3. The TES is voltage biased with a current bias I_{bias} and a shunt resistor R_{sh}. The sensor is coupled to readout electronics via the inductor L. R_{par} is the parasitic resistance in series with the TES.

The detection mechanism in a TES bolometer is an increased resistance resulting from the absorbed optical power and subsequent increase in local temperature. In a voltage biased scheme, the increased resistance from the sky signal power load decreases the electrical power $P_e = V^2/R$ in the sensor, allowing the TES to fall back into the phase transition. This bias scheme, coupled

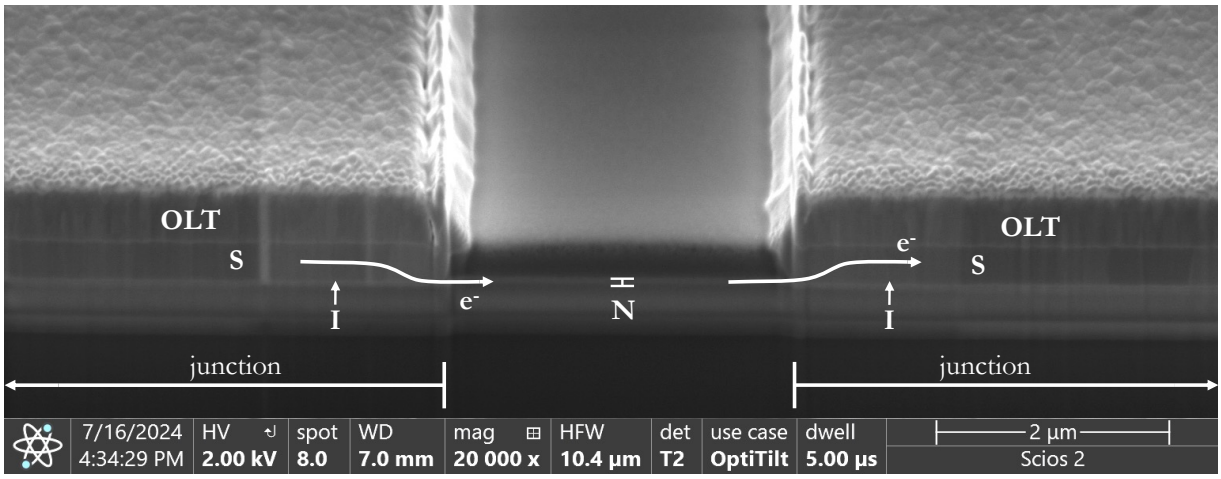

(a) SEM cross-section of an NIS Junction

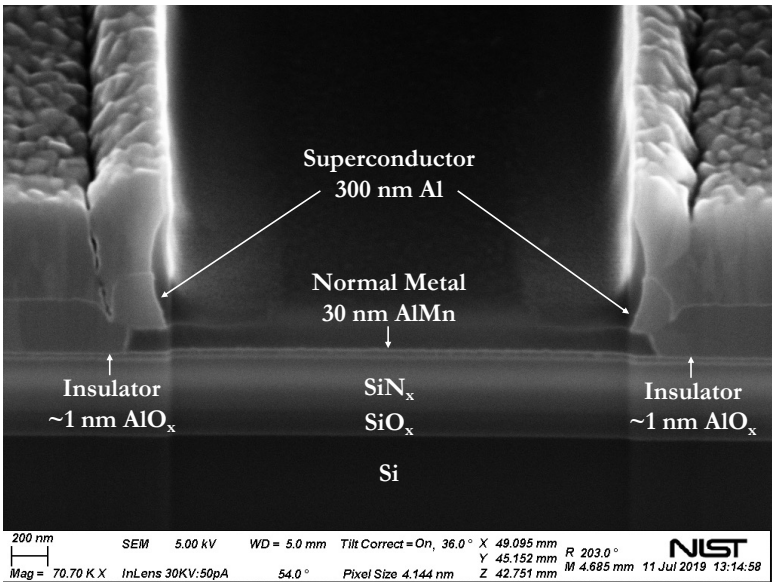

(b) Zoomed in SEM cross-section of a NIS Junction

Figure 6.1: Scanning electron scanning microscope images of two NIS junctions in series. (a) Tunneling current flows from the left-side superconductor through the normal metal base electrode into the superconductor on the right. Overlayer quasiparticle traps (OLTs) sit atop the S layers. The 30-nm-thick base electrode is barely visible. (b) Another SEM cross-section of a similar structure, but zoomed into the center structure. The junction sits on top of a SiO_x-SiN_x bi-layer membrane, all on a Si wafer.

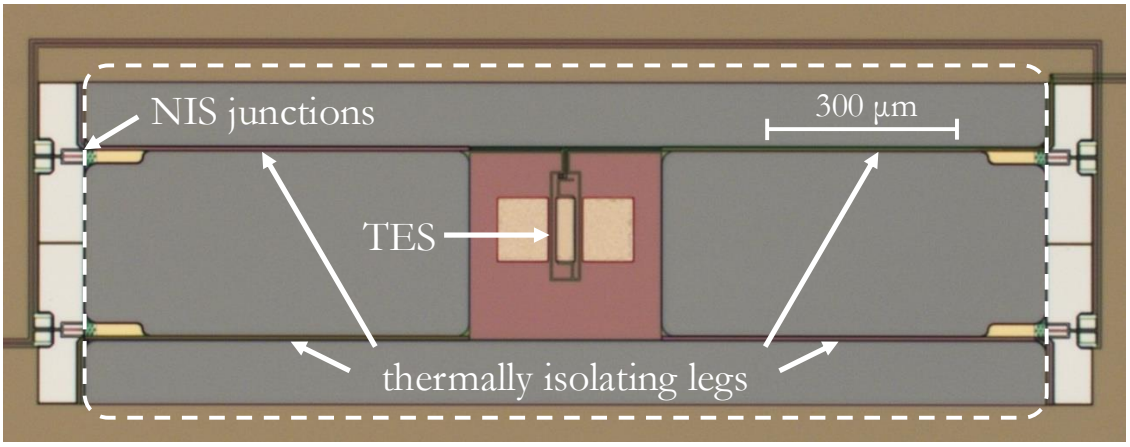

Figure 6.2: A photo of an integrated NIS-TES device. The white dashed line highlights the deep etch outline, which defines where the membrane is released from the Si substrate. Two NIS junctions are visible at the end of each TES bolometer leg.

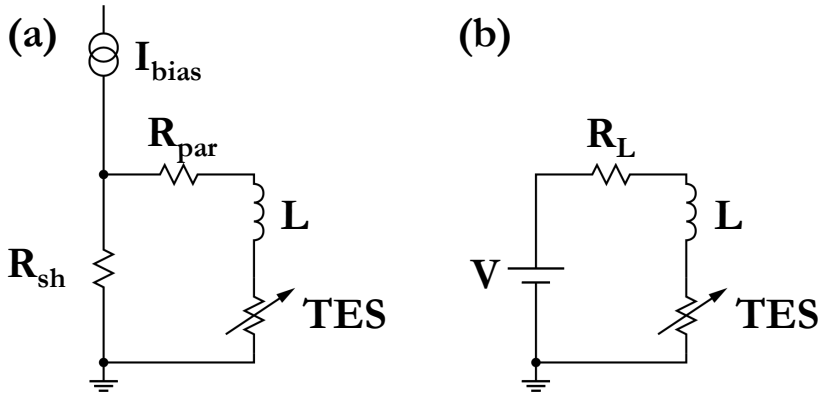

Figure 6.3: (a) The TES bias circuit, and (b) the Thévenin equivalent of the TES bias circuit, adapted from Irwin & Hilton 2005 [47].

with SQUID current amplifiers, has enabled multiplexing these detectors into large arrays.

6.3 Experimental Apparatus

6.3.1 Cryogenic Test Bed

Device measurements are performed across two adiabatic demagnetization refrigerators (ADRs) with a base temperature of ∼50 mK. An ADR utilizes electron spins in a paramagnetic salt pill to refrigerate a cold stage below the temperature of a thermal bath, which in our case is 4 K. One test bed is a "wet" ADR and is backed by a liquid ^{4}He tank from IR Labs shown in Figure 6.4. The other is a Model 103 "dry" ADR from High Precision Devices backed by a closed cycle helium compressor shown in Figure 6.5.

The ADR unit inside the wet dewar is shown in Figure 6.6 and the unit inside the dry dewar is shown in 6.7. At the center of the unit are two paramagnetic salt pills surrounded by a superconducting magnet solenoid. During operation, the magnet is ramped up to a maximum field, aligning the electronic spins in the salt pills while still in contact with the thermal bath. This exothermic process exchanges magnetic energy for thermal energy, which is absorbed into the thermal bath. Once the salt pills are once again in equilibrium with the 4 K bath, the thermal connection between the two is broken and the magnetic field slowly ramped back down.

During the magnetic ramp down, it is an entropically favorable for the electron spins to anti-align. As electrons anti-align, energy is absorbed from the thermal system and the salt pills are cooled to below the bath temperature. Since this process is adiabatic, the temperature of the cold stage can be controlled with a magnetic field to any temperature between the base temperature and the thermal bath.

A Kepco bipolar operational power supply drives the superconducting magnet in both ADRs. The current ramp up is monitored using an Agilent 34401A digital multimeter to ensure the voltage across the magnet never exceeds 200 mV. Voltages larger than this could generate enough EMF to drive the superconducting magnet wire normal, depositing a large amount of heat onto the cold

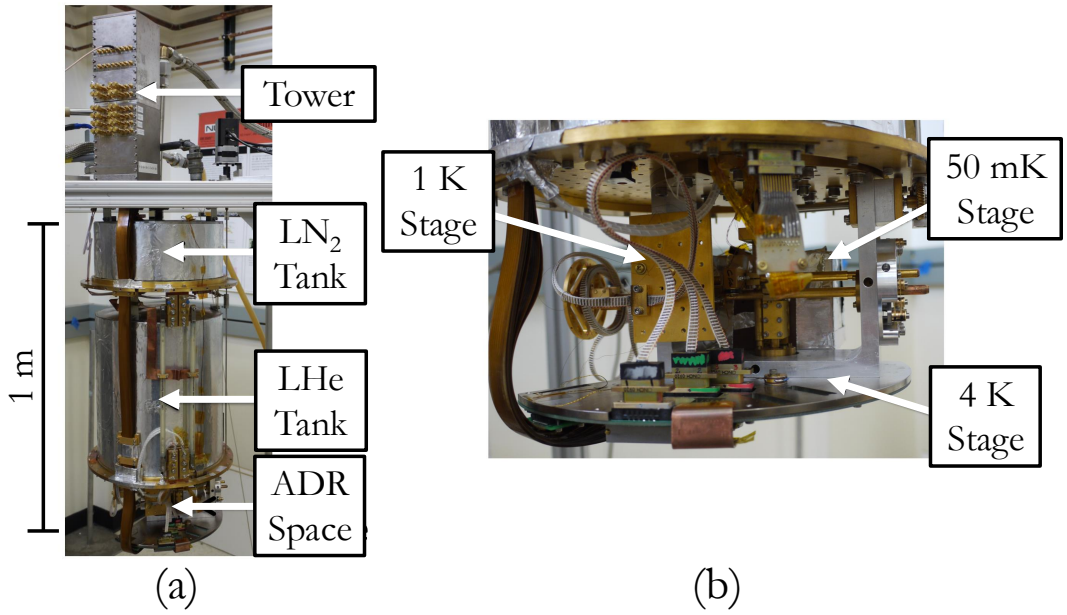

Figure 6.4: (a) Photograph of the wet cryostat, including the electronics tower and the liquid cryogen tanks. (b) Photograph of the ADR unit and cold stages.

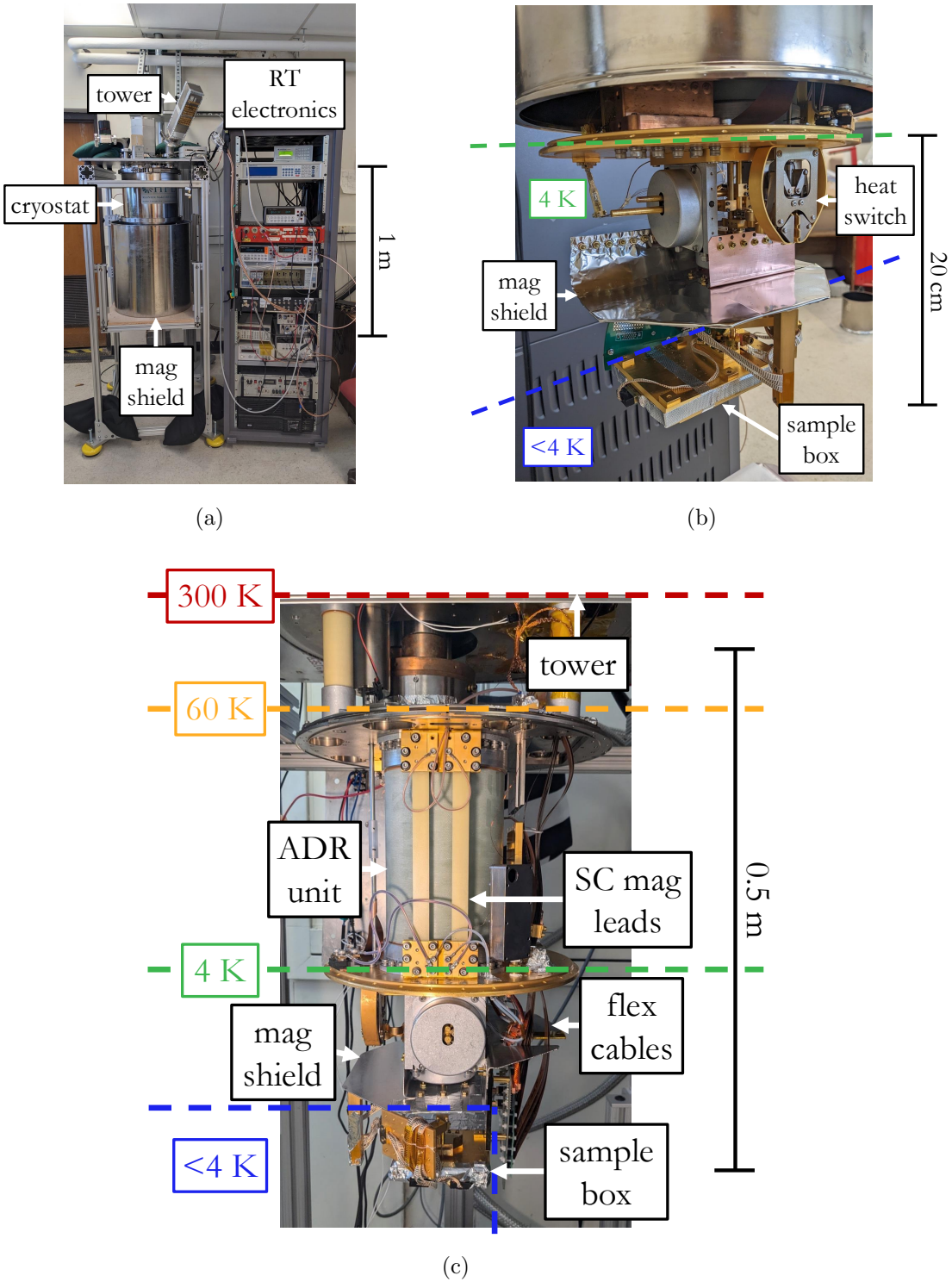

Figure 6.5: Photographs of the dry cryostat. (a) The cryostat configuration while taking measurements with a room-temperature magnetic field surrounding the sealed vacuum jacket. (b) The cold stages of the cryostat. All components are thermalized to the 4K plate except for the sample box, which is thermalized to the FAA at 50 mK, and the loom wires, which are heat sunk to the GGG at 1 K on their way to the sample box. (c) The cryostat with the vacuum and radiation shields removed. The cold stage in (b) exists below the 4 K plate.

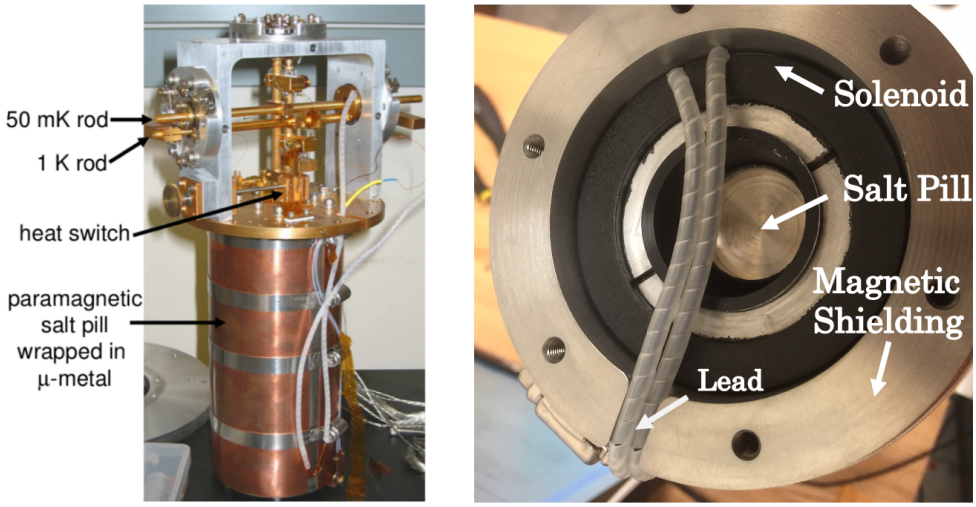

Figure 6.6: (a) Side view and (b) top view of the ADR unit in the wet dewar. The salt pills are at the center of the unit and are surrounded by the magnet solenoid, which is seated inside μ-metal magnetic shielding.

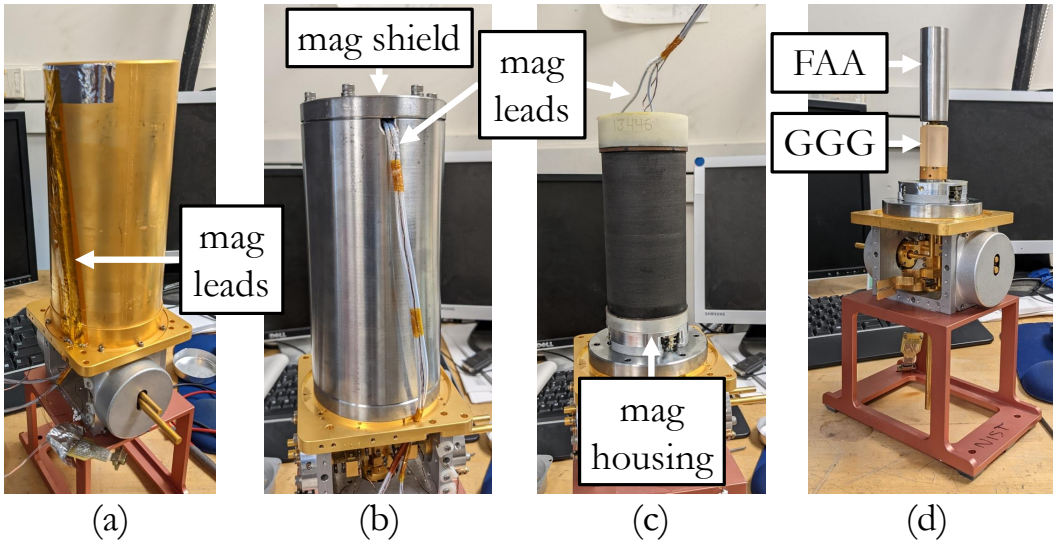

Figure 6.7: Photographs of the ADR unit in the dry cryostat, progressively removing components towards the ADR salt pills. a) The ADR package inside the thermalization shell made of gold-plated copper. b) The μ-metal magnetic shielding around the ADR magnet inside the thermalization. c) The solenoid that houses the superconducting magnet. d) The FAA and GGG salt pills inside the superconducting magnet.

stage and suddenly quenching the magnetic field, which would damage the magnet. As another protection against a current surge, back-to-back diodes are placed in parallel with the magnet that would provide an alternate route to ground for voltages ≥ 1 V.

The ADR consists of a Ferric ammonium alum (FAA) salt pill, which refrigerates the cold stage to 50 mK, and a Gadolinium-gallium garnet (GGG), which provides an intermediate stage to heat sink wires between the 4 K bath and the cold stage. The salt pills are thermally connected to the helium bath via a mechanical heat switch, which is opened to break the thermal connection between the salt pills and the 4 K bath during the ADR cycle.

The cold stage is isolated from room temperature by two nested radiation shields enclosed in a vacuum jacket. The innermost shield is connected to the 4 K helium bath. The intermediary shell is heat sunk to the 60 K pulse tube in the dry dewar and a 77 K liquid nitrogen tank in the wet dewar. The vacuum jacket seals the dewar under high vacuum ($\sim$10 μTorr) when in operation. All three shells attach at the top of the dewar but are mechanically isolated below the helium bath. A photo of the cryostat and the cold stages of the wet dewar is shown in Figure 6.4.

The temperature of the cold stage is controlled between 50 mK and 1 K with a PID loop controlled by a Lakeshore 370, which outputs a current between 0 and 316 μA. This is amplified $\times$20,000 by the Kepco power supply that sends current through the superconducting magnet. Temperature stability is best below 500 mK, where the temperature is stable to about 50 μK. The GGG, FAA, and sample box temperatures are measured using a Ruthenium Oxide (RuOx) resistance thermometer. The resistance is converted to temperature with a Lakeshore 370 resistance bridge using the calibrated temperature versus resistance curve. The magnet, pulse tube, and 4 K stage temperatures are monitored with silicon diode temperature sensors and read out using a Lakeshore 218 Temperature Monitor.

Devices are mounted in a gold-plated copper box and wire bonded to a printed circuit board (PCB). This sample box is shown in figure 6.8. The temperature of the sample box is measured with a RuOx thermometer soldered on the PCB that has been calibrated against a Johnson noise thermometer.

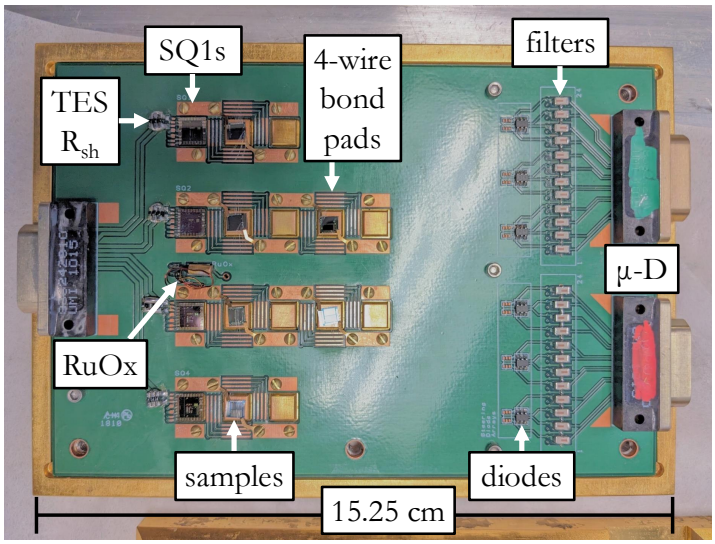

Figure 6.8: Photograph of the 50 mK sample box. Four-wire filtering and protection diodes are located on the right of the box. Chips are mounted on the left. Stage 1 SQUIDs (SQ1) and TES voltage bias shunt resistors R_{sh} are used for TES readout. Samples are mounted on Cu stages for thermal sinking. The sample box RuOx thermometer is located near the samples between two SQ1s. NIS four-wire measurement lines are connected to the μ-D connectors on the right. TES readout lines and connections to the RuOx thermometer are connected to the μ-D on the left.

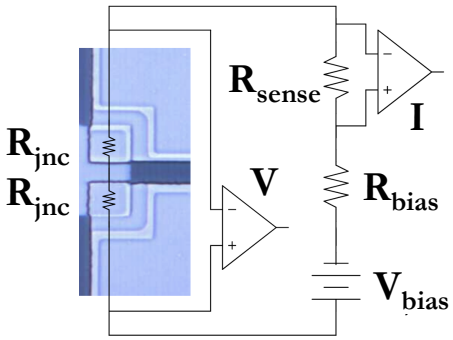

Figure 6.9: The four-wire measurement circuit of the voltage V and current I across two NIS junctions in series, each with resistance R_{jnc}.

Inside the sample box, each NIS measurement line is filtered with a Minicircuits LFCN-80 80 MHz low pass filter to remove stray RF signals. These lines are also connected to ground through a Schottky diode as a precaution against sudden electrostatic discharge (ESD), to which the NIS junctions are highly sensitive. Each TES bolometer is wire bonded to a SQUID amplifier in the sample box with 280 $\mu\Omega$ shunt resistors. Outside the sample box, both NIS and TES measurement lines are routed through two superconducting NbTi looms of 48 twisted pair DC wires on Micro-D 25 connectors. These wire looms are heat sunk at 800 mK, then filtered again through two Minicircuits LFCN-80 80 MHz filters and one LFCN-3000 filter at the 4 K stage.

Connections between 4 K and room temperature are made with low inductance flexible cables that are heat sunk to the 60/77 K heat plate. These cables terminate at the breakout box on the top of the cryostat with SMB connectors, where each NIS measurement line is filtered with a 1kΩ resistor and a 120 μH inductor in series as another protection against ESD.

6.3.2 NIS Characterization

Both NIS junctions and TES bolometers are fully characterized from measurements of current through the device as a function of voltage across the device, hereafter IV characteristics. An NIS IV characteristic is measured by current biasing the junction in a four-wire measurement scheme.

The IV measurement circuit for two NIS junctions in series is shown in Figure 6.9.

A four-wire measurement scheme separates the current-carrying and voltage-sensing connections between the volt/ammeter and the device under test, eliminating the contact resistance from the voltage measurement. To do this, the voltage leads are placed as close as possible on either side of the device under test, and the current leads are placed outside these voltage connections. In this configuration, very little current goes through the voltage sensing loop, minimizing the voltage drop across the sensing leads and providing a more accurate measurement of the voltage across the device.

The current bias is achieved using a low-noise dual-polarity voltage source, comprised of either two battery programmable voltage sources connected at their negative terminals or a Stanford Research Systems SIM928 module. This voltage is converted to a current bias with a known room temperature resistor R_{bias}. These voltage sources have a maximum output of at least ± 6 V, and R_{bias} is chosen such that the voltage across the junction at the maximum range of the voltage source is $\sim 5\Delta$.

The current through the junction is determined by measuring the voltage across a known room temperature resistor R_{sense}. This current sensing voltage and the voltage across the NIS junction are amplified by an INA 100 instrumentation amplifier and then measured with an Agilent 34401A digital multimeter. R_{sense} is chosen to be $\sim 10\times$ smaller than R_{bias} to not affect the current bias of the junction, but provide a large enough voltage drop for accurate measurement. A typical measurement configuration for measuring eight junctions in series is R_{bias} =1 kΩ and R_{sense} = 10 kΩ.

A single IV characteristic at base temperature is sufficient to measure both the quality factor of the junction Q and the specific resistance of the junction R_{sp}. Q, as shown in equation 5.14, is calculated as the ratio of the sub-gap resistance R_{sg} to the normal state resistance R_N. R_N is measured as the average numerical derivative dV/dI at voltages $\geq 2\Delta$, where the junction is in the normal branch. R_{sg} is measured as the maximum dV/dI, and should be measured at the base temperature where the excess current from the thermal smearing from the Fermi function is

minimized.

We see from Equation 5.17 that we can increase the cooling power of the junction by decreasing R_N. This is limited by the ability to yield thin oxidation layers, resulting in a lower limit on the product of the normal resistance and the junction area, defined as the specific resistance $R_{sp} = R_N A$ All refrigerator junctions in this work have an area of 7 µm × 32 µm, and a typical lower limit on R_{sp} from fabrication is $\sim 1000\Omega\mu m^2$.

The superconducting energy gap Δ can be estimated as the voltage corresponding to the minimum in dV/dI. A more precise measurement of Δ is made by fitting measured IV characteristics taken at a range of bath temperatures to the theoretical IV characteristics calculated using Equation 5.13 To do this, we first calculate theoretical IV curves at a range of temperatures using the previously measured R_N and Q for various values of Δ We then interpolate the temperature of the junction at each data point of a measured IV curve from the theoretical IV curves Finally, we do a least-squares minimization of the interpolated temperatures and the cold stage temperature during the IV measurement to determine which Δ value best describes the data.

The internal temperature of the junction changes as a function of voltage due to self-cooling, which is not included in the theoretical IV calculations. For this reason, we only fit data at voltages $\sim 10\%\Delta/e$ and temperatures above 150 mK to these theoretical IVs, where junction self-cooling is minimized.

The temperature of the NIS junction can be determined at each bias point of a measured IV by using the theoretical IV curves for temperature calibration. The isothermal theory IV characteristics in this measurement are calculated using the previously measured NIS characterization parameters for that particular junction. The optimal bias for self-cooling is again found by iterating through voltage biases centered around $90\%\Delta$.

An example measurement is shown in Figure 6.10, where the solid lines are the theoretically calculated IV characteristics and the dots are measured IV data points Below 0.1 mV, the data points follow the isothermal theory curves Above 0.1 mV, the data trends to lower current, crossing several isothermal curves before transitioning out of the subgap and onto the normal branch at

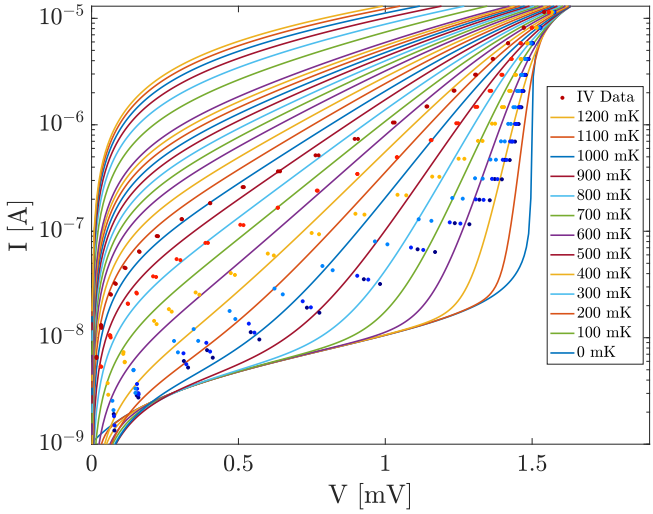

(a) Isothermal NIS IV curves (solid lines) and IV data (dots) at various bath temperatures.

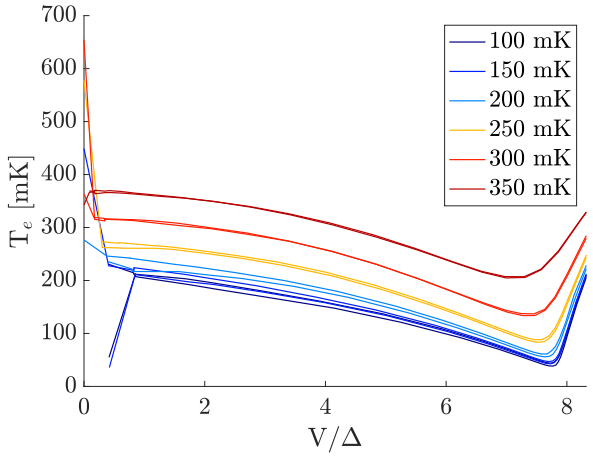

(b) Interpolated NIS electron temperatures from (a)

Figure 6.10: a) Theoretical isothermal IV characteristics and IV measurements of 8 NIS junctions in series from different bath temperatures. Both the data and the theoretical IVs transition out of the subgap and onto the normal branch at ∼1.5 mV. For a single junction, we measure a Q value of 3113 and $\Delta = 187.2$ eV, which is consistent with $8 \times \Delta/e \sim 1.5$ mV. b) NIS junction electron temperature at each data point in (a) interpolated from the isothermal theory curves.

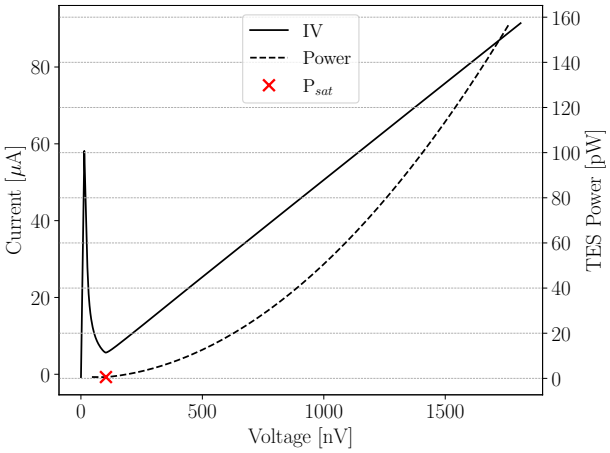

Figure 6.11: Measurement of TES saturation power at T_b=156 mK.

V∼1.5 mV This indicates that the NIS junctions are self-cooling above 0.1 mV.

6.3.3 TES Characterization

TES bolometers are also characterized by their IV characteristics. A single TES IV measurement provides the normal state resistance R_N and the saturation power of the detector at the bath temperature of the measurement $P_{sat}(T_b)$. We take the TES normal resistance to be the mean value of dV/dI in the normal branch. The saturation power $P_{sat}(T_b)$ is the IV power at the end of the superconducting-to-normal transition. An example P_{sat} measurement of an NIS-TES device is shown in Figure 6.11. Taking multiple IV characteristics while sweeping the bath temperature provides the TES thermal conductance $G(T)$ and transition temperature T_c by fitting $P_{sat}(T_b)$ measurements to Equation 6.4 described in the following section.

6.3.3.1 TES Readout

We measure the TES signal using a Superconducting Quantum Interference Device (SQUID)-based readout system akin to a time-division multiplexing (TDM) readout scheme. SQUIDs are low noise amplifiers that can easily be impedance-matched to TESs and are ubiquitous in the world of TES readout. In our readout system, shown in Figure 6.12, the TES is voltage biased with a shunt

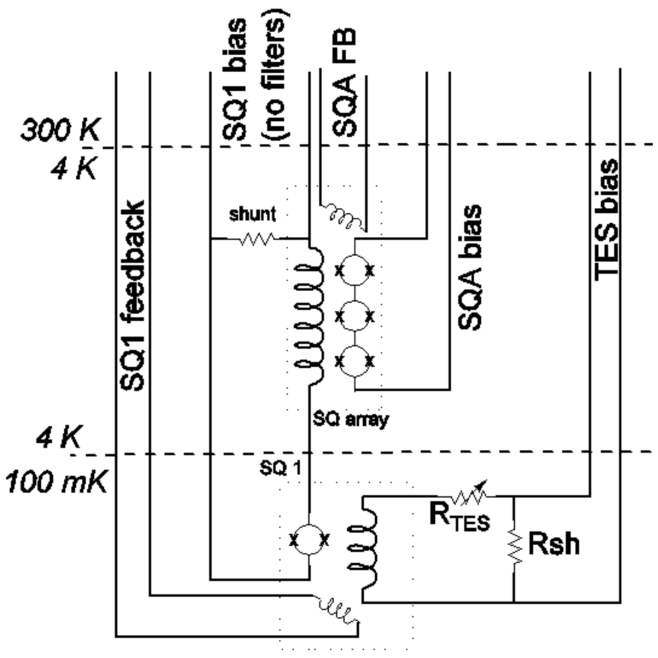

Figure 6.12: Circuit diagram of the SQUID-based TES readout circuit. At 100 mK, the current through the TES is inductively coupled to the stage 1 (S1) SQUID. SQ1 is also inductively coupled to the SQ1 feedback line, which injects a null current monitored and controlled by a feedback box at room temperature. At 4K, the SQUID array (SQA) amplifies the signal from SQ1 before sending it to the feedback box. The raw TES signal is the nulling bias in the SQ1 feedback line.

resistor R_{sh} for enhanced detector stability via negative electrothermal feedback and is connected in series to the input coil of a Stage 1 SQUID (SQ1) at 100 mK. The output of SQ1 is inductively coupled to a series array of 100 SQUIDs (SQA) at 4 K, which amplify the TES signal before sending it to a feedback box at room temperature. This feedback box injects a nulling current onto the SQ1 feedback line to cancel the signal from the TES. This active nulling technique is referred to as flux-locking the SQUID and greatly enhances its dynamic range.

The raw TES signal is the voltage placed on the feedback line V_{FB} used to keep SQ1 flux-locked, which is translated to current through the TES using measured values of the circuit components:

$$I_{TES} = \frac{V_{FB} - V_{off}}{R_{FB} M_r} \tag{6.1}$$

$$I_{bias} = \frac{V_{bias} - V_{b,off}}{R_{bias}} \tag{6.2}$$

$$V_{TES} = (I_{bias} - I_{TES} - I_{off}) R_{sh} - (I_{TES} + I_{off}) R_{par} \tag{6.3}$$

where V_{off} and I_{off} are the respective voltage and current offsets in the measurement circuit, $V_{b,off}$ is the voltage offset in the bias circuit, M_r is the mutual inductance between the SQ1 feedback and TES input coils, R_{FB} is the bias resistance on the SQ1 feedback line, and R_{par} is the parasitic resistance in the TES bias circuit.

6.3.3.2 TES Power Law

The power flowing between a TES and the thermal bath is $P = k(T_{TES}^n - T_b^n)$, where k is related to the leg geometry and materials, T_{TES} and T_b are the TES and bath temperatures, and the exponent n depends on the mode of phonon transport [47]. The thermal conductance is closely related to this power: $\mathrm{G} \equiv \frac{\partial P}{\partial T}| = nkT^{n-1}$. During operation, $T_{TES} \approx T_c$ and the maximum power the TES can absorb before saturation is $P_{sat} = k(T_c^n - T_b^n)$. Rearranging terms, the relationship between P_{sat} and G evaluated at T_c is made explicit:

$$P_{sat} = G(T_\mathrm{c}) \times \frac{T_\mathrm{c}}{n} \left[1 - \left(\frac{T_\mathrm{b}}{T_\mathrm{c}}\right)^n\right] \tag{6.4}$$

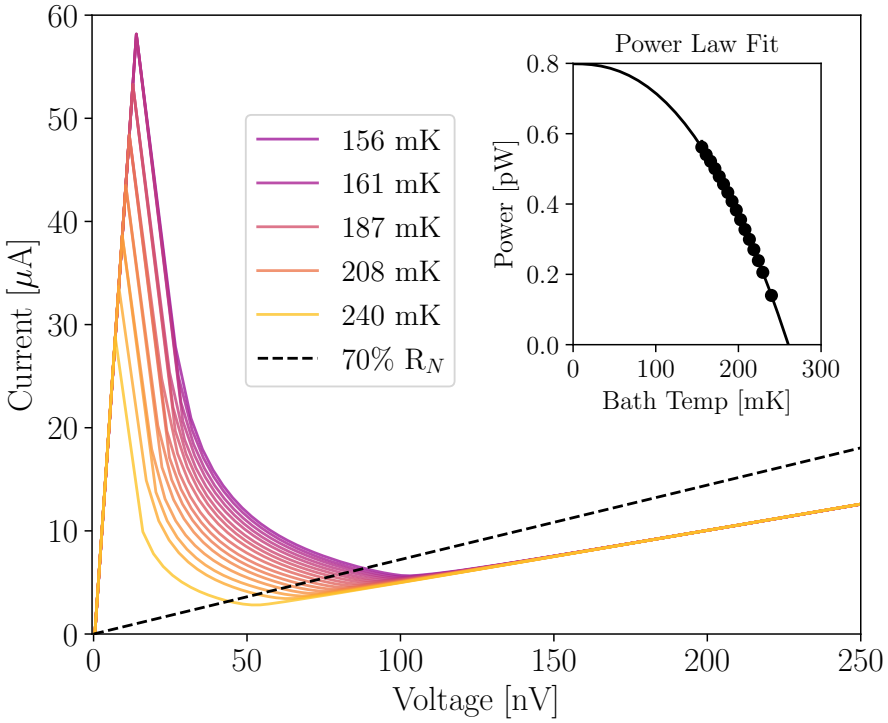

Figure 6.13: Characterization of the TES on the best-performing NIS-TES v2 device. IV characteristics were taken at a range of bath temperatures between 156 mK and 240 mK. The inset shows P_{sat} measurements from these IV characteristics evaluated at 70% R_N. These P_{sat} measurements are fit to Equation 6.4, and the resulting best fit parameters are given in Table 6.1.

The TES critical temperature T_c, thermal conductance G(T_c) evaluated at T_c, and power law exponent n are measured by fitting TES saturation power measurements from I-V characteristics measured at different values of T_b. At each T_b, we calculate saturation power P_sat as the current times the voltage at 80% percent of the normal state resistance for various T_b. We choose 70-80% because the resistance is approximately constant with current high in the transition.

The TES power measurement error σ_P is given as $\sigma_P = \sqrt{(I * \sigma_V)^2 + (V * \sigma_I)^2}$, where σ_V is taken to be the standard deviation of the voltage in the superconducting region of the TES IV, and σ_I is the standard deviation of the normal branch current after subtracting the best fit line. Errors on T_c, G(T_c), n are estimated as the square root of the diagonal entries in the power law fit covariance matrix. The parameters k and n are typically covariant, leading to large error bars propagating through when using these parameters to calculate G(T_c). We avoid overestimating σ_G by fitting for G explicitly.

Parameter	**Measurement**
T_c [mK]	260.4 ± 1.5
n	2.4 ± 0.04
$G(T_c)$ $[pW/K]$	7.2 ± 0.6
P_{sat} $[pW]$	0.71 ± 0.1
R_N $[m\Omega]$	19.7 ± 0.1

Table 6.1: TES parameters from the power law fit in Figure 6.13 at 80% R_N. All parameters with a temperature dependency, i.e., G(T) and $P_{sat}(T)$ are evaluated at 168 mK.

IV characteristic measurements of a TES bolometer at various bath temperatures are shown in Figure 6.13. The resulting $\mathrm{P_{sat}}$ measurements and power law fit are shown in the inset. The TES parameter fit results are given in Table 6.1.

At V = 0 V of the IV characteristics, the TES is superconducting and the current jumps to the TES critical current. At high voltages, $\geq$ 125 nV in this measurement, the TES is normal and the IV characteristic is ohmic. At intermediate voltages, the TES is in the superconducting phase transition. Unlike NIS junctions, the current through a TES in the phase transition is higher at lower temperatures. This temperature sensitivity makes the TES an excellent thermometer at

temperatures below T_c.

6.3.4 NIS-TES Refrigeration Measurements

We can use the same temperature sensitivity that makes the TES an ultra sensitive detector to determine the temperature of the TES during an NIS-TES refrigeration measurement. To use the TES as a thermometer, we first take TES IV characteristics while sweeping the ADR bath temperature with the NIS cooler off. In the same way that we interpolate NIS temperature using the isothermal theory curves, we can use these calibration IV curves to interpolate TES temperature from a TES IV characteristic. With these temperature calibration IV curves, we can continue with the NIS-TES cooling experiment.

During a cooling experiment, we set the ADR bath temperature to a constant 300 mK and iterate through a range of NIS voltage biases, taking a TES IV at each NIS bias point. NIS biases are finely sampled around the optimal bias point for NIS cooling $V_{opt} \sim N_{jnc} \times 90\%\Delta/e$, where N_{jnc} is the number of NIS junctions on the NIS-TES device. We then interpolate the TES temperature from IV curves taken at each NIS bias point to determine what temperature the NIS refrigerators cooled to the TES.

An example cooling experiment is shown in Figure 6.14. In (a), the TES temperature calibration curves taken with the NIS junction turned off are given as solid lines. TES IVs taken at an ADR bath temperature of 300 mK for various NIS biases are given as dashed lines. The optimal bias of 2.8 mV is highlighted with a solid black line. In (b), the TES temperature interpolated in (a) is shown as a function of NIS voltage bias. The TES in this NIS-TES integrated device was cooled to 187 mK from 300 mK at an NIS bias of 2.8 mV.

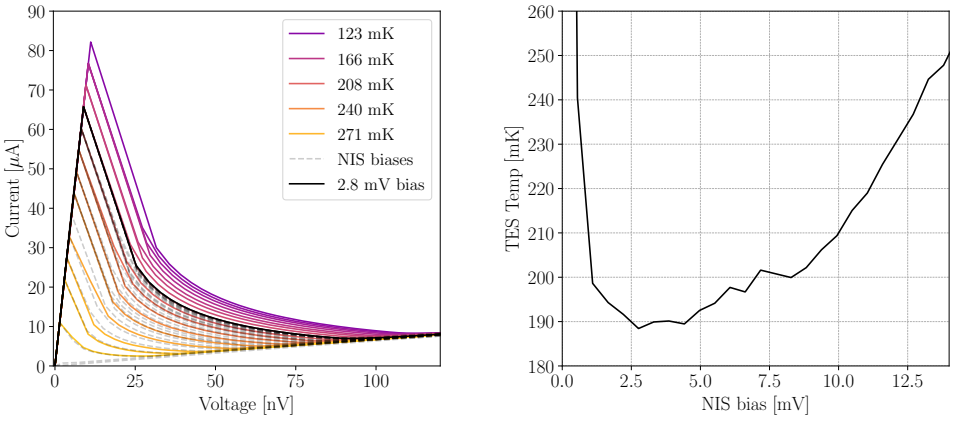

(a) (b)

Figure 6.14: (a) Cooling experiment for the best-performing NIS-TES v1 device that cooled the TES from 300 mK to 187 mK at the optimal NIS bias of 2.8 mV. The solid colored lines are TES temperature calibration IVs taken with the NIS off. The dashed curves are IVs taken while iterating through NIS V_{bias} at a 300 mK bath temperature. The optimal NIS bias is highlighted as a black solid line (b) Interpolated TES temperature at each NIS voltage bias using the calibration curves in (a).

6.4 Results & Discussion

6.4.1 NIS-TES v1 & v2

As discussed in Section 5.4.1, cooling performance is maximized when there is no dead length, i.e., when the membrane release lines up perfectly with the edge of the NIS junction. If the Si is insufficiently etched and extends past the NIS junctions, the cold finger is burdened with extra loading of the substrate phonons. If the device is overetched and the NIS junction extends past the Si wafer onto the TES leg, the cold finger is burdened with extra loading from the Joule heating in the junction.

One challenging aspect of integrated NIS-TES devices is aligning the membrane deep etch release for minimal dead length. The deep etch is one of the final fabrication steps that defines and releases the TES island from the substrate. The etch begins from the back of the wafer and removes material laterally as well as vertically. Each NIS-TES sample for all fabrication runs includes various iterations on the "deep etch gap," or the spacing between the edge of the junctions and where the Si etch begins at the back of the wafer, to account for the uncertainty in the extent of the lateral etching.

The first iteration of integrated NIS-TES devices, hereafter NIS-TES v1, demonstrated promising cooling performance but was plagued with a low NIS junction yield of 50%. We also found that the NIS coolers added negligible noise to the TES detector. In Figure 6.15, we show that there is no discernible difference in TES noise with the NIS refrigerators biased or unbiased.

The largest measured cooling of a TES was from 300 mK to 187 mK on a device with 6 out of 8 live junctions. The bath temperature of the TES is related to temperature of the NIS T_{NIS} and the number of functional junctions N_j via the equation

$$\frac{1}{8}k(T_b^n - T_c^n) + P_{sat}(T)_b) = \frac{N_j}{8}k(T_c^n - T_{NIS}^n) \tag{6.5}$$

where k and n are defined by the TES power law in Section 6.3.3.2. From this, we predict that with 8 working junctions, the TES would have cooled to 143 mK. Therefore, improving the junction

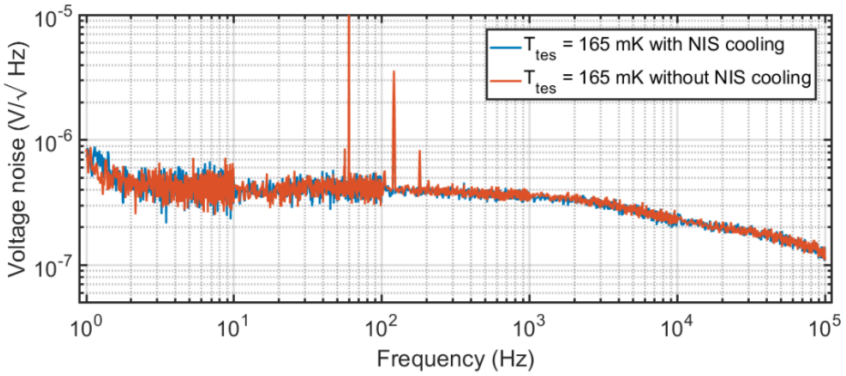

Figure 6.15: TES noise measurements at 165 mK. The orange curve is with NIS bias off, and the blue curve is with NIS bias on.

yield was the most straightforward route to achieving TES refrigeration from 300 mK to below 150 mK.

We found the low junction yield was due to high surface roughness in the commercially produced SiN_x substrate. This substrate was made to be very low stress and thus had a relatively high silicon content. This unintentionally resulted in a substrate with Si islands as tall as 12 nm, which can be seen in Figure 6.16a. These Si islands created topological defects that could pierce through the $\leq$10-nm-thick oxidation layers and short the junctions.

We resolved this yield issue by growing our own higher stress SiN_x substrate with lower Si content. To compare the two substrates, we measured the index of refraction n, which increases with silicon content in SiN_x. The index of refraction for the NIST-grown substrate is n = 2.2, compared to n = 2.27 in the vendor substrate. We also mapped the topology of the two substrates using atomic force microscopy (AFM), shown in Figure 6.16. We found that the surface roughness of the NIST-grown substrate was a large improvement over the vendor substrate. The peak height was reduced from 11.7 nm to 4.9 nm in the new substrate, with an RMS height reduction from 0.75 nm to $<$0.4 nm. We first fabricated a wafer of junction-only devices on this new lower Si substrate and recorded 100% yield in the 24 junctions measured.

The second version of integrated NIS-TES devices (v2) was then fabricated on the NIST-

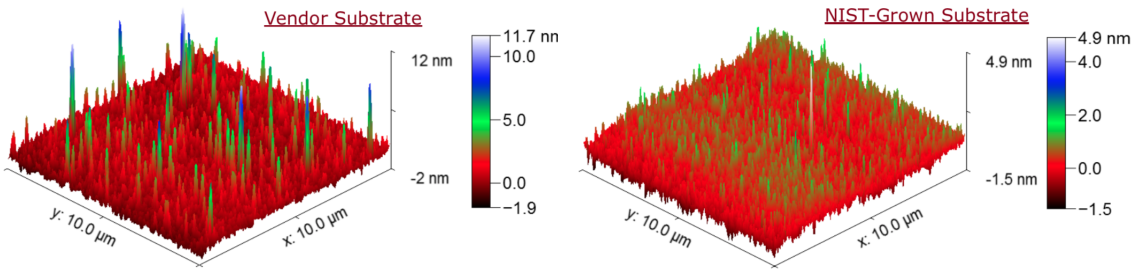

(a) (b)

Figure 6.16: AMF scans of (a) the vendor SiN_x substrate and (b) the NIST-grown substrate. Note that (a) and (b) have different color bars.

grown substrate. To decrease the loading from the hot substrate phonons, we included four unique "split" designs in which phononic filters were added in addition to baseline devices with nominally the same design as v1. Phononic filters are designed to disrupt the phonon path and lower membrane thermal conductance.

On split a devices, ∼150-nm-thick × 4-µm-long strips of PdAu in a 7-µm center-to-center spacing were added on top of the TES legs. Split b devices included PdAu strips with the same dimensions and spacing, but only along the cold finger. Split c devices replaced the PdAu strips in split b with strips of SiN_x. On split d devices, 4-µm-diameter holes were etched through the cold finger with a 7-µm triangular grid spacing. These phonon filter design choices were informed by the work in Zhang et al. 2019 [121], which measured reduction in the thermal conductance of SiN_x membranes by up to 56% with the addition of a single metal layer patterned into rings on top of the membrane surface.

The junction yield in v2 devices is nearly 100%, with 39 of 40 measured junctions operational, indicating that the smoother substrate alleviated the v1 junction yield issue. However, v2 devices have shown a significant reduction in cooling performance compared to v1. The greatest v2 temperature reduction measured was from 300 mK to 240 mK on a baseline device with seven live junctions. With eight operational junctions, we predict the TES would cool to 231 mK. The v1 and v2 devices with the best cooling performance are compared in Table 6.2. Including the microstrip

wiring layers, the NIS-TES legs have a cross-sectional area of $w \times d = (6\mu m \times 1.4\mu m = 8.4\mu m^2$ and a length of 600 µm.

Parameter	**v2**	**v1**
N_{jnc}	7	6
$G(T)$ $[pW/K]$	4.19	3.8
$\kappa(T)$ $[pW/(K\mu m)]$	419	380
$P_{sat}(T)$ $[pW]$	0.65	0.79
T_C [mK]	265.1	290.6
k [pW/K^n]	24.8	16.1
n	2.5	2.2
NIS R_N [Ω]	5.3	4.8
DL [µm]	0.5-2	0
Cooling from 300 mK	240 mK	187 mK
Cooling 8 Jncts	231 mK	143 mK

Table 6.2: The NIS-TES v1 and v2 devices with the best cooling performance. TES power law parameters are evaluated at 70% R_N and 156 mK. Cooling experiment measurements and projected cooling from 300 mK with eight live junctions are given at the bottom.

6.4.1.1 Substrate Heat Load

Thermal modeling in Section 5.4 shows that the electron system in the NIS junctions is predicted to self-cool from 300 mK to 112.8 mK (see Figure 5.9) and measurements in Section 6.3.2 show that the NIS junctions in the best-performing v2 device self-cool to ∼130 mK (see Figure 6.10). However, the TES only cools to 231 mK with eight working junctions, so there must be a thermal gradient of ≥100 mK between the NIS junctions and the TES. The cooling performance will be degraded if extra power loads or heat leaks to the substrate are introduced in v2, or if thermal conduction between the cold junction electrons and the TES phonons is impaired somewhere along the cooling chain.

Upon visual inspection, we have found the dead length increased significantly between v1 and v2. An example dead length comparison between v1 and v2 is given in Figure 6.17 in which this v1 device has negligible dead length and the v2 device has 5 µm of dead length. The v2 device in Table

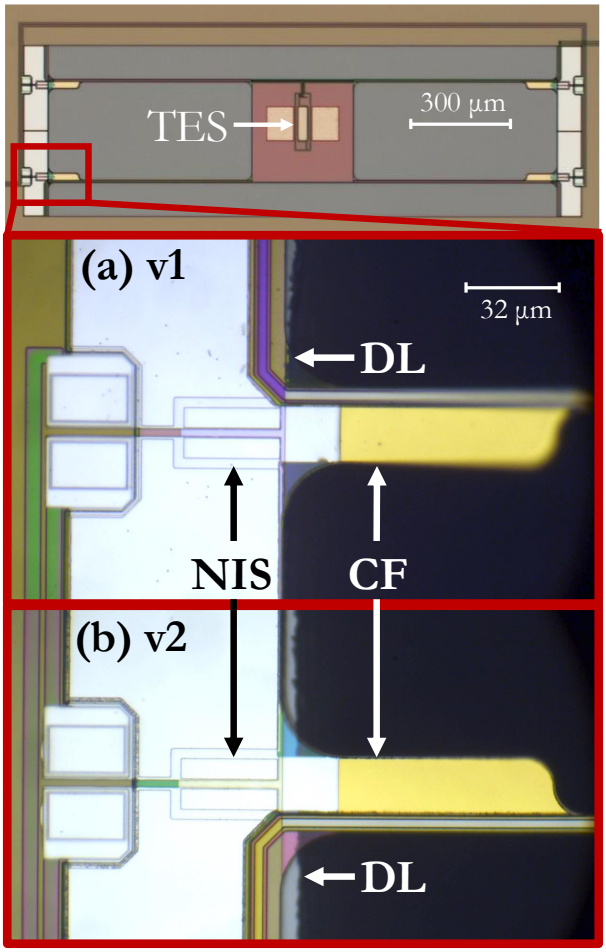

Figure 6.17: Dead length (DL) comparison between an NIS-TES (a) v1 and (b) v2 device. The v2 device DL is $\sim$ 5µm. The NIS refrigerator junctions are to the left of the TES leg, and the cold finger (CF) is the normal metal base electrode that extends onto the TES on the right. The top photo is an NIS-TES device, with the region imaged in (a) and (b) highlighted.

6.2 has 0.5-2 µm dead length on each leg, whereas the dead length on the v1 device is negligible. From Figure 5.11, a dead length of 2 µm theoretically increases the final TES temperature from 136 mK to 149 mK. The dead length increase does significantly impact TES refrigeration but does not fully explain the reduction in cooling performance between these two devices.

If the higher stress v2 substrate is more thermally conductive than the v1 substrate, the increased thermal loading from the Si wafer would negatively affect the cooling performance in v2. In Table 6.2, we see that the best-performing v2 device is slightly more conductive than the v1 device. In Figure 6.18, we use the power balance model in Section 5.4.1 to predict the TES temperature for a range of TES thermal conductivities, where in (a) $\kappa_0 = 272$ pW/(K µm) is the total TES thermal conductivity at 156 mK. This κ_0 is larger than κ_{SiN} given in Chapter 5 because it includes the thermal conductivity contribution of the microstrip. The beige area encompasses the range of conductivities measured in the v2 devices, spanning 80% to 325% κ_0. We find that using the measured values of κ fails to explain either the v1 or v2 data despite the wide variance in v2 κ.

In Figure 6.18b, we instead scale κ_0 to 797 pW/(K μm), the thermal conductivity required to predict the v1 data point. To assess the implications of the v2 cooling performance, we scale the v2 κ range accordingly. There is no obvious reason to scale the v1 conductivity by a factor of ~ 3, meaning κ =797 pW/(K μm) necessary to explain the v1 data point is likely unphysical. If we choose to entertain this treatment, including a large unexplained heat leak, we find that this higher κ still does not explain the v2 data.

While the model does begin to agree with the best measured v2 performance at the highest v2 κ range, the device associated with the highest κ failed to cool below the TES below T_c ~270 mK from 300 mK, instead cooling the TES from a bath temperature of 260 mK to 245 mK. Therefore, while a more conductive substrate may contribute to the issue, there must be other mechanisms behind the reduced v2 cooling performance.

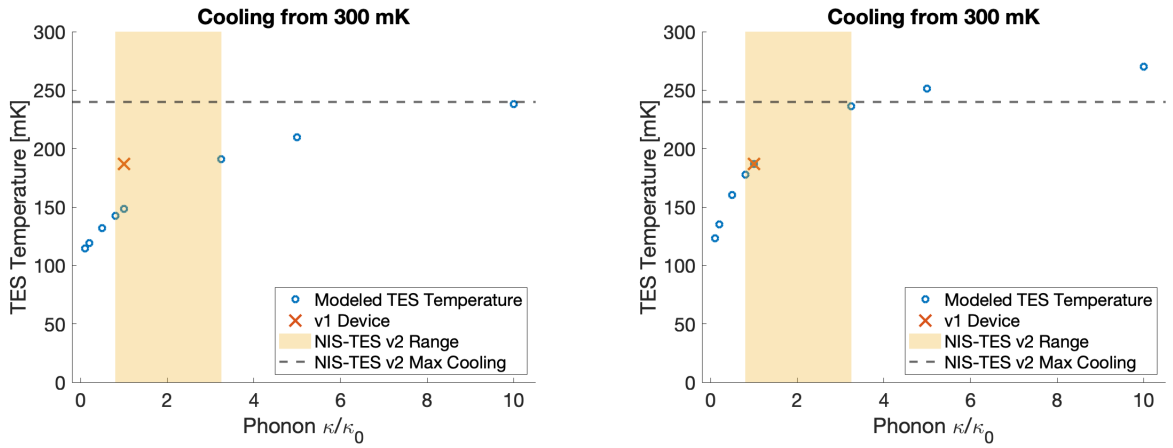

(a) (b)

Figure 6.18: Model predictions for TES temperature vs TES thermal conductivity with P_{TES} set to 0.5 pW. In (a), κ_0 is the measured NIS-TES v1 thermal conductivity of 272 pW/(K μm) at 156 mK. The beige area covers the 80% to 325% thermal conductivity range measured in the v2 devices. The gray dotted line is the maximum cooling measured with a v2 device. In (b), we instead scale κ_0 to 797 pW/(K μm), the value necessary to predict the v1 data point. We also scale the v2 κ range accordingly.

6.4.1.2 Cold Finger Electron Thermal Conductance

Since a larger thermal conductance in the TES leg fails to explain the v2 cooling performance, we also consider the thermal conductance in the cold finger. Unlike the dielectric and superconducting layers that make up the membrane and microstrip, the dominant heat carriers in the normal metal cold finger are electrons. The electron thermal conductivity is given by the Wiedemann-Franz law $\kappa_e = L_0 T/\rho$, which relates the electron thermal conductivity κ_e to the electrical resistivity ρ and the Lorentz number L_0 as a function of temperature T The thermal gradient ΔT is given by

$$\Delta T = P/G = \frac{PL}{A\kappa_e} = \frac{P\rho L}{L_0 T w d} \tag{6.6}$$

Using the properties of the AlMn cold finger $\rho_{AlMn} = 0.145\ \Omega$ µm, d = 30 nm, w = 5 µm, and $L = 100$ µm, and setting $P = 1$ pW, a typical TES power load per leg in sub-mm astronomy, we calculate a thermal gradient $\Delta T = 14$ mK across the cold finger, which also does not explain the large gradient we observe.

However, if there were physical defects in the cold finger introduced with the new substrate, there could be discontinuities in the electron thermal conductance unaccounted for in this calculation. Figure 6.19 is a SEM image of a v2 cold finger cross-section cut with a FIB. This image shows a few potential physical defects in the cold finger. For example, the normal metal layer does not span the entire width of the SiN_x layer underneath it, which is not as designed. We can also see debris and a dip in the thickness of the normal metal layer. Since thermal conductance depends on the thickness of the film, thinner regions in the normal metal can significantly reduce the electron thermal conductance and thus the electron-phonon coupling necessary to cool the TES.

6.4.2 NIS-TES v2b & v3

The v2 design was refabricated on a 150 mm wafer using the same higher stress NIST-grown substrate, but wiring discontinuities in the NIS biasing circuit prevented their use as refrigerators. We have recently finished NIS-TES v3 devices. For v3, we took the v2 design and reduced the microstrip width near the cold finger from 5 µm to 3 µm. This design change was made in light

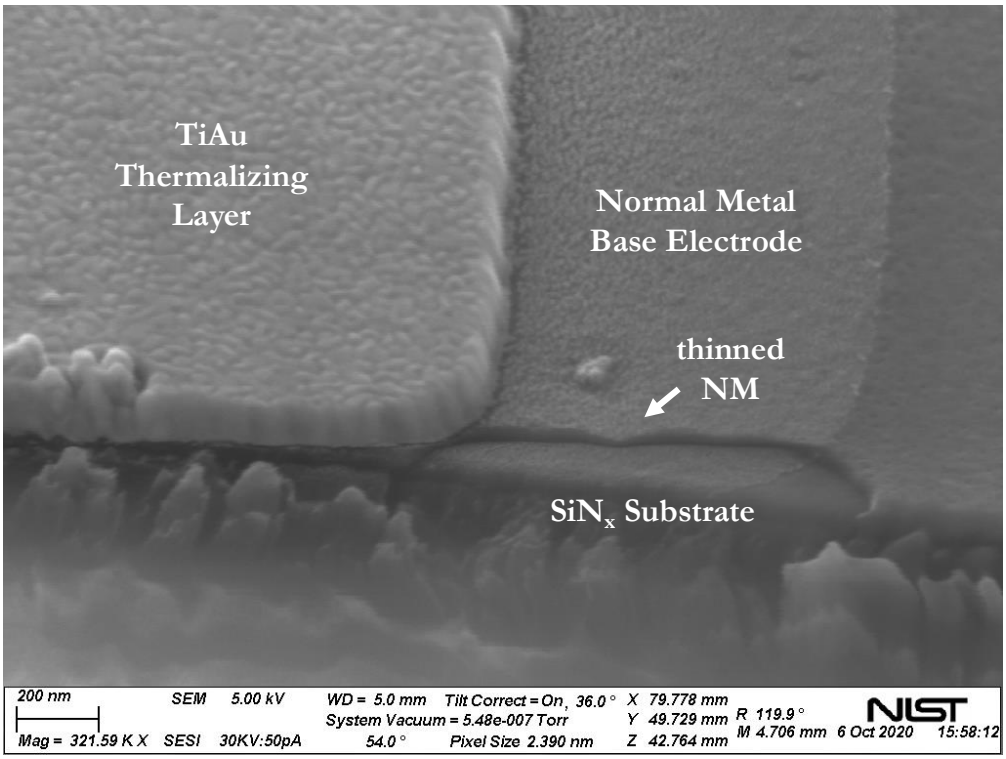

Figure 6.19: SEM image of a cold finger. The normal metal base electrode extends onto the SiN_x TES leg with a TiAu thermalization layer.

of our measurements in Chapter 4 that, in our case of very thin substrate layers, the microstrip dominates the TES thermal conductance. We also removed splits a and c to simplify the fabrication.

Unfortunately, the NIS junctions on v3 devices have anomalously high normal resistances ranging from 200 Ω to ∼ 1 MΩ, much larger than the design R_N ∼5 Ω. IV characteristics of v3 junctions show that we have maintained 100% junction yield, but do not function as TES refrigerators due to their low cooling power with such high R_N.

The NIS-TES devices are potentially the most complex fabrication done in the NIST clean room. The TES and NIS fabrication steps cannot be parallelized, meaning the process is essentially two fabrications completed in series on the same wafer. This process can take the most skilled clean room staff 3-6 months to fabricate, which does not allow for a quick fabrication-measurement feedback process. This ambitious fabrication process is the largest obstacle to recovering and improving the performance of NIS junction refrigeration of TES bolometers.

6.5 Future Work

While we suspect excess dead length and potential physical discontinuities in the cold finger are responsible for the diminished cooling performance in v2, further investigation is needed to recover the demonstrated v1 cooling performance while retaining a near 100% junction yield. Once this is accomplished, improved NIS-junction refrigeration of TES bolometers from 300 mK to the more optimal operation temperatures of 100-130 mK can be achieved with the following advancements on the current design: 1) increasing the cooling power by creating more transparent junctions and 2) lower thermal loading from further development of phononic filters and adjustments the microstrip design.

Nominally, the NIS refrigerator junctions have a normal resistance of ∼5Ω. Despite recent issues with high R_N junctions, we have previously demonstrated more transparent junctions with thinner oxides. When fabricated on the smoother substrate, we do not expect junction yield to suffer with a thinner oxide layer.

While we have fabricated integrated NIS-TES devices with various phononic structures as a

proof of concept, the effect is still under study and the design will require future iterations. The phononic filter development will require the most effort and provide the largest improvement in cooling efficiency and should be the priority once v1 performance is recovered. Furthermore, a microstrip redesign with a thinner to non-existent top insulating layer will also reduce the thermal loading from the substrate. Measurements in Chapter 4 suggest that removing the top insulating layer of the microstrip will decrease G_{TES} by 12%.

We have developed solid-state, on-chip refrigerators for cooling low temperature detectors below 300 mK. The refrigerator technology will be inexpensive, light, and compact, making it well suited for space applications. With the above improvements on the current design, we will have demonstrated optimized cooling of single pixels.

The next lucky graduate student will scale this technology to a full-sized array for deployment on a future balloon-born observatory. Though we will develop NIS refrigerators to cool TES bolometers for (sub-)mm astrophysics, this technology can be used to cool any cryogenic sensor tuned to any wavelength from sub-mm through gamma-ray. Once demonstrated on a balloon-borne experiment, NIS refrigerators will be a TRL 7 technology ready to enable the deployment of NASA's X-ray and FIR Probe missions, and eventually the future Flagship UV/O/NIR mission, on a faster timeline and a smaller budget.

Chapter 7

Future Work

7.1 TES Leg Thermal Conductance Modeling

Our treatment of thermal transport in multi-layered TES legs can be made more accurate by including two effects that we have thus far neglected. The first includes potential diffusive scattering at the edges of the films in addition to the top and bottom surfaces. This would require additional free parameters in our model, which can only be accommodated by measuring more unique TES leg geometries.

Additionally, we presently approximate the thermal conductance of the TES leg, which is a composite thin film structure, as the parallel sum of the thermal conductance of each film. This is equivalent to treating each film as a separate phonon channel. This treatment is accurate under the assumption of 100% internal phonon reflection at the interfaces between disimilar materials, which is not guaranteed in TES legs. A more accurate treatment would be calculating the dispersion curves of the multi-layer structure, which can be done using a spectral collocation method [88].

7.2 NIS-TES Integrated Detectors

Once the initial NIS-TES v1 cooling performance is recovered, improving upon this performance can be achieved with the following advancements to the current design: 1) lower junction normal resistance with thinner insulating layers to increase the cooling power of our junctions and 2) lower thermal loading with a redesign of the TES microstrip and the addition of phononic structures.

We have demonstrated the fabrication of more transparent junctions than the current junctions with $R_N \sim 5\Omega$. These thinner junctions will be fabricated on the smoother substrate and thus yield is not expected to diminish with the second advancement. The second advancement will require the most effort and provide the largest improvement in cooling efficiency. The microstrip redesign will thin or remove the top insulating layer, which our recent measurements indicate will decrease G_{TES} by 12%.

Phononic structures disrupt the phonon path, resulting in lower membrane thermal conductance. On NIS-TES integrated devices, we have introduced phononic filters to reduce the thermal loading from the substrate while maintaining high electron thermal conductance with the NIS refrigerator. We have fabricated integrated NIS-TES devices with various phononic structures as a proof of concept, but the effect is still under study and the design will require future iterations.

We will use our TES thermal conductance model and build on our established NIS thermal model to design, fabricate, and test the next iteration of NIS-TES integrated devices with these improvements. With these improvements, single-pixel NIS-cooled TES bolometers will optimized and ready to scale into full arrays for deployment on a balloon-borne cryogenic experiment.

Two potential experiments for this technology development are Taurus, an instrument funded by NASA's APRA program to measure the optical depth to reionization, and the Terahertz Intensity Mapper (TIM), which will study cosmic star formation history with KIDs [17, 64]. Both missions are technology pathfinders for future Probe- and Flagship-tier NASA missions that, if equipped with NIS refrigerators, will raise the Technology Readiness Level (TRL) of this refrigeration technology from 4 to 7. The R&D funded with this grant will enable future NASA satellites with cryogenic payloads, such as the two Probe-class missions and the future Flagship UV/O/NIR mission outlined in the Astro2020 Decadal, to fly unburdened by the financial, weight, and power demands of an ADR or DR.

7.2.1 Impacts Beyond (Sub-)mm Astronomy

Most of the development of NIS-cooled detectors has been for CMB balloon-borne TES polarimeters, but NIS refrigeration technology is sensor- and wavelength-agnostic. Both TES and KID detector technologies show strong promise in the X-ray, FIR, and optical; fields prioritized for both Probe-class missions and the next Flagship mission in the Astro2020 Decadal. KIDs also have applications in dark matter detection and quantum computing [40, 78], and TESs have been used in mm to gamma-ray astronomy [25, 108], X-ray material analysis [107, 108], and quantum information [38]. Deployment of a full NIS-TES array on a (sub-)mm balloon-borne observatory is the quickest route to raising the TRL of this refrigeration technology, and compelling science will be done in this context. However, once NIS refrigeration is demonstrated as a TRL 7 technology, it can be applied to any low temperature detector tuned to any wavelength.

Experiments that opt to keep ADRs in the cooling chain will also benefit from NIS refrigerators. When placed in series with an ADR, NIS refrigerators enhance ADR performance significantly by extending base temperature hold times and alleviating weight and magnetic shielding requirements. Due to the adiabatic refrigeration mechanism of an ADR, a 4 Tesla ADR will remain at 300 mK many times longer than 100 mK. Alternatively, an ADR designed to cool from 4 K to 300 mK requires a peak field of only $\sim$1 Tesla, alleviating much of the magnetic shielding and power requirements. An NIS-ADR cooling chain will provide the same benefits, though to a lesser degree, as ADR replacement with NIS refrigerators.

Bibliography

[1] Daniel Kwan & Daniel Scheinert and Jonathan Wang ; written and directed by Daniel Kwan & Daniel Scheinert Anthony Russo A24 and IAC Films present ; a Gozie Agbo production ; a Year of the Rat production ; in association with Ley Line Entertainment ; a Daniels film ; produced by Joe Russo, Mike Larocca ; producers. Everything everywhere all at once, 2022.

[2] Kevork N. Abazajian, Peter Adshead, Zeeshan Ahmed, Steven W. Allen, David Alonso, Kam S. Arnold, Carlo Baccigalupi, James G. Bartlett, Nicholas Battaglia, Bradford A. Benson, Colin A. Bischoff, Julian Borrill, Victor Buza, Erminia Calabrese, Robert Caldwell, John E. Carlstrom, Clarence L. Chang, Thomas M. Crawford, Francis-Yan Cyr-Racine, Francesco De Bernardis, Tijmen de Haan, Sperello di Serego Alighieri, Joanna Dunkley, Cora Dvorkin, Josquin Errard, Giulio Fabbian, Stephen Feeney, Simone Ferraro, Jeffrey P. Filippini, Raphael Flauger, George M. Fuller, Vera Gluscevic, Daniel Green, Daniel Grin, Evan Grohs, Jason W. Henning, J. Colin Hill, Renee Hlozek, Gilbert Holder, William Holzapfel, Wayne Hu, Kevin M. Huffenberger, Reijo Keskitalo, Lloyd Knox, Arthur Kosowsky, John Kovac, Ely D. Kovetz, Chao-Lin Kuo, Akito Kusaka, Maude Le Jeune, Adrian T. Lee, Marc Lilley, Marilena Loverde, Mathew S. Madhavacheril, Adam Mantz, David J. E. Marsh, Jeffrey McMahon, Pieter Daniel Meerburg, Joel Meyers, Amber D. Miller, Julian B. Munoz, Ho Nam Nguyen, Michael D. Niemack, Marco Peloso, Julien Peloton, Levon Pogosian, Clement Pryke, Marco Raveri, Christian L. Reichardt, Graca Rocha, Aditya Rotti, Emmanuel Schaan, Marcel M. Schmittfull, Douglas Scott, Neelima Sehgal, Sarah Shandera, Blake D. Sherwin, Tristan L. Smith, Lorenzo Sorbo, Glenn D. Starkman, Kyle T. Story, Alexander van Engelen, Joaquin D. Vieira, Scott Watson, Nathan Whitehorn, and W. L. Kimmy Wu. CMB-S4 Science Book, First Edition, October 2016. arXiv:1610.02743 [astro-ph, physics:gr-qc, physics:hep-ph, physics:hep-th].

[3] B. P. Abbott, R. Abbott, T. D. Abbott, M. R. Abernathy, F. Acernese, K. Ackley, C. Adams, T. Adams, P. Addesso, R. X. Adhikari, V. B. Adya, C. Affeldt, M. Agathos, K. Agatsuma, N. Aggarwal, O. D. Aguiar, L. Aiello, A. Ain, P. Ajith, B. Allen, A. Allocca, P. A. Altin, S. B. Anderson, W. G. Anderson, K. Arai, M. A. Arain, M. C. Araya, C. C. Arceneaux, J. S. Areeda, N. Arnaud, K. G. Arun, S. Ascenzi, G. Ashton, M. Ast, S. M. Aston, P. Astone, P. Aufmuth, C. Aulbert, S. Babak, P. Bacon, M. K. M. Bader, P. T. Baker, F. Baldaccini, G. Ballardin, S. W. Ballmer, J. C. Barayoga, S. E. Barclay, B. C. Barish, D. Barker, F. Barone, B. Barr, L. Barsotti, M. Barsuglia, D. Barta, J. Bartlett, M. A. Barton, I. Bartos, R. Bassiri, A. Basti, J. C. Batch, C. Baune, V. Bavigadda, M. Bazzan, B. Behnke, M. Bejger, C. Belczynski, A. S. Bell, C. J. Bell, B. K. Berger, J. Bergman, G. Bergmann, C. P. L. Berry, D. Bersanetti, A. Bertolini, J. Betzwieser, S. Bhagwat, R. Bhandare, I. A. Bilenko, G. Billingsley, J. Birch, I. A. Birney, O. Birnholtz, S. Biscans, A. Bisht, M. Bitossi, C. Biwer, M. A.

Bizouard, J. K. Blackburn, C. D. Blair, D. G. Blair, R. M. Blair, S. Bloemen, O. Bock, T. P. Bodiya, M. Boer, G. Bogaert, C. Bogan, A. Bohe, P. Bojtos, C. Bond, F. Bondu, R. Bonnand, B. A. Boom, R. Bork, V. Boschi, S. Bose, Y. Bouffanais, A. Bozzi, C. Bradaschia, P. R. Brady, V. B. Braginsky, M. Branchesi, J. E. Brau, T. Briant, A. Brillet, M. Brinkmann, V. Brisson, P. Brockill, A. F. Brooks, D. A. Brown, D. D. Brown, N. M. Brown, C. C. Buchanan, A. Buikema, T. Bulik, H. J. Bulten, A. Buonanno, D. Buskulic, C. Buy, R. L. Byer, M. Cabero, L. Cadonati, G. Cagnoli, C. Cahillane, J. Calderón Bustillo, T. Callister, E. Calloni, J. B. Camp, K. C. Cannon, J. Cao, C. D. Capano, E. Capocasa, F. Carbognani, S. Caride, J. Casanueva Diaz, C. Casentini, S. Caudill, M. Cavaglià, F. Cavalier, R. Cavalieri, G. Cella, C. B. Cepeda, L. Cerboni Baiardi, G. Cerretani, E. Cesarini, R. Chakraborty, T. Chalermsongsak, S. J. Chamberlin, M. Chan, S. Chao, P. Charlton, E. Chassande-Mottin, H. Y. Chen, Y. Chen, C. Cheng, A. Chincarini, A. Chiummo, H. S. Cho, M. Cho, J. H. Chow, N. Christensen, Q. Chu, S. Chua, S. Chung, G. Ciani, F. Clara, J. A. Clark, F. Cleva, E. Coccia, P.-F. Cohadon, A. Colla, C. G. Collette, L. Cominsky, M. Constancio, A. Conte, L. Conti, D. Cook, T. R. Corbitt, N. Cornish, A. Corsi, S. Cortese, C. A. Costa, M. W. Coughlin, S. B. Coughlin, J.-P. Coulon, S. T. Countryman, P. Couvares, E. E. Cowan, D. M. Coward, M. J. Cowart, D. C. Coyne, R. Coyne, K. Craig, J. D. E. Creighton, T. D. Creighton, J. Cripe, S. G. Crowder, A. M. Cruise, A. Cumming, L. Cunningham, E. Cuoco, T. Dal Canton, S. L. Danilishin, S. D'Antonio, K. Danzmann, N. S. Darman, C. F. Da Silva Costa, V. Dattilo, I. Dave, H. P. Daveloza, M. Davier, G. S. Davies, E. J. Daw, R. Day, S. De, D. DeBra, G. Debreczeni, J. Degallaix, M. De Laurentis, S. Deléglise, W. Del Pozzo, T. Denker, T. Dent, H. Dereli, V. Dergachev, R. T. DeRosa, R. De Rosa, R. DeSalvo, S. Dhurandhar, M. C. Díaz, L. Di Fiore, M. Di Giovanni, A. Di Lieto, S. Di Pace, I. Di Palma, A. Di Virgilio, G. Dojcinoski, V. Dolique, F. Donovan, K. L. Dooley, S. Doravari, R. Douglas, T. P. Downes, M. Drago, R. W. P. Drever, J. C. Driggers, Z. Du, M. Ducrot, S. E. Dwyer, T. B. Edo, M. C. Edwards, A. Effler, H.-B. Eggenstein, P. Ehrens, J. Eichholz, S. S. Eikenberry, W. Engels, R. C. Essick, T. Etzel, M. Evans, T. M. Evans, R. Everett, M. Factourovich, V. Fafone, H. Fair, S. Fairhurst, X. Fan, Q. Fang, S. Farinon, B. Farr, W. M. Farr, M. Favata, M. Fays, H. Fehrmann, M. M. Fejer, D. Feldbaum, I. Ferrante, E. C. Ferreira, F. Ferrini, F. Fidecaro, L. S. Finn, I. Fiori, D. Fiorucci, R. P. Fisher, R. Flaminio, M. Fletcher, H. Fong, J.-D. Fournier, S. Franco, S. Frasca, F. Frasconi, M. Frede, Z. Frei, A. Freise, R. Frey, V. Frey, T. T. Fricke, P. Fritschel, V. V. Frolov, P. Fulda, M. Fyffe, H. A. G. Gabbard, J. R. Gair, L. Gammaitoni, S. G. Gaonkar, F. Garufi, A. Gatto, G. Gaur, N. Gehrels, G. Gemme, B. Gendre, E. Genin, A. Gennai, J. George, L. Gergely, V. Germain, Abhirup Ghosh, Archisman Ghosh, S. Ghosh, J. A. Giaime, K. D. Giardina, A. Giazotto, K. Gill, A. Glaefke, J. R. Gleason, E. Goetz, R. Goetz, L. Gondan, G. González, J. M. Gonzalez Castro, A. Gopakumar, N. A. Gordon, M. L. Gorodetsky, S. E. Gossan, M. Gosselin, R. Gouaty, C. Graef, P. B. Graff, M. Granata, A. Grant, S. Gras, C. Gray, G. Greco, A. C. Green, R. J. S. Greenhalgh, P. Groot, H. Grote, S. Grunewald, G. M. Guidi, X. Guo, A. Gupta, M. K. Gupta, K. E. Gushwa, E. K. Gustafson, R. Gustafson, J. J. Hacker, B. R. Hall, E. D. Hall, G. Hammond, M. Haney, M. M. Hanke, J. Hanks, C. Hanna, M. D. Hannam, J. Hanson, T. Hardwick, J. Harms, G. M. Harry, I. W. Harry, M. J. Hart, M. T. Hartman, C.-J. Haster, K. Haughian, J. Healy, J. Heefner, A. Heidmann, M. C. Heintze, G. Heinzel, H. Heitmann, P. Hello, G. Hemming, M. Hendry, I. S. Heng, J. Hennig, A. W. Heptonstall, M. Heurs, S. Hild, D. Hoak, K. A. Hodge, D. Hofman, S. E. Hollitt, K. Holt, D. E. Holz, P. Hopkins, D. J. Hosken, J. Hough, E. A. Houston, E. J. Howell, Y. M. Hu, S. Huang, E. A. Huerta, D. Huet, B. Hughey, S. Husa, S. H. Huttner, T. Huynh-Dinh, A. Idrisy, N. Indik, D. R.

Ingram, R. Inta, H. N. Isa, J.-M. Isac, M. Isi, G. Islas, T. Isogai, B. R. Iyer, K. Izumi, M. B. Jacobson, T. Jacqmin, H. Jang, K. Jani, P. Jaranowski, S. Jawahar, F. Jiménez-Forteza, W. W. Johnson, N. K. Johnson-McDaniel, D. I. Jones, R. Jones, R. J. G. Jonker, L. Ju, K. Haris, C. V. Kalaghatgi, V. Kalogera, S. Kandhasamy, G. Kang, J. B. Kanner, S. Karki, M. Kasprzack, E. Katsavounidis, W. Katzman, S. Kaufer, T. Kaur, K. Kawabe, F. Kawazoe, F. Kéfélian, M. S. Kehl, D. Keitel, D. B. Kelley, W. Kells, R. Kennedy, D. G. Keppel, J. S. Key, A. Khalaidovski, F. Y. Khalili, I. Khan, S. Khan, Z. Khan, E. A. Khazanov, N. Kijbunchoo, C. Kim, J. Kim, K. Kim, Nam-Gyu Kim, Namjun Kim, Y.-M. Kim, E. J. King, P. J. King, D. L. Kinzel, J. S. Kissel, L. Kleybolte, S. Klimenko, S. M. Koehlenbeck, K. Kokeyama, S. Koley, V. Kondrashov, A. Kontos, S. Koranda, M. Korobko, W. Z. Korth, I. Kowalska, D. B. Kozak, V. Kringel, B. Krishnan, A. Królak, C. Krueger, G. Kuehn, P. Kumar, R. Kumar, L. Kuo, A. Kutynia, P. Kwee, B. D. Lackey, M. Landry, J. Lange, B. Lantz, P. D. Lasky, A. Lazzarini, C. Lazzaro, P. Leaci, S. Leavey, E. O. Lebigot, C. H. Lee, H. K. Lee, H. M. Lee, K. Lee, A. Lenon, M. Leonardi, J. R. Leong, N. Leroy, N. Letendre, Y. Levin, B. M. Levine, T. G. F. Li, A. Libson, T. B. Littenberg, N. A. Lockerbie, J. Logue, A. L. Lombardi, L. T. London, J. E. Lord, M. Lorenzini, V. Loriette, M. Lormand, G. Losurdo, J. D. Lough, C. O. Lousto, G. Lovelace, H. Lück, A. P. Lundgren, J. Luo, R. Lynch, Y. Ma, T. MacDonald, B. Machenschalk, M. MacInnis, D. M. Macleod, F. Magaña-Sandoval, R. M. Magee, M. Mageswaran, E. Majorana, I. Maksimovic, V. Malvezzi, N. Man, I. Mandel, V. Mandic, V. Mangano, G. L. Mansell, M. Manske, M. Mantovani, F. Marchesoni, F. Marion, S. Márka, Z. Márka, A. S. Markosyan, E. Maros, F. Martelli, L. Martellini, I. W. Martin, R. M. Martin, D. V. Martynov, J. N. Marx, K. Mason, A. Masserot, T. J. Massinger, M. Masso-Reid, F. Matichard, L. Matone, N. Mavalvala, N. Mazumder, G. Mazzolo, R. McCarthy, D. E. McClelland, S. McCormick, S. C. McGuire, G. McIntyre, J. McIver, D. J. McManus, S. T. McWilliams, D. Meacher, G. D. Meadors, J. Meidam, A. Melatos, G. Mendell, D. Mendoza-Gandara, R. A. Mercer, E. Merilh, M. Merzougui, S. Meshkov, C. Messenger, C. Messick, P. M. Meyers, F. Mezzani, H. Miao, C. Michel, H. Middleton, E. E. Mikhailov, L. Milano, J. Miller, M. Millhouse, Y. Minenkov, J. Ming, S. Mirshekari, C. Mishra, S. Mitra, V. P. Mitrofanov, G. Mitselmakher, R. Mittleman, A. Moggi, M. Mohan, S. R. P. Mohapatra, M. Montani, B. C. Moore, C. J. Moore, D. Moraru, G. Moreno, S. R. Morriss, K. Mossavi, B. Mours, C. M. Mow-Lowry, C. L. Mueller, G. Mueller, A. W. Muir, Arunava Mukherjee, D. Mukherjee, S. Mukherjee, N. Mukund, A. Mullavey, J. Munch, D. J. Murphy, P. G. Murray, A. Mytidis, I. Nardecchia, L. Naticchioni, R. K. Nayak, V. Necula, K. Nedkova, G. Nelemans, M. Neri, A. Neunzert, G. Newton, T. T. Nguyen, A. B. Nielsen, S. Nissanke, A. Nitz, F. Nocera, D. Nolting, M. E. N. Normandin, L. K. Nuttall, J. Oberling, E. Ochsner, J. O'Dell, E. Oelker, G. H. Ogin, J. J. Oh, S. H. Oh, F. Ohme, M. Oliver, P. Oppermann, Richard J. Oram, B. O'Reilly, R. O'Shaughnessy, C. D. Ott, D. J. Ottaway, R. S. Ottens, H. Overmier, B. J. Owen, A. Pai, S. A. Pai, J. R. Palamos, O. Palashov, C. Palomba, A. Pal-Singh, H. Pan, Y. Pan, C. Pankow, F. Pannarale, B. C. Pant, F. Paoletti, A. Paoli, M. A. Papa, H. R. Paris, W. Parker, D. Pascucci, A. Pasqualetti, R. Passaquieti, D. Passuello, B. Patricelli, Z. Patrick, B. L. Pearlstone, M. Pedraza, R. Pedurand, L. Pekowsky, A. Pele, S. Penn, A. Perreca, H. P. Pfeiffer, M. Phelps, O. Piccinni, M. Pichot, M. Pickenpack, F. Piergiovanni, V. Pierro, G. Pillant, L. Pinard, I. M. Pinto, M. Pitkin, J. H. Poeld, R. Poggiani, P. Popolizio, A. Post, J. Powell, J. Prasad, V. Predoi, S. S. Premachandra, T. Prestegard, L. R. Price, M. Prijatelj, M. Principe, S. Privitera, R. Prix, G. A. Prodi, L. Prokhorov, O. Puncken, M. Punturo, P. Puppo, M. Pürrer, H. Qi, J. Qin, V. Quetschke, E. A. Quintero, R. Quitzow-James, F. J. Raab, D. S. Rabeling, H. Radkins, P. Raffai, S. Raja, M. Rakhmanov, C. R.

Ramet, P. Rapagnani, V. Raymond, M. Razzano, V. Re, J. Read, C. M. Reed, T. Regimbau, L. Rei, S. Reid, D. H. Reitze, H. Rew, S. D. Reyes, F. Ricci, K. Riles, N. A. Robertson, R. Robie, F. Robinet, A. Rocchi, L. Rolland, J. G. Rollins, V. J. Roma, J. D. Romano, R. Romano, G. Romanov, J. H. Romie, D. Rosiıfmmode \acuten\else ń\fiska, S. Rowan, A. Rüdiger, P. Ruggi, K. Ryan, S. Sachdev, T. Sadecki, L. Sadeghian, L. Salconi, M. Saleem, F. Salemi, A. Samajdar, L. Sammut, L. M. Sampson, E. J. Sanchez, V. Sandberg, B. Sandeen, G. H. Sanders, J. R. Sanders, B. Sassolas, B. S. Sathyaprakash, P. R. Saulson, O. Sauter, R. L. Savage, A. Sawadsky, P. Schale, R. Schilling, J. Schmidt, P. Schmidt, R. Schnabel, R. M. S. Schofield, A. Schönbeck, E. Schreiber, D. Schuette, B. F. Schutz, J. Scott, S. M. Scott, D. Sellers, A. S. Sengupta, D. Sentenac, V. Sequino, A. Sergeev, G. Serna, Y. Setyawati, A. Sevigny, D. A. Shaddock, T. Shaffer, S. Shah, M. S. Shahriar, M. Shaltev, Z. Shao, B. Shapiro, P. Shawhan, A. Sheperd, D. H. Shoemaker, D. M. Shoemaker, K. Siellez, X. Siemens, D. Sigg, A. D. Silva, D. Simakov, A. Singer, L. P. Singer, A. Singh, R. Singh, A. Singhal, A. M. Sintes, B. J. J. Slagmolen, J. R. Smith, M. R. Smith, N. D. Smith, R. J. E. Smith, E. J. Son, B. Sorazu, F. Sorrentino, T. Souradeep, A. K. Srivastava, A. Staley, M. Steinke, J. Steinlechner, S. Steinlechner, D. Steinmeyer, B. C. Stephens, S. P. Stevenson, R. Stone, K. A. Strain, N. Straniero, G. Stratta, N. A. Strauss, S. Strigin, R. Sturani, A. L. Stuver, T. Z. Summerscales, L. Sun, P. J. Sutton, B. L. Swinkels, M. J. Szczepaıfmmode \acuten\else ń\ficzyk, M. Tacca, D. Talukder, D. B. Tanner, M. Tápai, S. P. Tarabrin, A. Taracchini, R. Taylor, T. Theeg, M. P. Thirugnanasambandam, E. G. Thomas, M. Thomas, P. Thomas, K. A. Thorne, K. S. Thorne, E. Thrane, S. Tiwari, V. Tiwari, K. V. Tokmakov, C. Tomlinson, M. Tonelli, C. V. Torres, C. I. Torrie, D. Töyrä, F. Travasso, G. Traylor, D. Trifirò, M. C. Tringali, L. Trozzo, M. Tse, M. Turconi, D. Tuyenbayev, D. Ugolini, C. S. Unnikrishnan, A. L. Urban, S. A. Usman, H. Vahlbruch, G. Vajente, G. Valdes, M. Vallisneri, N. van Bakel, M. van Beuzekom, J. F. J. van den Brand, C. Van Den Broeck, D. C. Vander-Hyde, L. van der Schaaf, J. V. van Heijningen, A. A. van Veggel, M. Vardaro, S. Vass, M. Vasúth, R. Vaulin, A. Vecchio, G. Vedovato, J. Veitch, P. J. Veitch, K. Venkateswara, D. Verkindt, F. Vetrano, A. Viceré, S. Vinciguerra, D. J. Vine, J.-Y. Vinet, S. Vitale, T. Vo, H. Vocca, C. Vorvick, D. Voss, W. D. Vousden, S. P. Vyatchanin, A. R. Wade, L. E. Wade, M. Wade, S. J. Waldman, M. Walker, L. Wallace, S. Walsh, G. Wang, H. Wang, M. Wang, X. Wang, Y. Wang, H. Ward, R. L. Ward, J. Warner, M. Was, B. Weaver, L.-W. Wei, M. Weinert, A. J. Weinstein, R. Weiss, T. Welborn, L. Wen, P. Weßels, T. Westphal, K. Wette, J. T. Whelan, S. E. Whitcomb, D. J. White, B. F. Whiting, K. Wiesner, C. Wilkinson, P. A. Willems, L. Williams, R. D. Williams, A. R. Williamson, J. L. Willis, B. Willke, M. H. Wimmer, L. Winkelmann, W. Winkler, C. C. Wipf, A. G. Wiseman, H. Wittel, G. Woan, J. Worden, J. L. Wright, G. Wu, J. Yablon, I. Yakushin, W. Yam, H. Yamamoto, C. C. Yancey, M. J. Yap, H. Yu, M. Yvert, A. Zadroıfmmode \dotz\else \.z\finy, L. Zangrando, M. Zanolin, J.-P. Zendri, M. Zevin, F. Zhang, L. Zhang, M. Zhang, Y. Zhang, C. Zhao, M. Zhou, Z. Zhou, X. J. Zhu, M. E. Zucker, S. E. Zuraw, and J. Zweizig. Observation of Gravitational Waves from a Binary Black Hole Merger. Phys. Rev. Lett., 116(6):061102, February 2016. Publisher: American Physical Society.

[4] P. A. R. Ade, Z. Ahmed, M. Amiri, D. Barkats, R. Basu Thakur, C. A. Bischoff, D. Beck, J. J. Bock, H. Boenish, E. Bullock, V. Buza, J. R. Cheshire Iv, J. Connors, J. Cornelison, M. Crumrine, A. Cukierman, E. V. Denison, M. Dierickx, L. Duband, M. Eiben, S. Fatigoni, J. P. Filippini, S. Fliescher, N. Goeckner-Wald, D. C. Goldfinger, J. Grayson, P. Grimes, G. Hall, G. Halal, M. Halpern, E. Hand, S. Harrison, S. Henderson, S. R. Hildebrandt,

G. C. Hilton, J. Hubmayr, H. Hui, K. D. Irwin, J. Kang, K. S. Karkare, E. Karpel, S. Kefeli, S. A. Kernasovskiy, J. M. Kovac, C. L. Kuo, K. Lau, E. M. Leitch, A. Lennox, K. G. Megerian, L. Minutolo, L. Moncelsi, Y. Nakato, T. Namikawa, H. T. Nguyen, R. O'Brient, R. W. Ogburn Iv, S. Palladino, T. Prouve, C. Pryke, B. Racine, C. D. Reintsema, S. Richter, A. Schillaci, R. Schwarz, B. L. Schmitt, C. D. Sheehy, A. Soliman, T. St. Germaine, B. Steinbach, R. V. Sudiwala, G. P. Teply, K. L. Thompson, J. E. Tolan, C. Tucker, A. D. Turner, C. Umiltà, C. Vergès, A. G. Vieregg, A. Wandui, A. C. Weber, D. V. Wiebe, J. Willmert, C. L. Wong, W. L. K. Wu, H. Yang, K. W. Yoon, E. Young, C. Yu, L. Zeng, C. Zhang, S. Zhang, and (Bicep /Keck Collaboration). Bicep/Keck XV: The Bicep3 Cosmic Microwave Background Polarimeter and the First Three-year Data Set. The Astrophysical Journal, 927(1):77, March 2022.

[5] P.A.R. Ade, Z. Ahmed, M. Amiri, D. Barkats, R. Basu Thakur, C.A. Bischoff, D. Beck, J.J. Bock, H. Boenish, E. Bullock, V. Buza, J.R. Cheshire, J. Connors, J. Cornelison, M. Crumrine, A. Cukierman, E.V. Denison, M. Dierickx, L. Duband, M. Eiben, S. Fatigoni, J.P. Filippini, S. Fliescher, N. Goeckner-Wald, D.C. Goldfinger, J. Grayson, P. Grimes, G. Hall, G. Halal, M. Halpern, E. Hand, S. Harrison, S. Henderson, S.R. Hildebrandt, G.C. Hilton, J. Hubmayr, H. Hui, K.D. Irwin, J. Kang, K.S. Karkare, E. Karpel, S. Kefeli, S.A. Kernasovskiy, J.M. Kovac, C.L. Kuo, K. Lau, E.M. Leitch, A. Lennox, K.G. Megerian, L. Minutolo, L. Moncelsi, Y. Nakato, T. Namikawa, H.T. Nguyen, R. O'Brient, R.W. Ogburn, S. Palladino, T. Prouve, C. Pryke, B. Racine, C.D. Reintsema, S. Richter, A. Schillaci, R. Schwarz, B.L. Schmitt, C.D. Sheehy, A. Soliman, T.St. Germaine, B. Steinbach, R.V. Sudiwala, G.P. Teply, K.L. Thompson, J.E. Tolan, C. Tucker, A.D. Turner, C. Umiltà, C. Vergès, A.G. Vieregg, A. Wandui, A.C. Weber, D.V. Wiebe, J. Willmert, C.L. Wong, W.L.K. Wu, H. Yang, K.W. Yoon, E. Young, C. Yu, L. Zeng, C. Zhang, S. Zhang, and BICEP/*Keck* Collaboration. Improved Constraints on Primordial Gravitational Waves using *Planck* , WMAP, and BICEP/ *Keck* Observations through the 2018 Observing Season. Physical Review Letters, 127(15):151301, October 2021.

[6] Adeela Afzal, Gabriella Agazie, Akash Anumarlapudi, Anne M. Archibald, Zaven Arzoumanian, Paul T. Baker, Bence Bécsy, Jose Juan Blanco-Pillado, Laura Blecha, Kimberly K. Boddy, Adam Brazier, Paul R. Brook, Sarah Burke-Spolaor, Rand Burnette, Robin Case, Maria Charisi, Shami Chatterjee, Katerina Chatziioannou, Belinda D. Cheeseboro, Siyuan Chen, Tyler Cohen, James M. Cordes, Neil J. Cornish, Fronefield Crawford, H. Thankful Cromartie, Kathryn Crowter, Curt J. Cutler, Megan E. DeCesar, Dallas DeGan, Paul B. Demorest, Heling Deng, Timothy Dolch, Brendan Drachler, Richard Von Eckardstein, Elizabeth C. Ferrara, William Fiore, Emmanuel Fonseca, Gabriel E. Freedman, Nate Garver-Daniels, Peter A. Gentile, Kyle A. Gersbach, Joseph Glaser, Deborah C. Good, Lydia Guertin, Kayhan Gültekin, Jeffrey S. Hazboun, Sophie Hourihane, Kristina Islo, Ross J. Jennings, Aaron D. Johnson, Megan L. Jones, Andrew R. Kaiser, David L. Kaplan, Luke Zoltan Kelley, Matthew Kerr, Joey S. Key, Nima Laal, Michael T. Lam, William G. Lamb, T. Joseph W. Lazio, Vincent S. H. Lee, Natalia Lewandowska, Rafael R. Lino Dos Santos, Tyson B. Littenberg, Tingting Liu, Duncan R. Lorimer, Jing Luo, Ryan S. Lynch, Chung-Pei Ma, Dustin R. Madison, Alexander McEwen, James W. McKee, Maura A. McLaughlin, Natasha McMann, Bradley W. Meyers, Patrick M. Meyers, Chiara M. F. Mingarelli, Andrea Mitridate, Jonathan Nay, Priyamvada Natarajan, Cherry Ng, David J. Nice, Stella Koch Ocker, Ken D. Olum, Timothy T. Pennucci, Benetge B. P. Perera, Polina Petrov, Nihan S. Pol, Henri A. Radovan, Scott M. Ransom, Paul S. Ray, Joseph D. Romano, Shashwat C. Sarde-

sai, Ann Schmiedekamp, Carl Schmiedekamp, Kai Schmitz, Tobias Schröder, Levi Schult, Brent J. Shapiro-Albert, Xavier Siemens, Joseph Simon, Magdalena S. Siwek, Ingrid H. Stairs, Daniel R. Stinebring, Kevin Stovall, Peter Stratmann, Jerry P. Sun, Abhimanyu Susobhanan, Joseph K. Swiggum, Jacob Taylor, Stephen R. Taylor, Tanner Trickle, Jacob E. Turner, Caner Unal, Michele Vallisneri, Sonali Verma, Sarah J. Vigeland, Haley M. Wahl, Qiaohong Wang, Caitlin A. Witt, David Wright, Olivia Young, Kathryn M. Zurek, and The NANOGrav Collaboration. The NANOGrav 15 yr Data Set: Search for Signals from New Physics. The Astrophysical Journal Letters, 951(1):L11, July 2023.

[7] Gabriella Agazie, Akash Anumarlapudi, Anne M. Archibald, Zaven Arzoumanian, Paul T. Baker, Bence Bécsy, Laura Blecha, Adam Brazier, Paul R. Brook, Sarah Burke-Spolaor, Rand Burnette, Robin Case, Maria Charisi, Shami Chatterjee, Katerina Chatziioannou, Belinda D. Cheeseboro, Siyuan Chen, Tyler Cohen, James M. Cordes, Neil J. Cornish, Fronefield Crawford, H. Thankful Cromartie, Kathryn Crowter, Curt J. Cutler, Megan E. DeCesar, Dallas DeGan, Paul B. Demorest, Heling Deng, Timothy Dolch, Brendan Drachler, Justin A. Ellis, Elizabeth C. Ferrara, William Fiore, Emmanuel Fonseca, Gabriel E. Freedman, Nate Garver-Daniels, Peter A. Gentile, Kyle A. Gersbach, Joseph Glaser, Deborah C. Good, Kayhan Gültekin, Jeffrey S. Hazboun, Sophie Hourihane, Kristina Islo, Ross J. Jennings, Aaron D. Johnson, Megan L. Jones, Andrew R. Kaiser, David L. Kaplan, Luke Zoltan Kelley, Matthew Kerr, Joey S. Key, Tonia C. Klein, Nima Laal, Michael T. Lam, William G. Lamb, T. Joseph W. Lazio, Natalia Lewandowska, Tyson B. Littenberg, Tingting Liu, Andrea Lommen, Duncan R. Lorimer, Jing Luo, Ryan S. Lynch, Chung-Pei Ma, Dustin R. Madison, Margaret A. Mattson, Alexander McEwen, James W. McKee, Maura A. McLaughlin, Natasha McMann, Bradley W. Meyers, Patrick M. Meyers, Chiara M. F. Mingarelli, Andrea Mitridate, Priyamvada Natarajan, Cherry Ng, David J. Nice, Stella Koch Ocker, Ken D. Olum, Timothy T. Pennucci, Benetge B. P. Perera, Polina Petrov, Nihan S. Pol, Henri A. Radovan, Scott M. Ransom, Paul S. Ray, Joseph D. Romano, Shashwat C. Sardesai, Ann Schmiedekamp, Carl Schmiedekamp, Kai Schmitz, Levi Schult, Brent J. Shapiro-Albert, Xavier Siemens, Joseph Simon, Magdalena S. Siwek, Ingrid H. Stairs, Daniel R. Stinebring, Kevin Stovall, Jerry P. Sun, Abhimanyu Susobhanan, Joseph K. Swiggum, Jacob Taylor, Stephen R. Taylor, Jacob E. Turner, Caner Unal, Michele Vallisneri, Rutger Van Haasteren, Sarah J. Vigeland, Haley M. Wahl, Qiaohong Wang, Caitlin A. Witt, Olivia Young, and The NANOGrav Collaboration. The NANOGrav 15 yr Data Set: Evidence for a Gravitational-wave Background. The Astrophysical Journal Letters, 951(1):L8, July 2023.

[8] Gabriella Agazie, Akash Anumarlapudi, Anne M. Archibald, Paul T. Baker, Bence Bécsy, Laura Blecha, Alexander Bonilla, Adam Brazier, Paul R. Brook, Sarah Burke-Spolaor, Rand Burnette, Robin Case, J. Andrew Casey-Clyde, Maria Charisi, Shami Chatterjee, Katerina Chatziioannou, Belinda D. Cheeseboro, Siyuan Chen, Tyler Cohen, James M. Cordes, Neil J. Cornish, Fronefield Crawford, H. Thankful Cromartie, Kathryn Crowter, Curt J. Cutler, Daniel J. D'Orazio, Megan E. DeCesar, Dallas DeGan, Paul B. Demorest, Heling Deng, Timothy Dolch, Brendan Drachler, Elizabeth C. Ferrara, William Fiore, Emmanuel Fonseca, Gabriel E. Freedman, Emiko Gardiner, Nate Garver-Daniels, Peter A. Gentile, Kyle A. Gersbach, Joseph Glaser, Deborah C. Good, Kayhan Gültekin, Jeffrey S. Hazboun, Sophie Hourihane, Kristina Islo, Ross J. Jennings, Aaron Johnson, Megan L. Jones, Andrew R. Kaiser, David L. Kaplan, Luke Zoltan Kelley, Matthew Kerr, Joey S. Key, Nima Laal, Michael T. Lam, William G. Lamb, T. Joseph W. Lazio, Natalia Lewandowska, Tyson B. Littenberg, Tingting Liu, Jing Luo, Ryan S. Lynch, Chung-Pei Ma, Dustin R. Madison, Alexander

McEwen, James W. McKee, Maura A. McLaughlin, Natasha McMann, Bradley W. Meyers, Patrick M. Meyers, Chiara M. F. Mingarelli, Andrea Mitridate, Priyamvada Natarajan, Cherry Ng, David J. Nice, Stella Koch Ocker, Ken D. Olum, Timothy T. Pennucci, Benetge B. P. Perera, Polina Petrov, Nihan S. Pol, Henri A. Radovan, Scott M. Ransom, Paul S. Ray, Joseph D. Romano, Jessie C. Runnoe, Shashwat C. Sardesai, Ann Schmiedekamp, Carl Schmiedekamp, Kai Schmitz, Levi Schult, Brent J. Shapiro-Albert, Xavier Siemens, Joseph Simon, Magdalena S. Siwek, Ingrid H. Stairs, Daniel R. Stinebring, Kevin Stovall, Jerry P. Sun, Abhimanyu Susobhanan, Joseph K. Swiggum, Jacob Taylor, Stephen R. Taylor, Jacob E. Turner, Caner Unal, Michele Vallisneri, Sarah J. Vigeland, Jeremy M. Wachter, Haley M. Wahl, Qiaohong Wang, Caitlin A. Witt, David Wright, Olivia Young, and The NANOGrav Collaboration. The NANOGrav 15 yr Data Set: Constraints on Supermassive Black Hole Binaries from the Gravitational-wave Background. The Astrophysical Journal Letters, 952(2):L37, August 2023.

[9] N. Aghanim, Y. Akrami, M. Ashdown, J. Aumont, C. Baccigalupi, M. Ballardini, A. J. Banday, R. B. Barreiro, N. Bartolo, S. Basak, R. Battye, K. Benabed, J.-P. Bernard, M. Bersanelli, P. Bielewicz, J. J. Bock, J. R. Bond, J. Borrill, F. R. Bouchet, F. Boulanger, M. Bucher, C. Burigana, R. C. Butler, E. Calabrese, J.-F. Cardoso, J. Carron, A. Challinor, H. C. Chiang, J. Chluba, L. P. L. Colombo, C. Combet, D. Contreras, B. P. Crill, F. Cuttaia, P. de Bernardis, G. de Zotti, J. Delabrouille, J.-M. Delouis, E. Di Valentino, J. M. Diego, O. Doré, M. Douspis, A. Ducout, X. Dupac, S. Dusini, G. Efstathiou, F. Elsner, T. A. Enßlin, H. K. Eriksen, Y. Fantaye, M. Farhang, J. Fergusson, R. Fernandez-Cobos, F. Finelli, F. Forastieri, M. Frailis, A. A. Fraisse, E. Franceschi, A. Frolov, S. Galeotta, S. Galli, K. Ganga, R. T. Génova-Santos, M. Gerbino, T. Ghosh, J. González-Nuevo, K. M. Górski, S. Gratton, A. Gruppuso, J. E. Gudmundsson, J. Hamann, W. Handley, F. K. Hansen, D. Herranz, S. R. Hildebrandt, E. Hivon, Z. Huang, A. H. Jaffe, W. C. Jones, A. Karakci, E. Keihänen, R. Keskitalo, K. Kiiveri, J. Kim, T. S. Kisner, L. Knox, N. Krachmalnicoff, M. Kunz, H. Kurki-Suonio, G. Lagache, J.-M. Lamarre, A. Lasenby, M. Lattanzi, C. R. Lawrence, M. Le Jeune, P. Lemos, J. Lesgourgues, F. Levrier, A. Lewis, M. Liguori, P. B. Lilje, M. Lilley, V. Lindholm, M. López-Caniego, P. M. Lubin, Y.-Z. Ma, J. F. Macías-Pérez, G. Maggio, D. Maino, N. Mandolesi, A. Mangilli, A. Marcos-Caballero, M. Maris, P. G. Martin, M. Martinelli, E. Martínez-González, S. Matarrese, N. Mauri, J. D. McEwen, P. R. Meinhold, A. Melchiorri, A. Mennella, M. Migliaccio, M. Millea, S. Mitra, M.-A. Miville-Deschênes, D. Molinari, L. Montier, G. Morgante, A. Moss, P. Natoli, H. U. Nørgaard-Nielsen, L. Pagano, D. Paoletti, B. Partridge, G. Patanchon, H. V. Peiris, F. Perrotta, V. Pettorino, F. Piacentini, L. Polastri, G. Polenta, J.-L. Puget, J. P. Rachen, M. Reinecke, M. Remazeilles, A. Renzi, G. Rocha, C. Rosset, G. Roudier, J. A. Rubiño-Martín, B. Ruiz-Granados, L. Salvati, M. Sandri, M. Savelainen, D. Scott, E. P. S. Shellard, C. Sirignano, G. Sirri, L. D. Spencer, R. Sunyaev, A.-S. Suur-Uski, J. A. Tauber, D. Tavagnacco, M. Tenti, L. Toffolatti, M. Tomasi, T. Trombetti, L. Valenziano, J. Valiviita, B. Van Tent, L. Vibert, P. Vielva, F. Villa, N. Vittorio, B. D. Wandelt, I. K. Wehus, M. White, S. D. M. White, A. Zacchei, and A. Zonca. Planck 2018 results - VI. Cosmological parameters. Astronomy & Astrophysics, 641:A6, September 2020. Publisher: EDP Sciences.

[10] A. C. Anderson and S. C. Smith. Effect of dislocations on the lattice thermal conductivity of superconducting niobium. Journal of Physics and Chemistry of Solids, 34(1):111–122, January 1973.

[11] Z. Arzoumanian, A. Brazier, S. Burke-Spolaor, S. J. Chamberlin, S. Chatterjee, B. Christy, J. M. Cordes, N. J. Cornish, K. Crowter, P. B. Demorest, X. Deng, T. Dolch, J. A. Ellis, R. D. Ferdman, E. Fonseca, N. Garver-Daniels, M. E. Gonzalez, F. Jenet, G. Jones, M. L. Jones, V. M. Kaspi, M. Koop, M. T. Lam, T. J. W. Lazio, L. Levin, A. N. Lommen, D. R. Lorimer, J. Luo, R. S. Lynch, D. R. Madison, M. A. McLaughlin, S. T. McWilliams, C. M. F. Mingarelli, D. J. Nice, N. Palliyaguru, T. T. Pennucci, S. M. Ransom, L. Sampson, S. A. Sanidas, A. Sesana, X. Siemens, J. Simon, I. H. Stairs, D. R. Stinebring, K. Stovall, J. Swiggum, S. R. Taylor, M. Vallisneri, R. Van Haasteren, Y. Wang, W. W. Zhu, and (The NANOGrav Collaboration). THE NANOGRAV NINE-YEAR DATA SET: LIMITS ON THE ISOTROPIC STOCHASTIC GRAVITATIONAL WAVE BACKGROUND. The Astrophysical Journal, 821(1):13, April 2016.

[12] B. A. Auld. Acoustic fields and waves in solids. , 1973.

[13] D.V. Averin and K.K. Likharev. Single Electronics: A Correlated Transfer of Single Electrons and Cooper Pairs in Systems of Small Tunnel Junctions. In Modern Problems in Condensed Matter Sciences, volume 30, pages 173–271. Elsevier, 1991.

[14] L. Balkenhol, D. Dutcher, A. Spurio Mancini, A. Doussot, K. Benabed, S. Galli, P.A.R. Ade, A.J. Anderson, B. Ansarinejad, M. Archipley, A.N. Bender, B.A. Benson, F. Bianchini, L.E. Bleem, F.R. Bouchet, L. Bryant, E. Camphuis, J.E. Carlstrom, T.W. Cecil, C.L. Chang, P. Chaubal, P.M. Chichura, T.-L. Chou, A. Coerver, T.M. Crawford, A. Cukierman, C. Daley, T. De Haan, K.R. Dibert, M.A. Dobbs, W. Everett, C. Feng, K.R. Ferguson, A. Foster, A.E. Gambrel, R.W. Gardner, N. Goeckner-Wald, R. Gualtieri, F. Guidi, S. Guns, N.W. Halverson, E. Hivon, G.P. Holder, W.L. Holzapfel, J.C. Hood, N. Huang, L. Knox, M. Korman, C.-L. Kuo, A.T. Lee, A.E. Lowitz, C. Lu, M. Millea, J. Montgomery, Y. Nakato, T. Natoli, G.I. Noble, V. Novosad, Y. Omori, S. Padin, Z. Pan, P. Paschos, K. Prabhu, W. Quan, M. Rahimi, A. Rahlin, C.L. Reichardt, M. Rouble, J.E. Ruhl, E. Schiappucci, G. Smecher, J.A. Sobrin, A.A. Stark, J. Stephen, A. Suzuki, C. Tandoi, K.L. Thompson, B. Thorne, C. Tucker, C. Umilta, J.D. Vieira, G. Wang, N. Whitehorn, W.L.K. Wu, V. Yefremenko, M.R. Young, J.A. Zebrowski, and SPT-3G Collaboration. Measurement of the CMB temperature power spectrum and constraints on cosmology from the SPT-3G 2018 T T , T E , and E E dataset. Physical Review D, 108(2):023510, July 2023.

[15] Didier Barret, Thien Lam Trong, Jan-Willem den Herder, Luigi Piro, Xavier Barcons, Juhani Huovelin, Richard Kelley, J. Miguel Mas-Hesse, Kazuhisa Mitsuda, Stéphane Paltani, Gregor Rauw, Agata Rożanska, Joern Wilms, Marco Barbera, Enrico Bozzo, Maria Teresa Ceballos, Ivan Charles, Anne Decourchelle, Roland den Hartog, Jean-Marc Duval, Fabrizio Fiore, Flavio Gatti, Andrea Goldwurm, Brian Jackson, Peter Jonker, Caroline Kilbourne, Claudio Macculi, Mariano Mendez, Silvano Molendi, Piotr Orleanski, François Pajot, Etienne Pointecouteau, Frederick Porter, Gabriel W. Pratt, Damien Prêle, Laurent Ravera, Etienne Renotte, Joop Schaye, Keisuke Shinozaki, Luca Valenziano, Jacco Vink, Natalie Webb, Noriko Yamasaki, Françoise Delcelier-Douchin, Michel Le Du, Jean-Michel Mesnager, Alice Pradines, Graziella Branduardi-Raymont, Mauro Dadina, Alexis Finoguenov, Yasushi Fukazawa, Agnieszka Janiuk, Jon Miller, Yaël Nazé, Fabrizio Nicastro, Salvatore Sciortino, Jose Miguel Torrejon, Hervé Geoffray, Isabelle Hernandez, Laure Luno, Philippe Peille, Jérôme André, Christophe Daniel, Christophe Etcheverry, Emilie Gloaguen, Jérémie Hassin, Gilles Hervet, Irwin Maussang, Jérôme Moueza, Alexis Paillet, Bruno Vella, Gonzalo Campos Garrido, Jean-Charles

Damery, Chantal Panem, Johan Panh, Simon Bandler, Jean-Marc Biffi, Kevin Boyce, Antoine Clénet, Michael DiPirro, Pierre Jamotton, Simone Lotti, Denis Schwander, Stephen Smith, Bert-Joost van Leeuwen, Henk van Weers, Thorsten Brand, Beatriz Cobo, Thomas Dauser, Jelle de Plaa, and Edoardo Cucchetti. The Athena X-ray Integral Field Unit (X-IFU). In Space Telescopes and Instrumentation 2016: Ultraviolet to Gamma Ray, volume 9905, pages 714–754. SPIE, August 2016.

[16] M. C. Begelman, R. D. Blandford, and M. J. Rees. Massive black hole binaries in active galactic nuclei. Nature, 287(5780):307–309, September 1980. Publisher: Nature Publishing Group.

[17] Steven J. Benton. Taurus: a balloon-borne polarimeter for cosmic reionization and galactic dust. In Millimeter, Submillimeter, and Far-Infrared Detectors and Instrumentation for Astronomy XI, volume PC12190, page PC121900H. SPIE, August 2022.

[18] Mariangela Bernardi, Ravi K. Sheth, James Annis, Scott Burles, Daniel J. Eisenstein, Douglas P. Finkbeiner, David W. Hogg, Robert H. Lupton, David J. Schlegel, Mark SubbaRao, Neta A. Bahcall, John P. Blakeslee, J. Brinkmann, Francisco J. Castander, Andrew J. Connolly, István Csabai, Mamoru Doi, Masataka Fukugita, Joshua Frieman, Timothy Heckman, Gregory S. Hennessy, Željko Ivezić, G. R. Knapp, Don Q. Lamb, Timothy McKay, Jeffrey A. Munn, Robert Nichol, Sadanori Okamura, Donald P. Schneider, Aniruddha R. Thakar, and Donald G. York. Early-type Galaxies in the Sloan Digital Sky Survey. II. Correlations between Observables. The Astronomical Journal, 125(4):1849–1865, April 2003.

[19] Rachel Bezanson, Pieter G. van Dokkum, Marijn Franx, Gabriel B. Brammer, Jarle Brinchmann, Mariska Kriek, Ivo Labbé, Ryan F. Quadri, Hans-Walter Rix, Jesse van de Sande, Katherine E. Whitaker, and Rik J. Williams. Redshift Evolution of the Galaxy Velocity Dispersion Function. The Astrophysical Journal, 737(2):L31, July 2011. arXiv:1107.0972 [astro-ph].

[20] M. G. Blamire, E. C. G. Kirk, J. E. Evetts, and T. M. Klapwijk. Extreme critical-temperature enhancement of Al by tunneling in Nb/ AlO x /Al/ AlO x /Nb tunnel junctions. Physical Review Letters, 66(2):220–223, January 1991.

[21] Asa F. L. Bluck, J. Trevor Mendel, Sara L. Ellison, Jorge Moreno, Luc Simard, David R. Patton, and Else Starkenburg. Bulge mass is king: the dominant role of the bulge in determining the fraction of passive galaxies in the Sloan Digital Sky Survey. Monthly Notices of the Royal Astronomical Society, 441(1):599–629, June 2014.

[22] R.J. Bruls, H.T. Hintzen, G. De With, and R. Metselaar. The temperature dependence of the Young's modulus of MgSiN2, AlN and Si3N4. Journal of the European Ceramic Society, 21(3):263–268, March 2001.

[23] D. Burgarella, V. Buat, C. Gruppioni, O. Cucciati, S. Heinis, S. Berta, M. Béthermin, J. Bock, A. Cooray, J. S. Dunlop, D. Farrah, A. Franceschini, E. Le Floc'h, D. Lutz, B. Magnelli, R. Nordon, S. J. Oliver, M. J. Page, P. Popesso, F. Pozzi, L. Riguccini, M. Vaccari, and M. Viero. Herschel PEP/HerMES: the redshift evolution (0 z 4) of dust attenuation and of the total (UV+IR) star formation rate density. Astronomy & Astrophysics, 554:A70, June 2013. Publisher: EDP Sciences.

[24] Sarah Burke-Spolaor. Gravitational-Wave Detection and Astrophysics with Pulsar Timing Arrays, November 2015. arXiv:1511.07869 [astro-ph, physics:gr-qc].

[25] J. Burney, T. J. Bay, J. Barral, P. L. Brink, B. Cabrera, J. P. Castle, A. J. Miller, S. Nam, D. Rosenberg, R. W. Romani, and A. Tomada. Transition-edge sensor arrays for UV-optical-IR astrophysics. Nuclear Instruments and Methods in Physics Research Section A: Accelerators, Spectrometers, Detectors and Associated Equipment, 559(2):525–527, April 2006.

[26] J. D. N. Cheeke. THE KAPITZA RESISTANCE AND HEAT TRANSFER AT LOW TEMPERATURES. Le Journal de Physique Colloques, 31(C3):C3–129–C3–136, October 1970.

[27] C. C. Chi and John Clarke. Enhancement of the energy gap in superconducting aluminum by tunneling extraction of quasiparticles. Physical Review B, 20(11):4465–4473, December 1979.

[28] Steve K. Choi, Matthew Hasselfield, Shuay-Pwu Patty Ho, Brian Koopman, Marius Lungu, Maximilian H. Abitbol, Graeme E. Addison, Peter A. R. Ade, Simone Aiola, David Alonso, Mandana Amiri, Stefania Amodeo, Elio Angile, Jason E. Austermann, Taylor Baildon, Nick Battaglia, James A. Beall, Rachel Bean, Daniel T. Becker, J Richard Bond, Sarah Marie Bruno, Erminia Calabrese, Victoria Calafut, Luis E. Campusano, Felipe Carrero, Grace E. Chesmore, Hsiao-mei Cho, Susan E. Clark, Nicholas F. Cothard, Devin Crichton, Kevin T. Crowley, Omar Darwish, Rahul Datta, Edward V. Denison, Mark J. Devlin, Cody J. Duell, Shannon M. Duff, Adriaan J. Duivenvoorden, Jo Dunkley, Rolando Dünner, Thomas Essinger-Hileman, Max Fankhanel, Simone Ferraro, Anna E. Fox, Brittany Fuzia, Patricio A. Gallardo, Vera Gluscevic, Joseph E. Golec, Emily Grace, Megan Gralla, Yilun Guan, Kirsten Hall, Mark Halpern, Dongwon Han, Peter Hargrave, Shawn Henderson, Brandon Hensley, J. Colin Hill, Gene C. Hilton, Matt Hilton, Adam D. Hincks, Renée Hložek, Johannes Hubmayr, Kevin M. Huffenberger, John P. Hughes, Leopoldo Infante, Kent Irwin, Rebecca Jackson, Jeff Klein, Kenda Knowles, Arthur Kosowsky, Vincent Lakey, Dale Li, Yaqiong Li, Zack Li, Martine Lokken, Thibaut Louis, Amanda MacInnis, Mathew Madhavacheril, Felipe Maldonado, Maya Mallaby-Kay, Danica Marsden, Loïc Maurin, Jeff McMahon, Felipe Menanteau, Kavilan Moodley, Tim Morton, Sigurd Naess, Toshiya Namikawa, Federico Nati, Laura Newburgh, John P. Nibarger, Andrina Nicola, Michael D. Niemack, Michael R. Nolta, John Orlowski-Sherer, Lyman A. Page, Christine G. Pappas, Bruce Partridge, Phumlani Phakathi, Heather Prince, Roberto Puddu, Frank J. Qu, Jesus Rivera, Naomi Robertson, Felipe Rojas, Maria Salatino, Emmanuel Schaan, Alessandro Schillaci, Benjamin L. Schmitt, Neelima Sehgal, Blake D. Sherwin, Carlos Sierra, Jon Sievers, Cristobal Sifon, Precious Sikhosana, Sara Simon, David N. Spergel, Suzanne T. Staggs, Jason Stevens, Emilie Storer, Dhaneshwar D. Sunder, Eric R. Switzer, Ben Thorne, Robert Thornton, Hy Trac, Jesse Treu, Carole Tucker, Leila R. Vale, Alexander Van Engelen, Jeff Van Lanen, Eve M. Vavagiakis, Kasey Wagoner, Yuhan Wang, Jonathan T. Ward, Edward J. Wollack, Zhilei Xu, Fernando Zago, and Ningfeng Zhu. The Atacama Cosmology Telescope: a measurement of the Cosmic Microwave Background power spectra at 98 and 150 GHz. Journal of Cosmology and Astroparticle Physics, 2020(12):045–045, December 2020.

[29] Peter K. Day, Henry G. LeDuc, Benjamin A. Mazin, Anastasios Vayonakis, and Jonas Zmuidzinas. A broadband superconducting detector suitable for use in large arrays. Nature, 425(6960):817–821, October 2003. Publisher: Nature Publishing Group.

[30] P. J. de Visser, J. J. A. Baselmans, P. Diener, S. J. C. Yates, A. Endo, and T. M. Klapwijk. Generation-Recombination Noise: The Fundamental Sensitivity Limit for Kinetic Inductance Detectors. Journal of Low Temperature Physics, 167(3-4):335–340, May 2012.

[31] P. B. Demorest, R. D. Ferdman, M. E. Gonzalez, D. Nice, S. Ransom, I. H. Stairs, Z. Arzoumanian, A. Brazier, S. Burke-Spolaor, S. J. Chamberlin, J. M. Cordes, J. Ellis, L. S. Finn, P. Freire, S. Giampanis, F. Jenet, V. M. Kaspi, J. Lazio, A. N. Lommen, M. McLaughlin, N. Palliyaguru, D. Perrodin, R. M. Shannon, X. Siemens, D. Stinebring, J. Swiggum, and W. W. Zhu. LIMITS ON THE STOCHASTIC GRAVITATIONAL WAVE BACKGROUND FROM THE NORTH AMERICAN NANOHERTZ OBSERVATORY FOR GRAVITATIONAL WAVES. The Astrophysical Journal, 762(2):94, January 2013.

[32] H. Dole, G. Lagache, J.-L. Puget, K. I. Caputi, N. Fernández-Conde, E. Le Floc'h, C. Papovich, P. G. Pérez-González, G. H. Rieke, and M. Blaylock. The cosmic infrared background resolved by Spitzer - Contributions of mid-infrared galaxies to the far-infrared background. Astronomy & Astrophysics, 451(2):417–429, May 2006. Number: 2 Publisher: EDP Sciences.

[33] S. M. Duff, J. Austermann, J. A. Beall, D. Becker, R. Datta, P. A. Gallardo, S. W. Henderson, G. C. Hilton, S. P. Ho, J. Hubmayr, B. J. Koopman, D. Li, J. McMahon, F. Nati, M. D. Niemack, C. G. Pappas, M. Salatino, B. L. Schmitt, S. M. Simon, S. T. Staggs, J. R. Stevens, J. Van Lanen, E. M. Vavagiakis, J. T. Ward, and E. J. Wollack. Advanced ACTPol Multichroic Polarimeter Array Fabrication Process for 150 mm Wafers. Journal of Low Temperature Physics, 184(3-4):634–641, August 2016.

[34] Albert Einstein. Näherungsweise Integration der Feldgleichungen der Gravitation. Königlich Preußische Akademie der Wissenschaften (Berlin). Sitzungsberichte, 22:688–696, 1916.

[35] Duncan Farrah, Kimberly Ennico Smith, David Ardila, Charles M. Bradford, Michael Dipirro, Carl Ferkinhoff, Jason Glenn, Paul Goldsmith, David Leisawitz, Thomas Nikola, Naseem Rangwala, Stephen A. Rinehart, Johannes Staguhn, Michael Zemcov, Jonas Zmuidzinas, James Bartlett, Sean Carey, William J. Fischer, Julia Kamenetzky, Jeyhan Kartaltepe, Mark Lacy, Dariusz C. Lis, Lisa Locke, Enrique Lopez-Rodriguez, Meredith MacGregor, Elisabeth Mills, S. Harvey Moseley, Eric J. Murphy, Alan Rhodes, Matt Richter, Dimitra Rigopoulou, David Sanders, Ravi Sankrit, Giorgio Savini, John-David Smith, and Sabrina Stierwalt. Review: Far-Infrared Instrumentation and Technology Development for the Next Decade. Journal of Astronomical Telescopes, Instruments, and Systems, 5(02):1, April 2019. arXiv:1709.02389 [astro-ph, physics:physics].

[36] A. V. Feshchenko, O.-P. Saira, J. T. Peltonen, and J. P. Pekola. Thermal conductance of Nb thin films at sub-kelvin temperatures. Scientific Reports, 7(1):41728, March 2017.

[37] Jessica A. Gaskin, Douglas Swartz, Alexey A. Vikhlinin, Feryal Özel, Karen E. E. Gelmis, Jonathan W. Arenberg, Simon R. Bandler, Mark W. Bautz, Marta M. Civitani, Alexandra Dominguez, Megan E. Eckart, Abraham D. Falcone, Enectali Figueroa-Feliciano, Mark D. Freeman, Hans M. Günther, Keith A. Havey Jr, Ralf K. Heilmann, Kiranmayee Kilaru, Ralph P. Kraft, Kevin S. McCarley, Randall L. McEntaffer, Giovanni Pareschi, William R. Purcell, Paul B. Reid, Mark L. Schattenburg, Daniel A. Schwartz, Eric D. Schwartz Sr, Harvey D. Tananbaum, Grant R. Tremblay, William W. Zhang, and John A. Zuhone. Lynx X-Ray Observatory: an overview. Journal of Astronomical Telescopes, Instruments, and Systems, 5(2):021001, May 2019. Publisher: SPIE.

[38] Thomas Gerrits, Adriana Lita, Brice Calkins, and Sae Woo Nam. Superconducting Transition Edge Sensors for Quantum Optics. In Robert H. Hadfield and Göran Johansson, editors, Superconducting Devices in Quantum Optics, Quantum Science and Technology, pages 31–60. Springer International Publishing, Cham, 2016.

[39] Ivar Giaever. Electron Tunneling Between Two Superconductors. Physical Review Letters, 5(10):464–466, November 1960.

[40] Sunil R. Golwala and Enectali Figueroa-Feliciano. Novel Quantum Sensors for Light Dark Matter and Neutrino Detection. Annual Review of Nuclear and Particle Science, 72(1):419–446, 2022. _eprint: https://doi.org/10.1146/annurev-nucl-102020-112133.

[41] K. E. Gray and H. W. Willemsen. Inhomogeneous state of superconductors by intense tunnel injection of quasiparticles. Journal of Low Temperature Physics, 31(5):911–925, June 1978.

[42] D. Hanson, S. Hoover, A. Crites, P. A. R. Ade, K. A. Aird, J. E. Austermann, J. A. Beall, A. N. Bender, B. A. Benson, L. E. Bleem, J. J. Bock, J. E. Carlstrom, C. L. Chang, H. C. Chiang, H-M. Cho, A. Conley, T. M. Crawford, T. De Haan, M. A. Dobbs, W. Everett, J. Gallicchio, J. Gao, E. M. George, N. W. Halverson, N. Harrington, J. W. Henning, G. C. Hilton, G. P. Holder, W. L. Holzapfel, J. D. Hrubes, N. Huang, J. Hubmayr, K. D. Irwin, R. Keisler, L. Knox, A. T. Lee, E. Leitch, D. Li, C. Liang, D. Luong-Van, G. Marsden, J. J. McMahon, J. Mehl, S. S. Meyer, L. Mocanu, T. E. Montroy, T. Natoli, J. P. Nibarger, V. Novosad, S. Padin, C. Pryke, C. L. Reichardt, J. E. Ruhl, B. R. Saliwanchik, J. T. Sayre, K. K. Schaffer, B. Schulz, G. Smecher, A. A. Stark, K. T. Story, C. Tucker, K. Vanderlinde, J. D. Vieira, M. P. Viero, G. Wang, V. Yefremenko, O. Zahn, and M. Zemcov. Detection of B -Mode Polarization in the Cosmic Microwave Background with Data from the South Pole Telescope. Physical Review Letters, 111(14):141301, September 2013.

[43] Michaela Hirschmann, Rachel S. Somerville, Thorsten Naab, and Andreas Burkert. Origin of the antihierarchical growth of black holes: Antihierarchical growth of black holes. Monthly Notices of the Royal Astronomical Society, 426(1):237–257, October 2012.

[44] N. Huang, L. E. Bleem, B. Stalder, P. A. R. Ade, S. W. Allen, A. J. Anderson, J. E. Austermann, J. S. Avva, J. A. Beall, A. N. Bender, B. A. Benson, F. Bianchini, S. Bocquet, M. Brodwin, J. E. Carlstrom, C. L. Chang, H. C. Chiang, R. Citron, C. Corbett Moran, T. M. Crawford, A. T. Crites, T. de Haan, M. A. Dobbs, W. Everett, B. Floyd, J. Gallicchio, E. M. George, A. Gilbert, M. D. Gladders, S. Guns, N. Gupta, N. W. Halverson, N. Harrington, J. W. Henning, G. C. Hilton, G. P. Holder, W. L. Holzapfel, J. D. Hrubes, J. Hubmayr, K. D. Irwin, G. Khullar, L. Knox, A. T. Lee, D. Li, A. Lowitz, M. McDonald, J. J. McMahon, S. S. Meyer, L. M. Mocanu, J. Montgomery, A. Nadolski, T. Natoli, J. P. Nibarger, G. Noble, V. Novosad, S. Padin, S. Patil, C. Pryke, C. L. Reichardt, J. E. Ruhl, B. R. Saliwanchik, A. Saro, J. T. Sayre, K. K. Schaffer, K. Sharon, C. Sievers, G. Smecher, A. A. Stark, K. T. Story, C. Tucker, K. Vanderlinde, T. Veach, J. D. Vieira, G. Wang, N. Whitehorn, W. L. K. Wu, and V. Yefremenko. Galaxy Clusters Selected via the Sunyaev–Zel'dovich Effect in the SPTpol 100-square-degree Survey. The Astronomical Journal, 159(3):110, February 2020.

[45] Edwin P. Hubble. 105. Extra-Galactic Nebulae. In Kenneth R. Lang and Owen Gingerich, editors, A Source Book in Astronomy and Astrophysics, 1900–1975, pages 716–724. Harvard University Press, December 1979.

[46] Johannes Hubmayr, James A. Beall, Jason E. Austermann, Daniel T. Becker, Steven J. Benton, A. Stevie Bergman, J. Richard Bond, Sean Bryan, Shannon M. Duff, Adri J. Duivenvoorden, H. K. Eriksen, Jeffrey P. Filippini, A. Fraisse, Mathew Galloway, Anne E. Gambrel, K. Ganga, Arpi L. Grigorian, Riccardo Gualtieri, Jon E. Gudmundsson, John W. Hartley, M. Halpern, Gene C. Hilton, William C. Jones, Jeffrey J. McMahon, Lorenzo Moncelsi, Johanna M. Nagy, C. B. Netterfield, Benjamin Osherson, Ivan Padilla, Alexandra S. Rahlin, B. Racine, John Ruhl, T. M. Rudd, J. A. Shariff, J. D. Soler, Xue Song, Joel N. Ullom, Jeff Van Lanen, Michael R. Vissers, I. K. Wehus, Shyang Wen, D. V. Wiebe, and Edward Young. Design of 280 GHz feedhorn-coupled TES arrays for the balloon-borne polarimeter SPIDER. page 99140V, Edinburgh, United Kingdom, July 2016.

[47] K.D. Irwin and G.C. Hilton. Transition-Edge Sensors. In Christian Enss, editor, Cryogenic Particle Detection, Topics in Applied Physics, pages 63–150. Springer, Berlin, Heidelberg, 2005.

[48] Kris Johnson, M. N. Wybourne, and N. Perrin. Acoustic-mode coupling and electron heating in thin metal films. Physical Review B, 50(3):2035–2038, July 1994.

[49] Russell Johnston. Shedding Light on the Galaxy Luminosity Function. The Astronomy and Astrophysics Review, 19(1):41, December 2011. arXiv:1106.2039 [astro-ph].

[50] A. A. Joshi and A. Majumdar. Transient ballistic and diffusive phonon heat transport in thin films. Journal of Applied Physics, 74(1):31–39, July 1993.

[51] Marc Kamionkowski and Ely D. Kovetz. The Quest for B Modes from Inflationary Gravitational Waves. Annual Review of Astronomy and Astrophysics, 54(1):227–269, September 2016.

[52] M. Kenyon, P. K. Day, C. M. Bradford, J. J. Bock, and H. G. Leduc. Progress on background-limited membrane-isolated TES bolometers for far-IR/submillimeter spectroscopy. page 627508, Orlando, Florida , USA, June 2006.

[53] Charles Kittel. Introduction to Solid State Physics. Wiley, Hoboken, NJ, 8th ed edition, 2005.

[54] C. S. Kochanek, M. A. Pahre, E. E. Falco, J. P. Huchra, J. Mader, T H Jarrett, T Chester, R Cutri, and S E Schneider. THE K-BAND GALAXY LUMINOSITY FUNCTION. The Astronomical Journal, 108(2), 1994.

[55] John Kormendy and Luis C. Ho. Coevolution (Or Not) of Supermassive Black Holes and Host Galaxies. Annual Review of Astronomy and Astrophysics, 51(1):511–653, August 2013. arXiv:1304.7762 [astro-ph].

[56] J. M. Kovac, E. M. Leitch, C. Pryke, J. E. Carlstrom, N. W. Halverson, and W. L. Holzapfel. Detection of polarization in the cosmic microwave background using DASI. Nature, 420(6917):772–787, December 2002. Publisher: Nature Publishing Group.

[57] T. Kühn, D. V. Anghel, J. P. Pekola, M. Manninen, and Y. M. Galperin. Heat transport in ultrathin dielectric membranes and bridges. Physical Review B, 70(12):125425, September 2004.

[58] T. Kühn and I.J. Maasilta. Ballistic phonon transport in dielectric membranes. Nuclear Instruments and Methods in Physics Research Section A: Accelerators, Spectrometers, Detectors and Associated Equipment, 559(2):724–726, April 2006.

[59] Thomas Kühn. Phononic Transport in Dielectric Membranes. PhD thesis, University of Jyväskylä, Finland, 2007.

[60] David Leisawitz, Edward Amatucci, Lynn Allen, Jonathan Arenberg, Lee Armus, Cara Battersby, James Bauer, Ray Bell, Dominic Benford, Edward Bergin, Jeffrey T. Booth, Charles M. Bradford, Damon Bradley, Sean Carey, Ruth Carter, Asantha Cooray, James Corsetti, Larry Dewell, Michael DiPirro, Bret G. Drake, Matthew East, Kimberly Ennico, Greg Feller, Angel Flores, Jonathan Fortney, Zachary Granger, Thomas P. Greene, Joseph Howard, Tiffany Kataria, John S. Knight, Charles Lawrence, Paul Lightsey, John C. Mather, Margaret Meixner, Gary Melnick, Craig McMurtry, Stefanie Milam, Samuel H. Moseley, Desika Narayanan, Alison Nordt, Deborah Padgett, Klaus Pontoppidan, Alexandra Pope, Gerard Rafanelli, David C. Redding, George Rieke, Thomas Roellig, Itsuki Sakon, Carly Sandin, Karin Sandstrom, Anita Sengupta, Kartik Sheth, Lawrence M. Sokolsky, Johannes Staguhn, John Steeves, Kevin Stevenson, Kate Su, Joaquin Vieira, Cassandra Webster, Martina Wiedner, Edward L. Wright, Chi Wu, David Yanatsis, Jonas Zmuidzinas, and the Origins Space Telescope Mission Concept Study Team. Origins Space Telescope: trades and decisions leading to the baseline mission concept. Journal of Astronomical Telescopes, Instruments, and Systems, 7(01), March 2021.

[61] M. M. Leivo, J. P. Pekola, and D. V. Averin. Efficient Peltier refrigeration by a pair of normal metal/insulator/superconductor junctions. Applied Physics Letters, 68(14):1996–1998, April 1996.

[62] L. Lentati, S. R. Taylor, C. M. F. Mingarelli, A. Sesana, S. A. Sanidas, A. Vecchio, R. N. Caballero, K. J. Lee, R. Van Haasteren, S. Babak, C. G. Bassa, P. Brem, M. Burgay, D. J. Champion, I. Cognard, G. Desvignes, J. R. Gair, L. Guillemot, J. W. T. Hessels, G. H. Janssen, R. Karuppusamy, M. Kramer, A. Lassus, P. Lazarus, K. Liu, S. Osłowski, D. Perrodin, A. Petiteau, A. Possenti, M. B. Purver, P. A. Rosado, R. Smits, B. Stappers, G. Theureau, C. Tiburzi, and J. P. W. Verbiest. European Pulsar Timing Array limits on an isotropic stochastic gravitational-wave background. Monthly Notices of the Royal Astronomical Society, 453(3):2577–2599, November 2015.

[63] H. A. Leupold and H. A. Boorse. Superconducting and Normal Specific Heats of a Single Crystal of Niobium. Physical Review, 134(5A):A1322–A1328, June 1964.

[64] L.-J. Liu, R. M. J. Janssen, C. M. Bradford, S. Hailey-Dunsheath, J. Fu, J. P. Filippini, J. E. Aguirre, J. S. Bracks, A. J. Corso, C. Groppi, J. Hoh, R. P. Keenan, I. N. Lowe, D. P. Marrone, P. Mauskopf, R. Nie, J. Redford, I. Trumper, and J. D. Vieira. Design of The Kinetic Inductance Detector Based Focal Plane Assembly for The Terahertz Intensity Mapper. Journal of Low Temperature Physics, 209(5-6):953–961, December 2022. arXiv:2211.09351 [astro-ph, physics:physics].

[65] Thibaut Louis, Emily Grace, Matthew Hasselfield, Marius Lungu, Loïc Maurin, Graeme E. Addison, Peter A. R. Ade, Simone Aiola, Rupert Allison, Mandana Amiri, Elio Angile, Nicholas Battaglia, James A. Beall, Francesco De Bernardis, J Richard Bond, Joe Britton,

Erminia Calabrese, Hsiao-mei Cho, Steve K. Choi, Kevin Coughlin, Devin Crichton, Kevin Crowley, Rahul Datta, Mark J. Devlin, Simon R. Dicker, Joanna Dunkley, Rolando Dünner, Simone Ferraro, Anna E. Fox, Patricio Gallardo, Megan Gralla, Mark Halpern, Shawn Henderson, J. Colin Hill, Gene C. Hilton, Matt Hilton, Adam D. Hincks, Renée Hlozek, S.P. Patty Ho, Zhiqi Huang, Johannes Hubmayr, Kevin M. Huffenberger, John P. Hughes, Leopoldo Infante, Kent Irwin, Simon Muya Kasanda, Jeff Klein, Brian Koopman, Arthur Kosowsky, Dale Li, Mathew Madhavacheril, Tobias A. Marriage, Jeff McMahon, Felipe Menanteau, Kavilan Moodley, Charles Munson, Sigurd Naess, Federico Nati, Laura Newburgh, John Nibarger, Michael D. Niemack, Michael R. Nolta, Carolina Nuñez, Lyman A. Page, Christine Pappas, Bruce Partridge, Felipe Rojas, Emmanuel Schaan, Benjamin L. Schmitt, Neelima Sehgal, Blake D. Sherwin, Jon Sievers, Sara Simon, David N. Spergel, Suzanne T. Staggs, Eric R. Switzer, Robert Thornton, Hy Trac, Jesse Treu, Carole Tucker, Alexander Van Engelen, Jonathan T. Ward, and Edward J. Wollack. The Atacama Cosmology Telescope: two-season ACTPol spectra and parameters. Journal of Cosmology and Astroparticle Physics, 2017(06):031–031, June 2017.

[66] Peter J. Lowell, Galen C. O'Neil, Jason M. Underwood, and Joel N. Ullom. Macroscale refrigeration by nanoscale electron transport. Applied Physics Letters, 102(8):082601, February 2013.

[67] Peter Joseph Lowell. Superconducting Tunnel Junction Refrigerators for Sub-Kelvin Cooling of Electrons, Phonons, and Arbitrary, User-Supplied Payloads. Ph.D., University of Colorado Boulder, United States – Colorado, 2014. ISBN: 9781321172010.

[68] I. J. Maasilta and T. Kühn. Effect of Thin Ballistic Membranes on Transition-Edge Sensor Performance. Journal of Low Temperature Physics, 151(1-2):64–69, April 2008.

[69] A. J. Manninen, M. M. Leivo, and J. P. Pekola. Refrigeration of a dielectric membrane by superconductor/insulator/normal-metal/insulator/superconductor tunneling. Applied Physics Letters, 70(14):1885–1887, April 1997. Publisher: American Institute of Physics.

[70] A. Marconi, G. Risaliti, R. Gilli, L. K. Hunt, R. Maiolino, and M. Salvati. Local Supermassive Black Holes, Relics of Active Galactic Nuclei and the X-ray Background. Monthly Notices of the Royal Astronomical Society, 351(1):169–185, June 2004. arXiv:astro-ph/0311619.

[71] Ronald O. Marzke, Margaret J. Geller, John P. Huchra, and Harold G. Corwin, Jr. The luminosity function for different morphological types in the CfA Redshift Survey. The Astronomical Journal, 108:437, August 1994.

[72] John C. Mather. Bolometer noise: nonequilibrium theory. Applied Optics, 21(6):1125, March 1982.

[73] P. D. Mauskopf. Transition Edge Sensors and Kinetic Inductance Detectors in Astronomical Instruments. Publications of the Astronomical Society of the Pacific, 130(990):082001, August 2018.

[74] Nicholas J. McConnell and Chung-Pei Ma. REVISITING THE SCALING RELATIONS OF BLACK HOLE MASSES AND HOST GALAXY PROPERTIES. The Astrophysical Journal, 764(2):184, February 2013.

[75] J. Trevor Mendel, Luc Simard, Michael Palmer, Sara L. Ellison, and David R. Patton. A CATALOG OF BULGE, DISK, AND TOTAL STELLAR MASS ESTIMATES FOR THE SLOAN DIGITAL SKY SURVEY. The Astrophysical Journal Supplement Series, 210(1):3, December 2013.

[76] N. A. Miller, G. C. O'Neil, J. A. Beall, G. C. Hilton, K. D. Irwin, D. R. Schmidt, L. R. Vale, and J. N. Ullom. High resolution x-ray transition-edge sensor cooled by tunnel junction refrigerators. Applied Physics Letters, 92(16):163501, April 2008.

[77] Nathan A Miller. Using electron-tunneling refrigerators to cool electrons, membranes, and sensors. Ph.D., University of Colorado Boulder, 2008.

[78] Dmitry V. Morozov, Alessandro Casaburi, and Robert H. Hadfield. Superconducting photon detectors. Contemporary Physics, 62(2):69–91, April 2021. Publisher: Taylor & Francis _eprint: https://doi.org/10.1080/00107514.2022.2043596.

[79] M. Nahum, T. M. Eiles, and John M. Martinis. Electronic microrefrigerator based on a normal-insulator-superconductor tunnel junction. Applied Physics Letters, 65(24):3123–3125, December 1994. Publisher: American Institute of Physics.

[80] Osamu Nakamura, Masataka Fukugita, Naoki Yasuda, Jon Loveday, Jon Brinkmann, Donald P. Schneider, Kazuhiro Shimasaku, and Mark SubbaRao. The Luminosity Function of Morphologically Classified Galaxies in the Sloan Digital Sky Survey. The Astronomical Journal, 125(4):1682–1688, April 2003.

[81] H. Q. Nguyen, M. Meschke, and J. P. Pekola. A robust platform cooled by superconducting electronic refrigerators. Applied Physics Letters, 106(1):012601, January 2015.

[82] H. Q. Nguyen, J. T. Peltonen, M. Meschke, and J. P. Pekola. Cascade Electronic Refrigerator Using Superconducting Tunnel Junctions. Phys. Rev. Appl., 6(5):054011, November 2016. Publisher: American Physical Society.

[83] Galen C O'Neil. Improving NIS Tunnel Junction Refrigerators: Modeling, Materials, and Traps. Ph.D., University of Colorado Boulder, United States – Colorado, 2011.

[84] Galen C. O'Neil, Peter J. Lowell, Jason M. Underwood, and Joel N. Ullom. Measurement and modeling of a large-area normal-metal/insulator/superconductor refrigerator with improved cooling. Physical Review B, 85(13):134504, April 2012.

[85] R. H. Parmenter. Enhancement of Superconductivity by Extraction of Normal Carriers. Physical Review Letters, 7(7):274–277, October 1961.

[86] Planck Collaboration, P. A. R. Ade, N. Aghanim, C. Armitage-Caplan, M. Arnaud, M. Ashdown, F. Atrio-Barandela, J. Aumont, C. Baccigalupi, A. J. Banday, R. B. Barreiro, J. G. Bartlett, E. Battaner, K. Benabed, A. Benoît, A. Benoit-Lévy, J.-P. Bernard, M. Bersanelli, P. Bielewicz, J. Bobin, J. J. Bock, A. Bonaldi, J. R. Bond, J. Borrill, F. R. Bouchet, M. Bridges, M. Bucher, C. Burigana, R. C. Butler, E. Calabrese, B. Cappellini, J.-F. Cardoso, A. Catalano, A. Challinor, A. Chamballu, R.-R. Chary, X. Chen, H. C. Chiang, L.-Y Chiang, P. R. Christensen, S. Church, D. L. Clements, S. Colombi, L. P. L. Colombo, F. Couchot, A. Coulais, B. P. Crill, A. Curto, F. Cuttaia, L. Danese, R. D. Davies, R. J. Davis, P. De Bernardis, A. De Rosa, G. De Zotti, J. Delabrouille, J.-M. Delouis, F.-X. Désert,

C. Dickinson, J. M. Diego, K. Dolag, H. Dole, S. Donzelli, O. Doré, M. Douspis, J. Dunkley, X. Dupac, G. Efstathiou, F. Elsner, T. A. Enßlin, H. K. Eriksen, F. Finelli, O. Forni, M. Frailis, A. A. Fraisse, E. Franceschi, T. C. Gaier, S. Galeotta, S. Galli, K. Ganga, M. Giard, G. Giardino, Y. Giraud-Héraud, E. Gjerløw, J. González-Nuevo, K. M. Górski, S. Gratton, A. Gregorio, A. Gruppuso, J. E. Gudmundsson, J. Haissinski, J. Hamann, F. K. Hansen, D. Hanson, D. Harrison, S. Henrot-Versillé, C. Hernández-Monteagudo, D. Herranz, S. R. Hildebrandt, E. Hivon, M. Hobson, W. A. Holmes, A. Hornstrup, Z. Hou, W. Hovest, K. M. Huffenberger, A. H. Jaffe, T. R. Jaffe, J. Jewell, W. C. Jones, M. Juvela, E. Keihänen, R. Keskitalo, T. S. Kisner, R. Kneissl, J. Knoche, L. Knox, M. Kunz, H. Kurki-Suonio, G. Lagache, A. Lähteenmäki, J.-M. Lamarre, A. Lasenby, M. Lattanzi, R. J. Laureijs, C. R. Lawrence, S. Leach, J. P. Leahy, R. Leonardi, J. León-Tavares, J. Lesgourgues, A. Lewis, M. Liguori, P. B. Lilje, M. Linden-Vørnle, M. López-Caniego, P. M. Lubin, J. F. Macías-Pérez, B. Maffei, D. Maino, N. Mandolesi, M. Maris, D. J. Marshall, P. G. Martin, E. Martínez-González, S. Masi, M. Massardi, S. Matarrese, F. Matthai, P. Mazzotta, P. R. Meinhold, A. Melchiorri, J.-B. Melin, L. Mendes, E. Menegoni, A. Mennella, M. Migliaccio, M. Millea, S. Mitra, M.-A. Miville-Deschênes, A. Moneti, L. Montier, G. Morgante, D. Mortlock, A. Moss, D. Munshi, J. A. Murphy, P. Naselsky, F. Nati, P. Natoli, C. B. Netterfield, H. U. Nørgaard-Nielsen, F. Noviello, D. Novikov, I. Novikov, I. J. O'Dwyer, S. Osborne, C. A. Oxborrow, F. Paci, L. Pagano, F. Pajot, R. Paladini, D. Paoletti, B. Partridge, F. Pasian, G. Patanchon, D. Pearson, T. J. Pearson, H. V. Peiris, O. Perdereau, L. Perotto, F. Perrotta, V. Pettorino, F. Piacentini, M. Piat, E. Pierpaoli, D. Pietrobon, S. Plaszczynski, P. Platania, E. Pointecouteau, G. Polenta, N. Ponthieu, L. Popa, T. Poutanen, G. W. Pratt, G. Prézeau, S. Prunet, J.-L. Puget, J. P. Rachen, W. T. Reach, R. Rebolo, M. Reinecke, M. Remazeilles, C. Renault, S. Ricciardi, T. Riller, I. Ristorcelli, G. Rocha, C. Rosset, G. Roudier, M. Rowan-Robinson, J. A. Rubiño-Martín, B. Rusholme, M. Sandri, D. Santos, M. Savelainen, G. Savini, D. Scott, M. D. Seiffert, E. P. S. Shellard, L. D. Spencer, J.-L. Starck, V. Stolyarov, R. Stompor, R. Sudiwala, R. Sunyaev, F. Sureau, D. Sutton, A.-S. Suur-Uski, J.-F. Sygnet, J. A. Tauber, D. Tavagnacco, L. Terenzi, L. Toffolatti, M. Tomasi, M. Tristram, M. Tucci, J. Tuovinen, M. Türler, G. Umana, L. Valenziano, J. Valiviita, B. Van Tent, P. Vielva, F. Villa, N. Vittorio, L. A. Wade, B. D. Wandelt, I. K. Wehus, M. White, S. D. M. White, A. Wilkinson, D. Yvon, A. Zacchei, and A. Zonca. *Planck* 2013 results. XVI. Cosmological parameters. Astronomy & Astrophysics, 571:A16, November 2014.

[87] Robert O. Pohl, Xiao Liu, and EunJoo Thompson. Low-temperature thermal conductivity and acoustic attenuation in amorphous solids. Reviews of Modern Physics, 74(4):991–1013, October 2002.

[88] F. Hernando Quintanilla, M. J. S. Lowe, and R. V. Craster. Modeling guided elastic waves in generally anisotropic media using a spectral collocation method. The Journal of the Acoustical Society of America, 137(3):1180–1194, March 2015.

[89] M. Yu. Reizer. Electron-phonon relaxation in pure metals and superconductors at very low temperatures. Physical Review B, 40(8):5411–5416, September 1989.

[90] K Rostem, D T Chuss, K L Denis, and E J Wollack. Wide-stopband aperiodic phononic filters. Journal of Physics D: Applied Physics, 49(25):255301, June 2016.

[91] Gregory V. Samsonov. Handbook of the Physicochemical Properties of the Elements. Springer Science & Business Media, 2012.

[92] P. Schechter. An analytic expression for the luminosity function for galaxies. The Astrophysical Journal, 203:297, January 1976.

[93] Maarten Schmidt. Space Distribution and Luminosity Functions of Quasi-Stellar Radio Sources. The Astrophysical Journal, 151:393, February 1968.

[94] K. Schwab, E. A. Henriksen, J. M. Worlock, and M. L. Roukes. Measurement of the quantum of thermal conductance. Nature, 404(6781):974–977, April 2000.

[95] A. Sergeev and V. Mitin. Electron-phonon interaction in disordered conductors: Static and vibrating scattering potentials. Physical Review B, 61(9):6041–6047, March 2000.

[96] Francesco Shankar, David H. Weinberg, and Jordi Miralda-Escude'. Self-Consistent Models of the AGN and Black Hole Populations: Duty Cycles, Accretion Rates, and the Mean Radiative Efficiency. The Astrophysical Journal, 690(1):20–41, January 2009. arXiv:0710.4488 [astro-ph].

[97] R. M. Shannon, V. Ravi, L. T. Lentati, P. D. Lasky, G. Hobbs, M. Kerr, R. N. Manchester, W. A. Coles, Y. Levin, M. Bailes, N. D. R. Bhat, S. Burke-Spolaor, S. Dai, M. J. Keith, S. Osłowski, D. J. Reardon, W. Van Straten, L. Toomey, J.-B. Wang, L. Wen, J. S. B. Wyithe, and X.-J. Zhu. Gravitational waves from binary supermassive black holes missing in pulsar observations. Science, 349(6255):1522–1525, September 2015.

[98] Luc Simard, J. Trevor Mendel, David R. Patton, Sara L. Ellison, and Alan W. McConnachie. A CATALOG OF BULGE+DISK DECOMPOSITIONS AND UPDATED PHOTOMETRY FOR 1.12 MILLION GALAXIES IN THE SLOAN DIGITAL SKY SURVEY. The Astrophysical Journal Supplement Series, 196(1):11, September 2011.

[99] Luc Simard, Christopher N. A. Willmer, Nicole P. Vogt, Vicki L. Sarajedini, Andrew C. Phillips, Benjamin J. Weiner, David C. Koo, Myungshin Im, Garth D. Illingworth, and S. M. Faber. The DEEP Groth Strip Survey. II. *Hubble Space Telescope* Structural Parameters of Galaxies in the Groth Strip. The Astrophysical Journal Supplement Series, 142(1):1–33, September 2002.

[100] Joseph Simon and Sarah Burke-Spolaor. Constraints on Black Hole/Host Galaxy Co-evolution and Binary Stalling Using Pulsar Timing Arrays. The Astrophysical Journal, 826(1):11, July 2016. arXiv:1603.06577 [astro-ph].

[101] Matthias Steinmetz and Julio F. Navarro. The hierarchical origin of galaxy morphologies. New Astronomy, 7(4):155–160, June 2002.

[102] E. T. Swartz and R. O. Pohl. Thermal resistance at interfaces. Applied Physics Letters, 51(26):2200–2202, December 1987.

[103] M. A. Tarasov, L. S. Kuz'min, M. Yu. Fominskii, I. E. Agulo, and A. S. Kalabukhov. Electron cooling in a normal-metal hot-electron bolometer. Journal of Experimental and Theoretical Physics Letters, 78(11):714–717, December 2003.

[104] Karun Thanjavur, Luc Simard, Asa F. L. Bluck, and Trevor Mendel. Stellar mass functions of galaxies, discs and spheroids at z 0.1. Monthly Notices of the Royal Astronomical Society, 459(1):44–69, June 2016.

[105] M. Tinkham and V. Emery. Introduction to Superconductivity, volume 49. Physics Today, 10 edition, 1996.

[106] Yoshihiro Ueda. Cosmological evolution of supermassive black holes in galactic centers unveiled by hard X-ray observations. Proceedings of the Japan Academy, Series B, 91(5):175–192, 2015.

[107] J.N. Ullom, W.B. Doriese, D.A. Fischer, J.W. Fowler, G.C. Hilton, C. Jaye, C.D. Reintsema, D.S. Swetz, and D.R. Schmidt. Transition-Edge Sensor Microcalorimeters for X-ray Beamline Science. Synchrotron Radiation News, 27(4):24–27, July 2014. Publisher: Taylor & Francis _eprint: https://doi.org/10.1080/08940886.2014.930806.

[108] Joel N Ullom and Douglas A Bennett. Review of superconducting transition-edge sensors for x-ray and gamma-ray spectroscopy. Superconductor Science and Technology, 28(8):084003, August 2015.

[109] Jason M. Underwood, Peter J. Lowell, Galen C. O'Neil, and Joel N. Ullom. Insensitivity of Sub-Kelvin Electron-Phonon Coupling to Substrate Properties. Physical Review Letters, 107(25):255504, December 2011.

[110] Vasundara Varatharajulu and Yih-Hsing Pao. Scattering matrix for elastic waves. I. Theory. The Journal of the Acoustical Society of America, 60(3):556–566, September 1976.

[111] N. Vercruyssen, R. Barends, T. M. Klapwijk, J. T. Muhonen, M. Meschke, and J. P. Pekola. Substrate-dependent quasiparticle recombination time in superconducting resonators. Applied Physics Letters, 99(6):062509, August 2011.

[112] Samantha Walker, Jason E. Austermann, James A. Beall, Bradley J. Dober, Shannon M. Duff, Gene C. Hilton, Johannes Hubmayr, Joel N. Ullom, Jeffrey L. Van Lanen, and Michael R. Vissers. Measurements of AlMn TES bolometers well described by simple electrothermal model. In Jonas Zmuidzinas and Jian-Rong Gao, editors, Millimeter, Submillimeter, and Far-Infrared Detectors and Instrumentation for Astronomy X, page 188, Online Only, United States, January 2021. SPIE.

[113] G. Wang, V. Yefremenko, V. Novosad, A. Datesman, J. Pearson, R. Divan, C. L. Chang, L. Bleem, A. T. Crites, J. Mehl, T. Natoli, J. McMahon, J. Sayre, J. Ruhl, S. S. Meyer, and J. E. Carlstrom. Thermal Properties of Silicon Nitride Beams Below One Kelvin. IEEE Transactions on Applied Superconductivity, 21(3):232–235, 2010.

[114] Anna K. Weigel, Kevin Schawinski, and Claudio Bruderer. Stellar mass functions: methods, systematics and results for the local Universe. Monthly Notices of the Royal Astronomical Society, 459(2):2150–2187, June 2016.

[115] Benjamin Westbrook, Bhoomija Prasad, Christopher R. Raum, Adrian T. Lee, Aritoki Suzuki, Johannes Hubmayr, Shannon M. Duff, Micheal J. Link, and Tammy J. Lucas. Thermal Annealing of AlMn Transition Edge Sensors for Optimization in Cosmic Microwave Background Experiments. Journal of Low Temperature Physics, 216(1):264–272, July 2024.

[116] E. A. Williams, S. Withington, C. N. Thomas, D. J. Goldie, and D. Osman. Superconducting transition edge sensors with phononic thermal isolation. Journal of Applied Physics, 124(14):144501, October 2018.

[117] S. Withington and D. J. Goldie. Low-dimensional phononic structures for ultra-low-noise transition edge sensors. page 84520D, Amsterdam, Netherlands, September 2012.

[118] S. Withington, E. Williams, D. J. Goldie, C. N. Thomas, and M. Schneiderman. Thermal elastic-wave attenuation in low-dimensional SiNx bars at low temperatures. Journal of Applied Physics, 122(5):054504, August 2017.

[119] R. C. Zeller and R. O. Pohl. Thermal Conductivity and Specific Heat of Noncrystalline Solids. Physical Review B, 4(6):2029–2041, September 1971.

[120] Nobuyuki Zen, Tuomas A. Puurtinen, Tero J. Isotalo, Saumyadip Chaudhuri, and Ilari J. Maasilta. Engineering thermal conductance using a two-dimensional phononic crystal. Nature Communications, 5(1):3435, March 2014.

[121] X. Zhang, S. M. Duff, G. C. Hilton, P. J. Lowell, K. M. Morgan, D. R. Schmidt, and J. N. Ullom. Controlling the thermal conductance of silicon nitride membranes at 100 mK temperatures with patterned metal features. Applied Physics Letters, 115(5):052601, July 2019.

[122] Xiaohang Zhang. Sub-Kelvin Refrigerators and Sensors. PhD thesis, University of Colorado Boulder, United States – Colorado, 2019.

[123] Xiaohang Zhang, Peter J. Lowell, Brandon L. Wilson, Galen C. O'Neil, and Joel N. Ullom. Macroscopic Subkelvin Refrigerator Employing Superconducting Tunnel Junctions. Physical Review Applied, 4(2):024006, August 2015.

[124] J M Ziman. Electrons and Phonons. Clarendon Press, 1963.

[125] B.L. Zink and F. Hellman. Specific heat and thermal conductivity of low-stress amorphous Si–N membranes. Solid State Communications, 129(3):199–204, January 2004.

[126] J. Zittartz, A. Bringer, and E. Müller-Hartmann. Impurity bands in superconductors with magnetic impurities. Solid State Communications, 10(6):513–516, March 1972.

[127] Jonas Zmuidzinas. Superconducting Microresonators: Physics and Applications. Annual Review of Condensed Matter Physics, 3(Volume 3, 2012):169–214, March 2012. Publisher: Annual Reviews.

Appendix A

Appendix

A.1 Thermal Conductance Equations

G_x is defined as the thermal conductance of a 400-nm-thick layer of material x at 170 mK, S refers to the the SiO_x-SiN_x substrate bi-layer, G_W refers to the Nb wiring layer, and G_I the SiN_x insulating layer. The substrate nitride is a furnace-grown layer deposited via Low Pressure Chemical Vapor Deposition, and the insulating nitride is grown at a lower temperature via Plasma Enhanced Chemical Vapor Deposition.

As deposited, the substrate layer is 300 nm of SiN_x on top of 300 nm of SiO_x which serves as an etch stop during the deep etch membrane release. We expect up to 30 nm of SiO_x is removed during the deep etch. Some of the nitride is also removed, and the amount varies with film stack geometry. The removal of both materials are reflected in the overall measured thickness in Table 4.1. The thermal conductances of bolometers 1-8 from Table 4.2 are expressed in terms of G_S, G_W, and G_I below.

A.1.1 G_{TES} of Bolometers 1-8

$$G_{\mathrm{TES}}(1) = 4 \times G(A) \tag{A.1a}$$

$$G_{\mathrm{TES}}(2) = 1 \times G(A) + 3 \times G(G) \tag{A.1b}$$

$$G_{\mathrm{TES}}(3) = 2 \times G(A) + 2 \times G(G) \tag{A.1c}$$

$$G_{\mathrm{TES}}(4) = 3 \times G(A) + 1 \times G(G) \tag{A.1d}$$

$$G_{\mathrm{TES}}(5) = 1 \times G(B) + 3 \times G(F) \tag{A.1e}$$

$$G_{\mathrm{TES}}(6) = 1 \times G(B) + 3 \times G(E) \tag{A.1f}$$

$$G_{\mathrm{TES}}(7) = 2 \times G(A) + 1 \times G(C) + 1 \times G(D) \tag{A.1g}$$

$$G_{\mathrm{TES}}(6) = 1 \times G(B) + 3 \times G(G) \tag{A.1h}$$

A.1.2 G_{leg} of Legs A-G

$$\begin{aligned} G(A) = {} & G_{S,0}\left(\frac{d_{S,A}}{400\ nm}\right)^{1+\alpha_S} \\ & + G_{W,0}\left[\left(\frac{d_{W1,A}}{400\ nm}\right)^{1+\alpha_W} + \frac{3}{5}\left(\frac{d_{W2,A}}{400\ nm}\right)^{1+\alpha_W}\right] \\ & + G_{I,0}\left[\left(\frac{d_{I1,A}}{400\ nm}\right)^{1+\alpha_I} + \left(\frac{d_{I2,A}}{400\ nm}\right)^{1+\alpha_I}\right] \end{aligned} \tag{A.2a}$$

$$\begin{aligned} G(B) = {} & G_{S,0}\left(\frac{d_{S,B}}{400\ nm}\right)^{1+\alpha_S} \\ & + G_{W,0}\left[\left(\frac{d_{W1,B}}{400\ nm}\right)^{1+\alpha_W} + \frac{3}{5}\left(\frac{d_{W2,B}}{400\ nm}\right)^{1+\alpha_W}\right] \\ & + G_{I,0}\left(\frac{d_{I1,B}}{400\ nm}\right)^{1+\alpha_I} \end{aligned} \tag{A.2b}$$

$$\begin{aligned} G(C) = {} & G_{S,0}\left(\frac{d_{S,C}}{400\ nm}\right)^{1+\alpha_S} \\ & + G_{W,0}\frac{3}{5}\left(\frac{d_{W2,C}}{400\ nm}\right)^{1+\alpha_W} \\ & + G_{I,0}\left[\left(\frac{d_{I1,C}}{400\ nm}\right)^{1+\alpha_I} + \left(\frac{d_{I2,C}}{400\ nm}\right)^{1+\alpha_I}\right] \end{aligned} \tag{A.2c}$$

$$G(D) = G_{S,0}\left(\frac{d_{S,D}}{400\ nm}\right)^{1+\alpha_S} + G_{W,0}\left(\frac{d_{W1,D}}{400\ nm}\right)^{1+\alpha_W} + G_{I,0}\left(\frac{d_{I1,D}}{400\ nm}\right)^{1+\alpha_I} \tag{A.2d}$$

$$G(E) = G_{S,0}\left(\frac{d_{S,E}}{400\ nm}\right)^{1+\alpha_S} + G_{W,0}\left[\left(\frac{d_{W1,E}}{400\ nm}\right)^{1+\alpha_W} + \frac{3}{5}\left(\frac{d_{W2,E}}{400\ nm}\right)^{1+\alpha_W}\right] \tag{A.2e}$$

$$G(F) = G_{S,0}\left(\frac{d_{S,F}}{400\ nm}\right)^{1+\alpha_S} + G_{I,0}\left(\frac{d_{I1,F}}{400\ nm}\right)^{1+\alpha_I} + \left(\frac{d_{I2,F}}{400\ nm}\right)^{1+\alpha_I} \tag{A.2f}$$

$$G(G) = G_{S,0}\left(\frac{d_{S,A}}{400\ nm}\right)^{1+\alpha_S} \tag{A.2g}$$

A.2 Non-Standard Width Scaling

In the case of the W1-W2 stack on Leg E, we treat the stack as a single W layer with a combined thickness and effective width that is the thickness-weighted average of the two. We found that I1 layers on leg stacks in which I2 are removed are trimmed to the 3-um-width of the W2 layer on top of I1.

A.3 Alternative Thin Film G Models

A.3.1 Four Layer Model

We treat the substrate SiO_x-SiN_x bi-layer as a single layer to minimize the number of free parameters in our model given amorphous solids have similar thermal conductivities at sub-Kelvin temperatures [87, 119]. When considering a model that separates the oxide and nitride layers in the substrate, we found the resulting measurements G_x and α_x to be statistically questionable and contradictory to historical measurements. This model fits 7 free parameters to 8 independent G_{TES} measurements, and the reduced χ^2 value for the four-layer model is larger than the three-layer

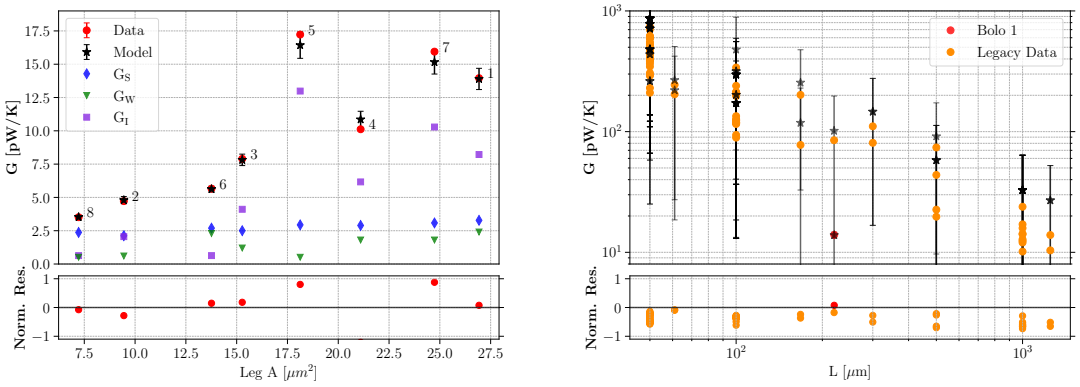

(a) (b)

Figure A.1: Constrained model predictions of a) the devices under test and b) the CMB legacy bolometer data.

model by a factor of ∼10. Measurements of more leg stack geometries are needed before considering a four-layer model.

A.3.2 Constrained α Model

As mentioned in Chapter 4, there is no obvious physical motivation for $\alpha > 1$, but constraining α_x to $[0, 1]$ misses the global minimum in parameter space and produces a higher reduced χ^2 value of 2.98 compared to the unconstrained model. This results in a higher estimations of G_S and G_I to compensate for the relatively suppressed α_I. Figure A.1 shows the constrained model thermal conductance predictions for a) the devices under test and b) the CMB legacy bolometer data. The constraint of $\alpha_I \leq 1$ underestimates G of Bolometers 5 or 7, both of which have I1-I2 layer stacks. The larger error bars on G_S lead to incredibly large errors on legacy bolometer G predictions, which have significantly thicker substrate layers than the devices under test. The constrained model also over predicts the entire data set as a consequence of the higher G_S and G_I values.